

Sulfur-Containing Functional Supramolecular Fibers for Filtration Applications

DISSERTATION

zur Erlangung des akademischen Grades eines
Doktors der Naturwissenschaften (Dr. rer. nat.)
im Promotionsprogramm „Polymer Science“

in der Bayreuther Graduiertenschule für Mathematik und Naturwissenschaften (BayNAT)
der Universität Bayreuth

vorgelegt von

David Michael Nardini

geboren in Nürnberg

Bayreuth, 2021

Der experimentelle Teil der vorliegenden Arbeit wurde in der Zeit von November 2016 bis Dezember 2020 in Bayreuth am Lehrstuhl Makromolekulare Chemie I und am Bayerischen Polymer Institut (BPI) unter Betreuung von Herrn Professor Dr. Hans-Werner Schmidt angefertigt.

Vollständiger Abdruck der von der Bayreuther Graduiertenschule für Mathematik und Naturwissenschaften (BayNAT) der Universität Bayreuth genehmigten Dissertation zur Erlangung des akademischen Grades eines Doktors der Naturwissenschaften (Dr. rer. nat.).

Dissertation eingereicht am: 13.12.2021

Zulassung durch das Leitungsgremium: 21.12.2021

Wissenschaftliches Kolloquium: 08.04.2022

Amtierender Direktor: Prof. Dr. Hans Keppler

Prüfungsausschuss:

Prof. Dr. Hans-Werner Schmidt (Gutachter)

Prof. Dr. Andreas Greiner (Gutachter)

Prof. Dr. Georg Papastavrou (Vorsitz)

Prof. Dr. Thomas Scheibel

Die vorliegende Arbeit ist als Monographie verfasst.

Teile der Arbeit sind bereits in der folgenden Publikation erschienen:

Helga Thomas, Xiomin Zhu, Martin Möller, Klaus Kreger, David Nardini, Hans-Werner Schmidt, *Supramolecular nanofiber composites for highly efficient and selective removal of gold(III) from aqueous media*, Technische Textilien, **2019**, 2. 80 E

[Diese Publikation ist als Literaturstelle 180 zitiert.]

*“Nine tenth of alchemy was chemistry.
And nine tenth of chemistry was waiting”*
Mandrag in
The Slow Regard of Silent Things

List of symbols and abbreviations

$^1\text{H-NMR}$	Nuclear magnetic resonance spectroscopy
Å	Angström
ATR	Attenuated total reflection
AgNP	Silver nanoparticle
a.u.	Arbitrary unit
BTA	1,3,5-Benzenetrisamide
BuLi	Butyllithium
CFU	Colony forming unit
CTA	1,3,5-Cyclohexanetrisamide
DCM	Dichloromethane
DMF	Dimethylformamide
DMSO	Dimethyl sulfoxide
DSC	Differential scanning calorimetry
δ	Chemical shift
eV	Electron volt
EDX	Energie disperse X-ray
<i>E.coli</i>	Escherichia coli
EtOH	Ethanol
FTIR	Fourier-transform infrared
Fmoc	Fluorenyl methoxycarbonyl
ICP-OES	Inductively coupled plasma-optical emission spectroscopy
IUPAC	International Union of Pure and Applied Chemistry
IPA	Isopropanol
iPP	Isotactic polypropylene
K	Permeability constant
λ	Wavelength
HEPA	High-efficiency particulate air filter
HOF	Hydrogen-bonded organic framework
L	Thickness of a filter media
LC	Liquid crystal
LDA	Lithiumdiisopropylamide
LASER	Light amplification by stimulated emission of radiation
M^+	Molecular ion peak
m	Mass

MeOH	Methanol
μm	Micrometer
m/z	Mass-to-charge ratio
MPPS	Most penetrating particle size
MS	Mass spectroscopy
η	Dynamic viscosity
nm	Nanometer
n.d.	Not determined
NP	Nanoparticle
Δp	Differential pressure
p.a.	per analysis
PAN	Polyacrylonitrile
PMMA	Poly(methyl methacrylate)
ppm	Parts per million
POU	Point of use
PS	Polystyrene
RT	Room temperature
ref.	Reference
rpm	Revolutions per minute
SEM	Scanning electron microscope
TEM	Transmission electron microscopy
TGA	Thermogravimetric analysis
T_c	Crystallization temperature
T_m	Melting temperature
ULPA	Ultra low penetration air filter
UV	Ultraviolet
v	Velocity
v/v	Volume ratio
wt.-%	Weight percent
w/w	Weight ratio

Table of content

Summary	1
Zusammenfassung.....	3
1 Introduction.....	5
1.1 Preparation of fibers in the micro-, submicron- and nanometer scale	6
1.2 Supramolecular Chemistry.....	11
1.2.1 Secondary interactions in supramolecular chemistry	11
1.2.2 The material class of 1,3,5-benzenetrisamides	15
1.3 Separation methods.....	27
1.3.1 Thermal and mechanical separation.....	27
1.3.2 Separation by filtration	28
1.3.3 Types of filter media	28
1.3.4 Properties of a hypothetical ideal filter medium.....	28
1.3.5 Filter Conditions.....	28
1.3.6 Filtration mechanisms.....	30
1.4 Adsorption.....	34
2 Aim of the thesis	37
3 Synthesis, characterization and self-assembly of 1,3,5-benzenetrisamides with sulfur-containing substituents.....	41
3.1 Synthesized sulfur-containing 1,3,5-benzenetrisamides	44
3.2 Thermal characterization and FTIR-studies.	55
3.2.1 Thermal properties	55
3.2.2 FTIR-Spectroscopy.....	61
3.3 Self-assembly of sulfur-containing 1,3,5-benzenetrisamides to supramolecular (nano)fibers..	66
3.3.1 Self-assembly processing schemes	66
3.3.2 Solubility and self-assembly behavior of sulfur-containing 1,3,5-benzenetrisamides in polar solvents at defined concentrations.....	67
3.3.3 Self-assembly behavior of sulfur-containing BTAs.....	72
3.4 Application of functional supramolecular fibers to adsorb silver nanoparticles.....	86
3.5 Conclusion.....	88

4	Multicomponent self-assembly to functional supramolecular fibers with core-shell structure..	89
4.1	Clear and cloud point investigations of selected 1,3,5-benzenetrisamides	95
4.2	Multicomponent self-assembly to core-shell fibers	98
4.2.1	Multicomponent self-assembly from 1-propanol.....	100
4.2.2	Multicomponent self-assembly from 1-propanol/water.....	107
4.2.3	Multicomponent self-assembly from 2-butanone.....	112
4.3	Adsorption of metal ions on supramolecular core-shell fibers from aqueous solution	118
4.3.1	Preparation of mechanically stable composites with supramolecular core-shell fibers...	118
4.3.2	Adsorption of metal ions on the composite	123
4.4	Conclusion.....	132
5	Sand–supramolecular nanofiber composites for the filtration of bacteria from water	133
5.1	Water treatment of polluted water	133
5.2	Supramolecular sea sand nanofiber composites for filtration	138
5.2.1	Components and preparation of sand-nanofiber composites as filter media	138
5.2.2	SEM-Characterization of the sea sand nanofiber composites.....	141
5.2.3	Investigation of the sea sand nanofiber composites stability at various water-flow conditions.....	144
5.3	Filtration with sea sand nanofiber composites.....	149
5.3.1	Filtration experiments of polymer model particles	149
5.3.2	Deposition of silver nanoparticles on functional supramolecular nanofiber	153
5.3.3	Filtration of <i>E.coli</i> bacteria	159
5.4	Conclusion.....	169
6	Experimental part	171
6.1	Materials	171
6.2	Analytical methods.....	171
6.3	Synthesis	174
6.3.1	Synthesis of the peripheral sulfur-containing amine side groups	174
6.3.2	Synthesis of 1,3,5-benzenetrisamides	177
6.4	Silver nanoparticle synthesis.....	212
7	Literature.....	213
8	Acknowledgement	227

Summary

Access to clean water is one of the global challenges of the 21st century, aiming to enable a healthy society. Contaminations of water with detrimental bacteria and metals burden the society and the environment. Therefore, novel approaches to efficient filter media based on fibrous materials with a high surface area are desirable. This includes also a high functionality at the fiber surface to specifically fixate contaminants. In this context, supramolecular chemistry provides an opportunity to straightforwardly prepare self-assembled *functional supramolecular fibers via a bottom-up* approach. The unique characteristic of a bottom-up approach, in contrast to a top-down approach, which is conventionally used in fiber spinning, is the possibility to carry out the fiber formation within pores and cavities of existing structures, such as nonwovens or sand fillings. In this respect, the thesis is dedicated to the synthesis and self-assembly of *sulfur-containing functional supramolecular fibers for filtration applications*.

The first part deals with the *synthesis, characterization and self-assembly of 1,3,5-benzenetrisamides with sulfur-containing substituents*. 1,3,5-Benzenetrisamides (BTAs) were selected because they are a well-established material class to prepare supramolecular nanostructures. So far very little is known from sulfur-containing BTAs in the above context. In total, sixteen different functional BTAs were synthesized and characterized, including BTAs with sulfur-containing aliphatic, amino acid-based and aromatic side groups. These functional BTAs were in particular studied in view of their solubility and subsequently their self-assembly behavior to form supramolecular objects. FTIR spectroscopy indicated intermolecular threefold directed hydrogen bonds between the amide groups leading to columnar self-assembly and the formation of supramolecular fibers. Almost all BTAs with aliphatic sulfur-containing side groups and with cysteine- or methionine-based side groups are soluble in polar organic solvents, but not or only slightly soluble in water. Comprehensive studies of the self-assembly behavior of the BTAs in different solvents showed that three BTAs in particular assembled very well to supramolecular nanofibers. To proof the functionality of the surface of the nanofibers, the adsorption of silver nanoparticles (AgNPs) was tested. TEM investigations revealed the successful adsorption of the AgNPs.

The second part of this work deals with *multicomponent self-assembly to functional supramolecular fibers with core-shell structure*, with a mechanically stable core and the function in the shell. For this, two different BTAs were selected. Based on the findings of the first chapter, a BTA with *L-methionine side groups* was selected as functional building block. The second one was an aliphatic BTA with *2-ethylhexyl side groups* which is known for excellent fiber formation. The idea of such a co-assembly is the formation of core-shell fibers with a functional shell. To achieve core shell structures, clear and cloud points of the neat components in selected solvent systems were systematically studied first. Two solvent systems were found in which the aliphatic BTA was less soluble than the functional

L-methionine based BTA. This finding points to an earlier self-assembly of the aliphatic BTA and the formation of a core structure in multicomponent self-assembly. Self-assembly experiments were performed and the resulting fibers were investigated with various techniques. Especially with Raman imaging, the formation of novel functional supramolecular core-shell fibers could be impressively demonstrated.

To utilize these core-shell fibers, composite structures were prepared by the *in-situ* formation of supramolecular fibers within nonwovens. These composites provide a sufficient mechanical stability to be used in aqueous media as demonstrated in experiments with a continuous flow of 60 mL/min. By the utilization of an aqueous H₂AuCl₄ solution under these conditions, Au ions could be efficiently deposited on the composite. For instance, up to 99 % of the Au ions were successfully immobilized within 24 h from an aqueous solution with a concentration of 877 mg/L. Furthermore, it was shown that the functional *L-methionine* BTA adsorbs metal-ions with affinities of Au³⁺>>Hg²⁺>Ag⁺>Pt²⁺ demonstrating also the selectivity of these composites.

The third part of this thesis deals with *sand-supramolecular nanofiber composites for the filtration of bacteria from water*. Here, the *in-situ* formation of supramolecular fibers was carried out within the cavities of a granular sand filling. The composites were prepared by co-self-assembly of mixtures of the *2-ethylhexyl* BTA and *L-methionine* BTA using 2-butanone as solvent within a sand filling. SEM studies revealed a dense supramolecular fiber network between and on the sand grains. The resulting enhanced mechanical stability of the sand-nanofiber composites was confirmed by applying a relatively high continuous waterflow of 500 mL/min. Under these conditions the composites were stable and filtration experiments were performed with 1.1 μm polystyrene model particles which have comparable dimensions as bacteria. Up to 90 % of PS particles were effectively filtered at a water flow rate of 500 mL/min. Silver nanoparticles (AgNPs) as antibacterial agents were immobilized on the surface of the supramolecular fibers. UV/Vis spectroscopy and SEM-EDX demonstrated efficient deposition of the AgNPs on the functional shell. To proof the effect of AgNPs during filtration, experiments with suspensions containing *E.coli* bacteria at concentrations of 10³ and 10⁴ CFU/mL were carried out. Here, the reduction of bacteria during filtration was shown to be impressively increased by the use of AgNPs. More than 99.99 % of the bacteria were removed or killed during filtration through the sand nanofiber composite.

Zusammenfassung

Die Verfügbarkeit von sauberem Wasser ist eine der globalen Herausforderungen des 21. Jahrhunderts für eine gesunde Gesellschaft. Insbesondere Verunreinigungen von Wasser mit Schadstoffen wie Bakterien und Metallen belasten sowohl unsere Gesellschaft als auch die Umwelt. Daher sind neuartige Ansätze für effiziente Filtermedien auf Basis von Fasermaterialien mit großer Oberfläche wünschenswert. Dazu gehört auch eine hohe Funktionalität der Faseroberfläche, um Verunreinigungen gezielt zu binden. In diesem Zusammenhang bietet die supramolekulare Chemie die Möglichkeit, durch einen *bottom-up*-Ansatz selbstassemblierte funktionale supramolekulare Fasern herzustellen. Das einzigartige Merkmal eines *bottom-up*-Ansatzes, im Gegensatz zu einem *top-down*-Ansatz, der üblicherweise beim Faserspinnen verwendet wird, ist die Möglichkeit, die Faserbildung innerhalb von Hohlräumen in bestehenden Strukturen wie Vliesstoffen oder Sandschüttungen zu realisieren. In diesem Zusammenhang beschäftigt sich diese Arbeit mit der Synthese und Selbstassemblierung von schwefelhaltigen funktionellen supramolekularen Fasern für Filtrationsanwendungen.

Der erste Teil der Arbeit befasst sich mit der *Synthese, Charakterisierung und Selbstorganisation von 1,3,5-Benzoltriamiden mit schwefelhaltigen Substituenten*. 1,3,5-Benzoltriamide (BTAs) wurden ausgewählt, weil es sich um eine etablierte Materialklasse zur Herstellung von supramolekularen Fasern handelt. Über schwefelhaltige BTAs ist jedoch bis jetzt wenig bekannt. Insgesamt wurden sechzehn verschiedene funktionelle BTAs synthetisiert und charakterisiert, darunter BTAs mit aliphatischen, aminosäurebasierten und aromatischen schwefelhaltigen Seitengruppen. Diese funktionellen BTAs wurden auf ihr Löslichkeitsverhalten und Selbstassemblierungsverhalten zu supramolekularen Objekten hin untersucht. FTIR-Spektroskopie wies auf intermolekulare, dreifach gerichtete Wasserstoffbrücken zwischen den Amidgruppen hin, die zum kolumnaren Aufbau der selbstassemblierten supramolekularen Fasern führen. Nahezu alle BTAs mit aliphatischen schwefelhaltigen Seitengruppen und mit Cystein- oder Methioninseitengruppen sind in polaren organischen Lösemitteln löslich, jedoch nur gering in Wasser. Umfassende Untersuchungen des Selbstassemblierungsverhaltens aller BTAs in verschiedenen Lösungsmitteln zeigten, dass insbesondere drei BTAs zu vielversprechenden supramolekularen Nanofasern assemblierten. Zum Nachweis der Funktionalität der Nanofaseroberfläche wurde die Adsorption von Silbernanopartikeln (AgNPs) untersucht. TEM-Untersuchungen bestätigten die erfolgreiche Adsorption der AgNPs.

Der zweite Teil dieser Arbeit befasst sich mit der *Multikomponenten-Selbstassemblierung zu funktionellen supramolekularen Fasern mit Kern-Schale-Struktur*. Hierfür wurden zwei unterschiedliche BTAs ausgewählt. Aufgrund der Ergebnisse des ersten Kapitels wurde das BTA mit *L-Methionin-Seitengruppen* als funktioneller Baustein ausgewählt. Der zweite Baustein ist ein aliphatisches BTA mit *2-Ethylhexyl-Seitengruppen*, das für die ausgezeichnete Faserbildung bekannt ist.

Ziel war die Co-Assemblierung von BTAs zur Herstellung funktionaler supramolekularer Kern-Schale-Fasern. Um Kern-Schale-Strukturen zu erhalten, wurden zunächst die Klar- und Trübungspunkte der einzelnen Komponenten in ausgewählten Lösungsmittelsystemen systematisch untersucht. Zwei Lösungsmittelsysteme wurden gefunden, in denen das aliphatische BTA weniger löslich ist als das funktionelle *L-Methionin*-BTA. Diese Ergebnisse sollten es ermöglichen eine vorgelagerte Selbstassemblierung des aliphatischen BTAs und die Bildung einer Schalenstruktur des funktionellen BTAs bei der Co-Assemblierung zu erreichen. Es wurden Experimente zur Selbstassemblierung durchgeführt und die resultierenden Fasern mit verschiedenen Techniken untersucht. Insbesondere mittels *Raman-Imaging* konnte die Bildung neuartiger funktionaler supramolekularer Kern-Schale-Fasern eindrucksvoll demonstriert werden. Um diese Kern-Schale-Fasern zu nutzen, wurden *Komposit-Strukturen* durch die *in-situ*-Bildung von supramolekularen Fasern in Vliesstoffen hergestellt. Diese Komposite bieten eine ausreichend hohe mechanische Stabilität für den Einsatz in wässrigen Medien. Anwendungen bei einem kontinuierlichen Fluss von 60 mL/min bestätigen die Stabilität der Komposite. Bei Verwendung einer wässrigen H₂AuCl₄-Lösung konnten unter diesen Bedingungen Au-Ionen effizient auf dem Komposit abgeschieden werden. Beispielsweise wurden so bis zu 99 % der Au-Ionen innerhalb von 24 h aus einer wässrigen Lösung mit einer Konzentration von 877 mg/L immobilisiert. Außerdem wurde gezeigt, dass das funktionelle *L-Methionin*-BTA Metallionen mit den Affinitäten Au³⁺>>Hg²⁺>Ag⁺>Pt²⁺ adsorbiert, was auch die Selektivität belegt.

Der dritte Teil befasst sich mit *Sand-Supramolekularen-Nanofaser-Kompositen für die Filtration von Bakterien aus Wasser*. Hierzu wurde die Bildung von supramolekularen Fasern *in-situ* in den Hohlräumen einer Sandschüttung durchgeführt. Die Komposite wurden durch Co-Assemblierung von Mischungen aus *2-Ethylhexyl* BTA und *L-Methionin* BTA mit 2-Butanon als Lösungsmittel innerhalb der Sandschüttung hergestellt. REM-Untersuchungen zeigten ein dichtes supramolekulares Fasernetzwerk zwischen und auf den Oberflächen der Sandkörner. Die ausgezeichnete Stabilität der Sand-Nanofaser-Komposite wurde durch Durchflussexperimente mit 500 mL/min bestätigt. Es wurden Filtrationsversuche mit 1.1 µm großen PS-Modellpartikeln, die eine vergleichbare Größe wie Bakterien haben, durchgeführt. Unter diesen Bedingungen wurden bis zu 90 % der PS-Partikel effektiv filtriert. Die Immobilisierung von AgNPs als antibakterielle Wirkstoffe auf der Oberfläche der supramolekularen Fasern wurde mit Hilfe von UV/Vis-Spektroskopie und REM-EDX nachgewiesen. Es zeigte sich, dass AgNPs effizient auf der funktionellen Schale abgeschieden wurden. Zum Nachweis der Wirkung der AgNPs wurden Experimente mit Suspensionen durchgeführt, die *E.coli*-Bakterien in Konzentrationen von 10³ und 10⁴ KBE/mL enthielten. Dabei zeigte sich, dass die Reduktion der Bakterien während der Filtration durch den Einsatz von AgNPs eindrucksvoll gesteigert werden konnte. So wurden mehr als 99.99 % der Bakterien während der Filtration durch die Sand-Nanofaser-Komposite entfernt oder abgetötet.

1 Introduction

A global challenge is the available amount of fresh water, which is currently needed. Due to climate change and a rising world population, this amount is expected to strongly increase in the future as claimed by the WHO.^[1] Already now, the usage of ground and surface water, which is contaminated by microbiological pathogens causes millions of deaths around the world.^[1-7] This contaminated water is one major source for different diseases like diarrhea, typhoid fever or bacterial diseases like cholera mainly harming children and older people.^[2,8,9] Furthermore, the pollution of rivers with heavy metal waste increased in the last years.^[10-13] An important aspect is to remove and recover the heavy metals from waste water and rivers as these metals are often detrimental for the environment in general and in case of an accumulation in a living body it is also harmful for animals and humans.^[14] Also industrial waste water may contain a high amount of heavy or noble metals and ions. For example, investigations of sewage sludge in Switzerland showed that in some cases economically relevant quantities of noble metals such as gold and silver were found.^[15] In this context, the sixth goal of the UN sustainable development aims to ensure access to water and sanitation for all people on the planet.^[16] Thus, one major target of many research groups is the development of novel, easy to use and cheap water filter systems to remove pathogens or other compounds from water. Many of these filter devices consist of a porous material like a ceramic or a granulate like sand.^[6,17-20] The existing technologies for the removal of heavy metals are mostly based on oxidation, flocculation, ion exchange, membrane filtration or adsorption processes.^[21-29] In the latter, activated carbon is frequently used.^[21,24,26]

Without doubt and to overcome the problems of water contamination, novel concepts are required. In this framework, the aim of this thesis is the fundamental investigation and development of novel filters to immobilize metal ions from aqueous solutions and to remove bacteria with high efficiency from a water flow. For this purpose, functional supramolecular fibers were investigated and self-assembled in different scaffolds like nonwovens or granular fillings.

The following introduction of this work will provide a short overview of the main topics that are important for this thesis and essential for a better understanding of the individual parts. The main part of this work deals with the formation of supramolecular fibers in the submicron- and nanometer scale by a "*bottom-up*" approach. In contrast to this process, fiber preparation with diameters in the micro- to nanometer scale as typically used on industrial scale and many academic researches is obtained by "*top-down*" approaches. Notably, the preparation technique of a "*bottom-up*" approach is very different to a "*top-down*" approaches and it is part of the field of supramolecular chemistry.

Therefore, the introduction covers following aspects: i) Preparation of fibers in micron-, submicron- and nanometer scale via top-down approaches, ii) self-assembly of supramolecular systems and iii) separation and adsorption methods.

1.1 Preparation of fibers in the micro-, submicron- and nanometer scale

Preparation processes for fiber formation

In the last decades, nanomaterials and especially micro- and nanofibers have become an important class of material for different applications like filtration, tissue engineering, protective clothes, sensors and many others. Among other things, this material class is highly attractive due to the large surface area to volume ratio and the fact that nanofibers are lightweight. Therefore, many academic and industrial research groups focused on this topic to develop new fiber preparation methods with tailored properties such as the morphology of fibers or the chemical and physical behavior.^[30–40]

In general, there are two different methods to prepare fibers in the micro- and nanometer scale. The most common techniques are so-called “*top-down*” approaches. Other methods are based on so-called “*bottom-up*” approaches. In the latter, small building blocks are used to form fibers by secondary interactions (see **Figure 1.1**).

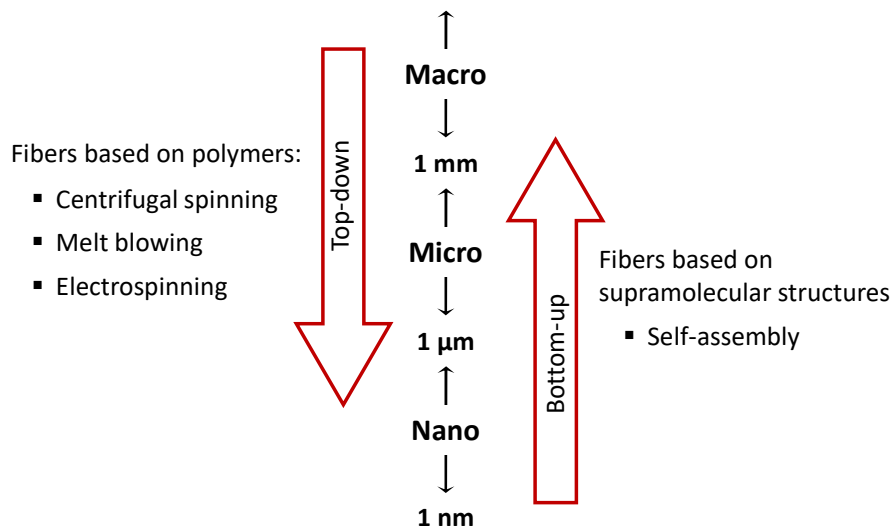


Figure 1.1: Schematic representation of so-called “*top-down*” and “*bottom-up*” approaches for the preparation of micro- or nanofibers.

Three prominent examples of such “*top-down*” processes, which in particular used to form micro- or nanofibers are melt-blowing, electro-spinning and centrifugal spinning. These techniques use a bulk material, e.g. in form of polymer granulates, and process the material to fibers on the micro- and nanometer scale. Polymer fiber processing typically requires a reasonable low viscosity and therefore these approaches often utilize polymer solutions or polymer melts. During the process, the liquified polymer is extruded through a small spinning die to obtain polymer fibers in the micro- or nanometer scale.^[32,36] The processing of these three examples of “*top-down*” approaches to achieve micro- and nanofiber differ significantly and require therefore different apparatus and considerations.

Melt Blowing

The melt blowing technology was invented in the 1950s and since then numerous studies were conducted by academic groups and industry to enhance its performance. Nowadays, it is possible to produce up to 30,000 m/min (500 m/s) of melt blown fibers.^[41,42] Also notably, nanofibers with a diameter down to 100 nm can be produced with melt blowing technologies. The fiber formation process is mainly controlled by the temperature and the viscosity of the spinning fluid, the temperature of the air stream and the distance between nozzle and collector. A large variety of polymers to produce fibers by melt blowing were successfully investigated including polypropylene, poly(methyl methacrylate), polyamides or polystyrene .^[43]

In general melt blowing is a spinning process in which a molten polymer or in seldom cases a dissolved polymer is extruded through a die into fibrous structures.^[41,43–46] A particular feature of this process is that the spinning fluid is dramatically accelerated and stretched due to a hot air stream, which surrounds the polymer jet.^[43] In **Figure 1.2**, the melt blowing die is shown schematically. The polymer is extruded through a thin die and subsequently an air stream with high velocities, up to 250 m/s, surrounds the polymer jet resulting in a draw.^[41] The polymer is further drawn by bending and flapping processes that take place during the melt blowing process. During the stretching of the polymer jet, the air stream cools down the molten polymer. In case of a polymer solution as spinning fluid, the air stream accelerates the evaporation of the solvent. The produced fiber is deposited on a collector.^[41] In particular the solvent free process, allows instantly to prepare nonwoven webs, which may wrapped up on a roll . Therefore, the collector often is like an assembly line allowing for a continuous production.

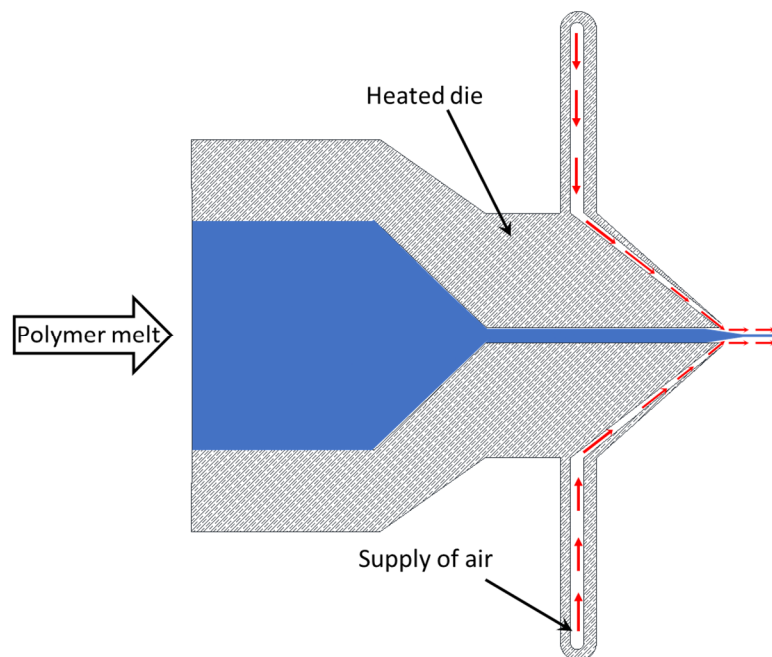


Figure 1.2: Schematic representation of a melt blowing spinning die. The polymer melt is fed into the hot die under pressure. At the end of the nozzle, the formed polymer strand is further deformed by the surrounding hot air (red arrows). Thin polymer fibers are formed. [Figure is based on ref.^[37,42,47]]

Electrospinning

Electrospinning is one of the most common techniques to produce fibers on the micro- and nanometer scale. A high amount of research was done by many academic groups in the last years investigating this kind of technology.^[38,39,47–52] In **Figure 1.3**, a schematic set-up of the electrospinning process is shown. A syringe equipped with a metal needle featuring an inner diameter of less than 1 mm is filled with the spinning dope, which can be a polymer melt, but is most typically a polymer solution. A high voltage of up to 50 kV is applied between the needle and the collector. The needle acts as one electrode and the collector, which is often an aluminum foil acts as counter electrode.^[38,48,49] By applying slight pressure on the plunger of the syringe, a droplet is formed on the tip of the metal needle. Due to the strong electrical field, the fluid is charged, which subsequently leads to the formation of a polymer jet. The charges in the polymer jet interact with the electric field and tensile forces apply on the jet. On the way from the tip to the collector during the spinning process, the diameter of the polymer fiber is reduced constantly. Fibers with a diameter in a range of a few nanometers up to a few micrometers can be formed. The solvent of the polymer solution evaporates due to the large surface to volume area continuously during the spinning process, which leads to solidification of the polymer. In case of a melt electrospinning process, the melt is cooled down on the way down to the collector and solidified fibers can be deposited on the surface of the collector. Finally, the formed fibers are deposited on the collector typically resulting in a web of nonwoven. With the help of electrospinning, many different kinds of nanofibers such as core-shell, hollow or functional nanofibers were demonstrated, which can be used for different applications in the field of filtration or tissue engineering.^[38,39,48,49]

Up to now, the electrospinning process is often uneconomical for industrial applications due to the relatively low throughput of micro- and nanofibers. As a typical value, only a few 10 meter per second can be produced with this technique. Another drawback in solution electrospinning is the use of hazardous solvents to dissolve polymers, which hampers an industrial application. Furthermore, influences between neighbored jets were observed by upscaled electrospinning set-ups for a higher fiber production rate. Thereby, partly non-dried fibers were collected.^[32]

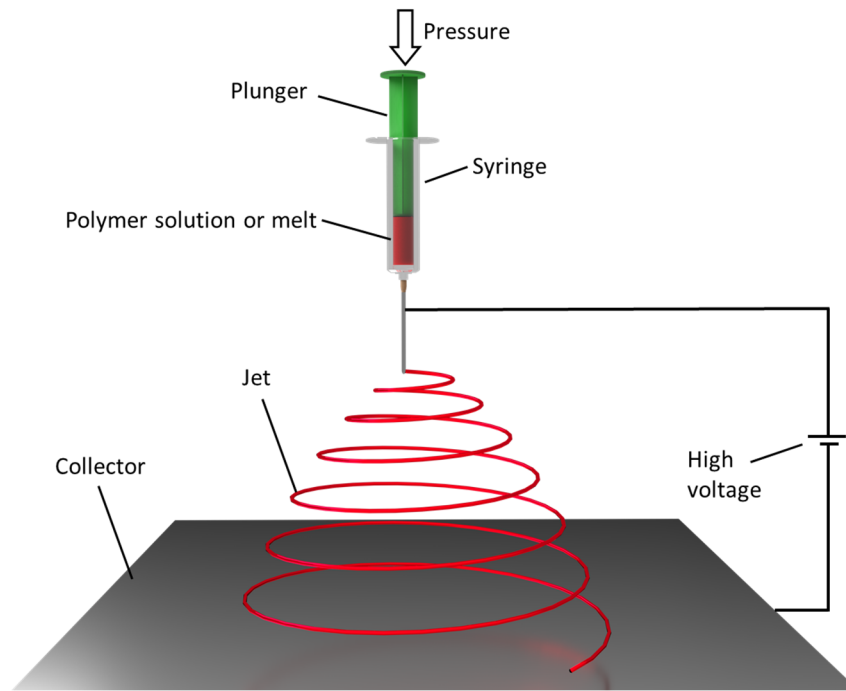


Figure 1.3: Schematic representation of the general electrospinning setup. A syringe is filled with a polymer melt or solution which is the spinning fluid. Pressure on the plunger leads to the extrusion of the spinning fluid. A high voltage is applied between the metal needle and the collector which often is an aluminum foil. The voltage leads to a formation of a polymer jet. Thus, polymer fibers are formed which will be deposited on the surface of the collector. [Figure based on ref.^[48]]

Centrifugal Spinning

Centrifugal spinning is based on the extrusion process of a polymer melt or a polymer solution through a spinning die.^[53–59] This technique only uses centrifugal forces of the rotary mold to produce fibers. Generally, this method is based on the techniques of cotton candy machines.^[59] In **Figure 1.4** the schematic representation of a centrifugal spinning setup is shown. During the fiber formation, a spinning fluid, often a polymer solution or melt, is filled continuously into a reservoir in the rotating spin head. If the number of revolutions per minute (rpm) reaches a critical value, the centrifugal forces overcome the surface tension of the liquid material in the spinning head and liquid jets are formed from the spinning die which is located on the side of the spinning head. Due to radial forces, the jets are elongated and by evaporation of the solvent or cooling of the melt, fibers in the micro- or nanometer scale are formed. These fibers are deposited on the surface of a collector which is placed around the spinning head.^[58] This collector often consists of a metal foil so the resulting fibers can be easily removed. A flexible foil, which is located above the die, ensures air turbulence during the spinning process (**Figure 1.4**). This turbulence further decreases the fiber diameter. In industrial processes, up to 12 kg fibers per hour can be achieved by centrifugal spinning. The production rate for melt blowing were at 1.5 kg/h and those for needle less Electrospinning at 0.2 kg/h.^[60]

The centrifugal spinning process is influenced by different parameters. Important parameters are the temperature and viscosity of the spinning fluid, the rotation speed as well as the geometrical dimensions of the spinning head and the distance between the nozzle and the collector.

Remarkably, different studies show that it is possible to produce fibers in the nanometer scale with polymers such as polyacrylonitrile, polyvinylpyrrolidone or poly(methyl methacrylate). It could also be shown that it is possible to form thin polyacrylonitrile fibers by a centrifugal spinning process which were produced to highly porous carbon microfibers by an additional process step.^[61] As a common feature of nanofiber production via “top-down” approaches, the nanofibers are deposited on top of a support. Thus, the term coating is coined.

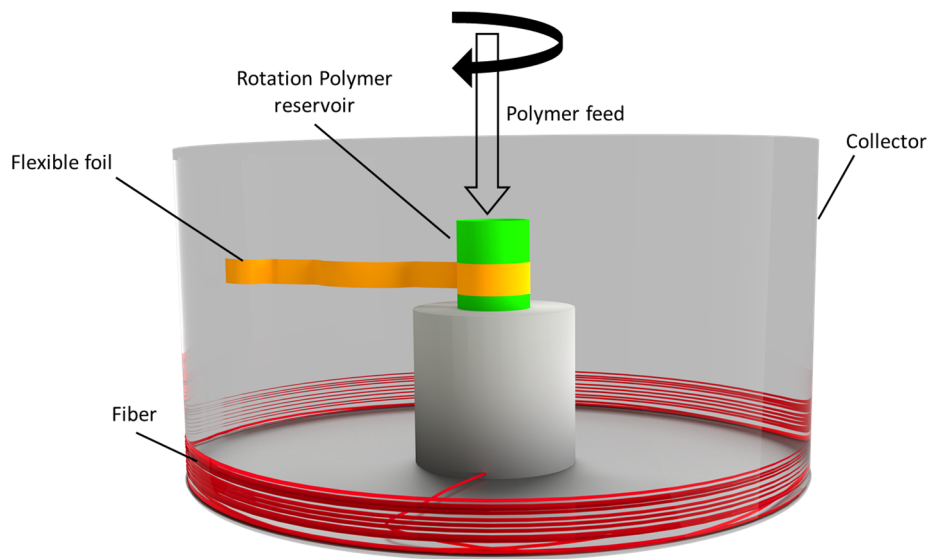


Figure 1.4: Schematic representation of the experimental set-up of a centrifugal spinning process. The spinning fluid is fed from the top to the rotating polymer reservoir in the middle of the centrifugal spinning plant. A flexible foil ensures air turbulence during the spinning process. Due to the high centrifugal forces, the spinning fluid is extruded through a die and fibers are formed. The fibers are deposited on the surface of the collector. [Figure based on ref.^[47]]

In contrast to the previously described “top-down” approaches, so-called “bottom-up” approaches can also be used for the formation of micro- or nanofibers. In particular, small molecules can be used to form supramolecular structures in the micro- or nanometer scale driven by directed secondary interactions between the individual building blocks. Here, various non-covalent intermolecular interactions, which allows for self-assembly of the building blocks into nanostructures. This includes π - π interactions, ion-ion interactions, van-der-Waals interactions, dipole-dipole interactions or hydrogen-bonds, which are established between the individual building blocks.^[62–65]

Notably, supramolecular chemistry provides the opportunity to achieve many different structures and not only fibers. Literature-known examples includes nanoribbons, nanosheets nanoparticles or nanospheres via a tailored self-assembly process.

Due to the importance of supramolecular chemistry to this thesis, the following chapter is dedicated to provide details on this research field.

1.2 Supramolecular Chemistry

Supramolecular chemistry is defined by the IUPAC as: “A field of chemistry related to species of greater complexity than molecules, that are held together and organized by means of intermolecular interactions. The objects of supramolecular chemistry are supermolecules and other polymolecular entities that result from the spontaneous association of a large number of components into a specific phase (membranes, vesicles, micelles, solid state structures etc.).”^[66] Thus, this field of chemistry is predominantly based on non-covalent, secondary interactions between individual molecular building blocks. These intramolecular interactions involve hydrogen bonds, van der Waals forces, dipole-dipole interactions, ion-ion interactions and π - π interactions. The different interactions differ significantly in their binding energies. Several types of them can occur in a single supramolecular system.^[67–71]

Supramolecular chemistry allows to control the type of the arrangement of individual molecules, the shape of individual supramolecular nanostructures and the mesoscopic morphology formed by the “*bottom-up*” process. The research field of supramolecular chemistry has grown strongly in recent years. Supramolecular chemistry can be found in a variety of research areas, ranging from the production of catalysts, photochemistry and the production of hydrogels for medical applications such as *tissue engineering*.^[63,72–78]

In the following, examples of supramolecular systems featuring hydrogen bonds, π - π -interactions or ion dipole interactions are briefly discussed.

1.2.1 Secondary interactions in supramolecular chemistry

Supramolecular chemistry relies on the formation of directed secondary interactions between individual molecules. Apart from the kind of secondary interactions, the most important ones are based on hydrogen bond, pi-pi interactions and ion-dipole interactions, which were discussed in the following.

Hydrogen bonds

The secondary interaction best known for supramolecular chemistry is the formation of (directed) hydrogen bonds. These interactions can be regarded as a kind of dipole-dipole interaction. Hydrogen bonds involve electropositive hydrogen atoms and electronegative atoms, such as oxygen or nitrogen. An example of a supramolecular system that forms self-assembled structures through hydrogen bonds consists of 1,2,4,5-benzenetetracarboxylic acid and 1,10-phenanthroline.^[79] The two-dimensional honeycomb structure formed is shown in **Figure 1.5**. Here 1,2,4,5-benzenetetracarboxylic acid interacts with water molecules, which are incorporated into the structure. Each of the 1,2,4,5-benzenetetracarboxylic acid molecules forms a hydrogen bond to another 1,2,4,5-benzenetetracarboxylic acid molecule. Furthermore, hydrogen bonds are formed to one of the contained water molecules and to two 1,2,4,5-benzenetetracarboxylic acid molecules. This always creates hydrogen bonds between the O-H and C=O groups, which leads to two-dimensional networks.

These two-dimensional networks can be layered to form the next hierarchical level. This results in cavities in which the 1,10-phenanthroline molecules are embedded. These phenanthroline molecules are fixated by hydrogen bonds between their nitrogen atoms and the water molecules, which are further connected to the carbonyl groups of the carboxylic acids.^[79]

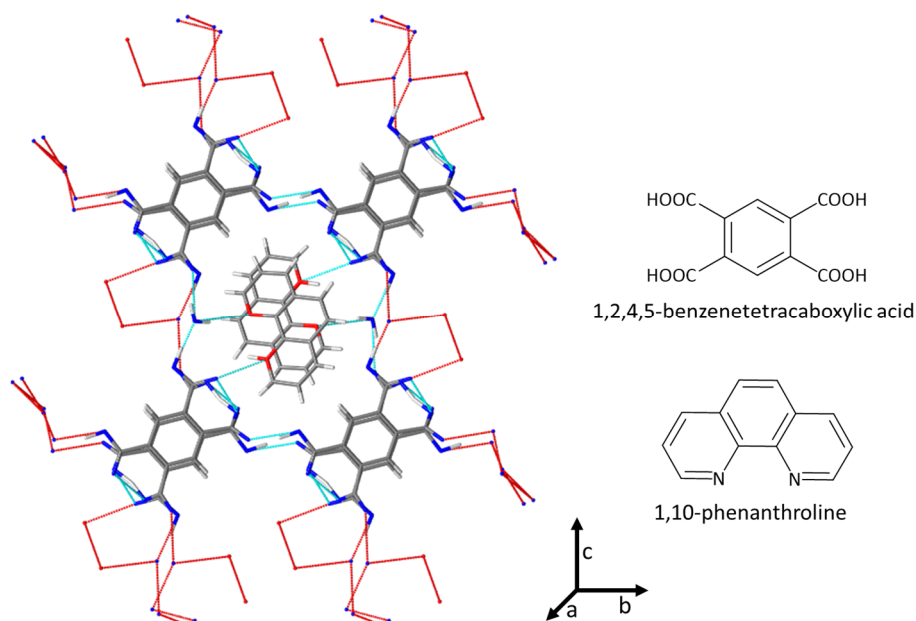


Figure 1.5: Representation of the crystal structure of the formed supramolecular structure. The formed honeycomb-like structure can be seen. The molecules of the 1,2,4,5-benzenetetracarboxylic acid form hydrogen bonds between C=O and the OH groups of the acid residues, also hydrogen bonds are formed to water molecules which are incorporated into the structure. In the cavities 1,10-phenanthroline molecules are incorporated. Here, the nitrogen atoms of the 1,10-phenanthroline interact with the carbonyl groups of the carboxylic acid and with the water molecules. [adapted from ref.^[79]]

π - π -interactions

π - π Interactions are also secondary interaction, which is often used during self-assembly processes.^[80-83] Here, the π -electrons of an aromatic core interact with π -electrons of other aromatic cores or with other molecules. Applying proper protocols, these processes are well known to result in supramolecular objects.^[67,84] For example, Würthner et. al used building blocks consisting of perylene bisimides as core and oligo(p-phenylene vinylene) as shell.^[85] The latter is connected to the core by further secondary interaction, e.g. hydrogen bonds, which are formed between the amide groups and the bisimide groups. The chemical structures of both primary aggregates including the hydrogen bonds and the resulting “core-shell” structures assemble to fibrous structures, in which the fiber-like structure is held together by π - π interactions as shown schematically in **Figure 1.6**. The formed fibers only consist of the connected supramolecular building blocks and do not aggregate. Thus single, polymer like fibers were formed. Since a direct overlap of the π - electrons is repulsive, the aromatics are typically shifted to each other resulting in an attractive interaction. In this case the building blocks

assemble in a twisted helical structure yielding a supramolecular structure with a slightly twisted fibrous morphology^[85]

This perylene bisimides and oligo(*p*-phenylene vinylene) form an acceptor-donor system which could be used for different application such as organo electronics.^[85]

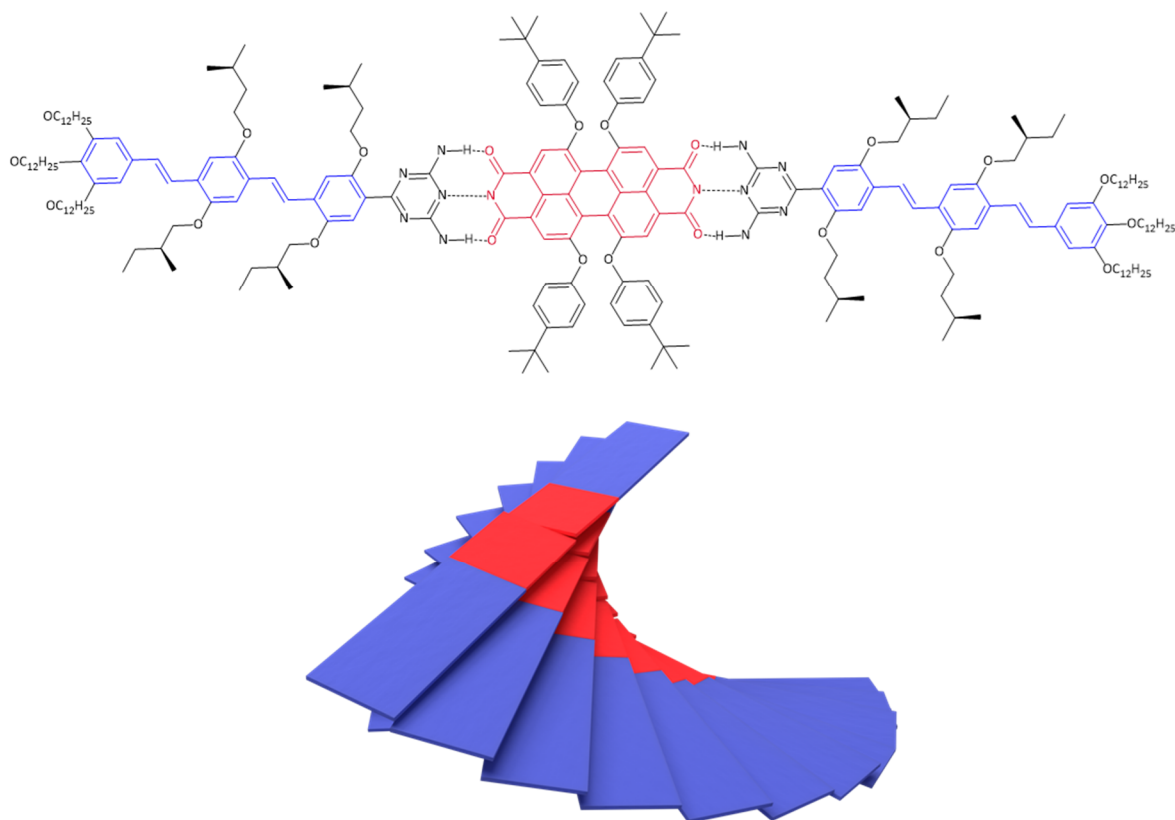


Figure 1.6: Chemical structure of the used supramolecular building blocks. Schematically representation of the formed supramolecular object. The building blocks assembled due to π - π -interactions to a columnar structure with a twisted shape. [Figure is adapted from ref.^[85]

Ion dipole interactions

There is also an amount of other supramolecular systems using ion dipole interactions for the formation of supramolecular structures.^[86,87] Example comprises ion dipole interactions is given by Yan et al. for a supramolecular system forming a so-called linear supramolecular polymer.^[86,87] For their studies, they used a large molecule, comprising a 1,2,3-triazole group, which is linked via spacers to a benzo-21-crown-7 ether and an ionic dialkylammonium salt. The structural formula is given in **Figure 1.7 A**. In the schematic, the benzo-21-crown-7 ether is colored red, the 1,2,3-triazole group is colored green and the dialkylammonium-ion is colored blue. During the self-assembly process, the crown ether can coordinate to the dialkylammonium salt resulting in supramolecular polymer (**Figure 1.7 B**), which form a highly viscous solution in the selected solvent. These supramolecular polymers form in chloroform at high concentrations rod-like structures as evidenced by SEM investigations. Due to its polymer-like behavior, it was also possible to use such solutions in electrospinning processes to produce thin fibers with a diameter between 0.2 to 4.0 μm . In another

study, the research group showed that xerogels with this molecule can be obtained. For this, they self-assembled the supramolecular motif from acetonitrile in presence of $[\text{PdCl}_2(\text{PhCN})_2]$ (**Figure 1.7 C**).^[86] During the self-assembly upon cooling, a stable gel was formed. The 1,2,3-triazole group in the supramolecular building block acts as a ligand for the palladium. Thus, the single supramolecular chains are crosslinked by the coordination of Pd at the triazole. These xerogel showed very good mechanical properties and were highly stable against external mechanical stress. In these two studies, it was also shown that the systems are responsive to different external stimuli like the variation of the pH-value or the change of the temperature.

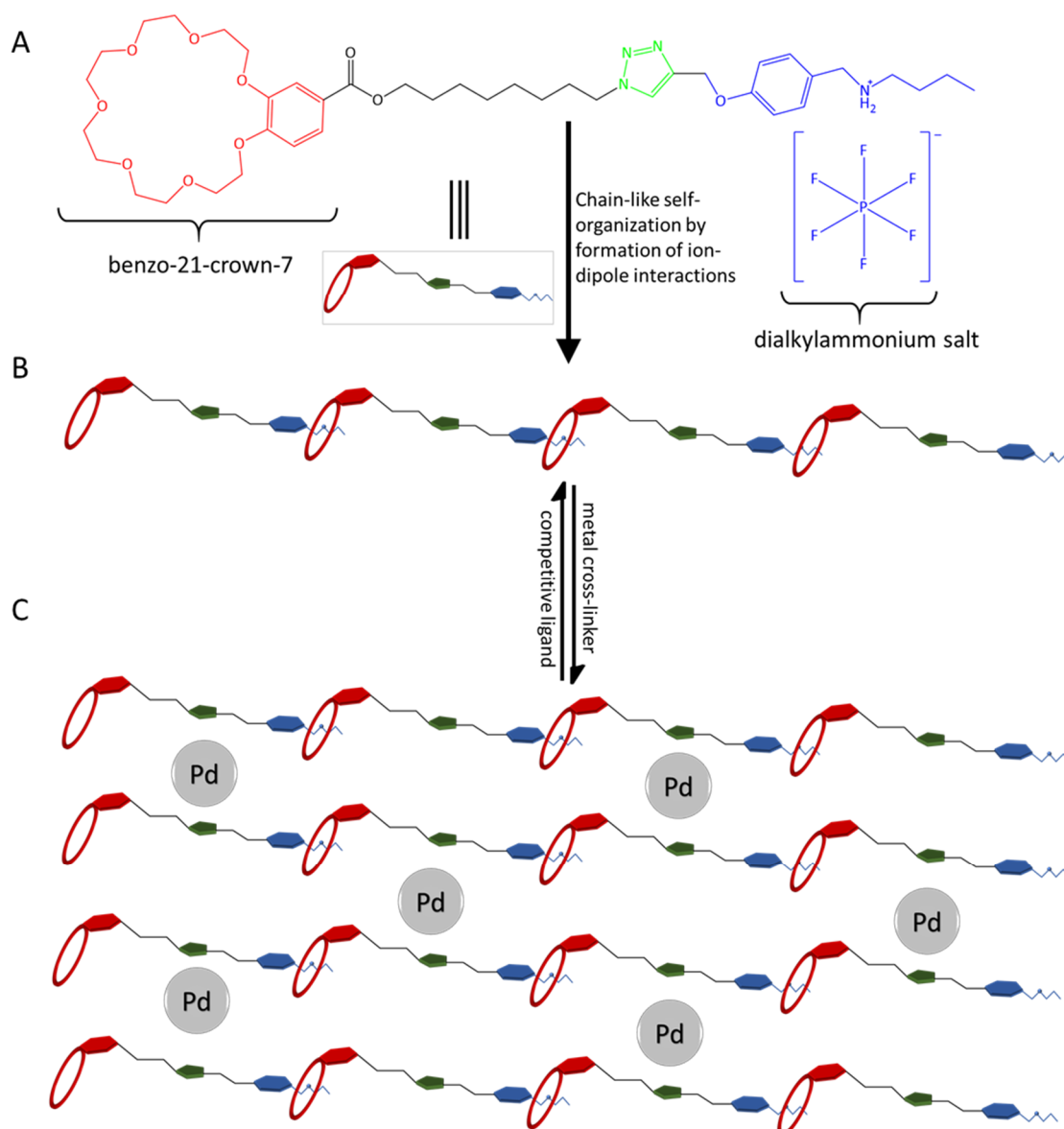


Figure 1.7: **A:** Molecular structure of the supramolecular building blocks which assemble to large linear supramolecular objects. **B:** Schematic representation of the large linear structure self-assembled by ion-dipole interactions. The host crown ether is colored red and the guest dialkylammonium ions are colored blue. **C:** Schematic representation of the structure of the formed gel by adding Pd to the solution. The Pd interacts with the triazole-groups (green parts). [Figure based on ref.^[86,87]]

1.2.2 The material class of 1,3,5-benzenetrisamides

Molecular design of 1,3,5-benzenetrisamides

A very well-known and versatile class in supramolecular chemistry is based on 1,3,5-benzenetrisamides.^[88–107] In particular, the class of 1,3,5-benzenetrisamides is a prominent example for forming supramolecular structures via three directed helical hydrogen bonds. Since BTAs are also widely used in this thesis as supramolecular systems, special emphasis is here dedicated to this class.

The schematic structure of the BTA material class is shown in **Figure 1.8**. The central core unit of this class typically comprises a benzene ring to which three amide groups are linked C_3 -symmetrically in 1, 3 and 5 positions. These can be attached to the ring in two different ways, via the carbon atom of the carbonyl group or via the nitrogen atom. In consequence, these compounds are based on the 1,3,5-benzenetricarboxylic acid or 1,3,5-triaminobenzene. A molecularly similar materials class comprises C_3 -symmetrically substituted cyclohexane as core. This 1,3,5-cyclohexanetrisamides (CTAs) will not be used in this thesis and thus will not be discussed further.

The substituents in the periphery of the molecule are linked to the amide group. These groups influence, among other things, the solubility and aggregation behavior as well as the thermal properties of the respective compound. The amide groups can form threefold hydrogen bonds with neighboring molecules. This usually leads to the formation of supramolecular columns with preferred 1D growth along the columnar axis. Such supramolecular columns can be found in crystalline or liquid crystalline phases as well as in solutions or suspensions.^[105,107,108]

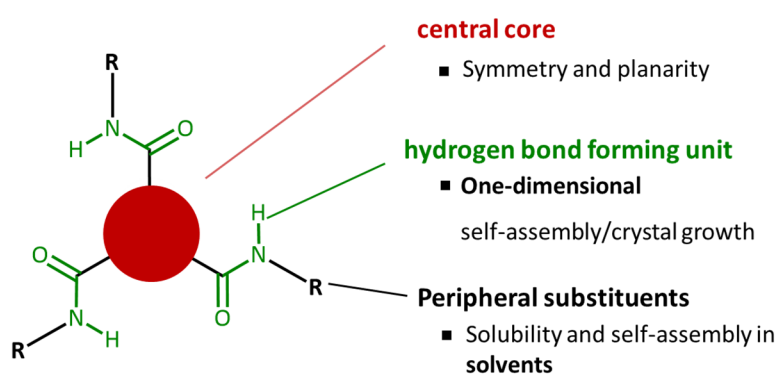


Figure 1.8: Schematic representation of a 1,3,5-trisamide. The core of this structure can be a benzene ring or cyclohexane. The amide groups can form threefold hydrogen bonds. Among other things, the periphery influences the solubility of the 1,3,5-trisamides in different solvents.

The properties of some 1,3,5-benzenetrisamides have been very well studied. In particular, the influence of the peripheral group has been studied in great detail. For example, Timme et al. investigated the liquid crystalline behavior of various 1,3,5-benzenetrisamides and were able to show that the transition temperature between two liquid crystalline phases of BTAs with a branched periphery increased when the branching was closer to the core.^[105] Furthermore, they showed that

molecules with a linear side-chain with at least six C-atoms show a Col_{ho} liquid crystal (LC) phase. BTA molecules with a branched side chain with four C-atoms in the main chain show no LC behavior. Instead these supramolecular building blocks showed a plastic crystalline mesophase. Which transferred by heating directly into the isotropic phase.^[105]

The focus of many scientific studies on 1,3,5-benzenetrisamides lies on the formation of supramolecular columns.^[107,109] As mentioned before, the aggregation behavior is strongly dependent on the substituents in the periphery. For a more detailed understanding of the secondary interactions between adjacent 1,3,5-benzenetrisamides (BTAs), the crystal structures of several BTAs have been elucidated.^[96,101,109,110]

A very prominent example was provided by Lightfoot et al. revealing the crystal structure of N,N',N'' -tris(2-methoxyethyl)benzene-1,3,5-tricarboxamide (**Figure 1.9**) after recrystallization from ethanol.^[109] This compound crystallizes in monoclinic $P2_1$ space group. The crystallographic data showed that this 1,3,5-benzenetrisamide forms strong threefold helical hydrogen bonds between the amide groups of adjacent molecules and weak π - π interactions between the aromatic compounds of the molecules. Compared to a molecule with the same periphery but cyclohexane as the core, there are some differences in the interactions formed. The amide bonds in the 1,3,5-benzenetrisamide are twisted with respect to the core. In this case the dihedral angles of the three amid units were about 36.8° , 42.4° and 45.5° to the benzene plane. Whereas in the molecule with cyclohexane ring the amide groups are perpendicular to the core. Here the dihedral angle is about 90° .^[109]

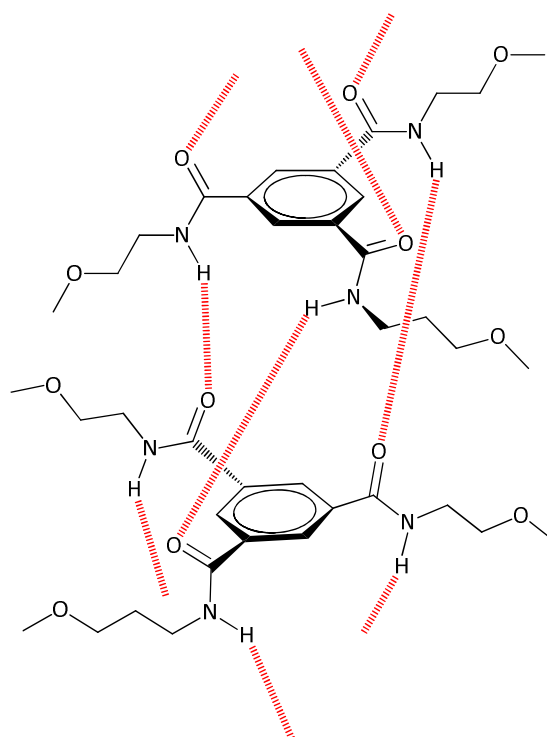


Figure 1.9: Structure of N,N',N'' -tris(2-methoxyethyl)benzene-1,3,5-tricarboxamide recrystallized from ethanol. The triple hydrogen bonds formed between two adjacent molecules are shown. [adapted from ref.^[109]]

Due to the directional threefold hydrogen bonds in the supramolecular columns, a macrodipole is formed. If these macrodipoles can interact with each other, they compensate upon aggregation of two or more supramolecular columns in an antiparallel manner.^[88,107]

Processing parameters and structure formation of supramolecular bundles of BTA nanofibers

Supramolecular bundles of BTA nanofibers are highly interesting because these objects can be used for a various number of applications. The basic step includes the formation of single columnar supramolecular nanofibers. As mentioned, the BTA form a three folded strand of hydrogen bonds resulting a columnar arrangement. Prior structure formation, the BTA molecules are fully dissolved in a liquid or viscous medium such as a solvent or polymer melt. During the self-assembly process hydrogen bonds to neighbored molecules are formed resulting in columnar stacks. These columnar stacks aggregate to dense bundles of comprising single nanofibers, which is typically denoted in this thesis to as supramolecular (nano)fibers. In **Figure 1.10** the basic self-assembly process to such supramolecular structures is schematically shown.^[109,111]

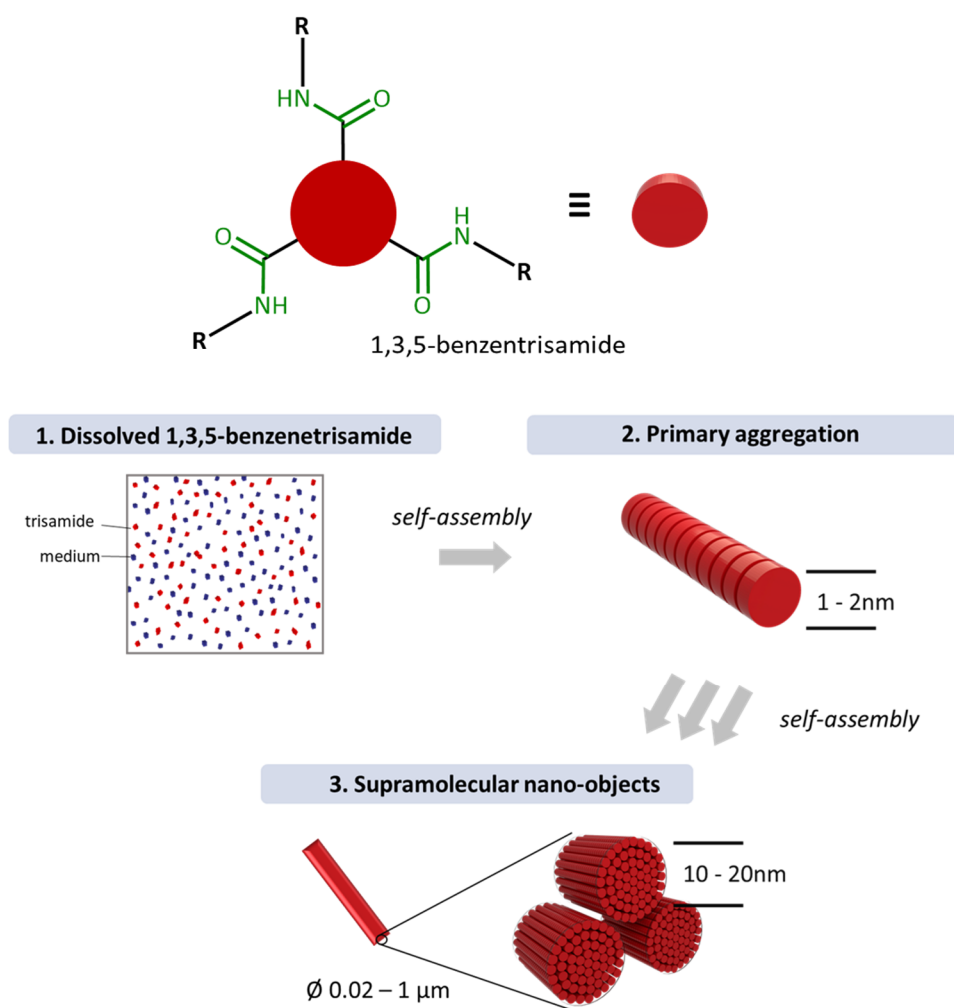


Figure 1.10: Schematic representation of the formation of supramolecular fibers.

Influences on the self-assembly behavior of 1,3,5-benzenetrisamides

The term self-assembly may be understood as an autonomous, spontaneous process of structure and pattern formation. From a thermodynamic point of view, the self-assembly process is associated with energy minimization yielding preferentially structures in a kinetically trapped form or in the thermodynamic equilibrium.^[71] Due to the comparable weak secondary interactions, the structure formation during self-assembly processes is in principle reversible.^[70,71] This apparently disadvantageous aspect is used in nature to repair or replace defects.^[112] Due to the higher mobility, self-assembly processes often take place in liquid media, such as melts or solutions.^[71] It is generally accepted that the self-assembly processes and the morphology of supramolecular nanoobjects depends on critical parameters including the molecular structure, the concentration of the molecules, the solvent and the applied temperature protocol (**Figure 1.11**).

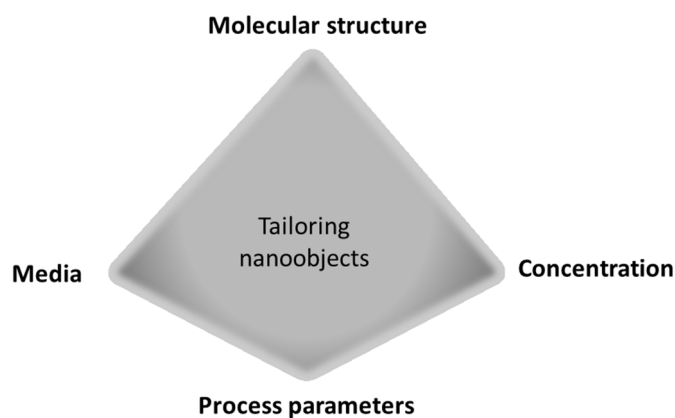


Figure 1.11: The influence of different parameters on the formation of nanoobjects is shown schematically. The molecular structure and the medium, often the solvent, play important roles in the formation process of supramolecular structures. Furthermore, the concentration of the molecular building blocks and the process parameters, such as cooling and evaporation rate of the solvent, influence the final supramolecular nanostructure.

In particular, self-assembly can be initiated in various ways, such as changing the temperature, the polarity of the solvent, the concentration or the pH value.^[64,113–118] These factors can also drive the aggregation process in a certain direction. Among other things, it is known that the assembly behavior and also the mesoscopic morphology is strongly dependent on the solvent.^[88,106] The molecular structure is of great importance for the formation of nanostructures. In the case of 1,3,5-benzenetrisamides, small changes in the peripheral substituents can lead to a significantly altered behavior in solubility and in the structures formed.^[90,106] The applied concentration of the compound plays a significant role in the production of nanostructures. Examples from the literature show that an increase in concentration can lead to changes in the morphology of the structures formed.^[119,120] For example, Zhang et. al investigated the self-assembly behavior of a mixture consisting of a nonionic surfactant and a peptide amphiphile. The concentration of the surfactant was constant, while the peptide amphiphile concentration was steadily increased.^[119] It could be seen that with increasing

peptide amphiphile concentration first vesicles, then star-like structures and finally fibrous structures were formed.^[119] The influence of the concentration was thus clearly visible.

Another important variable influencing the properties is the medium which is used. The medium is usually the solvent used for the self-assembly experiments. With the help of solvents of different polarities, it is also possible to influence the structures formed.^[112,121,122] Consequently, a different morphology may be obtained with a polar solvent, while other nanostructures would result from less polar solvents although the other parameters remains the same. Such solvent effects may be attributed to different way of solvation of the individual parts of the molecules during the self-assembly.

Other factors such as the cooling rate of the system or the evaporation rate of the solvent are also known to have a significant influence on the supramolecular structures.^[112] For instance, Abraham was able to show that the cooling rate has a significant influence on the structures formed when a thermo-responsive system was used. He demonstrated that the additive 1,3,5-tris(2,2-dimethylpropionylamino)benzene (cf. **Figure 1.12**) was assembled from 2,2,4,4,6,8,8-heptamethylnonane. It was shown that at a cooling rate of 60 K/min, considerably smaller fibers were formed than at a cooling rate of 10 K/min. It could also be shown that the distribution of fiber diameters is significantly smaller at a higher cooling rate, although the temperature window and solvent were comparable.^[112,123]

Weiß et al. showed similar results by investigating the morphology of alkoxy-substituted 1,3,5-benzenetrisamides. Here, the self-assembly process was studied by varying the cooling temperature and the stirring velocity of the solution. Fiber diameters were much smaller if the system was stirred with a high velocity or the cooling temperature was lower. In this context, the stirring velocity can be correlated to an improved transport of heat, which is removed from the system.^[37,124]

Another important factor influencing the assembly behavior is the periphery of the building blocks which was shown by Kluge.^[90] A 1,3,5-benzenetrisamide with a cycloaliphatic group (1,2-dimethylcyclohexan) in the periphery formed thinner supramolecular nanofibers than a 1,3,5-benzenetrisamide with a branched alkyl chain (isopentane).^[90] However, the exact role of the side chains for the self-assembly of supramolecular columns is not yet fully understood.^[125] The process parameters used are therefore of great importance for the production of supramolecular nanoobjects.

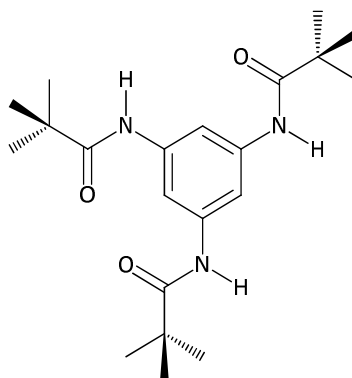


Figure 1.12: Structural formula of 1,3,5-tris(2,2-dimethylpropionylamino)benzene.

Properties of 1,3,5-benzenetrisamides with different non-functional and functional side groups

In general, a larger variety of different side groups were already used for the production of 1,3,5-benzenetrisamides. The spectrum ranges from aliphatic, non-polar groups to protic polar groups such as esters or acid derivatives. As described above, the properties of BTAs change significantly due to a change in the side group. BTAs only with aliphatic side groups are highly insoluble in aqueous solutions than those with a polar periphery.

For example, 1,3,5-tris(2,2-dimethylpropionylamino)benzene (**Figure 1.12**) described previously is a BTA with such a nonpolar aliphatic side chain. This BTA was intensively investigated at our department and can be, for instance, dissolved in and assembled from a nonpolar solvent as shown by Abraham et al.^[123] In further studies, the research group of Jürgen Senker (Inorganic Chemistry, University of Bayreuth) could determine the crystal structure of the BTA. They showed that this BTA self-assembles into a helical structure forming threefold hydrogen bonds to the neighbored BTA molecules.^[96] An further aliphatic BTA, i.e. with a 2-ethylhexyl side groups was largely used and investigated by Misslitz et al. The N,N',N''-tris(2-ethylhexyl)-1,3,5-benzenetricarboxamide (**Figure 1.13**) can be self-assembled from 2-butanone for the formation of supramolecular fibers. Here a more polar solvent was used for the dissolution of the compound and its self-assembly.^[102] This BTA will also be used in this thesis.

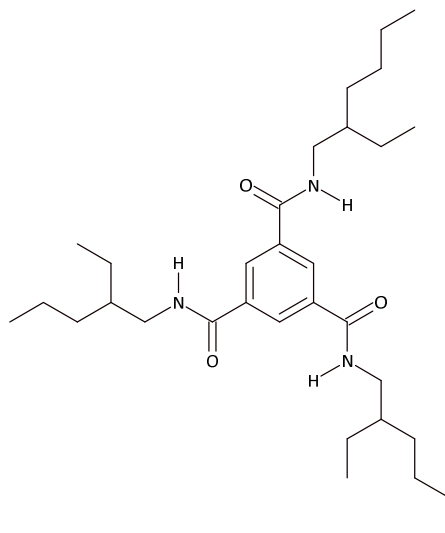


Figure 1.13: Structural formula of N,N',N''-tris(2-ethylhexyl)-1,3,5-benzenetricarboxamide.

In contrary to these 1,3,5-benzotrisamides without any functional group in the periphery also BTAs with side groups containing nitrogen, oxygen or sulfur atoms are literature known. Here, the periphery can consist for example of an ether, amide, pyridine or thioether.^[46,124,126,127] Since the use of functional side groups introduces potentially an additional secondary interaction, care must be taken or very precise self-assembly protocols employed to avoid interaction of the side groups with the structure forming supramolecular motif, i.e. the three amide groups. This would hinder the formation of triple hydrogen bonds to neighboring supramolecular building blocks. In **Figure 1.14** the schematic molecular design of such functional 1,3,5-benzotrisamides is given.

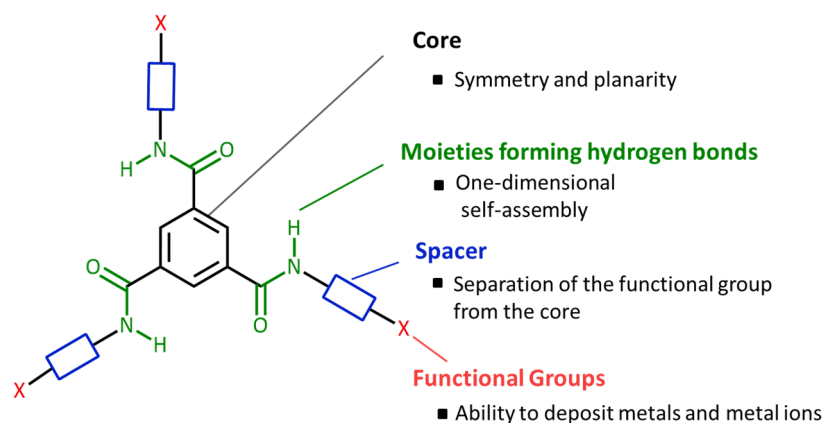


Figure 1.14: Schematic representation of different constituents of 1,3,5-benzotrisamides with functional substituents.

One example of BTAs with a functional amine group in the periphery is given by Frank et al.. Here, the researchers investigated different 1,3,5-benzotrisamides with tertiary N,N-dialkyl-ethylamino substituents. Special interest was focused on N,N',N''-tris[2-(diethylamino)-ethyl]-1,3,5-benzotricarboxamide (**Figure 1.15**). By using a tertiary amine, a potential backbiting would be hindered. This BTA was dissolved at room temperature in pure water up to a concentration of 100 g/L and self-assembles upon heating to supramolecular hollow fiber-like structures.^[126] Thus, the amine group influences the solubility behavior.

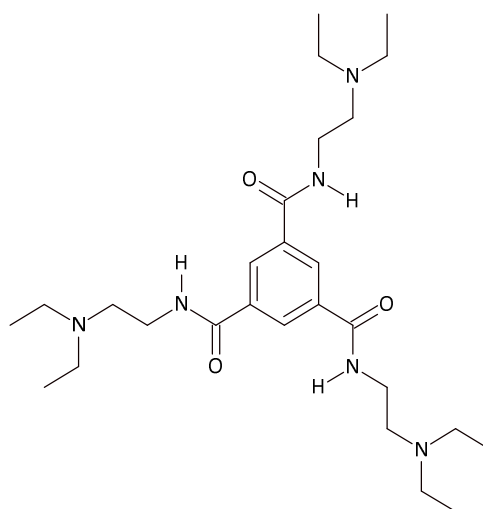


Figure 1.15: Structural formula of N,N',N'' -tris[2-(diethylamino)-ethyl]-1,3,5-benzenetricarboxamide.^[126]

As mentioned before, also Weiß et al. investigated BTAs with a functional group in the periphery. In this case 1,3,5-benzentrisamides with alkoxy-substituents were used for different self-assembly studies. For their studies, the researchers used a N,N',N'' -tris(1-(methoxymethyl)propyl)benzene-1,3,5-tricarboxamide. This BTA has an ether group in the periphery, very similarly to the molecular structure as used by Lightfoot. This compound was dissolved in an alcoholic/water mixture and was also assembled from this solvent system to supramolecular fibers.^[124]

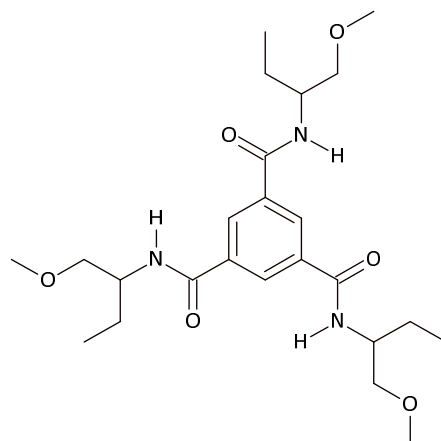


Figure 1.16: Structural formula of N,N',N'' -tris(1-(methoxymethyl)propyl)benzene-1,3,5-tricarboxamide.^[124]

Further functional BTAs based on trimesic acid in literature are for examples BTAs with pyridine based substituents or with derivatives of amino acids as side groups.^[122,127–130]

Maruyama et al. investigated a number of BTAs substituted with methyl esters of some amino acids like glycine, L-alanine, L-valine, L-leucine, L-methionine, and L-phenylalanine. In their studies, they formed supramolecular gels with BTAs in different ionic liquids.^[129] They also used a L-methionine based BTA molecule for their experiments.^[129] Jana et al. self-assembled the same BTA from methanol. In their study, they investigated the crystal structure of the self-assembled BTA. They could show that

a columnar structure with three-fold hydrogen bonds was formed. The distance between the benzene rings in the column was about 3.35 Å, an expected value for pi-pi stacking of benzene rings. Also, the FTIR-investigations of the self-assembled structure showed the characteristic vibrations for a three-fold hydrogen bonding. The crystal structure is schematically shown in **Figure 1.17**.^[128]

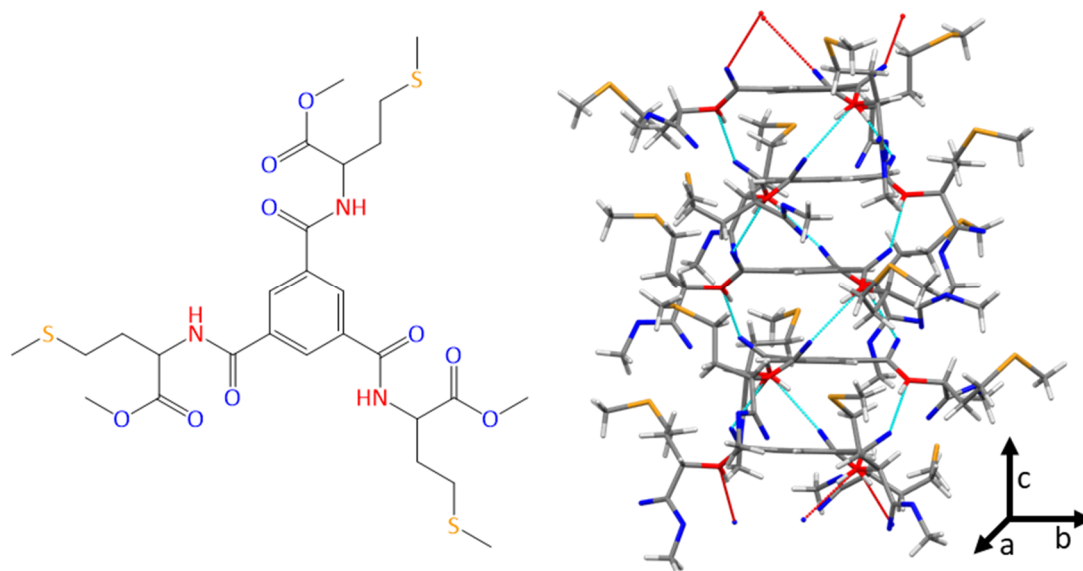


Figure 1.17: Crystal structure of 1,3,5-benzenetrisamide with L-methionine in the periphery. Threefold helical hydrogen bonds were formed to the neighboring molecules. The figure shows the columnar structure perpendicular to the b-axis. [adapted from ref.^[128]]

Finally, BTAs with mono pyridine-based side groups will be briefly discussed as BTA with a functional side group. The chemical structure of one pyridine based BTA is shown in **Figure 1.18**. This BTA was intensively investigated by different work groups.^[131,132] For instance, the research group of Zhong formed a so-called hydrogen-bonded organic framework (HOF) with this mono-pyridine BTA by recrystallization from a solvent mixture of chloroform/methanol (3:1 (v/v)).^[127] This HOF is extremely thermally stable and also stable in water and common organic solvents. The research group of Kumar et al. also investigated the crystal structure of this BTA. They obtained supramolecular structures after self-assembly in a methanol/DMSO (1:1) solvent mixture.^[131] The results of their investigations are based on characterizations of the group of Meijer. In particular, the research group of Meijer used a 1,3,5-tris(3-pyridyl)trimesic amide for their studies. In both research groups, no neat crystal structure could be obtained. Instead they found a solvent-containing HOF-like structure where the solvent was incorporated as guest-molecules.^[133] In detail, the pyridine-functionalized BTAs self-assemble into an infinite 2D hydrogen-bonded network involving hydrogen bonds between the amide-groups and the pyridine-units. There are no hydrogen bonds between the carboxyl and the amide-units. The BTAs formed a 30-membered macrocycle with participation of six molecules during the self-assembly process. The pyridyl side groups constitute the walls of a cavity with a mean diameter of 7.81 Å.^[127,131,133]

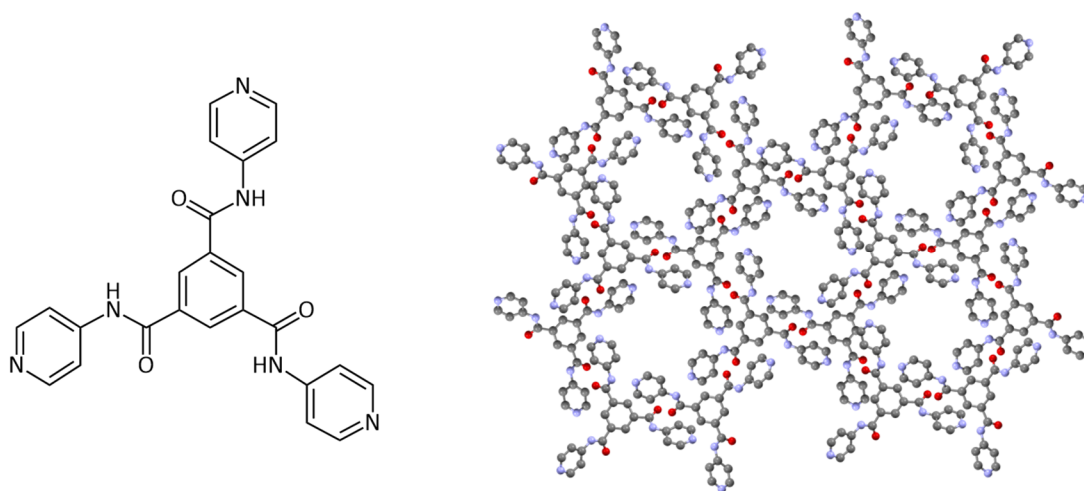


Figure 1.18: Schematic representation of the formed cavity of a 1,3,5-tris(3-pyridyl)trimesic amide. The formation of the cavity is a result of six-fold intermolecular hydrogen bonding. [Figure based on ref.^[127]]

The BTAs formed an infinite rosette structure with the cavities shown in **Figure 1.18**. These rosette structures stack exactly on top of each other. Thus, a three-dimensional, porous superstructure is formed. This 3D structure is based on optimal packing and on cooperative N-H \cdots O interactions between each amide oxygen and pyridyl N-H \cdots N belonging to an adjacent bilayer.^[127,131] The special aspect of this compound is that no threefold hydrogen bonds are formed with the neighboring BTA molecules. Thus, no columnar structures were formed but, a honeycomb structure.

Applications of 1,3,5-benzenetrisamides

1,3,5-Benzenetrisamides are in particular a class of supramolecular molecules, which were successfully used in various applications. Moreover, BTA 1,3,5-tris(2,2-dimethylpropionylamino)benzene is commercially used as nucleation agent and clarifier for iPP. In this context, the relatively simple synthesis and the possibility to change the substituents in the periphery is of great advantage.^[112] With an adequate polarity of the periphery, BTAs can act as organo- or hydrogels.^[88,89,112,134–138] Furthermore, 1,3,5-benzenetrisamides are used as additives in polymer processing for a large variety of semi-crystalline and also amorphous polymers. In different studies, they were used as nucleating agents or as clarification agents for instance.^[98,103,104,123] One example for such a clarification agent is 1,3,5-tris(2,2-dimethylpropionylamino)benzene, which is added in small amounts to isotactic polypropylene (iPP). This BTA increases the crystallization temperature of the polymer, reduces the haze and improves the clarity of the final product.^[97,99] The structural formula of the additive is shown in **Figure 1.12**.^[97]

Furthermore, 1,3,5-benzenetrisamides were used as foam cell nucleating agents in polymer foam production.^[139,140] In this context, our department showed that the cell size of polymeric foams can be reduced using BTAs as foam nucleating agent. Here, the BTA is added in small amounts to the polymer. During cooling of the polymer melt, the BTA forms supramolecular structures which then act as nuclei

for the foam formation. The physical blowing agent forms numerous bubbles initiated at the surface of the supramolecular objects. Due to the high surface-volume ratio of the supramolecular nanoobjects, many small cells can be formed. Therefore, a higher thermal isolation and a higher stability of these foams can be achieved. In **Figure 1.19**, the foam formation with 1,3,5-benzenetrisamides as nuclei is schematically shown.^[139,140]

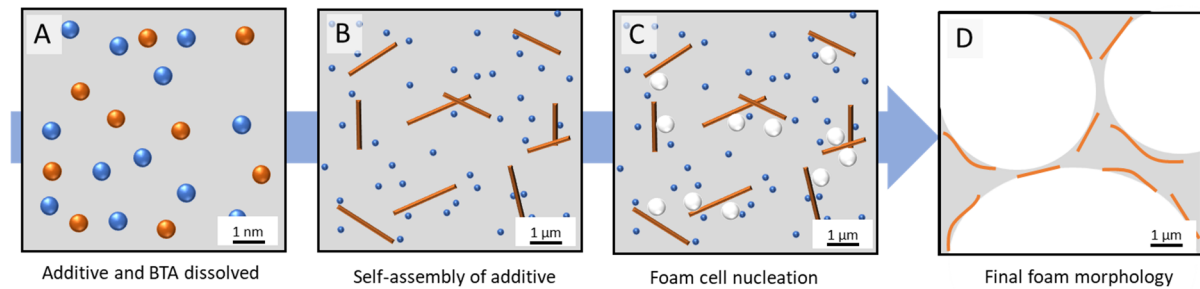


Figure 1.19: Schematic representation of the processing steps of polystyrene foams by controlling the morphology with supramolecular additives. **A:** Dissolved BTA (orange) and blowing agents (blue) in the polymer melt (grey). **B:** Self-assembled BTA nanoobjects upon cooling of the polymer melt. **C:** Foam nucleation on the surface of the self-assembled supramolecular structures. **D:** Polymer-foam cell structure with BTA structures around the cells. [Figure based on ref.^[139]]

Another field of application for 1,3,5-benzenetrisamides are air filtration applications. Here, the supramolecular molecules must be able to assemble into long supramolecular nanofibers. This was investigated by Misslitz et al. among others.^[102] For this purpose, a commercial nonwoven fabric based on a polyester/viscose mixture was treated with 1,3,5-benzenetrisamides with branched aliphatic chains in the periphery. The nanofiber-microfiber composites produced in this way were able to effectively separate particular matter with a diameter of 0.2 μm to 1.0 μm from an air stream. A more detailed study was provided by Weiss et al.. The researchers of the department from H.W.-Schmidt (University of Bayreuth) produced also filter for air filtration experiments. In addition, solvent influences on the assembly of supramolecular nanofibers were investigated.^[106] The general preparation of these nanofiber-microfiber composites is shown schematically in **Figure 1.20**.^[102] For this, a scaffold was immersed into a BTA-solution at elevated temperatures until the nonwoven is fully soaked with the solution. The self-assembly process is initiated upon cooling and evaporation of the solvent. Thus, supramolecular fibers were formed inside the scaffold and a nanofiber-microfiber composite was prepared.

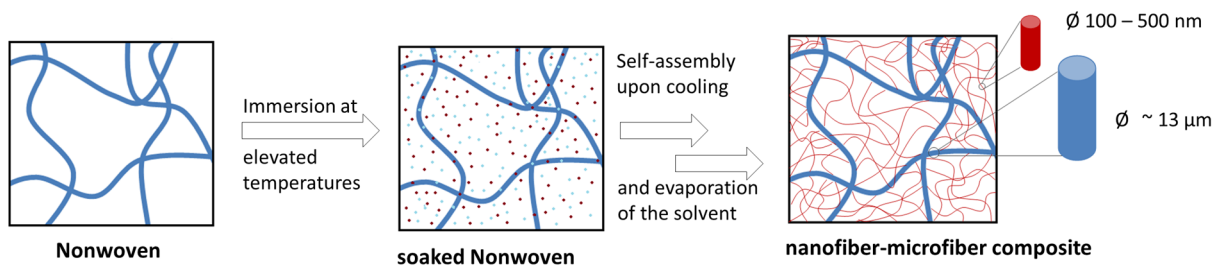


Figure 1.20: Schematic representation of the preparation of nanofiber-microfiber composites. First, the nonwoven is dipped into a hot BTA solution. The fleece soaked with BTA solution is dried in air (blue threads: fibers of the fleece; red dots: 1,3,5-benzenetrisamide molecules; blue dots: solvent molecules). By cooling and evaporation of the solvent, the self-assembly process is initiated and supramolecular nanofibers are formed in the carrier fleece (red fibers: supramolecular nanofibers). [adapted from ref. ^[102]]

An important feature of this composite morphology is that the supramolecular nanofibers wrapped around the chemically bonded nonwoven. This results in an overall mechanical stability of the supramolecular-nanofiber-microfiber-composite without a need for a further bonding of the supramolecular nanofibers to the polymer support structure.^[102]

1.3 Separation methods

For the present work, the fundamentals of separation techniques are of great importance. Therefore, basic aspects and fundamentals are outlined in the following. Particular emphasis is given on filtration and adsorption processes.

1.3.1 Thermal and mechanical separation

In a most basic definition, a separation process is understood as the separation of one or more substances from a mixture of substances. Considering the commonly employed separation methods, they can be classified in two types, i.e. thermal and mechanical separation processes.^[141] Thermal and mechanical separation processes can be distinguished according to Lohrengel by the following criteria:^[141] In mechanical separation processes, heterogeneous mixtures are ideally converted into homogeneous phases. In thermal separation processes, substances in homogeneous mixtures are separated from each other.

Accordingly, the separation of macroscopically large components such as solids or liquid droplets (representing a heterogeneous mixture) is achieved by mechanical separation processes. In these mixtures, the motion of these particles can be described by the laws of mechanics. and the speed of the particle movement is mainly dominated by external forces, such as gravity or inertia. Thermal molecular movements can be neglected, which is why the mechanical separation processes dominate with macroscopically large individual particles. Microscopically very small particles that move in a disordered and chaotic manner (*Brownian molecular motion*) are mainly separated by thermal separation processes. According to Lohrengel, the mass of the particles is decisive for whether the separation process is described by the laws of mechanics (mechanical separation processes) or by thermodynamics (thermal separation processes).^[141] The most important and representative examples for both types of separation processes are given in **Table 1.1**

Table 1.1: Examples of thermal and mechanical separation processes.^[141]

Thermal separation processes	mechanical separating processes
absorption and desorption	filtration
extraction	clarification
adsorption	sedimentation
ion exchange	centrifugation
chromatography	emulsion separation
dialysis	degassing
distillation	sieving

1.3.2 Separation by filtration

Filtration is predominantly a mechanical separation process in which solid particles are separated from a fluid, which can be gaseous or liquid.^[142] Sutherland and Purchas define a filter medium in the following way: “A filter medium is considered to be a physical barrier that is permeable to one or more components of a mixture, solution or suspension under operating conditions and impermeable to the other components.”^[40,143]

1.3.3 Types of filter media

The filter medium is the “heart” of any filter unit, it can basically consist of any material that is permeable or can be converted into a permeable form.^[143] Such permeable materials can be used in form of woven or non-woven fabrics, paper, natural or synthetic fibers, powders, felts, organic or inorganic membranes, plastic sheets and films, perforated metals, sintered metals, ceramics and many others.^[144,145]

It is important to mention that the type and parameters of filtration has a very large influence on the efficiency of the filter media. This includes for example, that a finely sintered metal medium can filter particles down to a size of 0.4 μm from the gas phase. In contrast, the same medium can only filter out particles larger than 2 μm in liquid filtration. Similarly, differences in the filter efficiency occur with aqueous and organic liquids. This is due to different electrostatic properties of the liquid medium that influence the static charges of the particles.^[143] Other examples are microporous plastics extruded into continuous sheets, tubes or irregularly shaped profiles, which are used in liquid and air filtration due to their good flow properties and the ability to retain particles relatively well. Particle removal by air filtration at very high temperatures can be achieved with the help of felts made of meta-aramid fibers. In this way, it is possible to reduce the emissions of industrial plants. Sintered metal fibers have a very high porosity. These fibers have very good properties to retain dirt particles.^[142,144]

1.3.4 Properties of a hypothetical ideal filter medium

A hypothetical ideal filter medium should have the following specifications. First, the filter medium should have an infinite capacity and should be able to separate all impurities from any fluid, regardless of particle size. Likewise, no pressure difference should be built up due to the filter medium. In an ideal system, the filter medium is also infinitely small. This point relates to the production of the filter medium, which should cost as little as possible.^[40]

1.3.5 Filter Conditions

Filters are often characterized or rated according to their performance to remove particles of a specific size from a fluid. There are many different methods to define the filtration efficiency depending on the industry sector or the country. The general equation for determining filtration efficiency is given in equation (1.1). E_x is the filtration efficiency given in percent. N_u represents the number of particles or

the mass per unit volume of fluid before filtration. N_d is the number of particles after the filter unit, which pass the filter and were not captured. If N_d becomes zero, the filtration efficiency will be 100 %.^[146]

$$E_x = 100 \cdot \frac{N_u - N_d}{N_u} \% \quad (1.1)$$

Other specific properties of the filtration process are among others the smallest particle retained, which means the smallest particle size that the filter will remove during the filtration process, and the flow resistance. The latter value depends on the size of the individual pores and the number of pores per unit area. In an ideal case, the filter medium would have the maximum open area through which the fluid can flow compared to the particles of the medium. In practice, the holes only have a small proportion to the surface of the filter medium. The flow resistance is of high interest in industrial applications, because it has a huge impact on the running costs. In general, the resistance is a combination of the porosity of the filter medium and the permeability of the medium to the used fluid.^[142,143,146,147]

The filtration process is also influenced by two additional significant parameters. On the one hand, it is determined by the pressure that is applied on the filter medium during the filtration process. On the other hand, the temperature of the medium and thus the viscosity of the liquid or gas phase plays a significant role.

The flow of a filtration process through a porous media is often described by Darcy's law. It is one of the fundamental equations in this field. Originally, Darcy described the flow of water through a sand filling in a vertical iron pipe. For this, he carried out a number of experiments involving the flow of water. The relationship between the flow velocity and a permeability constant is given in equation (1.2). The law is valid up to a Reynolds number ≤ 1 . The Reynolds number describes the flow behavior of fluids.^[40,143,147,148]

$$v = \frac{K}{\eta} * \frac{\Delta p}{L} \quad (1.2)$$

$$v \propto \Delta p$$

Here K corresponds to the permeability constant with the unit m^2 . η is the dynamic viscosity. Δp refers to the pressure difference in Pascal (Pa) across the filter medium and L is the thickness of the filter medium in meters.

Thus, the flow rate of a filter medium as given in 1.2 is proportional to the pressure difference, as all other parameters should remain constant during filtration.

It should be mentioned that v is a surface velocity with a laminar flow of the fluid. Although, Darcy's law was originally developed for flow through packed beds, it can be also applied for filtration processes with a nonwoven as filter media.^[40]

1.3.6 Filtration mechanisms

A first distinction can be made between four different types of filtration, which describes where particles are deposited in a filter medium. This includes two types with respect to a deposition on top of a filter medium, i.e. the surface filtration and cake filtration as well as two types dealing with a deposition of particles within a medium, i.e. depth filtration and deep saturation.^[40,143,146]

In surface filtration, particles that are larger than the pores of the filter medium are deposited on top of the surface. This type of filtration represents a kind of sieving mechanism and the particles remain on the surface until they are removed. Particles that are smaller than the pores may probably pass the filter medium as schematically depicted in **Figure 1.21 A**. This type of filtration plays an important role for example in membrane filters.^[40,143,146]

In the case of cake filtration, also smaller particles than the pore size accumulate on the surface of the filter medium until a so-called filter cake is formed. This filter cake reduces the pore size on top of the surface significantly, which is also referred to as filter clogging. Subsequently the filter cake acts itself as the active filter component, which resembles a kind of surface filtration. Filter clogging occurs especially when the concentration of the particle solid is very high.^[143] In liquid filtration, the structure of the filter cake depends not only on the properties of the solid particles and the properties of the liquid but also on the filter conditions. This type of filtration is shown schematically in **Figure 1.21 B**.^[142,143]

In depth filtration, particles are retained inside a filter medium, even if they are much smaller than the pores of the filter medium. This filter behavior involves a complex mixture of physical deposition mechanisms. The particles first come into contact with the filter surface, for example through inertial forces or Brownian molecular movements. Then, the particles adhere to the pore wall or to other particles already adhering to the pore wall due to van-der-Waals forces or further surface forces. The strength of the adhesive forces depends on various factors. For example, these forces are influenced by changes in the concentration and species of ions in an aqueous solution or the humidity of a gas. Depth filtration is the most important type for most of the filter media, but especially for highly efficient air filters. A disadvantage of this filtration is that it cannot be regenerated as it is the case in surface filtration, where the particles may be simply removed by an applied pulsed jet flow. Therefore, these filter media can only be used once. A schematic diagram of the filtration mechanism is shown in **Figure 1.21 C**.^[143]

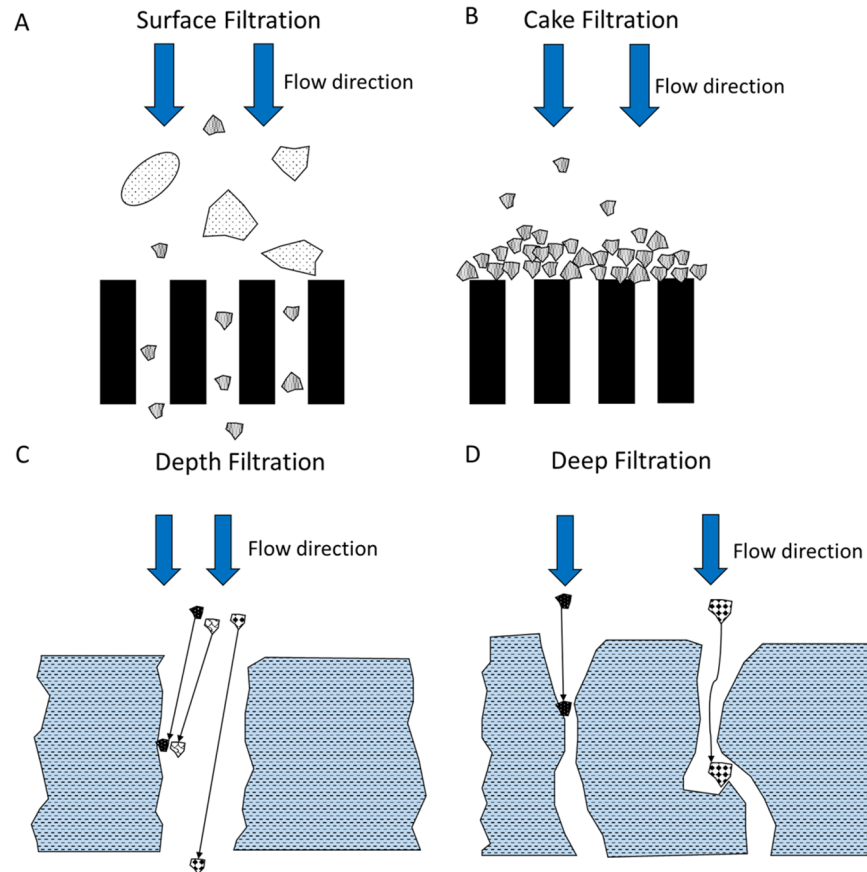


Figure 1.21: Schematic representation of various filtration mechanisms. **A:** Surface filtration, where particles larger than the pores of the filter medium are separated. **B:** Mechanism of cake filtration. **C:** The mechanism of depth filtration. Here particles adsorb in the pores of the filter medium on its wall or on previously adsorbed particles. **D:** Filtration mechanism of deep separation. [adapted from ref.^[143]

The last filtration type is the deep separation as shown schematically in **Figure 1.21 D**. This type of filtration is used for filter media that are relatively thick compared to their pore diameter. The particles to be filtered migrate along the pore to the point where the pore tapers so much that the particles cannot migrate any further. Thus, the particles are trapped in the pore. As with the depth filtration, the filter medium can only be used once, as it cannot be regenerated. This type of filtration is typical for filter media made of felt or nonwovens.^[143]

The concept of depth filtration is of high interest for this work, among other things, because supramolecular nanofibers, which are formed in situ within a scaffold and consequently resembling a depth-type filter medium. Therefore, the mechanisms for particle deposition on a fiber will be discussed in the following in more detail.

In general, the filtration mechanism of depth filtration is much more complex than simple separation, like sieving processes, where the particles are larger than the pores of the filter medium and therefore cannot diffuse through them. Depth filtration or separation is coupled with four basic mechanisms. These mechanisms are shown schematically in **Figure 1.22** and will be discussed below.

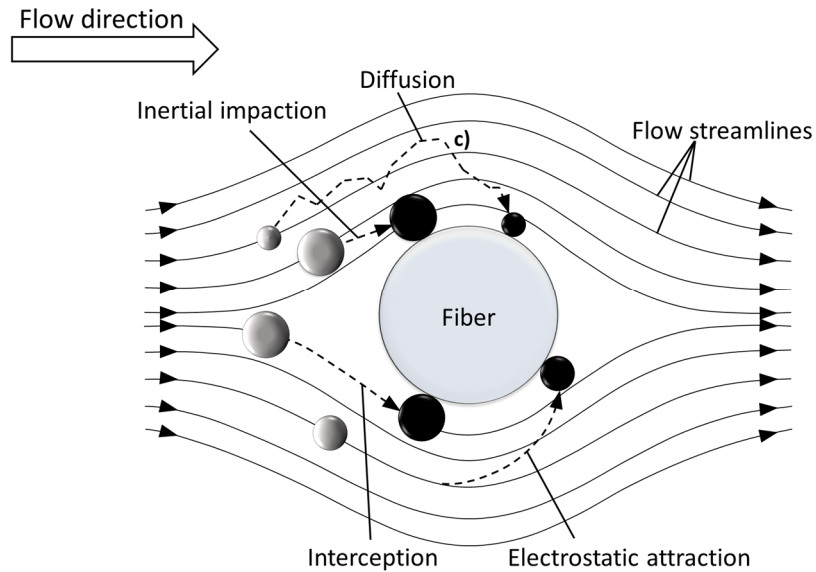


Figure 1.22: Schematic diagram of the mechanisms that can occur during depth filtration. [adapted from ref. ^[40,146]]

One of these phenomena is based on the accumulation due to the inertia of the particles. This phenomenon occurs when the inertia of the particle is big enough to have a sufficiently large momentum to break out of the flow stream line and directly deposit on the fiber. The process of interception occurs when the particles are small enough to follow the flow stream line but get sufficiently close to the fiber. As a result they are deposited on the fiber by surface interactions.^[40]

Another mechanism is diffusion. This phenomenon is based on the Brownian motion of very small particles ($\ll 0.5 \mu\text{m}$). The random movements allow the particles to leave the stream flow direction and randomly hit a filter fiber on which they are immobilized.^[40] The last mechanism is the electrostatic attraction. Here, the particle is deviates from the flow stream by attractive electrostatic interactions - most likely charges- between the particle and the fiber causing finally the deposition on the filter medium.^[40]

As outlined above, the kind of deposition mechanism of particles largely depends on the particle size. Very small particles perform a Brownian type of motion and are therefore mainly deposited by diffusion processes. Very large particles can break out of the flow stream due to the higher momentum and are separated by inertia mechanisms and finally, by interception. The overall efficiency resembles the sum of these mechanism. However, particles with a size between $0.04 \mu\text{m}$ and $0.4 \mu\text{m}$ may only be separated with great difficulty by using a filter medium. These contaminants are often too large for diffusion processes and are usually too light for mass inertia mechanisms. This region of particle sizes is called "most penetrating particle size" (MPPS) and must be specified specifically for each filter medium. The European standards for *High Efficiency Particulate Air filter* (HEPA) and *Ultra Low Penetration Air filter* (ULPA) are based on the MPPS.^[149] Since the filtration and filtration efficiency depends on parameters such as the flow velocity, the region of the MPPS varies in the same manner.

These phenomena are depicted in **Figure 1.23**, for resulting MPPS at different flow velocities. It can be seen that the MPPS decreases by an increasing flow velocity. So, the MPPS at a flow rate of 50 cm/s is shifted to smaller particle sizes and the penetration is higher than at 10 cm/s. It is assumed that for small particles below the velocity of maximum penetration, the diffusion processes for the separation from the fluid flow will dominate. Above this velocity, the inertia begins to dominate. Another factor which can influence the MPPS is the material of the particles which should be captured.^[40]

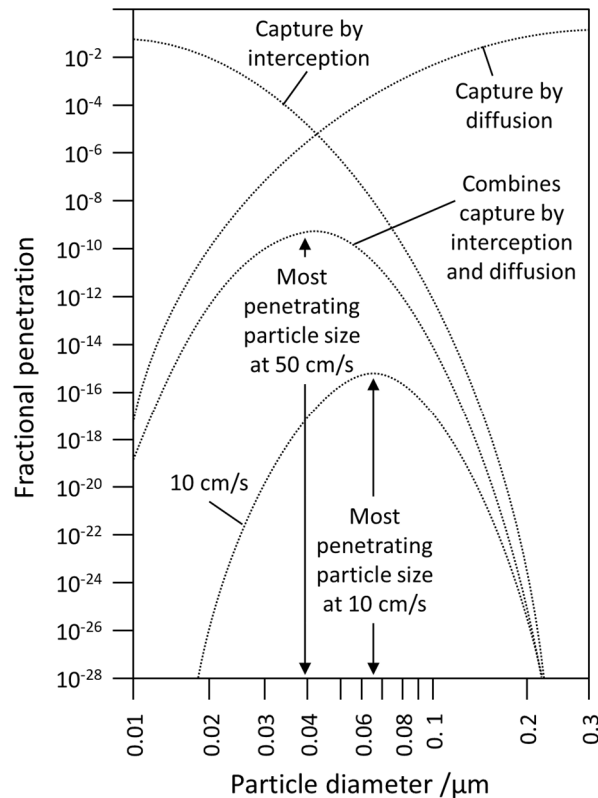


Figure 1.23: Graphical correlation between the diameter of the filtered particles and the separation mechanisms of the filter medium. Depending on the particle size and the velocity, interception or diffusion processes dominate the separation process. These two mechanisms lead to the resulting penetration of the filter. The location of the MPPS (most penetrating particle size) depends on the linear velocity of the filtration process. [Figure based on ref.^[37,40]

Irrespective of the above mentioned mechanisms, the extent how firmly a particle is deposited on the filter medium depends on physically or chemically attractive interactions.^[40] However, in filtration processes reentrainment of particles may occur, which means that already captured particles may release the filter medium during the filtration process. These particles may be detached by mechanical forces of the fluid flow. Thus, the filtration efficiency will be decreased if the filter medium is not thick enough to capture these particles again. Another issue is filter medium based migration processes, which also have a negative effect on the filtration performance. The medium migration occurs due to the release of fine fibers or particles migrating through the medium. These fibers and particles mainly result from the manufacturing process. With increasing fluid velocity, the tendency of medium migration and reentrainment increases.^[40]

1.4 Adsorption

Adsorption is the accumulation of one or more components, molecules or atoms, from a liquid or gas phase on a surface. In general, a distinction is made between two different types, *chemisorption* and *physisorption*. These two types basically resemble the extent to which the molecules adhere to the surface. The substance to be attached is called an adsorptive, the substance to which the adsorptive is attached is called an adsorbent.^[141]

In the case of *chemisorption*, a strong bond between adsorbent and adsorptive is formed. During a *chemisorption*, a substantial degree of electron transfer or electron sharing is involved. Therefore, the *chemisorption* is often regarded as irreversible. Like in chemical covalent or similar bonds, this type of adsorption is strongly directed. Thus, the *chemisorption* is highly specific and the resulting adsorption energy is much higher than that of *physisorption*. Therefore, the adsorptive always attaches to certain sides during *chemisorption*.

Physisorption is a mostly rapid and reversible process and a general phenomenon in adsorption processes. It always takes place in all kinds of adsorption processes. It occurs when an adsorptive is brought into contact with the adsorbent. All atoms and molecules form long-range van-der-Waals interactions. Therefore, almost all atoms and molecules are *physisorbed* when the temperature is low enough. For example, noble gases can only interact through van-der-Waals forces, so *physisorption* is the only way in which noble gases can adhere to a surface. The van-der-Waals forces not only occur between the adsorptive and the substrate, but also between the individual adsorptive molecules/atoms. Because of the weak adsorptive-surface interactions in the case of *physisorption*, lateral interactions are also of great importance. These lateral interactions between the molecules or atoms that are adsorbed can be as strong as those between the adsorptive and the surface. Furthermore, *physisorption* is less surface-specific than chemisorption, and multilayers of the adsorbed material can be formed. Therefore, disproportionate structures or ordered structures with a lack of coverage to the substrate can be formed at a high population density.^[150–152] In *physisorption*, in addition to the long-range attractive interactions, short-range repulsive interactions also occur. Additionally, specific molecular interactions such as polarization, field dipoles and field gradient quadrupoles can be found. They appear due to certain geometric and electrical properties of the adsorbates and the surface. Muscat et al. described that the energy for the *chemisorption* is much higher than those of the *physisorption*.^[153]

In the last thirty years, many research was done by different groups to investigate the adsorption of sulfur and sulfur-containing molecules on different metal surfaces like gold, copper, nickel or silver.^[154–161] In these cases, *chemisorption* dominates the adsorption process. Often, the self-assembled monolayers of the adsorbed molecules on the surface of a metal were investigated. Sellers et al. investigated so-called “amphifunctional” molecules which form spontaneously those monolayers.^[157]

The schematic structure of an amphifunctional molecule is shown in **Figure 1.24**. These structures are built up similar to surfactants and have three parts. The first part is the functional head group which provides the chemisorption. This headgroup can be for example a thiol group. In case of alkane thiolates on gold, the formed bond between the thiolate and the metal surface is a slightly polar Au-S bond. The second part of the amphifunctional molecule is the organic moiety. In most cases this is an alkyl chain. The last part could be an air-monolayer interface group. This group was not described in the work of Sellers et al. but they give a potential equation for the *chemisorption* of an alkanethiol on a gold surface:^[157]



However, it has to be mentioned that the reaction mechanism was not completely understood. It is clear that the species which is chemisorbed on the metal surface is the thiolate. It was found that the thiolates adsorbed on the surface of Au(111) in two chemisorption modes. In the first mode the S-C bond is about 180° (sp hybridization), in the second mode the angle is about 104° (sp³ hybridization).^[157]

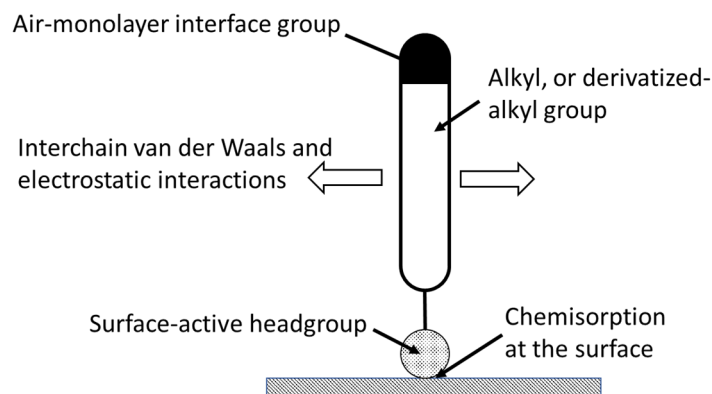


Figure 1.24: A schematic view of the forces in a self-assembled monolayer. [Figure based on ref.^[157]]

The work group of Patriito investigated the *chemisorption* and *physisorption* of alkanethiols on a Cu(111) surface.^[161] In their study, they mentioned the results of other work groups where the binding between the sulfur and the copper is much higher than between the sulfur and the alkyl chain. At high temperatures, the alkyl chain desorbed but the sulfur is still on the Cu surface. The group of Patriito found out that the chain length of the *n*-alkanethiols does not have an influence on the bonding of the *chemisorption* if the adsorbates are perpendicular to the surface.^[153,157,161]

In the different studies the strong binding between sulfur atoms and metal surfaces could be shown.

2 Aim of the thesis

One of the major challenges of this century is to gain access to clean water for everyone. A lack of clean water can lead to waterborne diseases and burdens on the society. For this reason, novel approaches to immobilize contaminations with functional nanofibers have to be developed.

Aim of this thesis is to fundamentally and comprehensively explore functional sulfur-containing 1,3,5-benzenetrisamides (BTAs) in particular in view of the formation of supramolecular fibers and their suitability in different filtration applications, including the removal of metal nanoparticles or metal ions and bacteria from aqueous media. To improve antibacterial properties of the filtration, the functional supramolecular fibers can be equipped with silver nanoparticles. To gain sufficient mechanical stability of the filter media and to provide access to a larger filtration volume, the functional supramolecular fibers shall be incorporated in different scaffolds, such as nonwovens or granular fillings. This leads to functional supramolecular fiber composites. The properties of the formed composites shall be investigated and principally demonstrated by different adsorption and filtration experiments.

The thesis is structured in three different parts as illustrated in **Figure 2.1**. This includes (i) the synthesis and structure property relation and fundamental investigation of the self-assembly behavior of sulfur-containing 1,3,5-benzenetrisamides, (ii) the investigation of such compounds as functional shell in supramolecular core-shell structures with the ability to adsorb metal ions and (iii) the use of such multicomponent supramolecular fibers in filtration applications such as sand-supramolecular fiber composites equipped with AgNPs to remove or kill bacteria during water filtration.

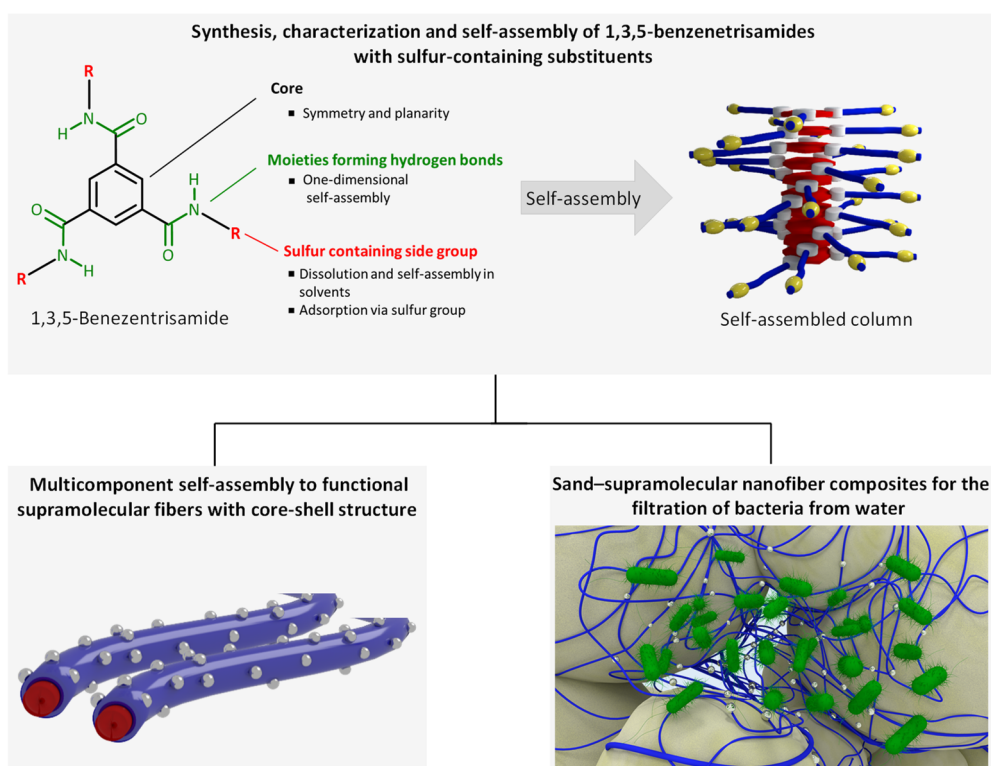


Figure 2.1: Schematic overview of the three main parts of this thesis.

Synthesis, characterization and self-assembly of 1,3,5-benzenetrisamides with sulfur-containing substituents

A large number of functional organic groups are well known in literature, which can be used for the immobilization of metals or metal ions. In particular, sulfur-, thiol- or thioether-containing groups are prominent examples to adsorb noble metals like silver or gold on their surfaces. For the purpose to form functional supramolecular fibers, a series of novel as well as four literature known functional sulfur-containing 1,3,5-benzenetrisamides shall be synthesized and investigated. The side groups are based on aliphatic thioethers, aromatic thioethers and sulfur-containing amino acids. These sulfur-containing BTAs shall be molecularly characterized by common methods of organic and polymer chemistry. An important aspect is their solubility behavior in selected solvents and subsequently their self-assembly behavior from those solutions. Selected self-assembly processes via cooling and evaporation shall be thoroughly investigated and discussed. Of particular interest is the formation of supramolecular fibers with a diameter in a range of 100 nm to 1 μm , since these fiber diameters are considered to be highly suited for filtration applications.

In this context, the following scientific questions will be addressed:

- How do different side groups based on aliphatic thioethers, aromatic thioethers and sulfur-containing amino acids vary the properties of 1,3,5-benzenetrisamides?
- How do sulfur-containing side groups of the synthesized 1,3,5-benzenetrisamides influence the solubility in organic solvents and aqueous media?
- How can such sulfur-containing 1,3,5-benzenetrisamides be tailored to defined supramolecular fibers by the processing conditions?
- Is it possible to adsorb silver nanoparticles on the surface of the supramolecular fibers?

Multicomponent self-assembly to functional supramolecular fibers with core-shell structure

A very current and interesting research topic relates to the self-assembly behavior of two or more chemically different 1,3,5-benzenetrisamides which are dissolved in the starting processing solution. Therefore, the aim of this part is dedicated to question if it is possible to prepare novel hierarchical core-shell supramolecular fibers. Thus, this research is directed to achieve core-shell supramolecular fibers featuring a defined functional shell capable of immobilizing metal nanoparticles and a non-functional core guiding the self-assembly and providing the mechanical stability. To achieve this goal, two selected 1,3,5-benzenetrisamides shall be identified for a multicomponent self-assembly process. One aliphatic BTA which is known in our research group for its good fiber formation shall be selected as supporting core material. As second component a functional sulfur-containing BTA shall be selected as shell material. By developing the right processing conditions, the desired core-shell fibers shall be produced. These supramolecular functional core-shell fibers shall be used to adsorb metal ions from

an aqueous solution. These adsorption experiments were planned to be performed in cooperation with and at the DWI–Leibniz Institute for Interactive Materials, RWTH Aachen, Germany.

In this context, the following scientific questions will be addressed:

- How can a multicomponent self-assembly process be controlled to obtain hierarchically structured core-shell fibers with defined morphology and functionality of the shell?
- How can co-self-assembled fibers be investigated to make a statement about their structure?
- How can supramolecular core-shell fiber/polymer fiber composites be established, which are stable enough to be used in continuous flow processes?
- To which extent and with which selectivity can metal ions be adsorbed on the surface of the functional shell of such supramolecular core-shell fiber/polymer fiber composites?

Sand–supramolecular nanofiber composites for the filtration of bacteria from water

Apart from the preparation and use of supramolecular nanofiber/polymer microfiber composites, previous research in our research group has also shown that supramolecular nanofibers can be formed *in-situ* within a granular filling. Such *sand–supramolecular nanofiber composites* are stable enough to be used to filtrate *E.coli* bacteria with high efficiency from an aqueous suspension. However, the use of such filter devices results in a rapid contamination of the filter device with living bacteria. In this chapter, such filters are further developed, in which the supramolecular nanofibers are designed to feature an antibacterial behavior. For this, functional-supramolecular-fiber-sea-sand-composites shall be prepared based on the previously developed multicomponent self-assembly process. These composites shall be investigated in view of their stability and the ability to adsorb silver nanoparticles as antibacterial agent inside the prepared composites. The working principle shall be demonstrated by the filtration of *E.coli* bacteria suspensions and the analysis of the filtrate. These filtration experiments were planned to be performed in cooperation with and at the DWI–Leibniz Institute for Interactive Materials, RWTH Aachen, Germany.

In this context, the following scientific questions will be addressed:

- How can a stable supramolecular core-shell fiber/ granular sand filling composite be formed?
- To which extent and how efficient can silver nanoparticles be immobilized on the shell of the supramolecular core-shell fibers inside an existing granular sand filling composite?
- How does such AgNP-loaded supramolecular core-shell fiber/granular sand filling composites improve the filtration efficiency of *E.coli* bacteria from water?

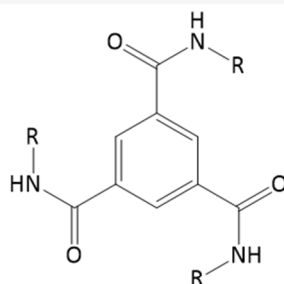
3 Synthesis, characterization and self-assembly of 1,3,5-benzenetrisamides with sulfur-containing substituents

The incorporation of a functional group into a system adds a new functionality and can lead to an increase in its performance also in view of an application. In filtration, a functional group on the surface of the fibrous material changes their chemisorption capabilities and therefore may allow for the removal of metals, metal ions or different organic materials from a media. As described in the introduction, in particular sulfur groups can strongly interact with metals, like ions or metal nanoparticles.^[158,160,161] This thesis focusses on 1,3,5-benzenetrisamides (BTAs) as supramolecular building blocks to form (nano)fibers and mostly on novel functional BTAs with sulfur-containing substituents. As of today, only a BTA with L-methionine as side group is literature-known. In this context, Jana et al. showed that this L-methionine-based BTA forms threefold hydrogen bonds to the neighbored supramolecular building blocks as it is commonly the case with BTAs during self-assembly.^[128] In the following, the syntheses and the molecular characterization of sixteen BTAs with sulfur-containing substituents will be discussed. Additionally, their thermal properties and their self-assembly behavior from different solvents will be unraveled in detail.

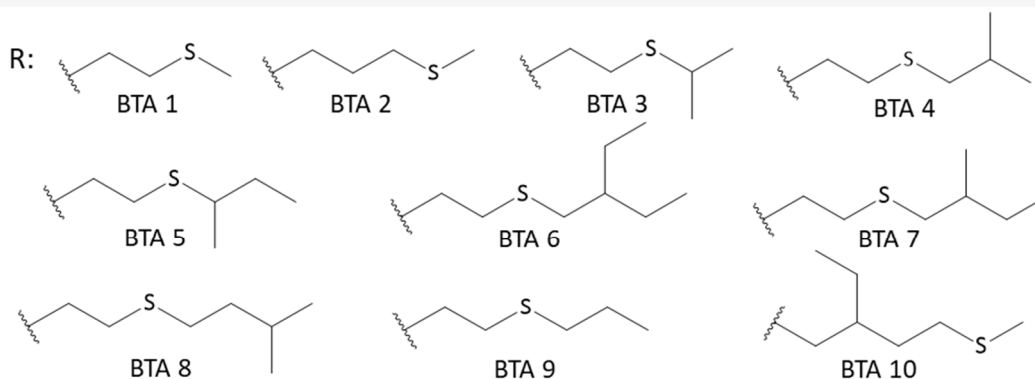
Side group selection and requirements for the sulfur-containing 1,3,5-benzenetrisamides for this work

For this work, the sulfur-containing 1,3,5-benzenetrisamides as shown in **Figure 3.1** were selected because it was expected that these molecular structures are capable to form functional supramolecular fibers applying appropriate self-assembly conditions. The first series comprises compounds with a predominantly aliphatic side chain in which the size of the aliphatic groups as well as the position of the sulfur group was varied (BTA 1 to BTA 10). In most cases, a terminal positioning was preferred but also a positioning in the middle was used to investigate their fiber formation as well as chemisorption capabilities. Apart from these BTAs with sulfur-containing aliphatic side groups in a second series, compounds with amino acids-based side groups such as cysteine (BTA 11 and BTA 12) and methionine (BTA 13) were investigated. For both sulfur-containing amino acids, the respective methyl esters and one compound with a terminal mercapto group were used. The third series consists of BTAs with aromatic sulfur-containing side groups (BTA 14 to BTA 16). Fully aromatic BTAs typically feature a very high stability at elevated temperatures. Furthermore, these components often have high transition temperature which often goes along with a poorer solubility behavior.

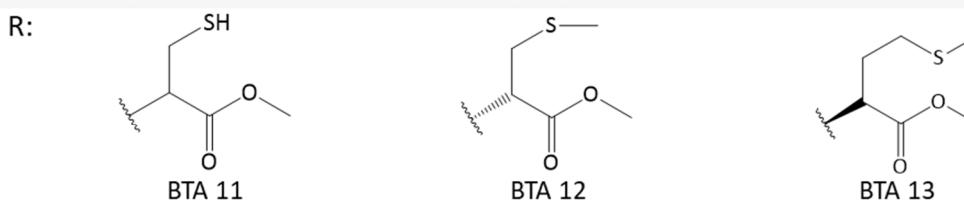
1,3,5-Benzenetrisamides (BTA) with sulfur containing side groups



BTAs with aliphatic sulfur containing side group



BTA with cysteine or methionine-based side groups



BTA with aromatic sulfur containing side group

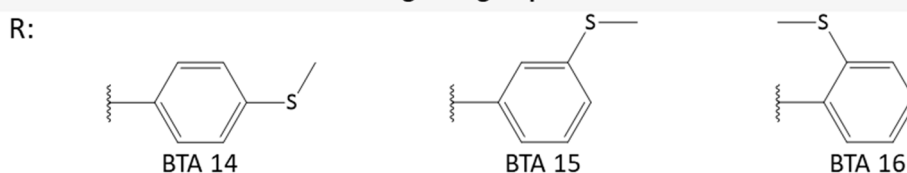


Figure 3.1: Overview of the sixteen synthesized sulfur-containing BTAs. The synthesized BTAs can be classified into three series: BTAs with aliphatic sulfur-containing side groups (BTA 1 to BTA 10); BTAs with side groups based on derivatives of cysteine and methionine (BTA 11 to BTA 13) and BTAs with aromatic sulfur-containing side groups (BTA 14 to BTA 16).

In view of further studies and their suitability in applications, which will be discussed in the chapter 4 and 5, the sulfur-containing 1,3,5-benzenetrisamides have to fulfill distinct selected requirements. First of all, the BTAs have to be soluble in one of six selected polar and comparable environmentally benign solvents such as ethanol, isopropanol, 1-propanol, 2-butanone and water. The BTAs have to be at least soluble at a concentration of 0.5 wt. % in these solvents or mixtures of those. Secondly, the BTAs have to form supramolecular fibers preferable with a diameter in a range from 100 nm to 1 μ m by self-assembly from the selected solvents because this fiber diameter is expected to provide sufficient mechanical stability of the supramolecular fibers within the composites in view of filtration and

adsorption applications. Furthermore, the formed fibers should be capable for the assemble on different scaffolds like polymer fibers of nonwovens or sea sand grains and should be suitable for metal adsorption applications. These properties will be investigated in the following part of this chapter among others by temperature-dependent solubility studies and investigation of the self-assembly behavior with the help of scanning electron microscopy.

3.1 Synthesized sulfur-containing 1,3,5-benzenetrisamides

A typical BTA comprises the chemical connection of a benzene core and the side groups via three symmetrical arranged amide linkages to form the desired structure. In general, BTA syntheses are well known as demonstrated in different numerous publications.^[37,95,124] In contrary to that, synthetic effort is required for the side group formation. As indicated in **Figure 3.1**, numerous sulfur-containing side groups were synthesized for the synthesis of the used BTAs in this thesis. Both the syntheses of the side groups and the subsequent syntheses of the BTAs will be discussed in the following part.

All compounds (including side groups and BTAs) were synthesized by Sandra Ganzleben and Jutta Failner according to my instructions at the chair of Macromolecular Chemistry I and characterized and interpreted by me with the common methods of organic and polymer chemistry, except the intermediate stages and final step for BTA 10. This compound was synthesized and characterized by Dr. Markus Winterer.

Synthesis of aliphatic sulfur-containing BTAs

The side groups for the aliphatic sulfur-containing BTAs BTA 3 to 9 had to be synthesized, the side groups for BTA 1 and 2 were commercially available.

The syntheses of the amines for BTAs 3 to 9 can be achieved in a single step, which was adapted from Kohn et al..^[162] The general reaction scheme to the sulfur-containing aliphatic side groups is shown in **Figure 3.2**. For this, 2-mercaptoethylamine hydrochloride was dissolved in a solution of NaOH in methanol to deprotonate the thiol moiety. Afterwards, a bromoalkyl, e.g. 2-bromopropane, was added to form the new S-C bond by a S_N2 reaction. Thereafter, the solution was filtrated and the solvent was removed. The obtained oily crude product was dissolved in diethyl ether and filtrated afterwards to remove precipitated salt. The solvent was removed and the oil was purified by vacuum distillation. As product, a colorless oil was obtained. The yield of the amines was in a range of 32-74 %.

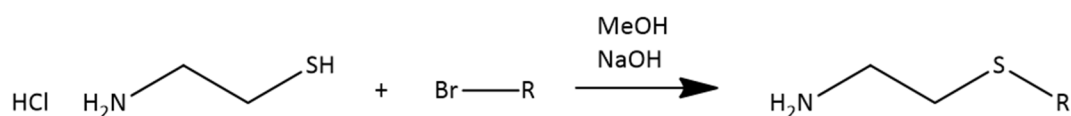


Figure 3.2: General reaction scheme of the side groups of BTA 3 to BTA 9.

As an example, the reaction scheme for the side group of BTA 3 is shown in the following **Figure 3.3**.

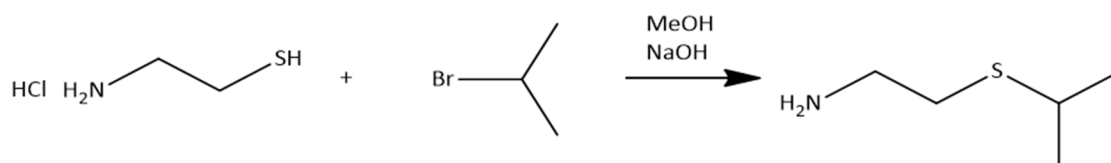


Figure 3.3: Reaction scheme of the side group of BTA 3.

For the sake of completeness, **Table 3.1** depicts the yields of the synthesized side groups. The lowest amount of product was obtained for the synthesis of the side group of BTA 5 and the highest for the amine of BTA 8. Thus, all side groups can be obtained in a rather good yield suitable for the further synthesis steps

Table 3.1: Yield of the synthesized side groups of BTA 3 to 9. Amines of BTA 1 and 2 were purchased.

Side group of BTA:	1	2	3	4	5	6	7	8	9
Yield	commercially available	commercially available	61 %	49 %	31 %	61 %	32 %	74 %	50 %

The general synthetic procedure of the aliphatic sulfur-containing BTAs (BTA 1 to BTA 9) is shown in **Figure 3.4** comprising the conversion of trimesic acid chloride with amino-functionalized side groups to the respective BTA. The synthesis was performed as it is described in the following in detail as exemplarily depicted for the synthesis of BTA 1 in **Figure 3.5**.

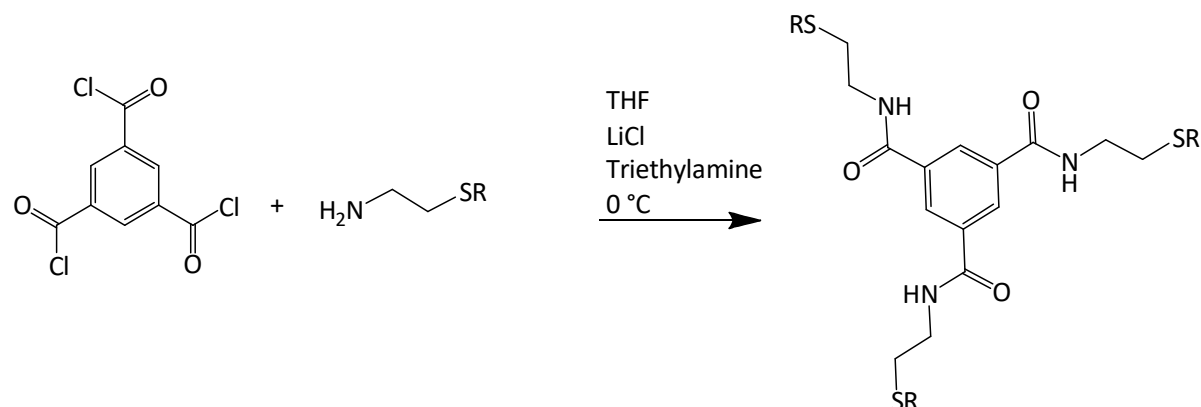


Figure 3.4: General reaction scheme of trimesic acid chloride with a thioether amine for the synthesis of the BTAs with aliphatic sulfur-containing side groups.

As an example, the synthesis of BTA 1 is shown in **Figure 3.5**.

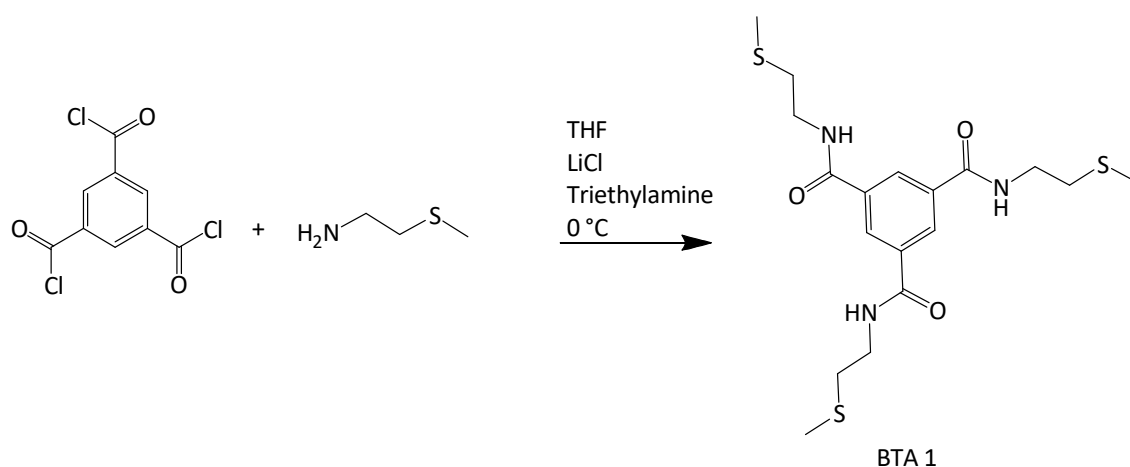


Figure 3.5: Reaction scheme of the synthesis of BTA 1.

Trimesic acid chloride was reacted with the amine, here 2-(methylthio)ethylamine, in the presence of LiCl and triethylamine. This synthesis was carried out according to the Schotten-Baumann method for the amide formation. Trimesic acid chloride was used due to fact that Cl is a very good leaving group. The used salt LiCl can break hydrogen bonds and thus it is used to avoid agglomerate formation during the synthesis as it can coordinate to the carbonyl group. The base triethylamine is used as acid scavenger but also removes a proton of the formed intermediate. As solvent, the relatively polar and aprotic THF was used to dissolve all components. The reaction was carried out under protective gas (argon) and initially at a temperature of 0 °C. To complete the reaction, the reaction solution was stirred under reflux overnight (approximately 15 h). For purification, the solution was precipitated in water to remove all educts, salts and formed hydrochlorides. Furthermore, intermediate products formed typically stays dissolved in the relatively large amount of water. Subsequently the solvent was filtered off. The crude product was recrystallized twice in methanol and then dried. A white powder was obtained as product with a yield of 69 %.

All other compounds of this series, except BTA 10, were synthesized, characterized and identified in the same manner. **Table 3.2** provides the yields after the purification and recrystallization for the compounds BTA 1 to 9. Also, the solvents for recrystallization are given if a recrystallization step was necessary. All BTAs were achieved in good yield ranging from 50 % to 100 %.

Table 3.2: Yield of the synthesized trisamides BTA 1 to 9 and the used solvents for recrystallization if necessary.

	BTA 1	BTA 2	BTA 3	BTA 4	BTA 5	BTA 6	BTA 7	BTA 8	BTA 9
Yield of BTA	69 %	72 %	99 %	100 %	56 %	50 %	90 %	73 %	79 %
Solvent for recrystallisation	MeOH	Hexane	*	*	MeOH	EtOH	MeOH	EtOH	*

* As received from precipitation

Exemplary, the ¹H-NMR spectroscopy of successful synthesis of BTA 1 is investigated here where all signals could be clearly assigned to the corresponding hydrogen atoms (**Figure 3.6**). Spectroscopic features are provided in more detail in the following. Due to the symmetrical substitution of the benzene ring, the protons of only one side arm were numbered in **Figure 3.6**. The singlet at 2.11 ppm with an integral of about 9 can be assigned to the CH₃-group (1') in the periphery next to the sulfur-group. These hydrogen atoms all have the same chemical shift and show no interaction to other hydrogen atoms in the molecule. The relatively high low-field shift for alkyl hydrogens is attributed to the adjacent sulfur atom. The triplet at 2.67 ppm with an integral of 6 is assigned to the CH₂-group (2') in direct proximity to the sulfur atom. Here, a triplet appears since the hydrogen atoms can interact with the adjacent CH₂-group. The signal at a chemical shift of 3.48 ppm is assigned to the CH₂-group

(3') adjacent to the amide group as this group leads to a low-field shift. Furthermore, a quadruplet appears here, since the H-atoms can interact with the hydrogen atoms of the amide group and those of the adjacent CH₂-group. The singlet at 8.41 ppm corresponds to the aromatic protons (1) and the triplet at 8.87 ppm is assigned to the amide protons (4'). Here, the hydrogen atom can interact with the adjacent CH₂-group so that a triplet was obtained as signal.

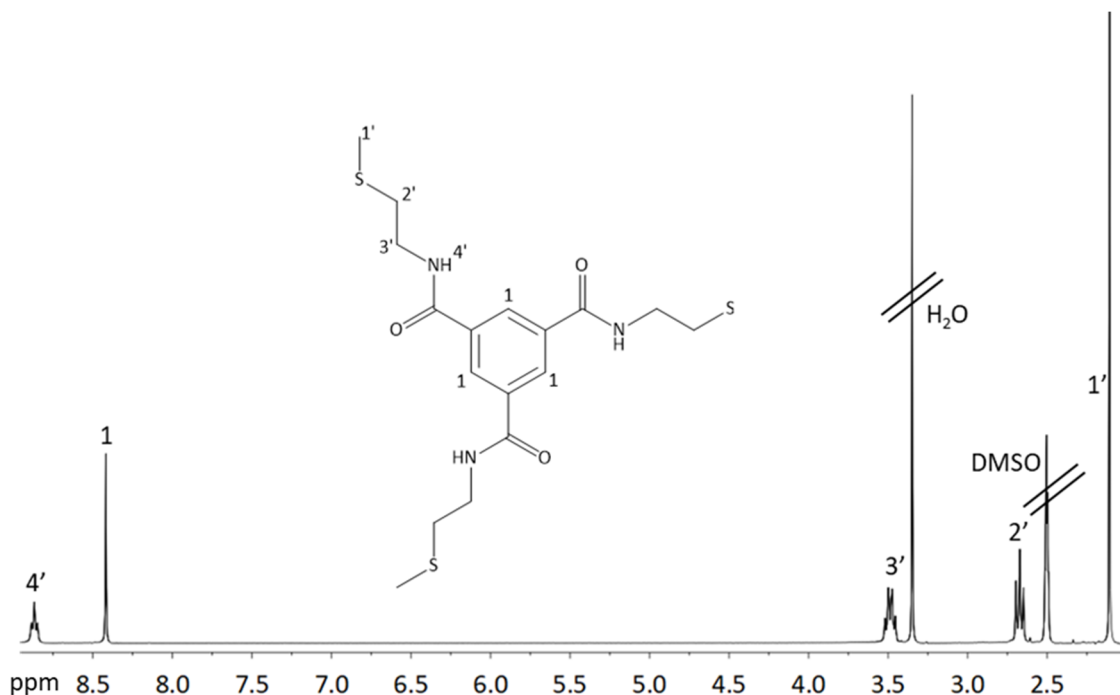


Figure 3.6: ¹H-NMR-spectrum of BTA 1, taken with a Bruker 300 MHz NMR. The signals were assigned to the corresponding hydrogen atoms.

Apart from the comparable simple preparation for the side groups 1-9, the synthesis of BTA 10 will be discussed in more detail due to the more sophisticated synthesis route.

Synthesis of the functional BTA 10

BTA 10 as a target molecule features an isoelectronically analogous structure of the side groups to the reference BTA (BTA 17) with a 2-ethylhexyl side group, yet, a CH_2 moieties at the 5th position was replaced by a sulfur atom, as shown in **Figure 3.7**.

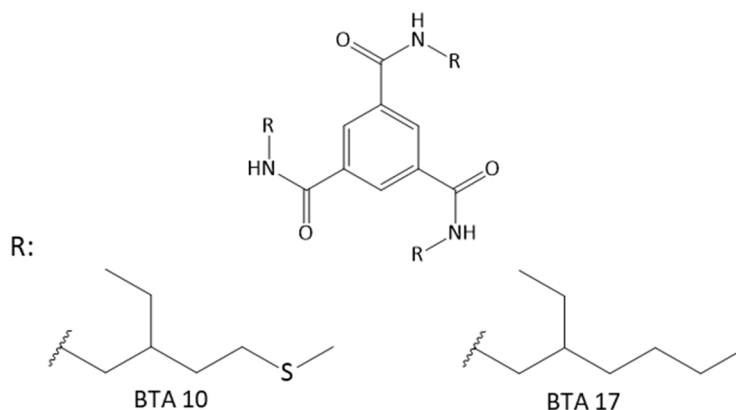


Figure 3.7. Chemical structure of BTA 10 and the isoelectronically analogous structure of the aliphatic reference BTA 17.

Therefore, it is expected that BTA 10 features similar properties particular in view of the supramolecular fiber formation. Furthermore, the relatively far outward positioned sulfur group is expected to favor a potential adsorption of metals or metal ions. The reaction performed by Dr. Markus Winterer. The reaction scheme of BTA 10 is shown in **Figure 3.8**. For the sake of clarity, details on the synthetic procedure are provided in the following

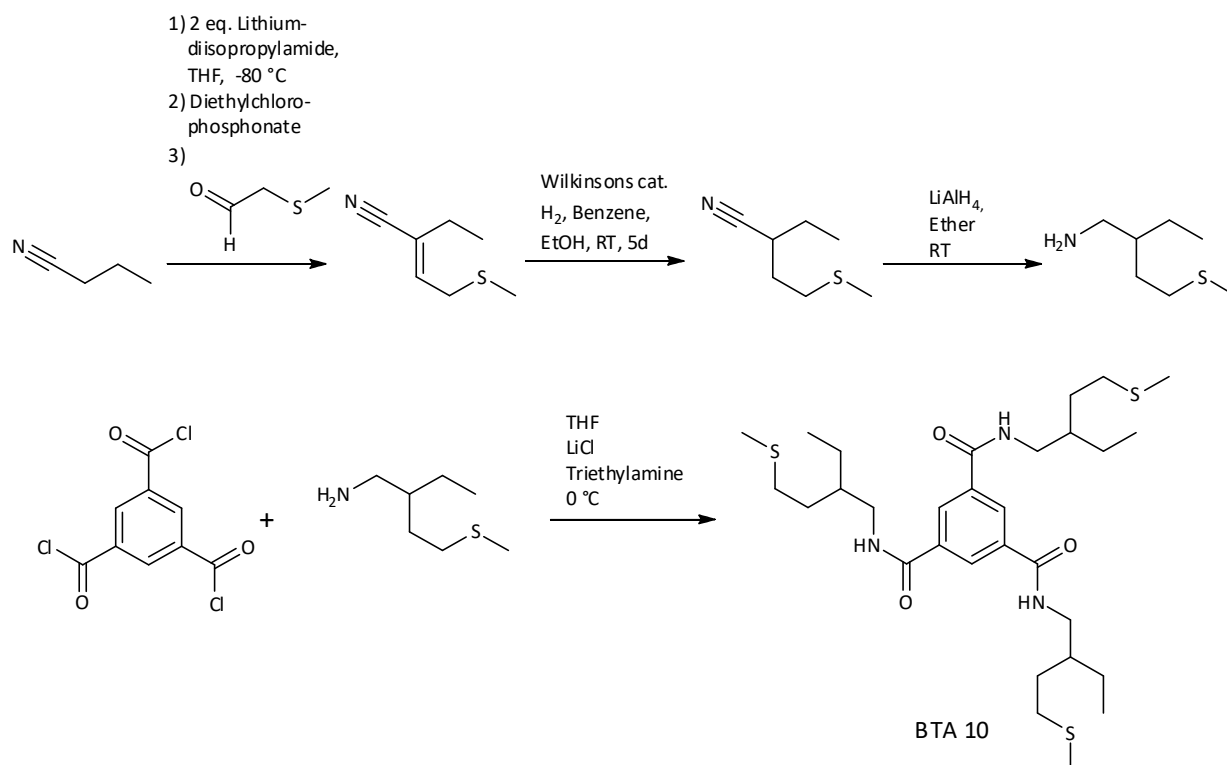


Figure 3.8. Reaction scheme of the synthesis of BTA 10. The products of each step could be achieved with a yield between 70 % and 99 %.

The first synthetic step was a one pot three step reaction starting from butyronitrile to achieve (trans)-2-ethyl-4-(methylthio)but-2-enenitrile via a Horner-Wadsworth-Emmons-Reaction of butyronitrile and 2-(methylthio)acetaldehyde. Previous to that reaction the 2-(methylthio)acetaldehyde was synthesized by the reaction of (methylthio)acetaldehyde-dimethyl-acetal and p-toluene sulfonic acid monohydrate. For the Horner-Wadsworth-Emmons-Reaction, n-butyllithium (BuLi) and diisopropylamine were dissolved in THF at -80 °C. By means of BuLi the proton of the amine was removed and lithium diisopropylamide (LDA) was formed as reagent for further conversion. Thereafter, butyronitrile in THF was added to the solution. The previously formed LDA reacts with butyronitrile and a proton at α -position was removed. To this solution, diethylchlorophosphate in THF was added. This component reacts with the formed lithium salt of butyronitrile to a phosphonate, the diethyl(1-cyanopropyl)phosphonate. With LDA present in the solution, this phosphonate reacts to diethyl(1-cyanopropylidene)phosphite. Subsequently, 2-(methylthio)acetaldehyde of the previous step was added. By means of the Horner-Wadsworth-Emmons reaction the phosphite and 2-(methylthio)acetaldehyde react to obtain the desired product. After purification steps like extraction with dichloromethane (DCM) and liquid chromatography, the product (trans)-2-ethyl-4-(methylthio)but-2-enenitrile was obtained with a yield of 71 %.

In a following synthesis step the obtained (trans)-2-ethyl-4-(methylthio)but-2-enenitrile was hydrogenated. For this, a Wilkinson-catalysator, benzene and ethanol as solvents for the catalysator and the compound was placed in a hydrogenation reactor and the reaction was performed at 3 bar hydrogen pressure and a temperature of 35 °C. After a reaction time of more than 72 h, the obtained product was purified by means of liquid chromatography to remove intermediate products. Thereafter, the solvents were removed and the crude product was washed with chloroform to remove remaining impurities. After solvent Removal, the product 2-ethyl-4-(methylthio)butanenitrile, was obtained with a yield of 79 %.

In the last step of the side group synthesis, 2-ethyl-4-(methylthio)butanenitrile was reduced with LiAlH_4 in ether under inert gas atmosphere and ice cooling. During the reaction, the nitrile group was reduced to a primary amide group. For the work-up of the product, a saturated NaOH solution was added to the synthesis solution under ice-cooling to prevent the formation of an ammonium salt. The result is a white solid. A half-molar potassium sodium tartrate solution and water were added to this solid. Sodium tartrate is used for complexation of the metals. The solution was extracted with ether and washed with brine to dissolve the organic compounds preferentially in the organic phase. Afterwards, the solution was dried over sodium sulfate and the solvent was removed. As product 2-ethyl-4-(methylthio)butan-1-amine was obtained with a yield of 99 %.

The final step comprises the conversion of 1,3,5-benzenetricarbonyl trichloride and the synthesized side group 2-ethyl-4-(methylthio)butan-1-amine to achieve BTA 10. This synthesis was performed

according to standard procedure as described at the beginning of this chapter. BTA 10 was obtained with a yield of 93 %.

In **Figure 3.9**, the $^1\text{H-NMR}$ -spectrum of BTA 10 is given. The protons of the compound were assigned to the corresponding signals. The triplet at 8.66 ppm is assigned to the amide protons (8') and is caused by the two neighbored hydrogen-atoms. The singlet at 8.37 ppm corresponds to the aromatic hydrogen atoms. The atoms have no direct neighbors thus a singlet appears. Furthermore, the peaks are downfield-shifted due to the aromatic benzene ring. The multiplet at 3.19 ppm can be assigned to the CH_2 -group (5'), which is directly neighbored to the amide group causing the downfield shift. The signal for the CH -group (4') appears at 1.54 ppm. The signals for the CH_2 -groups 3' and 6' appear at 1.36 ppm and 1.32 ppm. These cannot be clearly assigned to one specific CH_2 -group. The triplet at 0.89 ppm corresponds to the CH_3 -group (7') and appears due to the neighbored CH_2 -group. The peak for the CH_3 -group (1') appears as a singlet at 2.03 ppm. The signal for the CH_2 -group (2') overlays with the signal of the used solvent, DMSO. Nevertheless, all protons could be assigned to the corresponding signals in the NMR-spectra demonstrating that the received product was clearly identified as BTA 10 featuring a high purity.

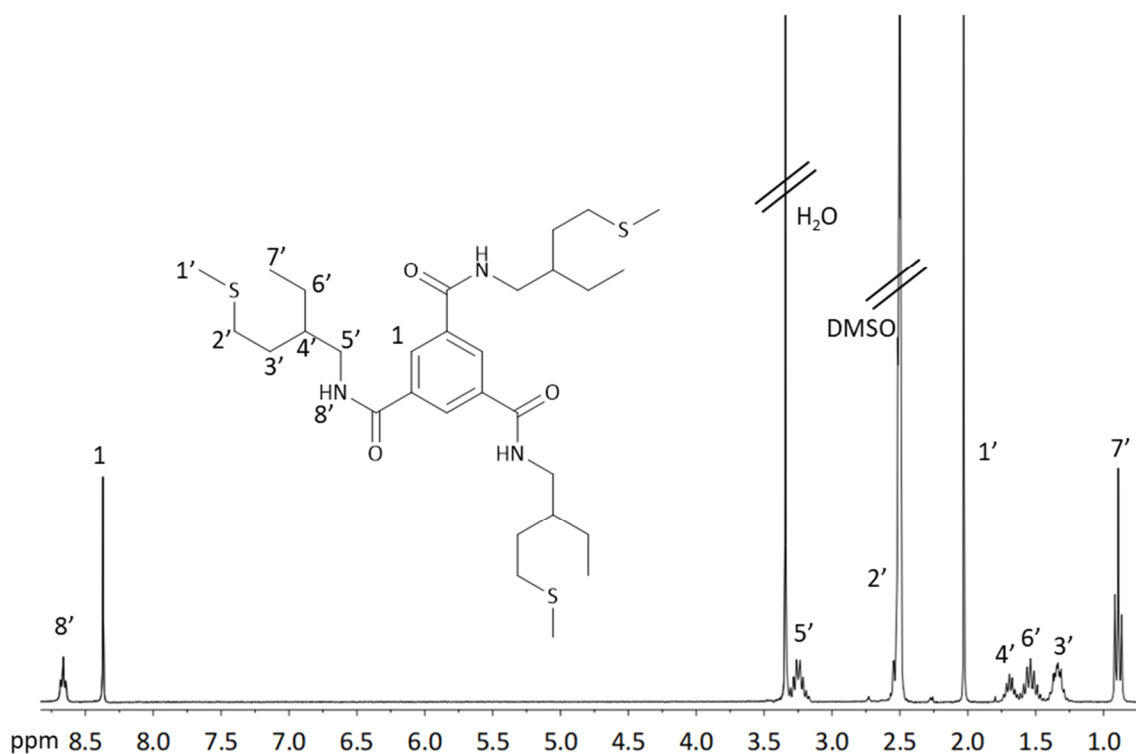


Figure 3.9: $^1\text{H-NMR}$ -spectrum of the purified 1,3,5-benzenetrisamide BTA 10. The protons were assigned to the corresponding signals.

Synthesis of BTAs with cysteine or methionine-based side groups

The side groups of these BTAs were commercially available except that of BTA 12. Here, a simple standard esterification reaction to the corresponding cysteine methyl ester derivative was synthesized first, comprising the conversion of S-methyl-L-cysteine and thionyl chloride to S-methyl-L-cysteine-amine. The synthesis of BTA 13 is shown in **Figure 3.10** as an example of the synthesis of this series of sulfur-containing BTAs. The syntheses of BTAs with amino acid derivatives as side groups were performed analogously as described at the beginning of the chapter.

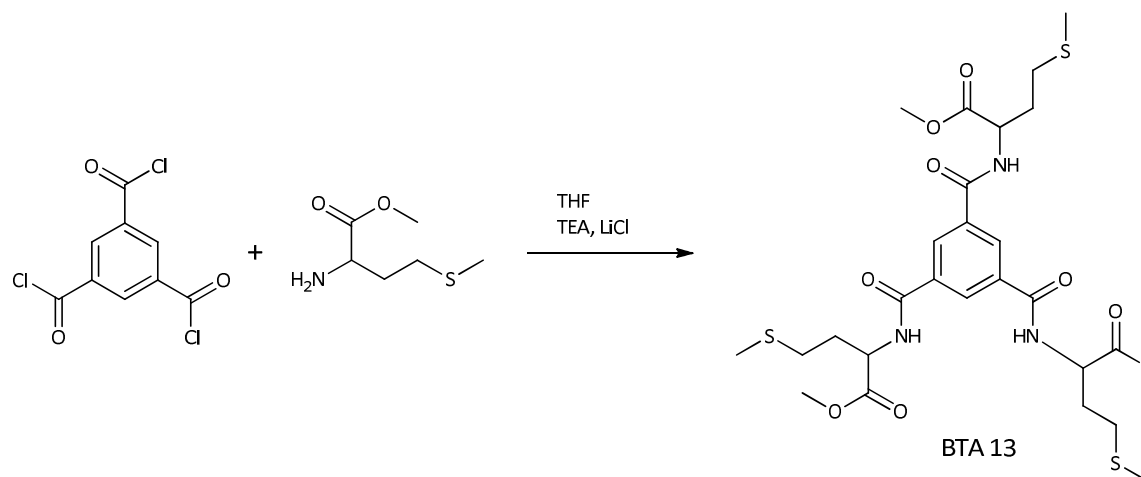


Figure 3.10: Reaction scheme of the synthesis of BTA 13.

All compound of this series of sulfur-containing BTAs were synthesized, characterized and identified in the same manner. **Table 3.3**, provides the yields after the purification and recrystallization for the compounds BTAs 11 to 13. Also, the solvents for recrystallization are given. BTAs of this group were achieved with a relatively high yield between 52 % and 72 %.

Table 3.3: Yields and solvents for recrystallization of BTAs 11 to 13.

	BTA 11	BTA 12	BTA 13
Yield of BTA	52 %	72 %	58 %
Solvent for recrystallisation	DMF	MeOH	MeOH

Exemplarily for this series, in **Figure 3.11**, the corresponding $^1\text{H-NMR}$ -spectrum of BTA 13 is shown. All protons of the BTA 13 can be assigned to the corresponding signals. The doublet at 9.16 ppm can be assigned to the amide proton (6'). The signal appearing at 8.5 ppm corresponds to the protons of the benzene (1) core. Both signals are downfield shifted due to their position near an amide group or benzene ring. At 4.6 ppm, the signal for the proton of the CH-group (4') next to the amide group emerges. This signal is also slightly downfield shifted due to the neighbored amide-group and ester group. The singlet at 3.67 ppm (5') corresponds to the protons of the CH_3 -group at the ester. The multiplet at 2.6 ppm can be assigned to a CH_2 -group (3'). The multiplet at 2.09 ppm can be assigned to

two proton groups. Once the CH₂ group (2') which is adjacent to the sulfur and the CH₃ group (1') which is also adjacent to the sulfur atom. Thus, the received product was clearly identified as BTA 13.

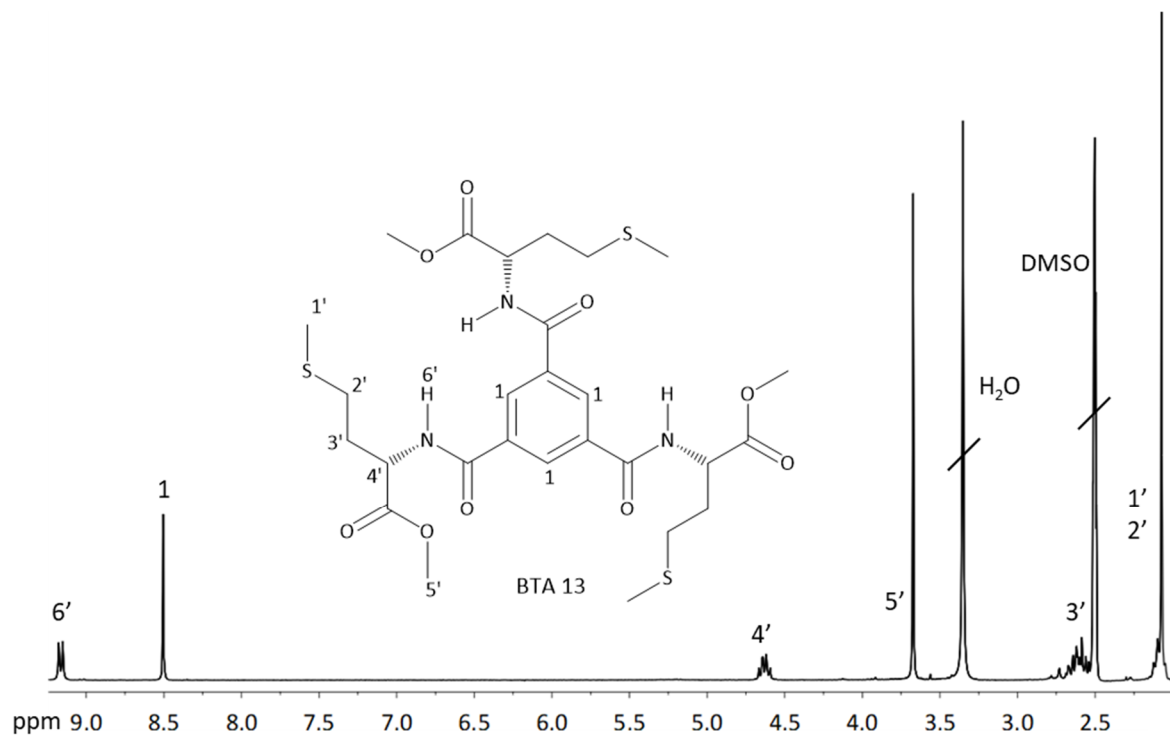


Figure 3.11: ¹H-NMR-spectrum of the purified 1,3,5-benzenetrisamide BTA 13. The protons were assigned to the corresponding signals.

Synthesis of BTA with aromatic sulfur-containing side group

All of the used side arms were commercially available and used without further purification and all BTAs with aromatic sulfur-containing side groups were synthesized in an analogous manner as described before. **Figure 3.12** depicts exemplarily the synthesis of the aromatic sulfur-containing BTA 15. In case of this series all synthesized BTAs were recrystallized in dimethylformamide (DMF) for further purification.

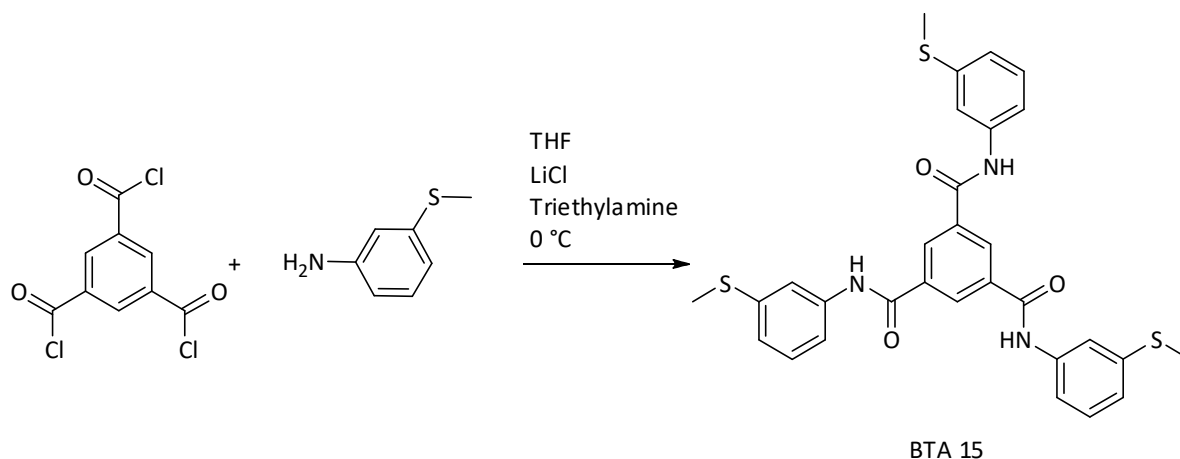


Figure 3.12: Reaction scheme of the synthesis of BTA 15.

All compounds of this series were synthesized, characterized and identified in the same manner. **Table 3.4**, provides the yields after the purification and recrystallization for the compounds BTA 14 to 16. Also, the solvents for recrystallization are given. All BTAs were achieved in good yield ranging from 73 % and 90 %.

Table 3.4: Yields and solvents for recrystallization of BTAs 14 to 16.

	BTA 14	BTA 15	BTA 16
Yield of BTA	73 %	87 %	90%
Solvent for recrystallisation	DMF	DMF	DMF

Exemplarily for this series, in **Figure 3.13** the corresponding $^1\text{H-NMR}$ -spectrum of BTA 15 is shown. Likewise, before, all protons were assigned to the corresponding signals.

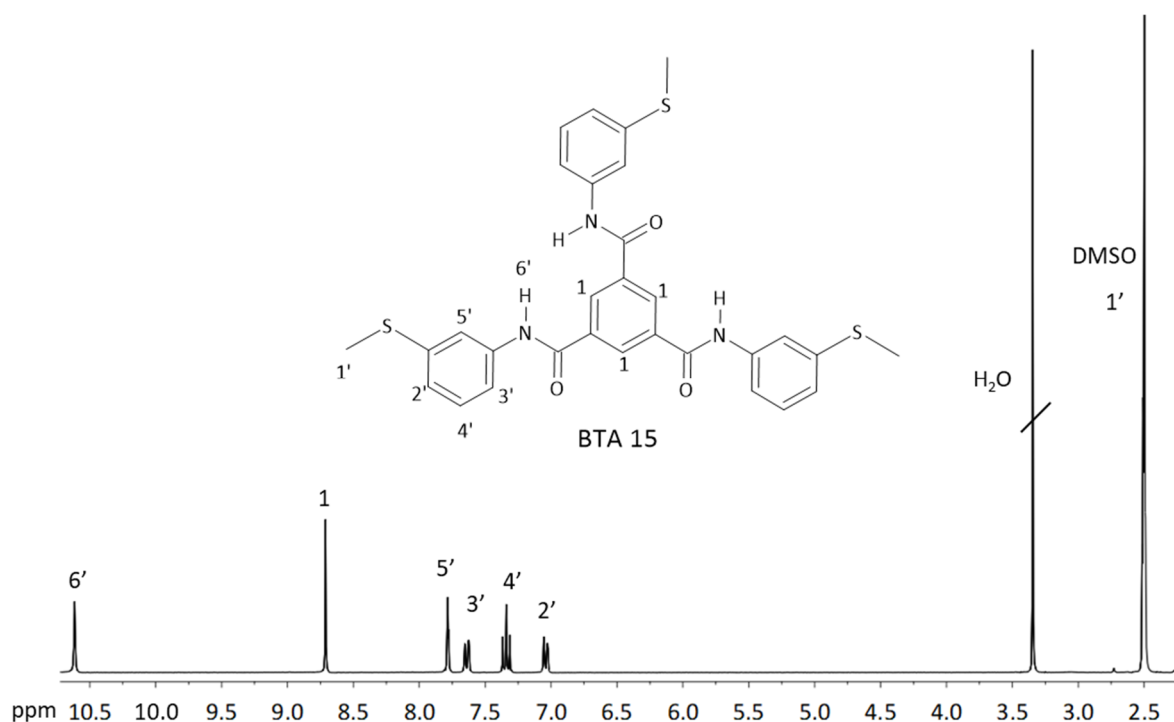


Figure 3.13: ¹H-NMR-spectrum of the purified 1,3,5-benzenetrisamide BTA 15. The protons were assigned to the corresponding signals.

The singlet at 10.6 ppm can be assigned to the amide proton (6'). The signal appearing at 8.7 ppm corresponds to the protons of the benzene core (1). Both signals are downfield shifted due to their position near or at an amide group or benzene ring. At 7.78 ppm, a triplet appears which can be assigned to the CH-group (5') at the benzene ring in the periphery next to the amide group and the thioether. This signal is also downfield shifted due to the position. The multiplet at 7.6 ppm (2') corresponds to the protons of the CH-group next to the thioether at the benzene ring. The doublet of a doublet at 7.3 ppm can be assigned to the CH proton (4') at the meta position between amide and thioether group. The multiplet at 7.0 ppm can be assigned to CH (3') next to the amide group. All these signals are downfield shifted due to their position near or at an aromatic component or functional group. The signal at 2.5 ppm partly corresponds to the CH₃-group (1') also neighbored to the sulfur atom. It has to be mentioned that also the used solvent DMSO appears at this region. Nevertheless, the received product was clearly identified as BTA 15.

3.2 Thermal characterization and FTIR-studies.

Apart from the molecular characterization as shown before, this chapter deals with a basic characterization of BTAs in view of their thermal properties as well as FTIR-spectroscopic behavior.

Investigation of the thermal properties provides information on their maximal usage temperature use as well as end use temperature which is important for some applications at elevated temperatures.

In particular, the crystallization temperatures are indicative for the self-assembly. Therefore, the thermal properties of the sulfur-containing 1,3,5-benzenetrisamides (BTA 1 to BTA 16) were investigated by means of differential scanning calorimetry (DSC) and thermogravimetric analysis (TGA) and will be discussed in the following

Moreover, FTIR spectroscopy provides information on the arrangement of the formed hydrogen bounds between the investigated BTA molecules. The position of the amide A, the C=O stretching (amide I) and the amide II vibrations (N-H bend or the C-N stretching vibration) of a FTIR-spectra of the sulfur-containing BTAs can give a hint whether there are triple helically arranged hydrogen bonds between the adjacent amide groups of the BTAs.

3.2.1 Thermal properties

The thermal behavior and stability of the 1,3,5-benzenetrisamides are of fundamental interest as this is critical to the desired continuous operating temperatures of self-assembled nanofibers. For this purpose, BTAs were investigated by means of differential scanning calorimetry (DSC) and thermogravimetric analysis (TGA) using standard conditions (heating rate: 10 K/min, N₂ atmosphere). Here, the temperature value after a mass loss of 5 %, the melting temperature according to DSC measurement and the recrystallization temperature were investigated because with these values the thermal stability, continuous operating temperatures can be determined. Furthermore, the crystallization temperature can give a hint to the self-assembly behavior of the BTAs.

Thermogravimetric analysis (TGA)

In a typical experiment for thermogravimetric analysis (TGA), approximately 10 mg of the substance is weighed and then heated up to 700 °C at a heating rate of 10 K/min under a nitrogen atmosphere. As a rule, the temperature at which a mass loss of 5 % was detected is given. This temperature is indicative either for a decomposition of the compounds or evaporation.

As typical examples for each investigated group of sulfur-containing BTAs, **Figure 3.14** shows the graph of the TGA measurement of BTA 1, BTA 13 and BTA 15.

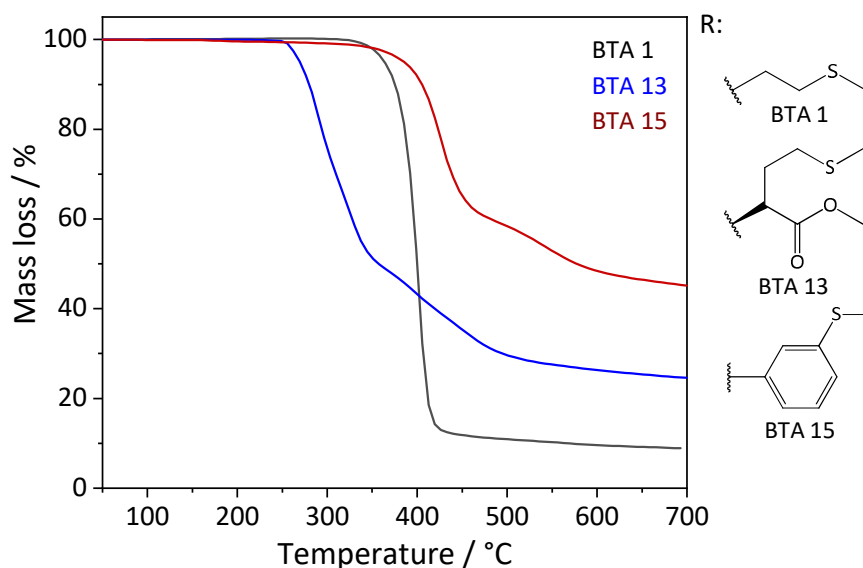


Figure 3.14: Graphs of the TGA measurements of BTA 1 (black), BTA 13 (blue) and BTA 15 (red). Experimental conditions: 10 K/min, N₂ atmosphere.

As displayed in **Figure 3.14**, the compounds show no mass loss up to 250°C. Consequently, in none of these compounds volatile components such as excess reagents or solvents were present. For BTA 1, a mass loss of 5 % was detected at a temperature $T_{-5wt\%}$ of 371 °C. Demonstrating a very high thermal stability of this organo-compounds, which also seems to represent an evaporation of the compounds since almost no residue remains after 400°C. The other two compounds show a mass loss of 5 % at 262 °C (BTA 13) and 378 °C (BTA 15), respectively. The curve of the TGA measurement of BTA 13 shows step-wise course, which is indicative for a decomposition of the compound and probably due to an ester decomposition releasing CO₂. In contrast, the BTA with an aromatic sulfur-containing side group shows a higher thermal stability, but feature also a multi-step decomposition, which may be attributed to a thioether cleavage as a first step.

Differential scanning calorimetry (DSC)

In addition to thermogravimetric analysis, DSC measurements were carried out to investigate the phase transitions of the 1,3,5-benzenetrisamides. In a typical experiment, the sample was heated under a nitrogen atmosphere with a heating rate of 10 K/min and cooled down afterwards to 25 °C with a cooling rate of 10 K/min. The resulting scans of the 2nd heating and 1st cooling of the DSC measurements of BTA 1 (**A**), BTA 13 (**B**) and BTA 16 (**C**) are shown in **Figure 3.15** representing typical examples for each group of investigated sulfur-containing BTAs.

The upper curves in **Figure 3.15 A** and **C** show the heat flow of the second heating cycle depending on the surrounding temperature. In **B**, only the first heating curve and the first cooling curve are shown. First heating shows a melting peak at 241 °C. First cooling no phase transition observed, which is attributed to BTA 13 decomposed during the melting process.

For BTA 1, a peak at 172 °C can be detected at the heating curve. This temperature represents the melting temperature of the investigated compound. The lower curve represents the heat flow of the first cooling cycle. Here, a phase transition at a temperature of 152 °C can be observed, which is attributed to the BTA crystallization. Thus, it can be claimed that the BTA does not form any further phases like a liquid crystalline phase.

In case of BTA 13, a melting point at 241 °C appears. This compound starts to decompose during the melting process. Thus, no crystallization temperature was detected during cooling. Even by performing experiments with a second heating cycle the heating curve shows no phase transition which confirms the statement made previously that the BTA degrades during melting.

From all investigated compounds, BTA 16 (**C**) shows the highest melting temperature, which was observed at 254 °C. This is a typical behavior for full aromatic amide systems. This was also expected, due to the aromatic side groups of the BTA which should lead to a higher melting temperature because more intra- and intermolecular interactions have to be overcome by thermal energy to melt this compound. Notably, the crystallization temperature was found to be at 107 °C of this BTA, which is in general a very large supercooling of 150°C. This can be probably attributed to the ortho-side groups, which represents a sterically demanding group and hampers the crystallization process.

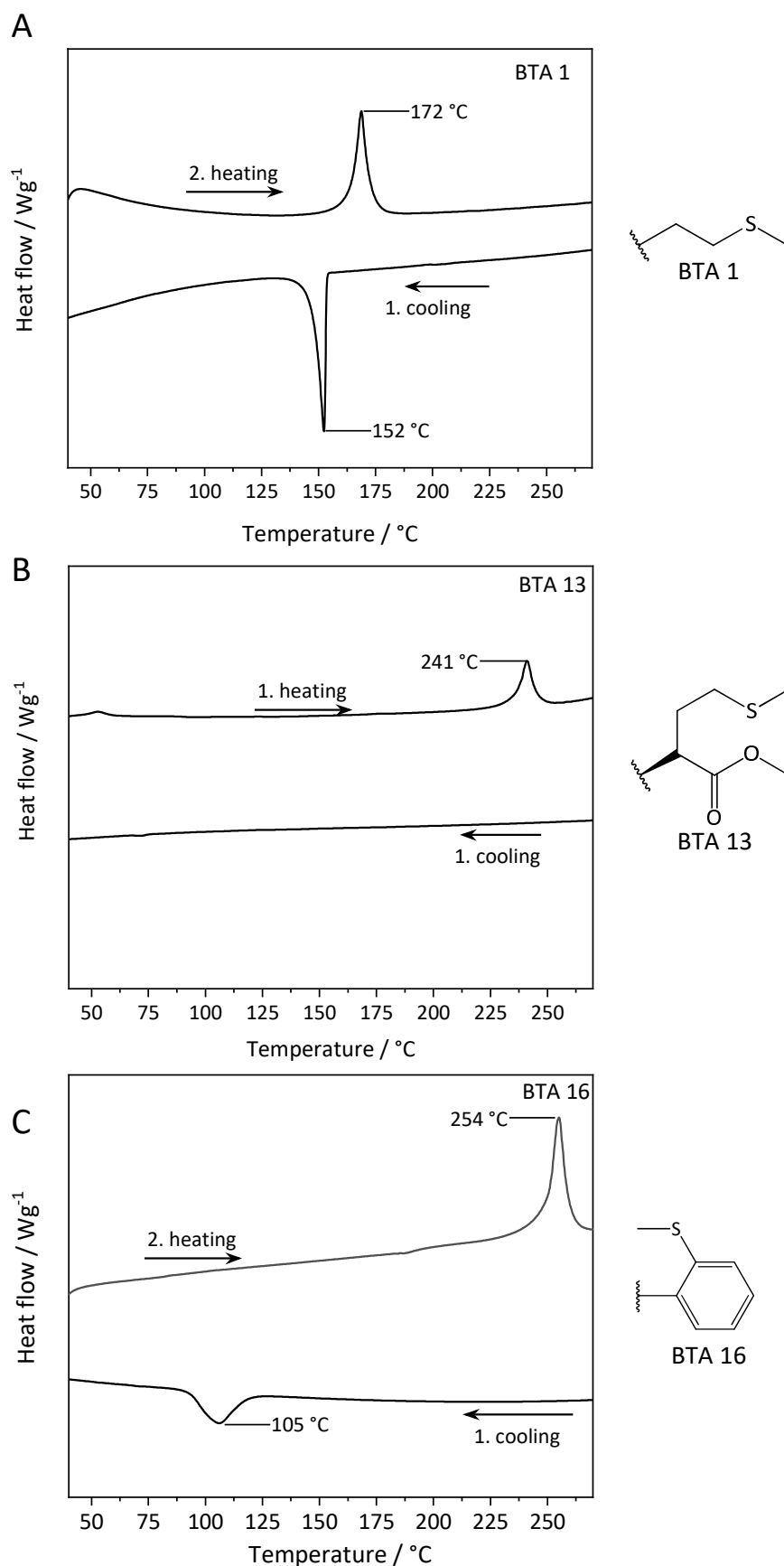
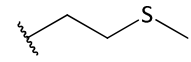
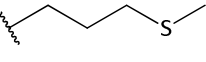
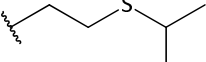
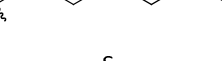
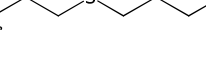
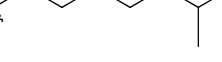
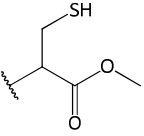
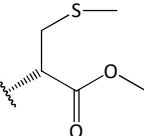
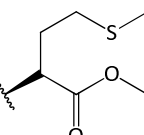
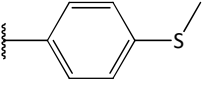
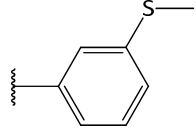
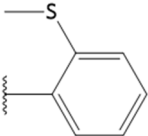


Figure 3.15: DSC measurements of BTA 1 (A), BTA 13 (B) and BTA 16 (C). For BTA 1 and BTA 16, the second heating curve (top) and the first cooling curve (bottom) are shown. In case of BTA 13 the first heating and the first cooling curve are shown. Experimental conditions: Heating rate: 10 K/min; N_2 atmosphere; two cycles.

All BTAs thermal data of all investigated sulfur-containing BTAs are listed in **Table 3.5**.

Table 3.5: Overview of the thermal properties of the sulfur-containing 1,3,5-benzenetrisamides.

1,3,5-Benzenetrisamides with aliphatic sulfur-containing side group				
		5 % mass loss [°C]^a	Melting point [°C]^b	Crystallization temperature [°C]^c
BTA 1		371	172	152
BTA 2		379	136	114
BTA 3		337	141	138
BTA 4		351	124	109
BTA 5		330	144	n.d
BTA 6		344	131	125
BTA 7		344	138	n.d
BTA 8		344	140	140
BTA 9		357	153	124
BTA 10		323	240	227
1,3,5-Benzenetrisamides with Cysteine or Methionine based side groups				
		5 % mass loss [°C]^a	Melting point [°C]^b	Crystallization temperature [°C]^c
BTA 11		260	228 ^d	-
BTA 12		263	228 ^d	-
BTA 13		262	240 ^d	-

1,3,5-Benzenetrisamide with aromatic sulfur-containing side group				
		5 % mass loss [°C] ^a	Melting point [°C] ^b	Crystallization temperature [°C] ^c
BTA 14		399	260	164
BTA 15		378	193	/
BTA 16		392	254	105

^a: TGA: heating rate of 10 K/min under N₂-atmosphere

^b: DSC: 2. Heating with a rate of 10 K/min under N₂-atmosphere

^c: DSC: 1. Cooling with a rate of 10 K/min under N₂-atmosphere

^d: Melting point of first heating. BTA decomposes upon melting

It can be seen, that the temperature of the 5 % mass loss of the BTAs with aliphatic sulfur-containing side groups (BTA 1-10) are in a range between 323 °C and 379 °C. Thus, they are all in a similar level. The melting points in the first series, lie within a temperature range of 124 °C to 240 °C. BTA 10 had the highest melting temperature with 240 °C here, since it is branched relatively close to the benzene core and thus there is a steric hindrance which must be overcome. The remaining BTAs show no branching or only a branching removed from the core. In addition, the side groups are relatively long, so that they are flexible and less energy is needed to overcome the intermolecular interactions to melt these compounds. When looking at the crystallization temperature, it is possible to deduce the nature of the shaped structure from the melt. If the temperature of recrystallization is equal to or almost equal to the melting temperature, a glassy substance is obtained. This was the case for BTA 3 and BTA 8.

The series of 1,3,5-benzenetrisamides with cysteine or methionine-based side groups (BTA 11-13), all BTAs have a 5 % mass loss at a temperature of about 260 °C. The melting points of this series are in the range from 228 °C to 240 °C. These compounds decompose during melting so that no recrystallization temperature can be determined. Due to the very similar structure of the side groups, the melting temperatures are very similar.

BTAs with aromatic sulfur-containing side groups (BTA 14-16) have compared to the other series the highest mass loss temperatures with 378 °C up to 399 °C. This can be explained by the very stable aromatic peripheral groups of the BTA molecules. BTAs of this series also show the highest melting points were reached with values from 193 °C to 260 °C.

3.2.2 FTIR-Spectroscopy

Based on the findings of the Palmans and Meijer groups, it was demonstrated that FTIR is a powerful tool to make structural statements on the BTAs.^[163] They showed that the position of the N-H stretching vibration (amide A), the C=O stretching vibration (amide I) and the amide II vibrations (N-H bend or the C-N stretching vibration) is indicative to determine a triple helically arrangement of hydrogen bonds between the adjacent amide groups. Thus, it can be predicted whether the respective 1,3,5-benzenetrisamide will form a columnar supramolecular structure on the crystallographic scale and in turn can give a hint for the formation of supramolecular fibrous structures on the mesoscale. In particular, the latter may be also dependent on the macrodipole character of the columnar aggregates and their tendency to compensate each other by an antiparallel alignment of the supramolecular columns.^[164]

A basic characterization of the sulfur-containing BTAs by means of FTIR in view of a columnar arrangement was therefore also a purpose of this work. It should be noted that the solvent and other external influences can greatly influence the formation of a columnar arrangement or fibrous mesoscale structure, as it was discussed in the introduction of this work. In detail, Meijer et al. described that the amide A and the amide II vibrations for a columnar stacking should feature a wavenumber in the range of around 3220 cm^{-1} and 1550 cm^{-1} , respectively.^[163] The amide I is typically located at 1630 cm^{-1} . But often rather insensitive to the kind of the arrangement pattern.

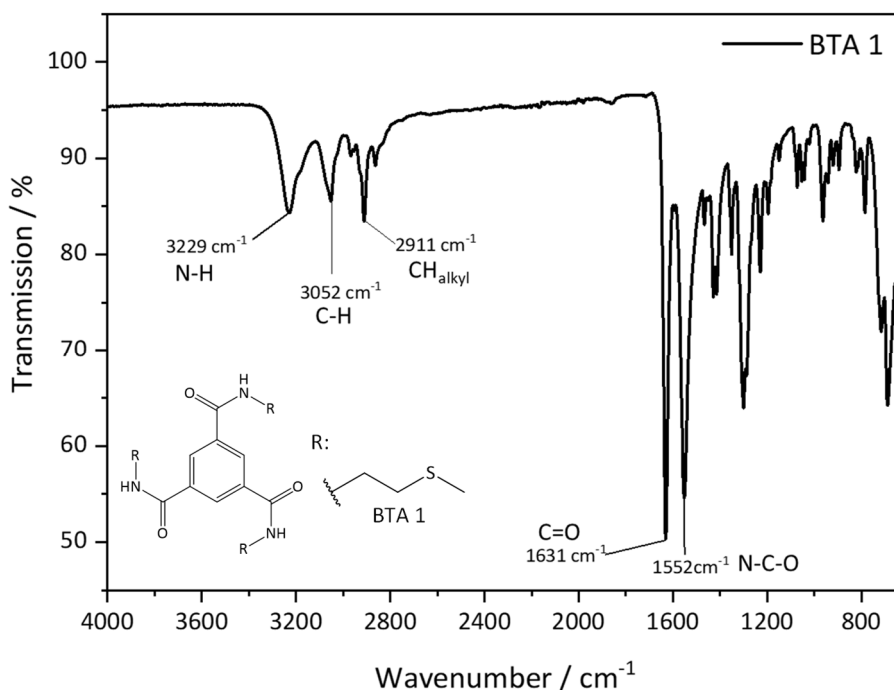


Figure 3.16: FTIR spectrum of BTA 1. The characteristic amide II vibration appears at 1552 cm^{-1} , the C=O stretching vibration appears at 1631 cm^{-1} and the N-H stretching vibration at 3229 cm^{-1} .

The FTIR spectrum of BTA 1 is shown in **Figure 3.16** as an example. For BTA1, the characteristic signals appear at 3229 cm^{-1} (N-H stretching vibration), 1631 cm^{-1} (C=O stretching vibration) and at 1552 cm^{-1}

(N-H bending or the C-N stretching vibration). The C=O stretching vibration at 1631 cm^{-1} suggests that only the amide is observed and no significant portions of the educts such as a carbonyl acids or acid chlorides are present. Thus, FTIR-spectroscopy provides also insights as to whether the reaction was completed and the desired product was obtained. This was also proven via NMR-spectroscopy measurements before. Furthermore, a possible columnar structure can be assumed.

In the following, the FTIR-spectra of the sulfur-containing BTAs are given in three diagrams, each for the single series. In all cases, the main attention was paid to the investigation of a potential columnar stacking of BTA molecules. Thus, the areas of the amide A, the amid II and the amide I vibrations are highlighted.

1,3,5-Benzenetrisamides with aliphatic sulfur-containing side groups

Figure 3.17 shows the FTIR-spectra of BTAs 1 to 10. The characteristic amide vibrations, which indicate a columnar stacking are marked green. The amide I vibrations are marked grey.

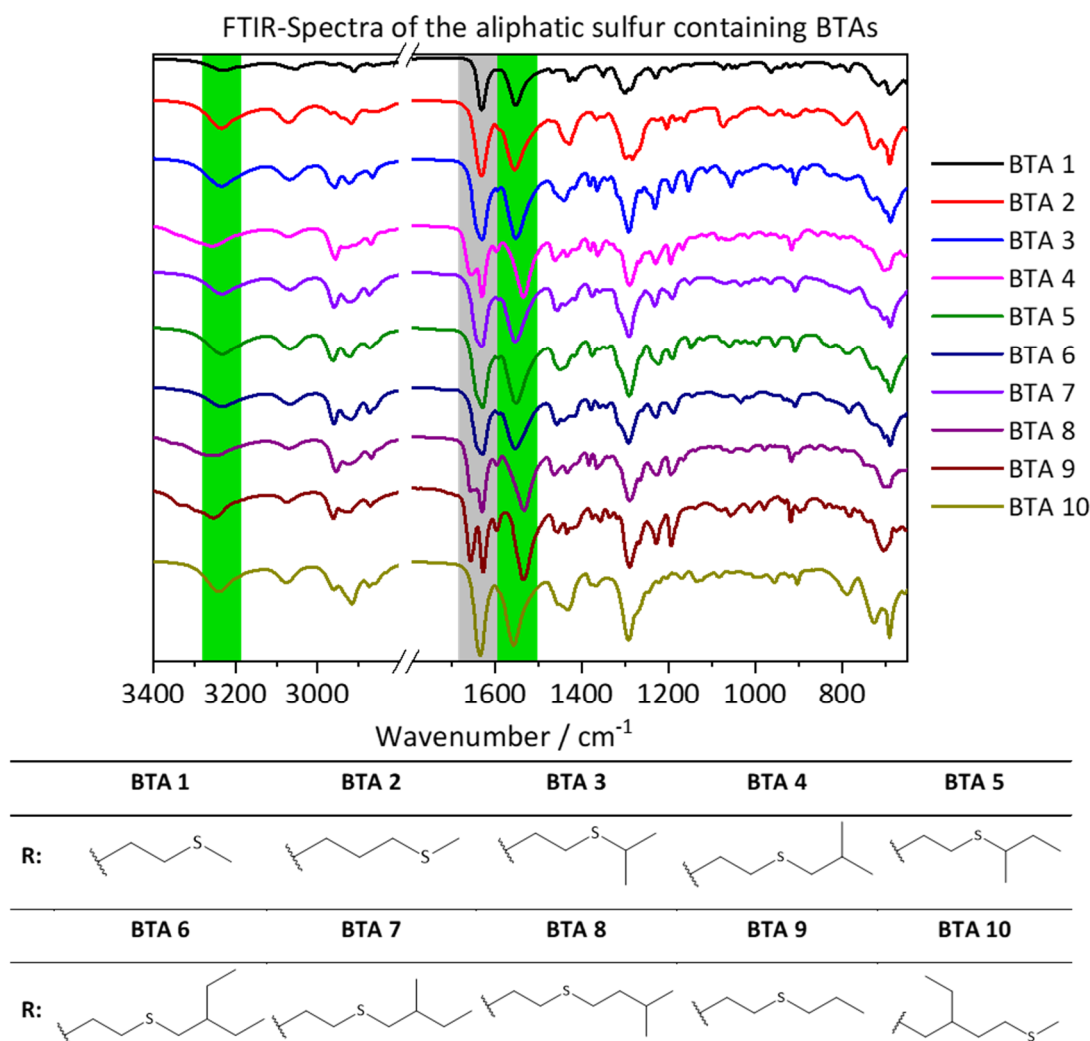


Figure 3.17 FTIR-Spectra of BTAs 1 to 10 detected in a range of 650 cm^{-1} to 3400 cm^{-1} . The areas of the characteristic wavenumbers for the N-H stretch amide II vibration which indicate the threefold hydrogen bonds are marked green (3240 cm^{-1} and 1560 cm^{-1}). The area of the C=O stretch vibration is marked grey (1640 cm^{-1}).

The FTIR-spectra for the 1,3,5-benzenetrisamides with sulfur-containing aliphatic side groups indicate that in all cases the amide A and the amid II vibrations appear in the range where they indicate a columnar aggregation of the single BTA building blocks. In all cases, the amide II vibration is relatively sharp. A second vibration next to the main vibrations could give a hint to a second species. Thus, it might be possible that no threefold hydrogen bonds were formed. Then, another amount of energy would be needed for the vibration of the amide II vibration due to the change of the reduced mass.^[165] With a columnar structure of the stacked BTA molecules, it is likely to obtain supramolecular nanofibers by a self-assembly process. It has to be noted that the samples were investigated as obtained from the synthesis and no further self-assembly was preceded. Dependent of the used solvent, it could be possible to get a non-columnar stacking, because the arrangement of the formed hydrogen bond could be changed. It would be also possible that solvent molecules were built in the formed self-assembled structure.

1,3,5-Benzenetrisamides with cysteine or methionine-based side groups

Figure 3.18 shows the FTIR-spectra of BTAs 11 to 13. Again, the characteristic amide vibrations, which indicate a columnar stacking are marked green. The amide I vibrations are marked grey.

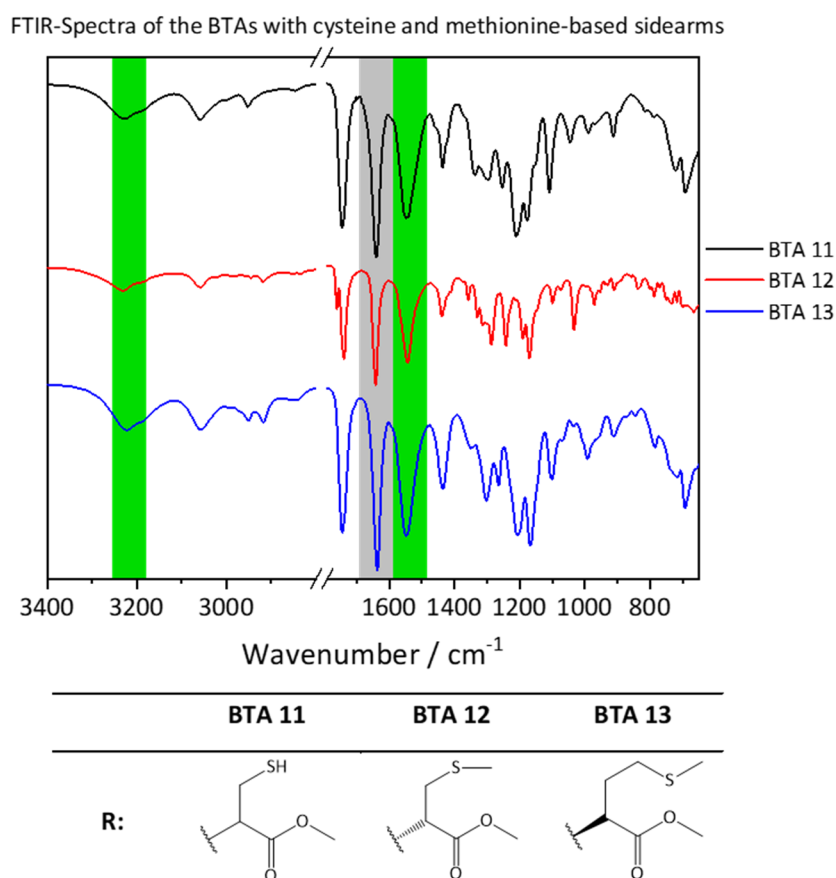


Figure 3.18: FTIR-Spectra of BTAs 11 to 13 detected in a range of 650 cm^{-1} to 3400 cm^{-1} . The areas of the characteristic wavenumbers for the N-H stretch amide II vibration which indicate the threefold hydrogen bonds are marked green (3240 cm^{-1} and 1560 cm^{-1}). The area of the C=O stretch vibration is marked grey (1640 cm^{-1}).

The three FTIR-spectra for the 1,3,5-benzenetrisamides with cysteine or methionine-based side groups indicate that in all cases the amide A vibrations appear in a small area around 3240 cm^{-1} and the amide II vibration appears in a small area around 1560 cm^{-1} . The signals especially for the amide I and amide II vibrations are very sharp. For this series of BTAs another vibration is very prominent. At 1740 cm^{-1} the ester vibration of these components appears. The results indicate that the supramolecular building blocks might assemble into a columnar structure. For BTA 13, the formation of threefold hydrogen bonds was already described in literature before.^[128] Likewise in the series of BTAs with sulfur-containing aliphatic side groups, the BTAs were investigated as they were obtained from synthesis. Nevertheless, the results give important information if the building blocks might form supramolecular nanofibers via a self-assembly process.

1,3,5-Benzenetrisamides with aromatic sulfur-containing side groups

Figure 3.19 shows the FTIR-spectra of BTAs 14, 15 and 16. In the same manner, the characteristic amide vibrations, which indicate a columnar stacking are marked green and the amide I vibrations are marked grey.

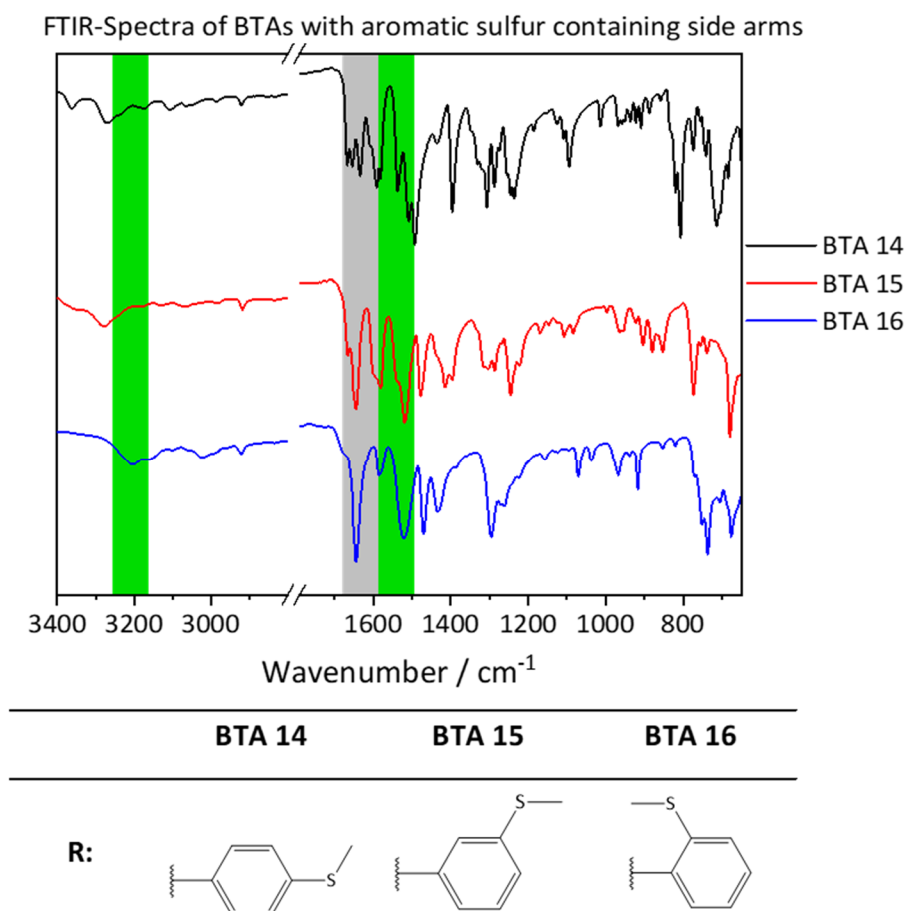


Figure 3.19: FTIR-Spectra of BTAs 14 to 16 detected in a range of 650 cm^{-1} to 3400 cm^{-1} . The areas of the characteristic wavenumbers for the N-H stretch amide II vibration which indicate the threefold hydrogen bonds are marked green (3240 cm^{-1} and 1560 cm^{-1}). The area of the C=O stretch vibration is marked grey (1640 cm^{-1}).

In the case of BTA 14, there are multiple signals in the area of 1560 cm^{-1} . This indicates that there are different species, which form hydrogen bonds to the amide group, because in a similar manner, the amide A vibration is shifted to multiple higher wavenumbers. The amide A, which is attributed to the columnar stacking is assigned here to the vibration located at 3273 cm^{-1} . In the case of BTA 15, there is a shoulder in the signal for the amide II signal which indicates a second species forming hydrogen bonds. Likewise, for BTA 14 the amide A vibration is shifted to higher wavenumbers. These results indicate that BTAs 14 and 15 do not aggregate into a triple helical columnar structure. Thus, it is less possible to form stable supramolecular nanofibers with these BTAs. Only one of the molecules, BTA 16, might show the characteristic vibrations for a columnar aggregation of the supramolecular building blocks. Also, the amide A vibration appears in the expected area for columnar arranged BTAs. It might be possible that BTA 16 forms threefold hydrogen bonds.

Likewise, in the groups of aliphatic sulfur-containing BTAs investigated before, BTAs with aromatic sulfur-containing side groups were investigated like they were obtained from the synthesis. Nevertheless, the results give important information if the building blocks can possibly form supramolecular nanofibers via a self-assembly process.

3.3 Self-assembly of sulfur-containing 1,3,5-benzenetrisamides to supramolecular (nano)fibers

3.3.1 Self-assembly processing schemes

Self-assembly can be regarded as an autonomous, spontaneous process of structure and pattern formation. The resulting supramolecular structures are created by a bottom-up process and driven by directed intermolecular interactions such as the three-fold hydrogen bond formation as it is commonly known for BTAs and used in this work. Due to the non-covalent nature of the secondary interactions, this process is reversible. In principle, self-assembly can be initiated in various ways, such as changing the temperature, the polarity of the solvent, the concentration. These factors can also drive the aggregation process in a certain direction. **Figure 3.20** depicts several self-assembly processes plotted in corresponding phase diagrams, which are relevant in this work. In all cases the red circles represent the BTA molecules and the blue circles the solvent molecules, respectively. The red lines represent self-assembled supramolecular (nano)fibers. In scheme **A**, the self-assembly upon cooling is shown, which starts with the completely dissolved BTAs at elevated temperatures and at a given concentration (I). Upon cooling, the “quality of the solvent” changes till a threshold is reached where the self-assembly takes place which lead to the formation of supramolecular fibers (II). Such supramolecular fibers can be used for example for further investigations, if the solvent is removed. This process is depicted in more detail in scheme **B** if a constant cooling or heating rate is applied, which is typically the case in experimental conditions. Depending on the cooling rate, the solution becomes supersaturated and nuclei are formed which results in the supramolecular fiber formation. Typically, the solution becomes turbid and therefore are referred to as the cloud point. Upon heating, the aggregates disassemble at higher temperatures until a clear solution is obtained again. This temperature is typically referred to as the clear point. Since the supersaturation and nuclei formation is cooling rate dependent, a hysteresis between the cloud and clear point is typically observed. The points where the BTA is fully dissolved and where it starts to self-assemble are schematically marked in the figure by black circles at the corresponding cooling or heating arrows where those cross the red or blue border line, respectively.

In contrast to **A** and **B**, which describes self-assembly and disassembly by a temperature change at constant concentration, scheme **C** depicts the self-assembly upon evaporation of the solvent at a constant temperature. Upon increasing the concentration, nuclei formation is initiated which results in supramolecular fiber formation. Ultimately, scheme **D** combines the processes as discussed in **A** and **C**. In this situation, a BTA solution at elevated temperatures upon cooling of the solution and evaporation of the solvent, the self-assembly takes place when nuclei are formed and ends when all BTA molecules are consumed resulting in supramolecular fibers. This situation can be easily achieved

by placing a hot solution on a surface, however with limited control on the cooling rate and concentration increase. After complete drying, the formed structures can be directly investigated. Since the self-assembly upon cooling and evaporation is a straightforward method to screen and investigate supramolecular nanofiber morphology, it will be mainly used in this chapter for the investigation of the self-assembly behavior of the sulfur-containing BTAs.

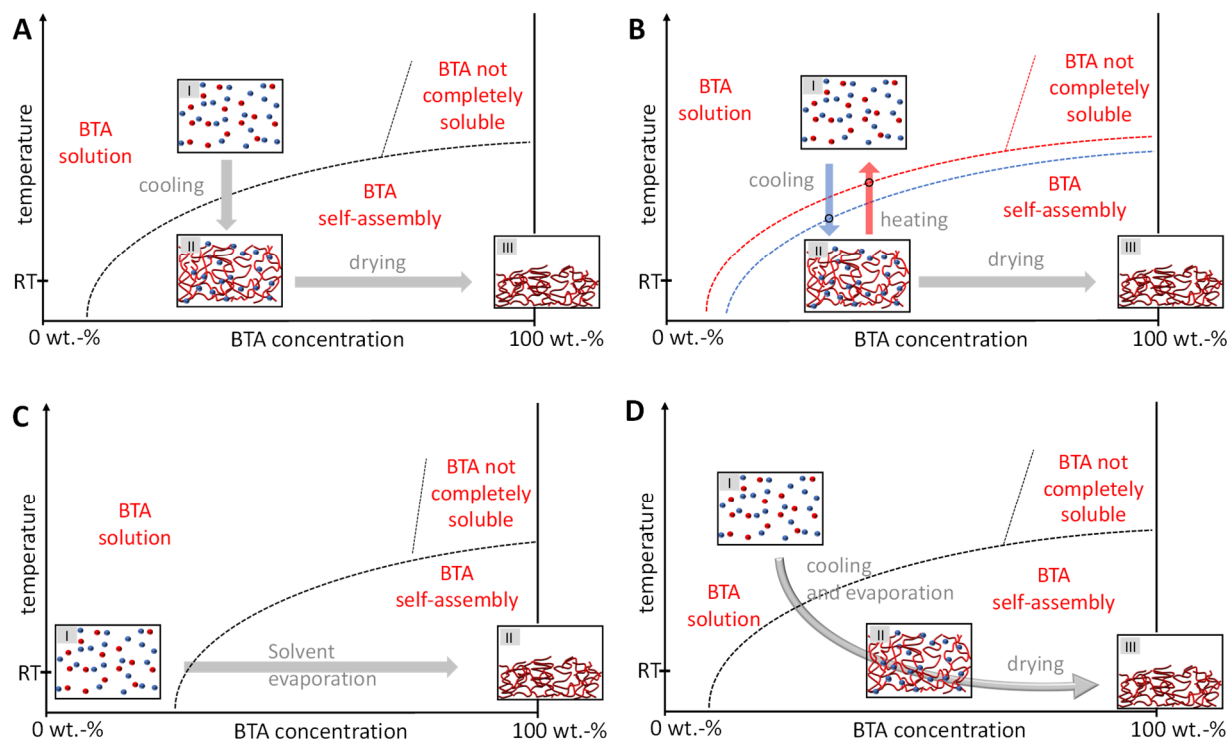


Figure 3.20: Schematic representations of four different self-assembly processes. The blue circles represent solvent and the red circles BTA molecules. The red lines represent the formed supramolecular (nano)fibers. **A:** Self-assembly upon cooling. **B:** Self-assembly process upon cooling. The system must be supercooled in comparison to heat up in order to initiate self-assembly. The red dashed line represents the phase border upon heating and the blue dashed the line phase border upon cooling. **C:** Self-assembly process upon solvent evaporation. **D:** Self-assembly process upon cooling and evaporation of the solvent.

3.3.2 Solubility and self-assembly behavior of sulfur-containing 1,3,5-benzenetrisamides in polar solvents at defined concentrations

Prior to the self-assembly of sulfur-containing 1,3,5-benzenetricarboxamides, solubility studies were performed. The knowledge of the solubility is important because it determines the applicability of selected solvents. The primary aim of the measurement was to determine the temperature at which the BTAs appeared to be completely dissolved (clear point) as pointed out before. As solvents ethanol, isopropanol, 1-propanol, 2-butanone and water were selected, because they represent to a large extent environmentally benign liquid media. The solubility behavior was investigated with the help of a Crystal16™ device from Technobis. With this device, it is possible to detect the solubility via photo turbidity simultaneously in four reactors with four chambers with a volume of 1.5 mL each resulting in a total number of 16 parallel conducted experiments. The turbidity is detected with a laser at a

wavelength of 645 nm. Each reactor vessel can be cooled and heated independently. The maximum operating temperatures are in a range from $-15\text{ }^{\circ}\text{C}$ to $150\text{ }^{\circ}\text{C}$.

The solubility of the BTAs at first were investigated at a BTA-concentration of 0.5 wt.-%. This was selected as a minimum concentration at which the BTAs should be soluble for a potential application. The solution was stirred at 600 rpm with an overhead stirrer. For the solvents ethanol, isopropanol, 1-propanol and 2-butanone, the solubility was investigated in a temperature range from $-10\text{ }^{\circ}\text{C}$ up to $75\text{ }^{\circ}\text{C}$. The samples with water were investigated in a range from $1\text{ }^{\circ}\text{C}$ to $90\text{ }^{\circ}\text{C}$. The temperatures were chosen due to the boiling and melting points of the selected solvents. The heating and cooling rate in all cases was 0.5 K/min or -0.5 K/min , respectively. All samples were heated up and cooled down two times.

In the following **Figure 3.21**, the values for the transmission of the second heating and cooling cycle of BTA 1 in 1-propanol at a concentration of 0.5 wt.-% were plotted against the temperature. With these plots it is possible to extract the values for the corresponding clear and the cloud points if applicable.

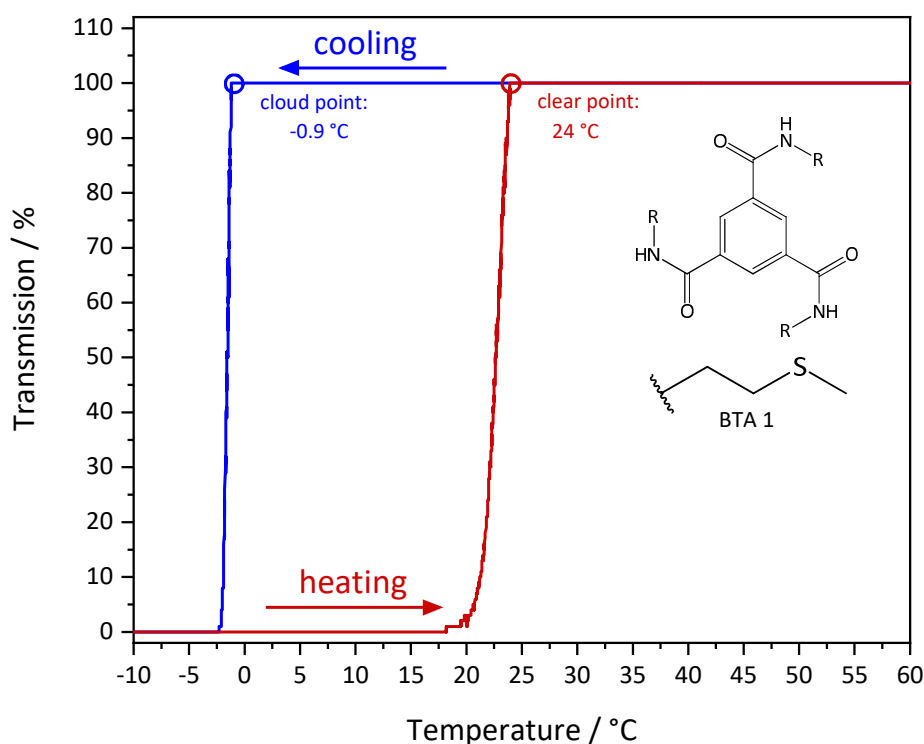


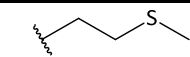
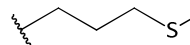
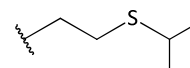
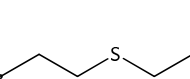
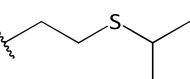
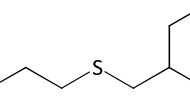
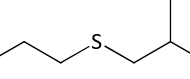
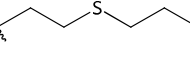
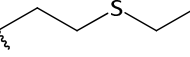
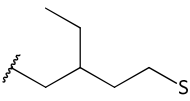
Figure 3.21: Plot of the transmission against the temperature of BTA 1 in 1-propanol. The red line represents the second heating, the blue line represents the second cooling. The red circle marks the clear point where the BTA is completely dissolved. The blue circle represents the cloud point where the BTA starts to self-assemble.

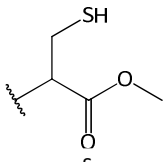
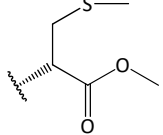
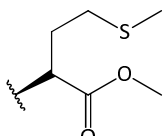
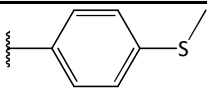
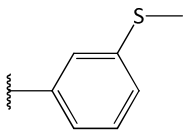
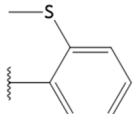
For example, the temperature-dependent transmission plots in **Figure 3.21**, allows to determine at which temperature BTA 1 is fully dissolved and at which temperature the BTA self-assembles from the used solvent 1-propanol. The red curve represents the second heating and the blue curve represents the second cooling cycle. The temperatures for the dissolution and the self-assembly for all investigated 1,3,5-benzenetrisamides are given in **Table 3.6** and were evaluated with such a graph. The

clear point where all BTA molecules are completely dissolved in the used is in this thesis determined where a transmission is 100 % is reached as it is indicated in the **Figure 3.21** by the red circle. In this example, BTA 1 is fully dissolved at a temperature of about 24 °C in the second heating cycle. The cloud point where the BTA starts to self-assemble is determined in thesis where the transmission starts to deviate from 100 % and will decrease rapidly in the course of the cooling scan. In the figure above, this cloud point is marked with a blue circle. In this case, the BTA starts to self-assemble at a temperature of about -0.9 °C. Since the clear and cloud point are concentration dependent it become clear that deviation from a BTA concentration of 0.5 wt.-% will alter the position of the cloud and clear point.

The solubility of each sulfur-containing BTA in the selected solvents is given in the following table.

Table 3.6: The table shows the clear points and the cloud points of the sulfur-containing 1,3,5-benzenetrisamides in the selected solvents for a BTA concentration of 0.5 wt.-%. RT represents BTAs which were soluble at room temperature (about 20 °C). The X represents samples where the BTA was not soluble at selected conditions.

		Ethanol	Isopropanol	1-Propanol	2-butanone	Water
		Clear point ¹⁾ / cloud point ¹⁾ (°C)				
1,3,5-Benzenetrisamides with aliphatic sulfur-containing side groups						
BTA 1		15 / -1	33 / 13	24 / -0.9	26 / n.d. ³⁾	X
BTA 2		RT / n.d. ³⁾	RT / n.d. ³⁾	RT / n.d. ³⁾	RT / n.d. ³⁾	X
BTA 3		RT / n.d. ³⁾	RT / n.d. ³⁾	RT / n.d. ³⁾	RT / n.d. ³⁾	X
BTA 4		RT / n.d. ³⁾	RT / n.d. ³⁾	RT / n.d. ³⁾	RT / n.d. ³⁾	X
BTA 5		RT / n.d. ³⁾	RT / n.d. ³⁾	RT / n.d. ³⁾	RT / n.d. ³⁾	X
BTA 6		RT / n.d. ³⁾	RT / n.d. ³⁾	RT / n.d. ³⁾	RT / n.d. ³⁾	X
BTA 7		RT / n.d. ³⁾	X	X	X	X
BTA 8		RT / n.d. ³⁾	RT / n.d. ³⁾	RT / n.d. ³⁾	RT / n.d. ³⁾	X
BTA 9		RT / n.d. ³⁾	16 / n.d. ³⁾	RT / n.d. ³⁾	RT / n.d. ³⁾	X
BTA 10		21 / 9	35 / 25	20 / 0	41 / n.d. ³⁾	X

		Ethanol	Isopropanol	1-Propanol	2-butanone	Water
Clear point ¹⁾ /cloud point ¹⁾ (°C)						
1,3,5-Benzenetrisamides with cysteine or methionine-based side groups						
BTA 11		X	X	X	X	X
BTA 12		64 / 44	72 / 49	62 / 35	32 / n.d. ³⁾	X
BTA 13		45 / 36	58 / 49	53 / 41	RT / n.d. ³⁾	X
1,3,5-Benzenetrisamides with aromatic sulfur-containing side groups						
BTA 14		X	X	X	50 / n.d. ³⁾	X
BTA 15		55 / 50	70 / 60	68 / 40	1 / n.d. ³⁾	X
BTA 16		X	X	X	X	X

¹⁾ Clear point determined upon heating with a rate of 0.5 K/min under stirring with 600 rpm. BTA concentration was 0.5 wt.-%.

²⁾ Cloud point determined upon cooling with a rate of 0.5 K/min under stirring with 600 rpm. BTA concentration was 0.5 wt.-%.

³⁾ n.d. not determined

Nearly all of the 1,3,5-benzenetrisamides of the first series (1,3,5-benzenetrisamides with aliphatic sulfur-containing side groups) were soluble in all selected solvents at a BTA concentration of 0.5 wt.-% except of water. It has to be mentioned that BTA 1 and BTA 2 were investigated in further experiments. Here, a water solubility at very low concentration (\ll 0.5 wt.-%) was detected. At higher BTA-concentrations, the BTAs were determined to be insoluble in water within the measuring accuracy with the Crystal16 device. Remarkably, BTA 1 featured a good solubility in alcohols. For instance, it was completely soluble in ethanol at 15 °C and started to self-assemble at a temperature of -1 °C upon cooling. With increasing carbon-content of the alcohol, the dissolution temperature increased. In 1-propanol, it was completely soluble at temperatures above 24 °C and crystallized at -0.9 °C. Moreover, BTA 1 featured a pronounced solubility in 2-butanone. Here, it dissolved at 26 °C and did not self-assemble again in the investigated temperature range. The other aliphatic sulfur-containing

BTAs, BTA 2 to BTA 9 except BTA 7, are very well soluble in the selected organic solvents. In nearly all cases, the BTAs dissolved at room temperature during the addition of the solvent to the BTA and did not reassemble at temperatures down to -15 °C. As described before, these BTAs have a very similar structure. The low thermal energy required to dissolve these molecules can be explained by the fact that the side groups are not branched near the amide group, thus the solvent molecules can easily break the hydrogen bonds between neighboring amide groups. BTA 10 was also well soluble in the selected organic solvents. It reassembled only by using alcoholic solvents at the investigated conditions but not from 2-butanone. The side group of BTA 10 is branched near the amide group. Thus, the solvent molecules are more hindered to break the intermolecular interactions and higher temperatures are required for a dissolution compared to most of the previous BTAs. In case of BTA 1, the higher temperatures to dissolve this compound can be explained by the short side group containing a relatively big atom. So, the solvent molecules could be hindered to break the hydrogen bonds or other secondary intermolecular interactions.

In the series of BTAs with cysteine or methionine-based side groups, BTA 11 was not soluble in any used solvent. In contrast, BTA 12, which is structural relatively similar, was soluble in every used solvent except of water. Compared to the first series, higher temperatures were needed to dissolve this compound. As it can be seen in **Table 3.6**, BTA 13 was better soluble in the organic solvents than BTA 12. This might be due to the little bit higher flexibility of BTA 13 because of the additional CH₂ group in the side group. Thus, less energy was needed to dissolve this compound.

The last group of aromatic sulfur-containing BTAs, BTA 14 to 16, were not or only partly soluble in the selected solvents. The structures of the BTAs are very similar. The only difference is the substitution of the thioether. The ortho substituted BTA was not soluble in any selected solvent. The para substituted BTA was only soluble in 2-butanone. The meta substituted component was soluble in all the selected solvents except water. Here, high temperatures were needed for alcohols to dissolve this BTA. This behavior is probably attributed to the fully aromatic character of the amides or the much less solubility of the aromatic side groups.

To conclude, nearly all BTAs of the series with aliphatic sulfur-containing side groups were soluble in the used solvents and conditions. The majority remains dissolved at room temperature at a concentration of 0.5 w.-t%, which renders the use of self-assembly according to **Figure 3.20 A and B** unlikely. However, these compounds can be still beneficially self-assembled using the processing method **Figure 3.20 D** if simultaneously cooling and evaporation of the solvent is applied. Similarly, this applies for BTAs with cysteine or methionine-based side groups, which are well soluble in the selected solvents. BTAs with aromatic sulfur-containing side groups show a less pronounced solubility considering the chosen solvent systems.

3.3.3 Self-assembly behavior of sulfur-containing BTAs

Experimental procedure

As mentioned before, solubility of the BTAs in selected solvents at given conditions is important. In particular, the aim of this chapter pursues the self-assembly behavior of all sulfur-containing to defined supramolecular structures upon cooling and evaporation. Therefore, sulfur-containing 1,3,5-benzenetrisamides were investigated if the components were fully soluble in the selected solvents at BTA concentrations of 0.5 wt.-%. The self-assembled samples were investigated by means of scanning electronic microscopy. The main focus here was on the fiber formation of the supramolecular building blocks since supramolecular fibers can be used for various applications, such as filtration as already demonstrated at our work group.^[102,106] In this earlier work it was demonstrated that especially fibers with a diameter of 100 nm to 1 μm are of high interest for such an application, because these fibers provide a sufficient mechanical stability.^[102,106] Therefore, fiber diameter histograms of promising samples were prepared and at least the diameters of 150 individual BTA fibers were measured. All samples were prepared using the same procedure. A fully dissolved BTA-solution at elevated temperatures was dropped on a substrate and the self-assembly process was initiated by evaporation of the solvent and cooling of the system. In **Figure 3.22**, a schematic of the experimental procedure together with the self-assembly process in the phase diagram are shown. In detail, a 50 °C to 70 °C hot BTA solution was dropped on a surface of a silicon wafer at ambient conditions. The system cools down due to the lower temperature of $\sim 40^\circ\text{C}$ and the evaporation of the solvent. Depending on the solvent, evaporation proceeds relatively quick and initiates the self-assembly process mostly due to an increase in concentration. Looking at the phase diagram, the system then enters the area where the BTA is not soluble anymore. Here, nuclei are formed and the self-assembly process starts as indicated in **Figure 3.22 B**. The hot BTA-solution in **Figure 3.22 B-I** starts to cool down and the solvent begins to evaporate. Upon further cooling, the system enters the regime **II** in the phase diagram where the BTA is not fully soluble anymore and the self-assembly process starts resulting in the formation of supramolecular fibers. Full drying of the sample allows to investigate the supramolecular nanofibers by analytical methods (**Figure 3.22 B-III**).

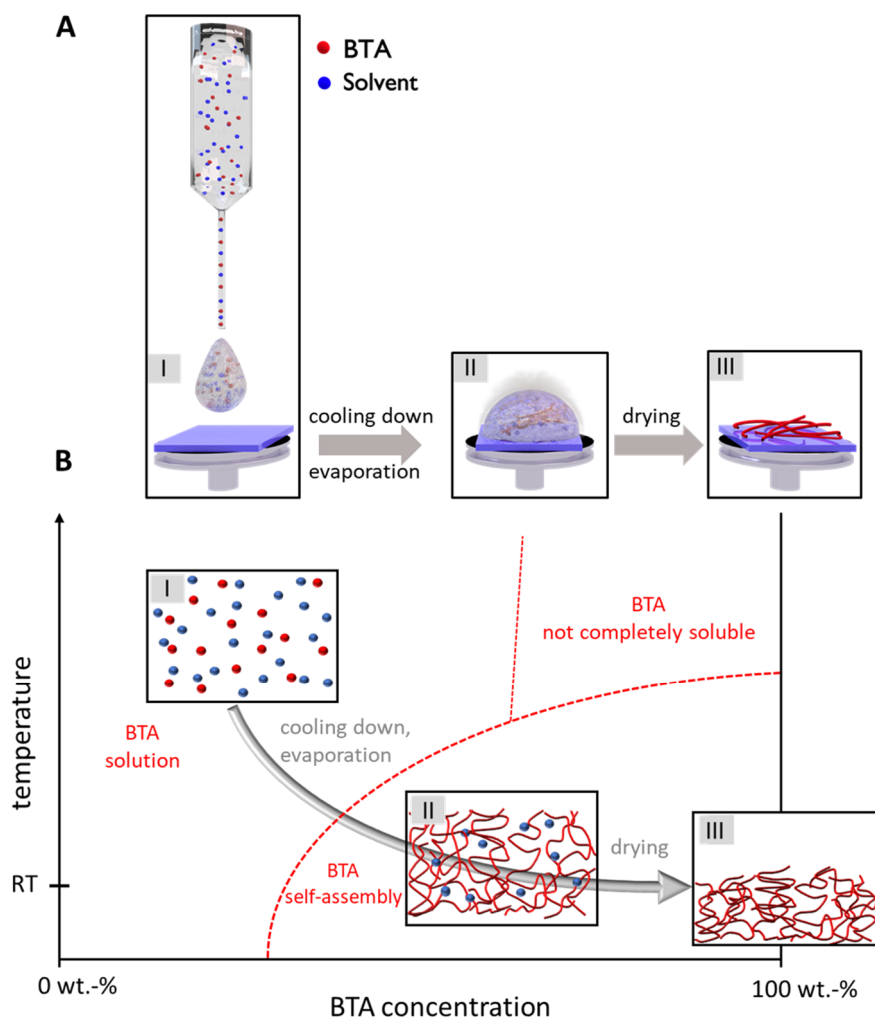


Figure 3.22: **A:** Schematic representation of the sample preparation for the self-assembly experiments. **B:** Schematic representation of the self-assembly process. The self-assembly is initiated by evaporation of the solvent and cooling of the system. **I:** The used BTA (red dots) is fully dissolved in the selected solvent (blue dots) at ambient temperatures. **II:** After dropping on a silicon wafer the solvent begins to evaporate and the system cools down to room temperature. Here, the BTA concentration begins to increase up to the point in the phase diagram where it is not soluble anymore and the self-assembly process starts. During the self-assembly process supramolecular nanofibers can be formed. **III:** After the complete drying, the sample can be investigated by different analytical methods like scanning electron microscopy.

Self-Assembly of 1,3,5-benzenetrisamides with aliphatic sulfur-containing side groups

In the following, exemplarily the self-assembly behavior of three selected aliphatic sulfur-containing 1,3,5-benzenetrisamides (BTA 1, BTA 6 and BTA 10) will be presented and discussed. As solvents ethanol, 1-propanol, isopropanol and 2-butanone are used. Those solvents all have a similar boiling point of around 80 °C, but they differ in their polarity and their vapor pressure. The alcoholic solvents ethanol and isopropanol have relatively similar vapor pressures. In contrast, 1-propanol has the lowest vapor pressure and 2-butanone has the highest value for the vapor pressure. Thus, 2-butanone evaporates significantly faster than ethanol and isopropanol and 1-propanol evaporates slowest. Consequently, this behavior gives rise to varying cooling profiles. All of these parameters, kind of solvent, evaporation velocity and cooling profile, may result in differences in the morphology of the

supramolecular structures, which may be attributed to the different number of formed nuclei upon cooling and probably to the formation of different hierarchical levels. The SEM images of the self-assembled structures and the corresponding mean fiber diameter histograms of BTA 1 from different solvents are shown in **Figure 3.23**. For the histograms at least 150 supramolecular fibers were measured.

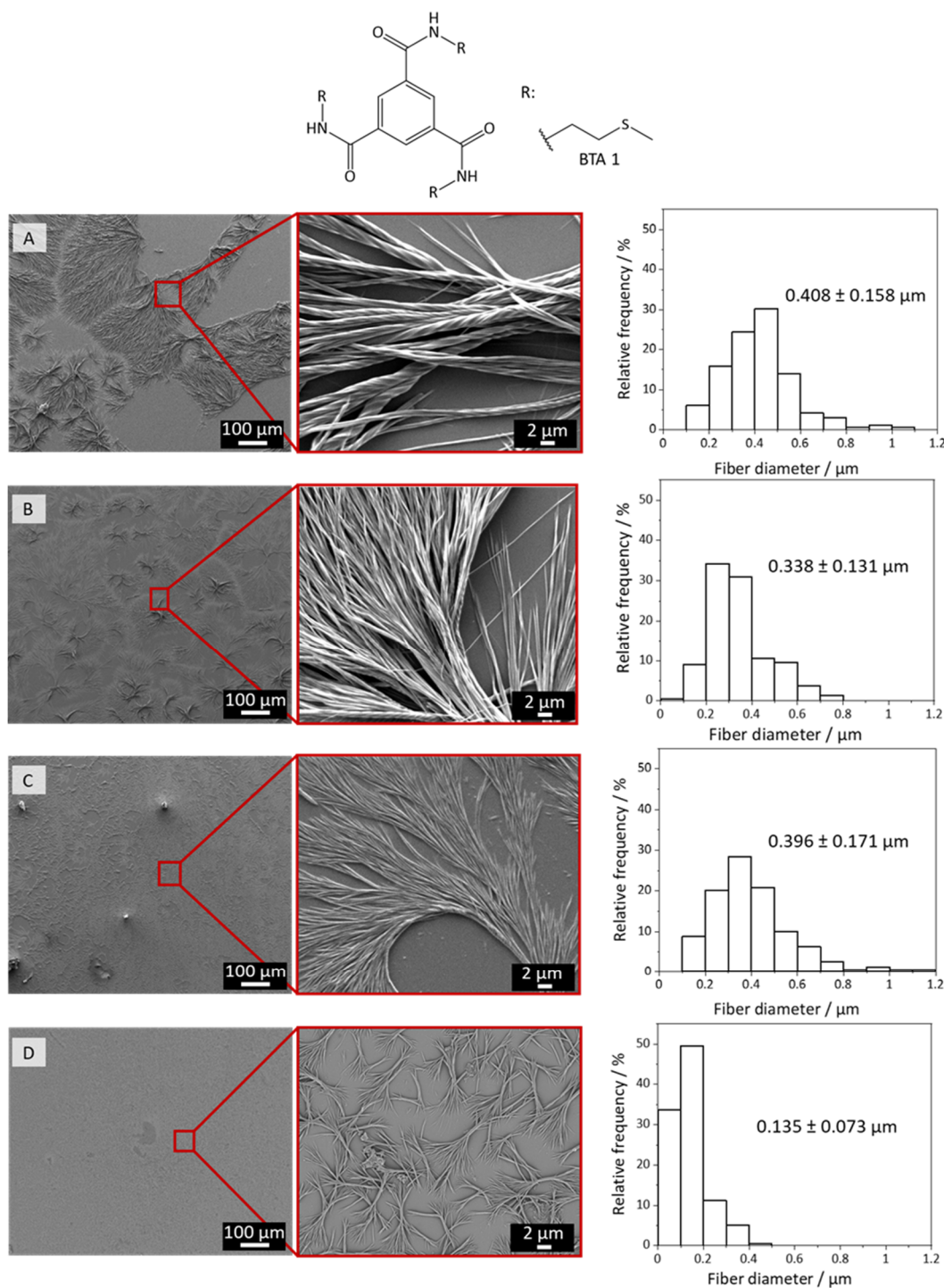


Figure 3.23: SEM-images of BTA 1 self-assembled from **A:** ethanol, **B:** isopropanol, **C:** 1-propanol and **D:** 2-butanone. On the left side, there are images with a lower magnification (100x), in the middle, the supramolecular objects are shown in detail with a higher magnification (2500x). The samples were prepared with a BTA-concentration of 0.5 wt.-% at a temperature of ca. 70 °C. For the fiber diameter histograms on the right side, at least 150 individual fibers were used.

In **Figure 3.23**, both overview images and magnifications of the self-assembled structures of BTA 1 are shown. All overview images of the assembled samples by alcoholic solvents as well as 2-butanone provides the impression of a film, film-like layer or very dense fiber networks. In the magnification, however, clearly self-assembled fibrous structures can be detected.

It can be recognized that the morphology of formed supramolecular fibers strongly depends on the used solvent as pointed out above. The supramolecular fibers self-assembled from 2-butanone (**D**) feature the smallest fiber diameter, which was determined to be 135 nm with a standard deviation of 73 nm. The fibers formed from ethanol (**A**) show the highest fiber diameter with $408 \text{ nm} \pm 158 \text{ nm}$, which still can be regarded as supramolecular fiber with a relatively narrow and defined distribution of the diameters. Fibers self-assembled from isopropanol (**B**) and 1-propanol (**C**) are relatively thin and have an average fiber diameter of $338 \text{ nm} \pm 131 \text{ nm}$ and $396 \text{ nm} \pm 171 \text{ nm}$, respectively. Remarkably, a closer look reveals that the fibers assembled from alcoholic solvents have a twisted shape, which cannot be explained till date. In general, it can be seen that these samples have a relatively narrow distribution of the fiber diameters.

All in all, BTA 1 assembled from nearly all selected solvents into supramolecular fibers. Also, it can be seen that the solvent has a strong influence on the morphology of the formed supramolecular structures.

In the following the morphology of BTA 6 is shown as another example. BTA 6 was selected exemplarily, because its chemical structure is very similar to those of BTAs 3 to BTA 9 and thus it is expected to feature representative structures. In fact, a similar self-assembly behavior was found for all BTAs with comparable side groups. Surprisingly, as it can be seen in **Figure 3.24**, BTA 6 does not form the supramolecular fibers using these conditions during cooling and evaporation of the selected organic solvents, which can be observed by SEM investigations. In some SEM-images, less defined and broad fiber-like structures can be seen. Especially in the samples assembled from ethanol (**A**) and 2-butanone (**D**), ribbon-like structures can be detected. Those structures may consist of columnar stacked supramolecular building blocks. In the case of ethanol, next to the ribbon structures also a film-like structure can be seen. Similarly, the samples assembled from isopropanol (**B**) and 1-propanol (**C**) only show the film structure. In both cases, some substructures can be detected. Thus, it may be assumed that the BTA-film consists of a high amount of very small supramolecular fibers which are so close to each other that they can no longer be resolved and it appears as if a layer is being considered. An argument for this is the fact that the BTA shows the characteristic FTIR-vibrations (**Figure 3.17**) for a columnar stacking which is indicative for the presence of columnar stacked supramolecular building blocks.

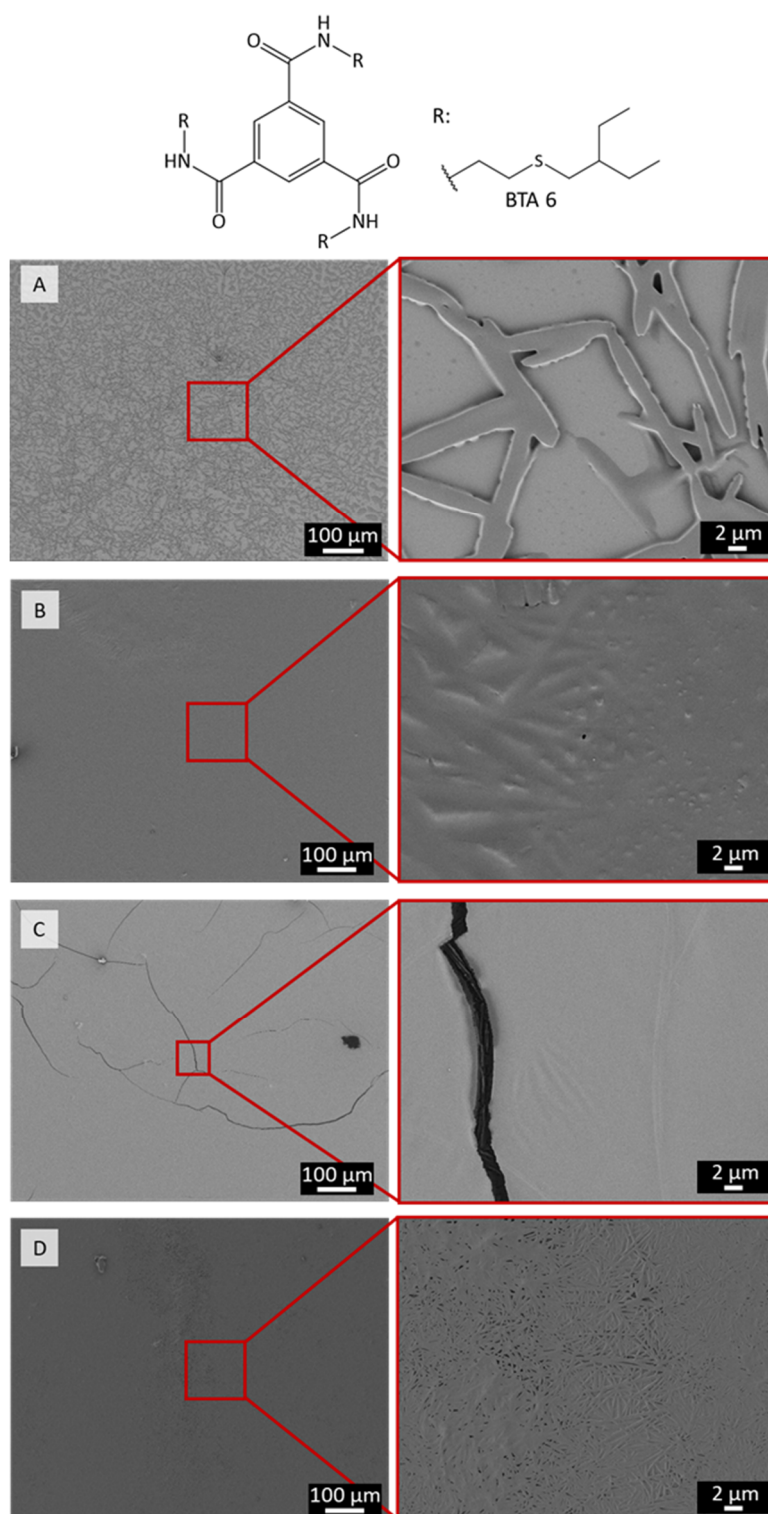


Figure 3.24: SEM-images of BTA 6 self-assembled from **A:** ethanol, **B:** isopropanol, **C:** 1-propanol and **D:** 2-butanone. On the left side, there are images with a lower magnification (100x), in the middle, the supramolecular objects are shown in detail with a higher magnification (2500x). The samples were prepared with a BTA-concentration of 0.5 wt.-% at a temperature of ca. 70 °C.

In **Figure 3.25** both overview images and detail images of the self-assembled BTA 10 are shown. In this case, it can be seen that dense fiber networks can be detected in all overview images of the self-assembled samples. However, on the basis of the detailed images, it can be seen in **Figure 3.25**, BTA 10 assembled into supramolecular fiber-like structures from the selected solvents.

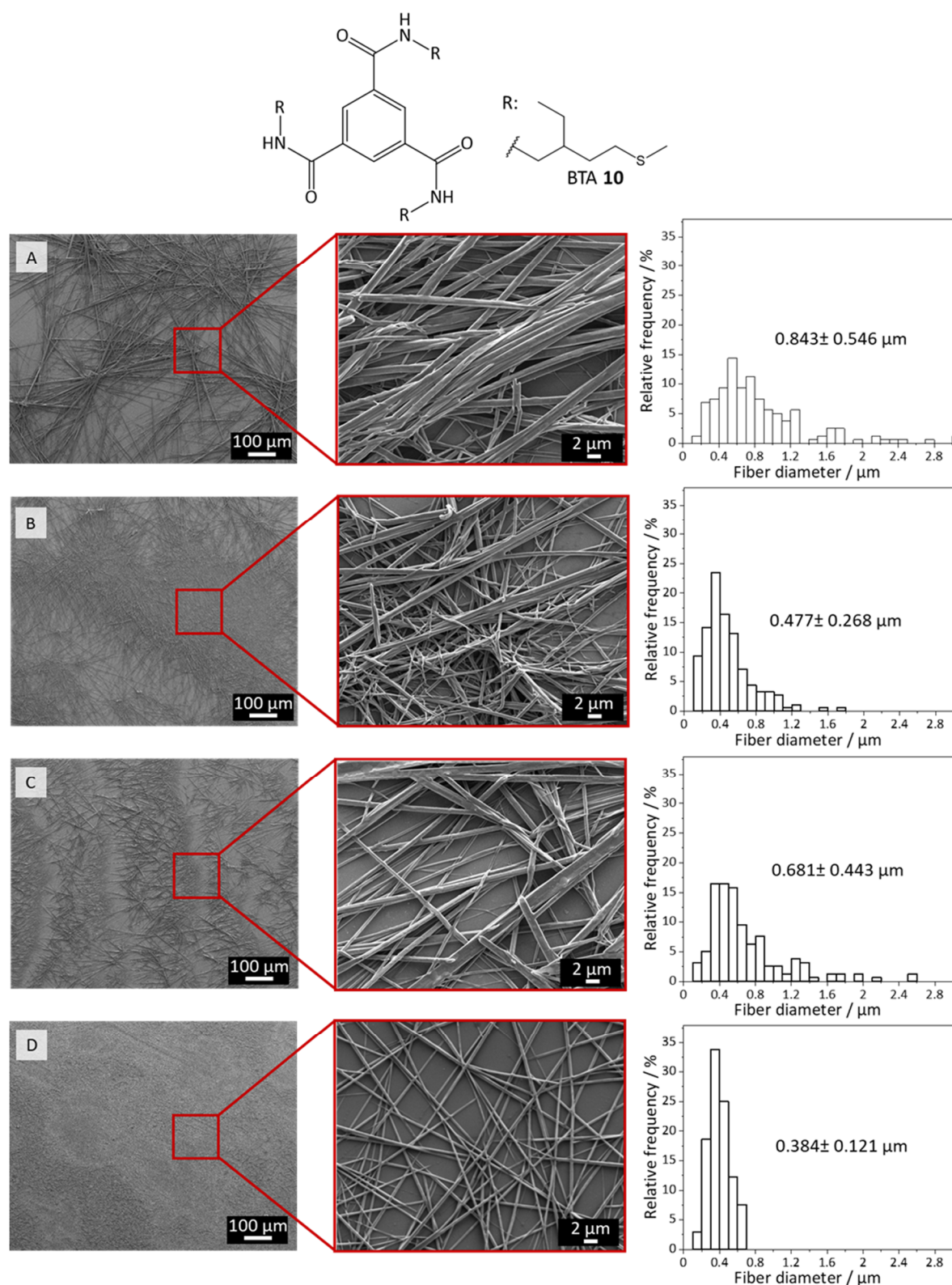


Figure 3.25: SEM-images of BTA 10 self-assembled from **A:** ethanol, **B:** isopropanol, **C:** 1-propanol and **D:** 2-butanone. On the left side, there are images with a lower magnification (100x), in the middle, the supramolecular objects are shown in detail with a higher magnification (2500x). The samples were prepared with a BTA-concentration of 0.5 wt.-% at a temperature of ca. 70 °C. For the fiber diameter histograms on the right side, at least 150 individual fibers were used.

At the first glance, the supramolecular fibers assembled from ethanol (**A**) and isopropanol (**B**) look very similar. But the mean fiber diameter of the fibers assembled from ethanol (843 nm \pm 546 nm) is almost

twice as large as the diameter of the fibers assembled from isopropanol ($477 \text{ nm} \pm 268 \text{ nm}$). Furthermore, the distribution of fiber diameters of the sample prepared from ethanol is relatively inhomogeneous. There are some fibers with a diameter in an area of a few hundred nanometers and there are also fibers with a diameter with more than a micron. On the fibers, some structures can be detected which might be a result of the self-assembly process. These structures are also found on the ribbon structures of the supramolecular structures assembled from 1-propanol (**C**).

The SEM image of the sample prepared from isopropanol shows also some fibers with higher fiber diameters. Nevertheless, the fiber histogram shows that the fiber diameter distribution is relatively homogeneous. There are only a few fibers with much higher diameters.

The formed BTA-fibers from 2-butanone (**D**) have a mean fiber diameter of 384 nm featuring a relatively narrow diameter distribution with a standard deviation of 112 nm. Thus, the self-assembled fibers have a homogeneous morphology. Rendering these supramolecular structures promising candidates for further investigations.

An interesting aspect is the high similarity of BTA 10 with the sulfur-containing side groups with the aliphatic reference BTA (BTA 17). In particular, BTA 17 is well investigated and known to form suitable nanofibers for filtration applications.^[37,102,106] In detail, BTA 17 have a 2-ethylhexyl-side group, whereas BTA 10 have a 2-ethylhexyl-like side group in the periphery in which one of the CH_2 groups is substituted by a sulfur atom. Therefore, supramolecular fibers of BTA 10 with the sulfur-containing side groups formed from 2-butanone are compared with supramolecular fibers of the aliphatic reference BTA 17, which were processed from 2-butanone on the same manner (**Figure 3.26**).

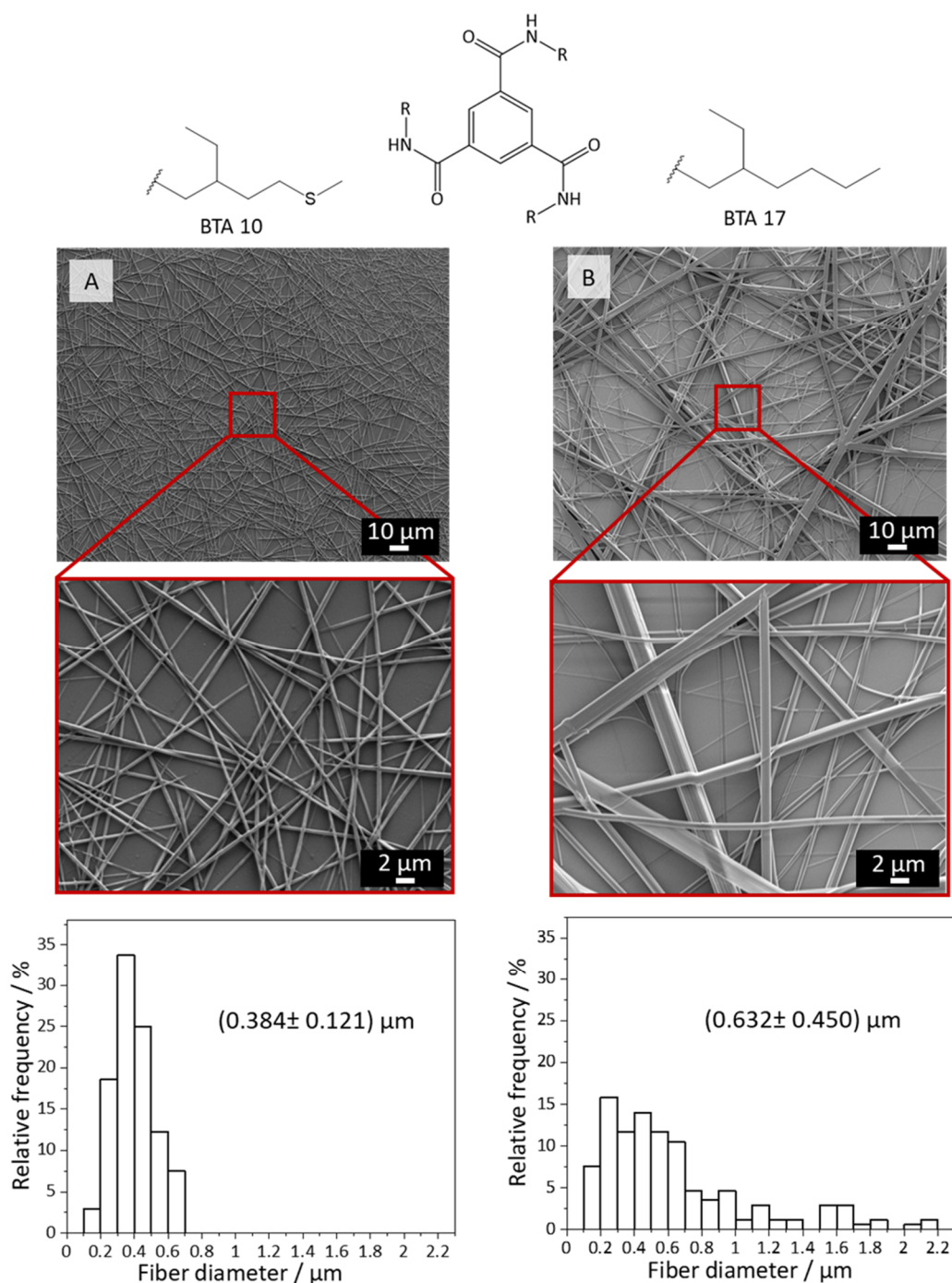


Figure 3.26: Comparison of the self-assembled supramolecular fibers of **A:** BTA 10 and **B:** BTA 17. On the top, overview (500x) SEM images of the samples are shown and, in the middle row, images with a higher magnification (2500x) are shown. Both BTAs were assembled from 2-butanone with a BTA-concentration of 0.5 wt.-%. For the fiber diameter histograms at the bottom, at least 150 individual fibers were used.

As it can be seen in **Figure 3.26**, in both cases supramolecular fibers were formed. Surprisingly, these fibers differ significantly from each other although the molecular structure is highly similar. The fibers formed from BTA 17 ($632 \text{ nm} \pm 450 \text{ nm}$) have a diameter twice of the fibers formed from BTA 10 ($384 \text{ nm} \pm 121 \text{ nm}$). It can be also seen that in this sample, the fiber diameter distribution of the supramolecular fibers formed with the aliphatic BTA is relative broad. BTA17 fibers also comprise some

fibers with a diameter up to 2 μm . Moreover, the morphology of the self-assembled BTA 17 might consist of ribbon-like and fiber-like structures. Thus, the structures with large diameters may represent ribbon structures. Compared to BTA 17, the fiber diameter distribution of BTA 10 fibers is relatively narrow and homogeneous featuring a mean fiber diameter of about 384 nm with a standard derivation of 121 nm. Which may render fibers of BTA 10 useful as functional alternative for the aliphatic BTA 17 fibers.

Self-Assembly of 1,3,5-benzenetrisamides with cysteine or methionine-based side groups

The self-assembly behavior of BTA 13 with a methionine-based side group will be discussed as an example of the series of 1,3,5-benzenetrisamides with cysteine or methionine-based side groups. The SEM images of the self-assembled samples of BTA 13 are shown in **Figure 3.27**.

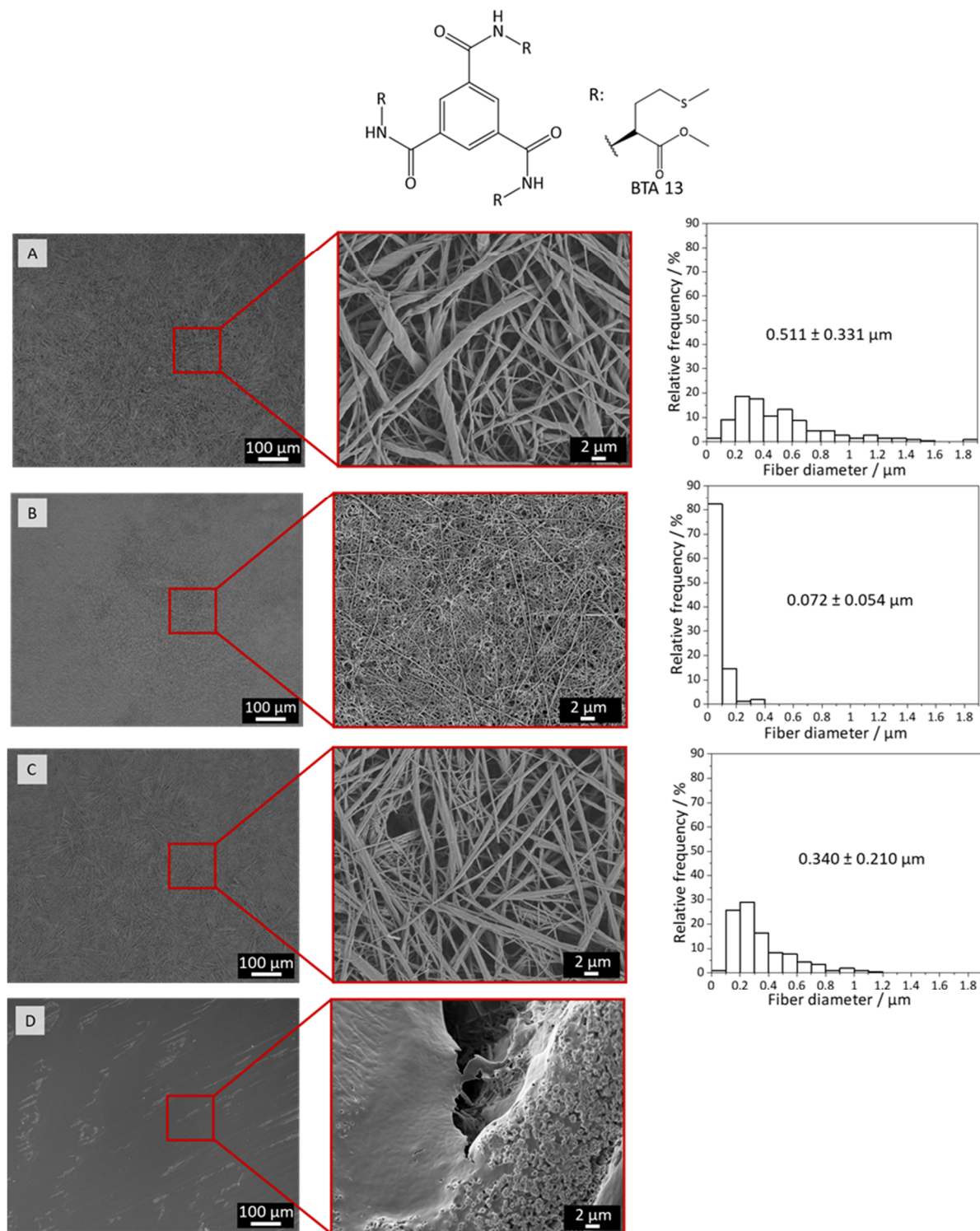


Figure 3.27: SEM-images of BTA 13 self-assembled from **A:** ethanol, **B:** isopropanol, **C:** 1-propanol and **D:** 2-butanone. On the left side, there are images with a lower magnification (100x), in the middle, the supramolecular objects are shown in detail with a higher magnification (2500x). The samples were prepared with a BTA-concentration of 0.5 wt.-% at a temperature of ca. 70 °C. For the fiber diameter histograms on the right side, at least 150 individual fibers were used.

The samples were prepared as described before and as mentioned previously, the formation of supramolecular fibers was favored. **Figure 3.27** show both overview images and detail images of the self-assembled BTA 13. In this case, it can be seen that dense fiber-like networks can be detected in all overview and detailed images of the self-assembled samples using ethanol, isopropanol or 1-propanol. The images from the sample prepared from 2-butanone only show film-like structures.

The self-assembly process of BTA 13 depends strongly on the used solvent. Using ethanol (**A**), isopropanol (**B**) and 1-propanol (**C**), supramolecular nanofibers were formed. By using 2-butanone (**D**), no fibers or only fiber-like structures were formed. Therefore, for this sample, no fiber diameter histogram was created.

The morphology of the formed fibers varies depending on the solvent used. In the case of ethanol (**A**), the mean fiber diameter was $511 \text{ nm} \pm 331 \text{ nm}$. The supramolecular structures feature a rather large structure width compared to the fibers formed from isopropanol ($72 \text{ nm} \pm 54 \text{ nm}$) or 1-propanol ($340 \text{ nm} \pm 210 \text{ nm}$). The BTA-structures assembled from ethanol do not have a homogeneous structure and feature a broad distribution as it can be seen in the fiber diameter histogram. Moreover, there seems to be two maxima for the diameter be present at 200 nm to 300 nm and 500 nm to 600 nm, respectively. The fibers with the largest diameter were found to be more than $1.5 \mu\text{m}$.

The fibers assembled from isopropanol (**B**) are relatively thin with a mean diameter of about 72 nm. As it can be seen in the fiber diameter histogram on the right side, more than 80 % of the measured fibers had a diameter less than or equal to 100 nm.

The self-assembled supramolecular BTA-fibers formed from 1-propanol (**C**) have a mean diameter of 340 nm. The measured objects had a broader distribution than the sample assembled from isopropanol. Fibers with diameters of up to $1.2 \mu\text{m}$ were measured. Looking on the SEM image with the higher magnification, the fiber morphology does not look completely homogenous and feature a broad fiber diameter distribution. Interestingly, the objects do not show the twisted structure as those self-assembled from ethanol.

In the case of the self-assembled sample from 2-butanone (**D**), no defined structure can be seen. The BTA-molecules seem to assemble into a film-like structure. It could be possible that this film consists of very small supramolecular BTA-fibers which cannot be resolved in the SEM anymore. This assumption may be supported by the magnification images, where at the edges of the formed film some small fiber-like objects can be detected. The interesting self-assembly behavior of this system was further investigated and will be shown in the later chapters where the formation of supramolecular fibers could be demonstrated.

Self-Assembly of 1,3,5-benzenetrisamides with aromatic sulfur-containing side groups

The self-assembly behavior of BTA 15 with an aromatic sulfur-containing side group will be investigated in the following as example of the series of 1,3,5-benzenetrisamides with aromatic sulfur-containing side groups. The SEM-images of the self-assembled samples from the selected solvents are shown in **Figure 3.28**.

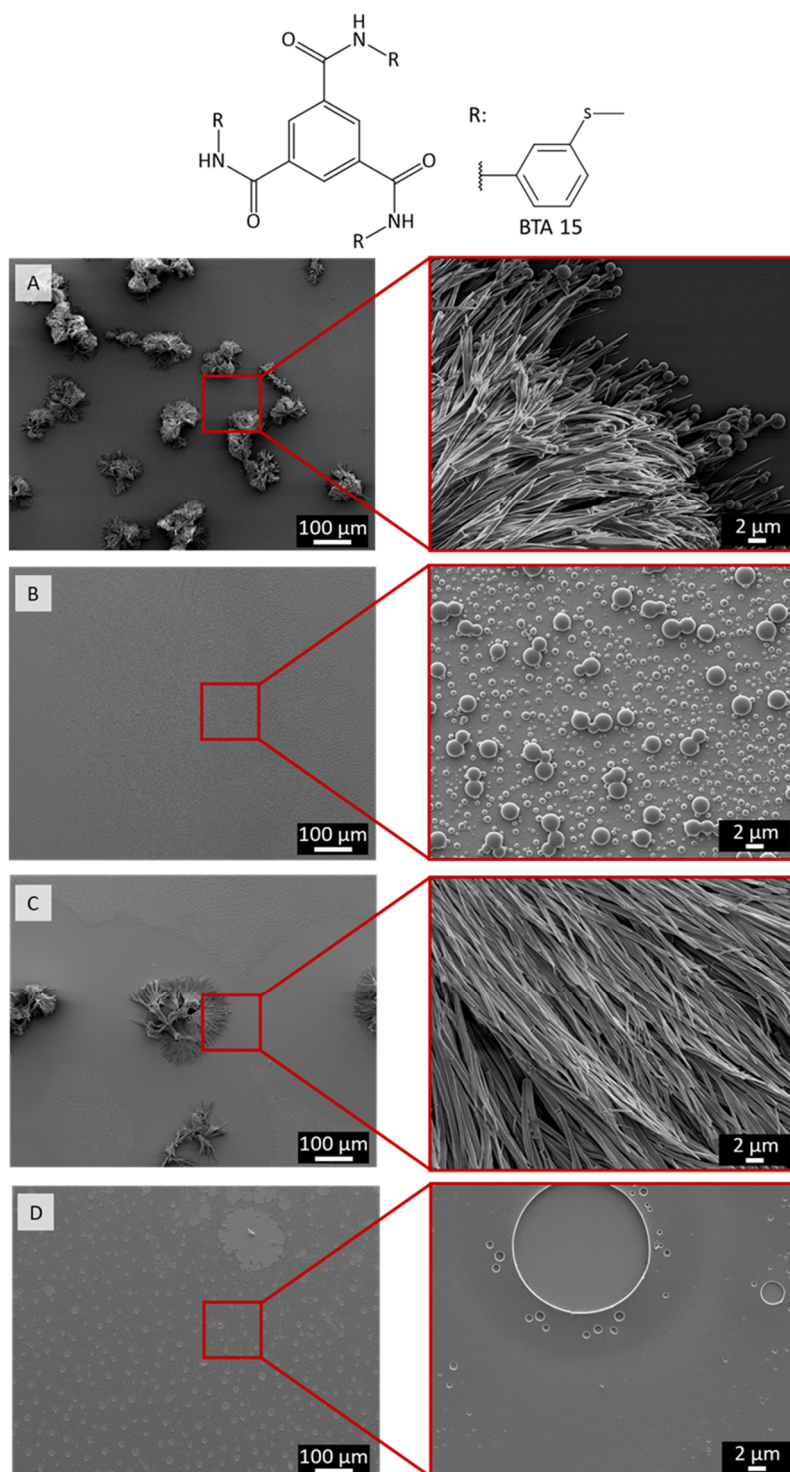


Figure 3.28: SEM-images of BTA 15 self-assembled from **A:** ethanol, **B:** isopropanol, **C:** 1-propanol and **D:** 2-butanone. On the left side, there are images with a lower magnification (100x), in the middle, the supramolecular objects are shown in detail with a higher magnification (2500x). The samples were prepared with a BTA-concentration of 0.5 wt.-% at a temperature of ca. 70 °C.

The FTIR spectroscopy investigations done before (**Figure 3.19**) indicated that the component as it was received from synthesis does not form threefold hydrogen bonds. Nevertheless, in **Figure 3.28** partly fiber-like or ribbon-like structures can be detected. However, from some solvents highly ordered non-fiber supramolecular structures were formed.

The BTA 15 in **Figure 3.28** assembled into ribbon-like structures from ethanol (**A**) or 1-propanol (**C**). The supramolecular objects formed from ethanol (**A**) seem to assemble from one nucleation point and grow from there. The structures are mainly ribbon like but at the end of the ribbons, there are spherical objects with a diameter between 1 μm and 2 μm . Those spheres seem to consist also of the supramolecular building blocks of BTA 15. The formed ribbons have some cracks and some of them seem a little short. Self-assembly from 1-propanol (**C**) also seems to start from one nucleation point where the supramolecular structure grows away. The formed structures are partly ribbon and fiber-like. But there are a lot of structures with cracks inside. Thus, small fragments of the formed supramolecular structure can be seen.

The results of the sample prepared from isopropanol (**B**) look very different to the sample assembled from ethanol or 1-propanol. The supramolecular building blocks form spherical objects. The smaller spheres have a diameter of 0.7 μm and the bigger spheres have a diameter of around 2 μm .

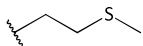
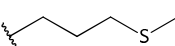
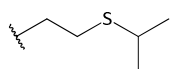
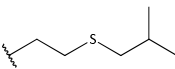
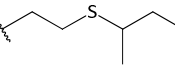
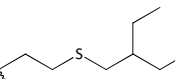
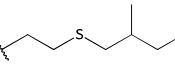
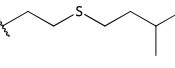
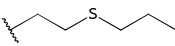
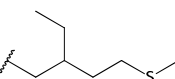
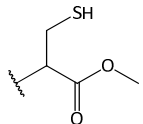
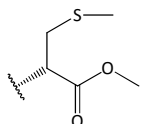
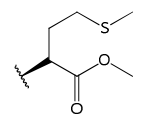
One explanation for the formation of spheres from isopropanol and in the case of ethanol the formation of spheres and ribbons could be that some microscopically small parts of the BTA were not completely dissolved in the solvents and thus act as nucleation points. Another explanation could be that the limit of solubility is fallen below so quickly that some building blocks form ribbon-like structures in the case of ethanol and others with less material content form the spherical structures. Nevertheless, highly ordered structures were formed during the self-assembly process from the alcoholic solvents.

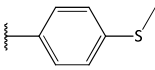
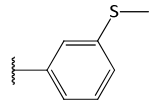
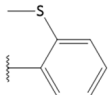
During the self-assembly of BTA 15 from 2-butanone (**D**), a supramolecular film-like structure was formed. It could be possible that the film consists of very small supramolecular objects. But the resolution of the SEM images is too low to confirm this theory. The formed film has some circular holes, but no other supramolecular structures can be seen.

The results do not meet the requirements set at the beginning of this chapter. Therefore, no further investigations were carried out with this BTA.

Table 3.7, summarizes the results of the investigation of the self-assembled structures. In a couple cases supramolecular fibers were formed which meet the requirements set at the beginning of this chapter. The three BTAs (BTA 1, BTA 10 and BTA 13) formed fibers in a range between 100 nm and 1 μm under the used conditions.

Table 3.7: Summary of the morphology of sulfur-containing BTAs after self-assembly from solution (ethanol, isopropanol, 1-propanol, 2-butanone and water). The classification was performed according to (✓): supramolecular fibers with diameters in the range of 100-1000 nm. (X): supramolecular fibers with diameters larger than 1000 μm or smaller than 100 nm or if a film like structures were observed. In case of ribbon like or fiber-like structures it was mentioned in the table. Note, that a film structures may represent a dense ensemble of very thin supramolecular fibers.

BTA	R:	Ethanol	Isopropanol	1-Propanol	2-Butanone	Water
1,3,5-Benzenetrisamides with aliphatic sulfur-containing side group						
BTA 1		✓	✓	✓	✓	X
BTA 2		ribbon-like	ribbon-like	X	X	X
BTA 3		X	X	X	ribbon-like	X
BTA 4		X	X	X	ribbon-like	X
BTA 5		X	X	X	X	X
BTA 6		ribbon-like	X	X	ribbon-like	X
BTA 7		X	X	X	X	X
BTA 8		ribbon-like	X	X	X	X
BTA 9		X	X	X	X	X
BTA 10		✓	✓	✓	✓	X
1,3,5-Benzenetrisamides with Cysteine or Methionine based side groups						
BTA 11		X	X	X	X	X
BTA 12		ribbon-like	ribbon-like	ribbon-like	ribbon-like	X
BTA 13		✓	✓	✓	X	X

BTA	R:	Ethanol	Isopropanol	1-Propanol	2-Butanone	Water
1,3,5-Benzenetrisamides with aromatic sulfur-containing side groups						
BTA 14		X	X	X	X	X
BTA 15		fiber-like	X	fiber-like	X	X
BTA 16		X	X	X	X	X

3.4 Application of functional supramolecular fibers to adsorb silver nanoparticles

The presented sulfur-containing 1,3,5-benzenetrisamides exhibits a functional group in the periphery and thus can be potentially used to immobilize metal ions or metal nanoparticles from liquids or aqueous fluid flows. Those properties were evaluated and will be presented in the following in detail by the model experiment, i.e. the adsorption of silver nanoparticles (AgNP) from an aqueous suspension on the surface of a functional supramolecular fiber. As compounds, BTA 10 and BTA 13 was used with a mercapto-group or amino acid group in the periphery, since they were shown to feature a high fiber stability if they are exposed to water. BTA 17 was used as a non-functional reference compound. Silver nanoparticles were used due to the straightforward preparation and availability. For the experiments, BTA 17 and BTA 13 were assembled from 2-butanone and BTA 10 from isopropanol on a TEM-grid. After self-assembly of the BTA and complete drying, the TEM-grid was dipped for 10 seconds into a silver nanoparticle suspension. The excess liquid was removed with the help of a filter paper. Thereafter, the dried sample was investigated with the help of a TEM. The resulting transmission electronic images are given in **Figure 3.29**.

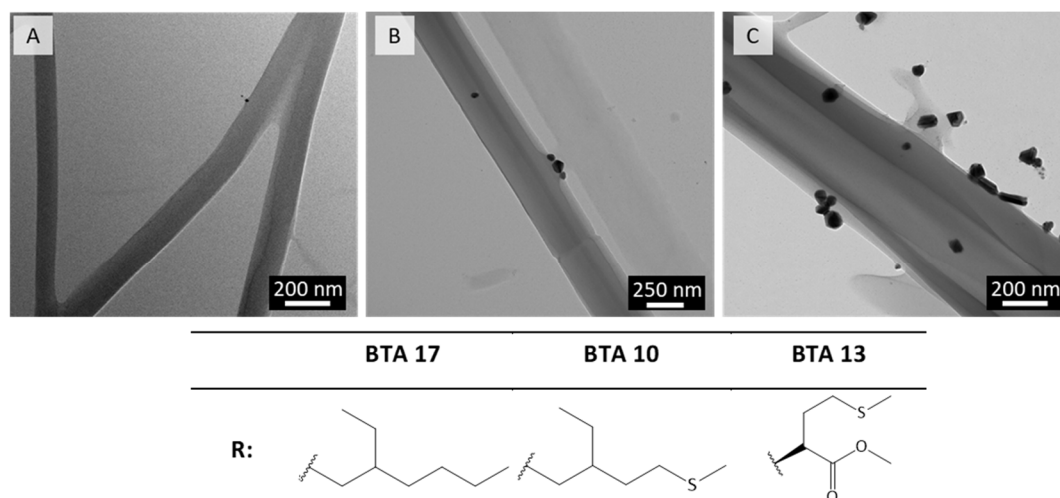


Figure 3.29: TEM images of supramolecular fibers self-assembled on TEM-grids **A:** BTA 17, **B:** BTA 10 and **C:** BTA 13 which were immersed into a suspension of silver nanoparticles (AgNP) to adsorb them on the fiber surface.

The supramolecular fiber in **Figure 3.29 A** shows nearly no adsorbed silver nanoparticles on the surface of the fiber. This behavior is attributed to a statistical adsorption due to a Brownian molecular movements of the AgNPs, which results in a highly ineffective particle capture due physical absorption by weak Van der Waals interaction forces. The supramolecular fiber in **Figure 3.29 B** is covered with more silver nanoparticles than the previous one. There are some adsorbed silver nanoparticles on the surface of the supramolecular fiber. Supramolecular fibers self-assembled from BTA 13 are shown in **Figure 3.29 C** after the adsorption of silver nanoparticles. On the surface of these fibers, a large amount of metal nanoparticles adsorbed. The adsorption takes place after a relatively short time in the nanoparticle suspension. Some silver nanoparticles can be detected, which lie next to the supramolecular fibers, but the majority of the silver was adsorbed on the functional fibers. It seems that BTA 13 had the highest affinity to adsorb these AgNPs.

This demonstrates that the sulfur-containing 1,3,5-benzenetrisamides feature a significant tendency to effectively adsorb metal nanoparticles from an aqueous suspension. This promising adsorption behavior of the sulfur-containing BTAs will be further investigated and used as active component in the following chapters.

3.5 Conclusion

In this chapter, sixteen, mostly literature-unknown, 1,3,5-benzenetrisamides with sulfur-containing side groups were synthesized, characterized and investigated in view of their self-assembly behavior from solution and their capability to adsorb silver nanoparticles.

Five of the sulfur-containing side groups (for BTA 1, 2, 11 and 13 to 16) were commercially available. The side groups for BTA 3 to 9 were obtained by a straightforward one step syntheses and were received with a yield between 34 % and 74 %. The synthesis of the periphery of BTA 10 was more complex comprising a four synthetic steps. Each step could be performed with a yield between 80 % to 99 %. Finally, all BTAs were synthesized according to literature-known procedures^[97], obtained in good yield ranging from 50 % to 100 % and purity and clearly identified by common analytical methods. The thermal properties of the synthesized BTAs were investigated by means of TGA and DSC. All BTAs 1-10 with aliphatic sulfur-containing side group show a thermal stability between 320 °C and 380 °C with their melting points being in the range of 140 °C to 150°C and in exceptional cases up to 240 °C. The BTAs with cysteine and methionine-based side groups feature slightly lower thermal stability at approximately 260 °C. However, their melting points are significantly higher between 230 °C and 240 °C. These close values are indicative that the BTAs degrade during melting. BTAs with aromatic sulfur-containing side group feature the highest thermal stability at temperatures between 380 °C and 400 °C and relatively high melting points in the range from 190 °C to 260 °C.

All synthesized BTAs were also investigated by means of FTIR-spectroscopy. In particular, the amide A and the amide II vibration are highly indicative for a threefold hydrogen bond arrangement of the BTAs to supramolecular columns. All BTAs with aliphatic and amino acid side groups were found to feature those characteristic vibrations. In the case of the BTAs with aromatic side groups, only BTA 16 seems to have these vibrations which indicate a threefold hydrogen bonding.

The solubility of the BTAs, whose determination is an essential prerequisite to evaluate their self-assembly behavior, was investigated in five selected polar and non-toxic solvents such as ethanol, isopropanol, 1-propanol, 2-butanone and water with the help of a Crystal16™. The majority of the BTAs was soluble in most of the solvents except water at the selected initial concentration of 0.5 wt.-% at temperatures of about 50 °C to 70 °C. Soluble BTAs at these conditions were used for self-assembly studies by means of cooling and evaporation of the solvent. These samples were investigated via SEM. Mainly BTA 1, BTA 10 and BTA 13 form supramolecular fibers at the selected conditions with fiber diameters in the range 100 nm to 1000 nm. Finally, the functionality of the fiber surface was demonstrated by the selective adsorption of silver nanoparticles on self-assembled supramolecular fibers of BTA 13 and BTA 10. In contrast to the non-functional aliphatic reference BTA 17, which does not adsorb silver nanoparticles, these BTA nanofibers were found to be highly effective to immobilize metal nanoparticles.

4 Multicomponent self-assembly to functional supramolecular fibers with core-shell structure

Core-shell structures

The formation of core-shell structures and especially of core-shell fibers is very attractive as they potentially combine the beneficial properties of two different materials. The general structure of such a core-shell or so-called core-sheath fiber is schematically represented in **Figure 4.1**.

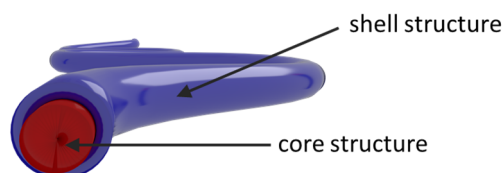


Figure 4.1: Schematic representation of a core-shell or core-sheath fiber.

Different approaches are described in literature to create such objects like coaxial or co-electrospinning, co-polymerization, microfluidic spinning, multicomponent self-assembly processes or a combination of those.^[166–172] Core-shell fibers processed in this manner were used for various and different applications such as drug delivery, sensors or tissue engineering.^[168,171]

From the preparation point of view, the majority of these core-shell structures were formed by electrospinning processes, in particular using coaxial electrospinning. For this, two solutions or melts are processed simultaneously in a side-by-side geometry.^[173,174] In **Figure 4.2**, a typical set-up of such a coaxial electrospinning process is shown schematically.

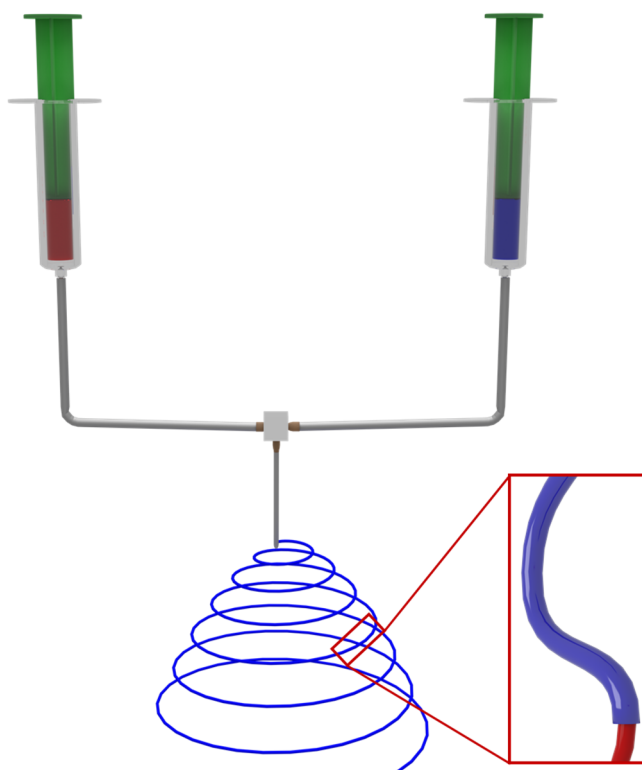


Figure 4.2: Schematic representation of coaxial electrospinning. [adapted from ref.^[166]]

In detail, with the aid of a syringe pump, the two components as solution or melt are combined into a mixing nozzle. Typically a special coaxial nozzle comprising a double wall geometry is employed.^[173] Conceptually, the core component is extruded through the inner outlet and the shell component through the outer outlet.^[173] At the outlet of the nozzle, a droplet is formed of both components. Subsequently, applying a strong electric field results in a jet and the formation of core-shell fibers which are deposited on a collector.

In the following, two selected examples and approaches of such prepared electro-spun fibers will be discussed in more detail. Zussman et al. described hollow fibers, which were prepared by previously formed electro-spun core-shell fibers^[173]. For this, core-shell nanofibers were co-electro-spun from PMMA (poly(methyl methacrylate)) and PAN (polyacrylonitrile) using a co-electrospinning set-up as shown in **Figure 4.2**.^[175] For the core-shell-fiber preparation, PMMA was used as core material and PAN as shell material. Here, PMMA was dissolved in acetone/DMF (60:40) and PAN was dissolved in DMF, respectively. These core-shell fibers showed an average shell thickness of 2.6 μm and an average core diameter of 2.1 μm . In order to prepare the hollow structure, the as-spun fibers were placed in a tube furnace for 30 min at 250 °C. Thereby, the PMMA core decomposes resulting in hollow tubes comprising the PAN shell. Thereafter, the fibers were carbonized under nitrogen atmosphere at 750 °C to 1100 °C resulting in carbon micro-/nanotubes with high mechanical stability. Such fibers are proposed to be used for applications such as drug delivery or hydrogen storage.^[175]

In a second example, Liu et al investigated self-assembled core-shell fibers, which were prepared by a simple single-nozzle electrospinning process. In this example, the core-shell structure formation is a result of a spontaneous phase separation. For the fiber formation, a blend solution consisting of PQT-12 (poly(3,3''-didodecyl quarter thiophene)) and PEO (poly(ethylene oxide)) in chlorobenzene was electro-spun. During the fiber formation, PQT-12 migrated to the surface of the fiber and self-assembled there into a homogeneous layer. Thus, a core-shell fiber with a PEO core and a PQT-12 shell can be created. The thickness of the shell could be adjusted by the content of PQT-12 in the blend solution. A higher proportion led to a thicker shell. These fibers can be used as sensor material to detect small amounts of ammonia.^[171]

Apart from the preparation of core-shell fibers by coaxial electrospinning, such fibers can also be obtained by self-assembly processes in solution. In this context, co-assembly or multicomponent-assembly approaches were performed. For instance, Abul-Haija et al. investigated the bio-catalytically triggered multicomponent assembly to form core-shell nanofibers with a shell which contains functional groups.^[176] For this, they mixed phosphatase responsive 9-fluorenylmethoxycarbonyl-phenylalanine-tyrosine (Fmoc-FYp) as a so called pre-gelator and an amino acid or peptide Fmoc-X (X = serine, threonine or arginine-glycine-aspartic acid) acting as surfactant in a phosphate buffered solution. The resulting suspension consisted of spherical aggregated structures of the individual

components (**Figure 4.3 A**). The self-assembly process to core-shell nanofibers was subsequently initiated by adding the enzyme, alkaline phosphatase. Fiber formation was investigated 24 h after adding the enzyme to the solution resulting in the disappearance of the spherical aggregates (**Figure 4.3 B**). Due to the formation of a fiber network of Fmoc-FYp triggered by the enzyme, a gel was formed. These hydrophobic Fmoc-FYp nanofibers are proposed to be coated with the surfactant-like amino acid or peptide derivatives. The resulting core shell fibers were investigated using different methods such as FTIR, fluorescence spectroscopy and zeta potential measurements.^[176]

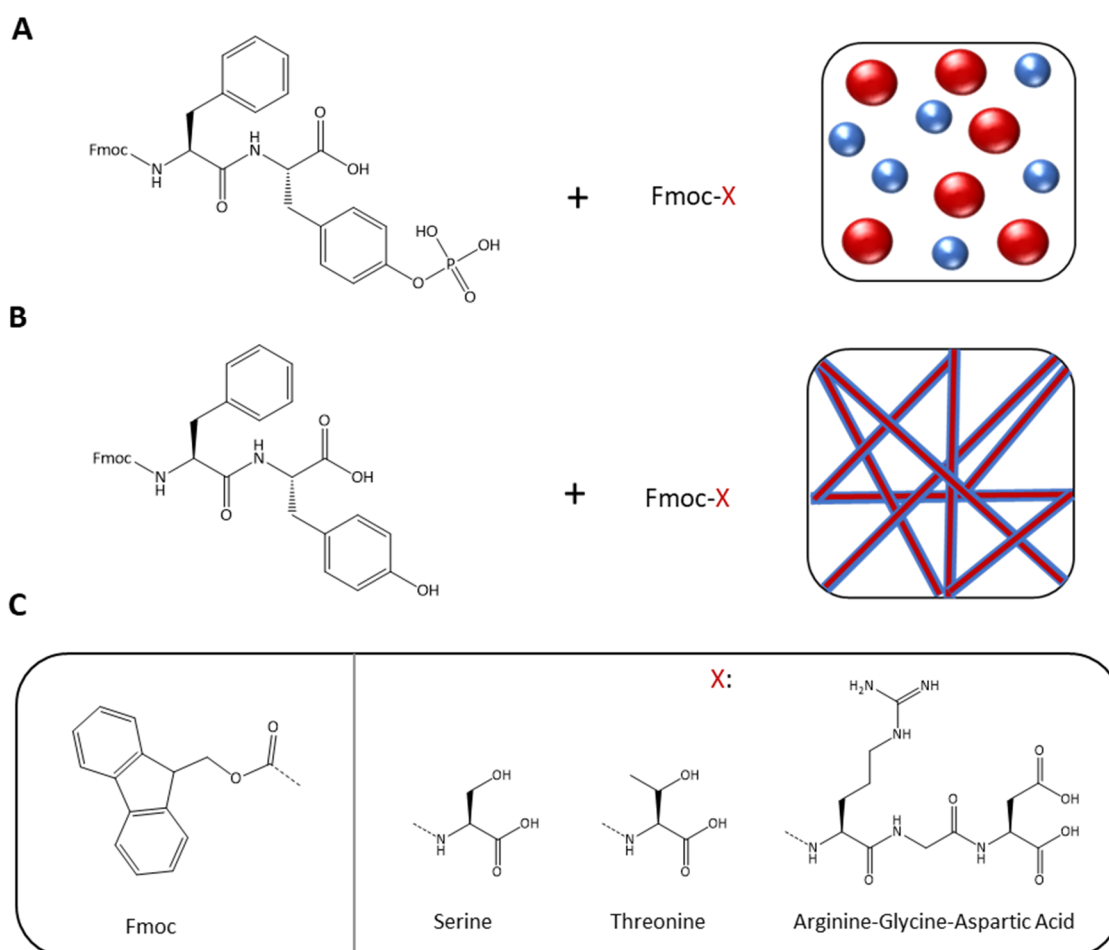


Figure 4.3: Schematic representation of bio-catalytically triggered co-assembly for the formation of core-shell fibers. **A:** Fmoc-FYp and Fmoc-X mixed in a buffer solution. Spherical aggregates were formed. **B:** Co-assembled functional nanofiber gel after addition of the enzyme alkaline phosphatase. **C:** Chemical structures of the used components. [adapted from ref.^[176]]

Since in such a self-assembly process two compounds are used, the term multicomponent self-assembly is coined. This term will be also used in this thesis if self-assembly approaches with two components are employed.

Multicomponent self-assembly

Since the term *self-assembly of multiple components* provides a new complexity in terms of the potentially resulting structure, the following section aims to outline definitions and subsequently terms, which will be used in this thesis.

The International Union of Pure and Applied Chemistry (IUPAC) defines *self-assembly* as following: It is the “spontaneous and reversible organization of molecular entities by noncovalent interactions. Typical noncovalent interactions are van der Waals interactions, π - π interactions, electrostatic interactions, and hydrogen bonds.”.^[177] In a similar and very general manner, the Royal Society of Chemistry (RSC) defines *co-assembly* as “The process of two individual components of a sample associating to form a new pattern or structure.”.^[178]

The terminus of *multicomponent-assembly* may be used as synonym for the process of *co-assembly*. The aim of this work is to investigate two 1,3,5-benzenetrisamides that are molecularly dissolved in a solvent or solvent system and self-assemble from this system. The BTA molecules may not incorporate simultaneously into the same columns. They can also assemble simultaneously or parallel from the same solution into individual different structures, which is sometimes referred to as self-sorting. Moreover, they can also assemble simultaneously or subsequently from the same solution into a defined structure. This may give rise to a complex structure formation such as a core-shell structure. Thus, a broad range of known and new morphologies is possible by performing co-assembly processes. It should be noted that in literature co-assembly processes are also often referred to as supramolecular copolymers. Supramolecular polymers are described as one dimensional single molecular chains.^[179] However, the formed and investigated supramolecular fibers or objects in this thesis are aimed to consist of a bundle of single supramolecular columns, i.e. the supramolecular polymer (compare **Figure 1.10** of the introduction). Since bundles of supramolecular polymers or single supramolecular columns already exhibit a further level of aggregation, the term supramolecular polymer will not be used in this thesis.

Even if two components, for example a functional and a non-functional BTA, assemble in separate columns, different hierarchical superstructures are possible by the arrangement of the individual columns. This is shown schematically in **Figure 4.4**. Here, the red discs represent the nonfunctional components and the blue discs the functional components.

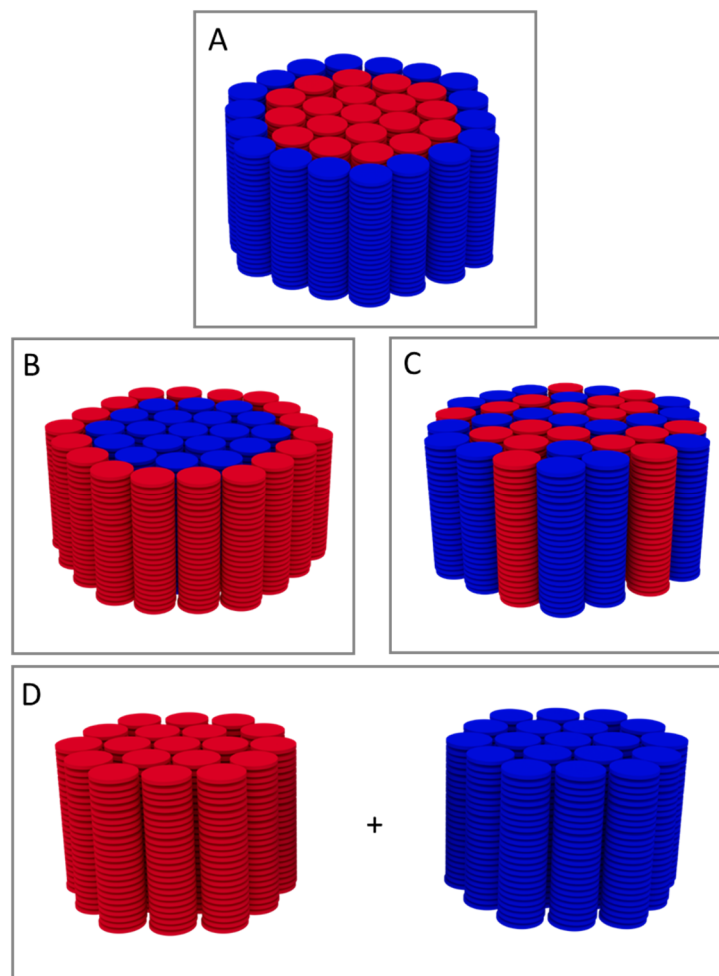


Figure 4.4: Schematic representation of different hierarchical, self-assembled structures due to multicomponent self-assembly of functional components (blue discs) and non-functional components (red discs). **A:** Supramolecular core-shell superstructure with non-functional components as core and functional components as shell material. Functional groups are on the surface of the superstructure. **B:** Supramolecular core-shell superstructure with functional components as core and non-functional components as shell material. **C:** Hierarchical, self-assembled structures with random distribution of domains of supramolecular polymers. **D:** Hierarchical structures of individually self-assembled supramolecular building blocks which might not influence each other during self-assembly.

From an application point of view, the formation of the structure in **Figure 4.4 A** is favored, because a core-shell structure is formed where the functional component forms the shell and the non-functional component acts as core material. Also, **Figure 4.4 B** shows a core-shell structure but here, the arrangement is reverse to the previous example. The core structure would be the functional component and the shell the non-functional. The functional groups would be covered and thus are not available for their purpose. The structure in **C** is probably less favored since the different single columns are built statistically into a hierarchical structure. However, such a structure feature different space requirement of the different individual columns used. In **Figure 4.4 D**, the two building blocks assemble individually into separated hierarchical structures. In this case, the two components are expected to not significantly influence each other during the self-assembly process from the same solution. This

structure is also possible due to the strong differences in the chemical structure of the used functional and non-functional components.

Of major relevance for this thesis are the two-component system, functional BTA 13 and the aliphatic BTA 17, which will be used for the multicomponent-assembly processes. The chemical structures of these compounds are shown in **Figure 4.5**. Likewise, in the scheme shown before, a core-shell fiber shall be prepared in which the functional component, BTA 13, is forming the surface structure. BTA 17 was chosen because it is well known in our group for its defined and robust fiber formation from different solvents.^[102] Typically robust fiber formation was obtained by the self-assembly from 2-butanone, but fiber formation from alcohols was also demonstrated.^[37] In particular, due to its straightforward use and the mechanical robustness of the fibers, this BTA was already demonstrated by our work group to be suitable for air filtration applications.^[102] However, this BTA lacks of functional groups in its periphery. For this reason, BTA 13 was selected, featuring cysteine as-functional groups in its periphery. The selected methionine side group comprises an ester and a thiol-ether functional group. In particular, this BTA was chosen due to the pronounced self-assembly behavior and properties and the ability to immobilize metal nanoparticles or metal ions from an aqueous suspension as already shown in chapter 3. A further advantage is related to the ester group or the sulfur-atom in the side chains of BTA13, which can be used for spectroscopic investigations to differentiate the two used supramolecular building blocks.

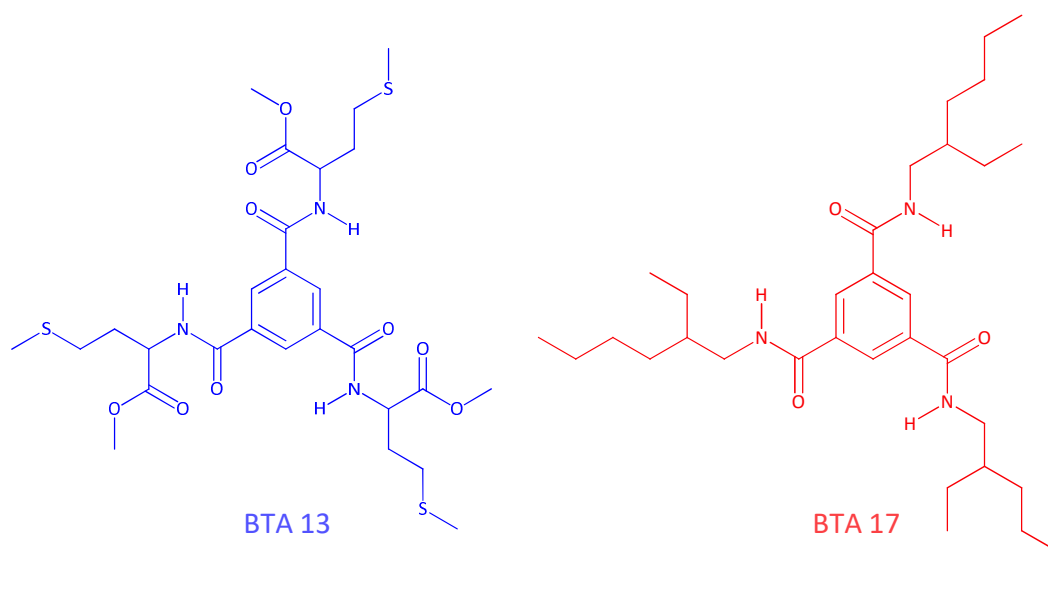


Figure 4.5: Chemical structures of BTA 13 with sulfur-containing periphery and BTA 17 with aliphatic periphery.

4.1 Clear and cloud point investigations of selected 1,3,5-benzenetrisamides

The temperature-dependent solubility behavior or in other words clear and cloud points determination using of a Crystal16™ device for various BTAs in different solvent systems was already described in chapter 3.3.2. Here, a detailed analysis of the BTA 13 was performed using 2-butanone, 1-propanol, and alcoholic water-based mixtures as solvents. The findings of the clear and the cloud point investigations are used as a basis of the potential multicomponent self-assembly process. The clear and cloud points of the single components in the selected solvents were investigated. The solutions were heated and cooled in temperature steps of 0.5 K/min in a temperature range of -15 °C to 75 °C. The BTA concentration was 0.5 wt.-%. The solutions were stirred with 600 rpm over the whole period of the experiment. At the clear point, the temperature was as high that the BTA was fully dissolved and the transmission was 100 %. The cloud point is similar to the temperature where the BTA starts to self-assemble.

Depending on the solubility and self-assembly behavior of the components it might be possible to design experiments to form super structures as shown in **Figure 4.4**. A core shell structure might be formed if one component is less soluble and start to self-assemble at first and the second component assembles on the previously formed structures.

The resulting graphs of the solubility behavior and thus evaluation of the clear and cloud points of the single components using 1-propanol, 1propanol : water (3 : 2 w/w) and 2-butanone are shown in **Figure 4.6**. Here, the transmission was plotted against the temperature. The second heating curve is colored in red and the second cooling curve is colored in blue. Furthermore, the clear and cloud points have been marked with the corresponding colors and the values obtained have been indicated accordingly. The graphs in **Figure 4.6 A** show the clear and cloud point of BTA 13 and BTA 17 using 1-propanol, respectively. BTA 13 dissolved completely at a temperature of 48 °C and started to reassemble at a temperature of 37 °C. Contrary to that, BTA 17 dissolved completely in solvent and did not reassemble at the chosen conditions of the experiment. Therefore, the graph for BTA 17 only shows a straight line at 100 % transmission resembling the dissolved compound at any condition. These results indicate that BTA13 is less soluble than BTA17 in 1-propanol. The graphs in **Figure 4.6 B** represent the solubility behavior of the two chosen BTAs in the solvent mixture 1-propanol : water (3 : 2 w/w). Interestingly, BTA 13 dissolved completely in the solvent system at 27 °C and reassembled at 17 °C. Compared to the previous system, the sulfur-containing 1,3,5-benzenetrisamide was better soluble in an alcoholic water mixture than in the neat alcohol. Also, interestingly, BTA 17 was significant less soluble in this solvent system. It features a clear point at 67 °C and a cloud point at 62 °C. This behavior may be explained by the addition of water and the hydrophobic nature of the aliphatic side groups. Finally, both BTAs were investigated and compared in the solvent 2-butanone. The resulting graphs are shown in **Figure 4.6 C**. In this case, BTA 13 dissolved completely by adding the

solvent and did not reassemble during the experiment and the set conditions as indicated by the straight line at 100% transmission. BTA 17 showed in contrary a clear point at 27 °C and a cloud point at 10 °C for the used BTA concentration of 0.5 wt.-%.

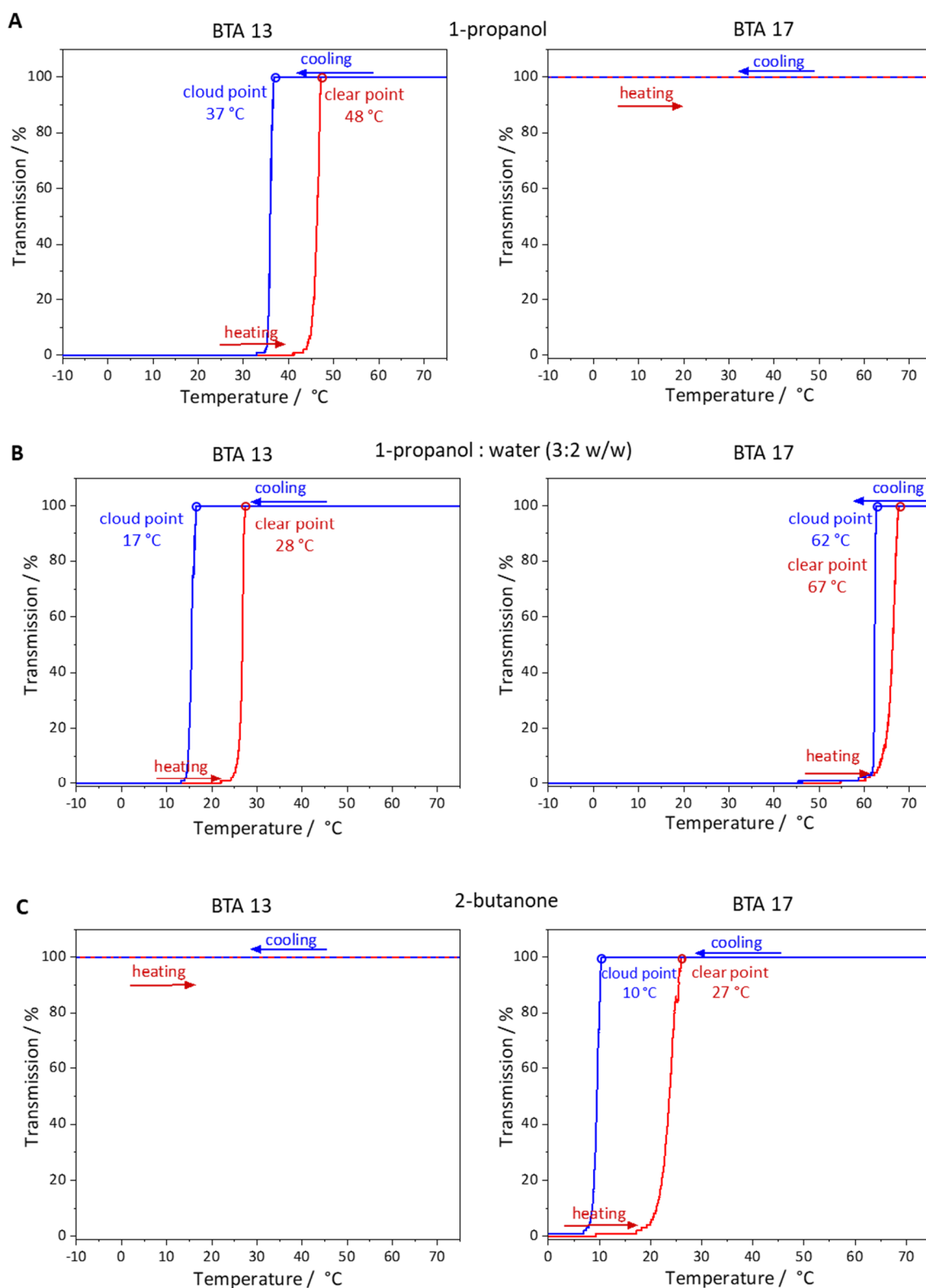


Figure 4.6: Plot of the transmission against the temperature of BTA 13 and BTA 17 in **A:** 1-propanol, **B:** 1-propanol : water (3 : 2 w/w) and **C:** 2-butanone . The red lines represent the second heating, the blue lines represent the second cooling. The red circles mark the clear points where the BTA is completely dissolved. The blue circles represent the cloud points where the BTA starts to reassemble.

To sum up, BTA 13 feature in contrast to BTA 17 a better solubility behavior in 2-butanone as solvent. BTA 17 show in contrast BTA 13 a better solubility behavior in 1-propanol. This situation is reversed in the case of the solvent mixture 1-propanol : water. This is also surprising since the solvent behavior does not follow a clear trend in view of the gradually varying solvent polarity or potential degree of hydrogen bonds present in the solvent system.

In all cases, upon self-assembly process self-sorting may occur. In view of a potential core-shell formation a subsequently step may be useful. Consequently, these results indicate that upon evaporation in system with 1-propanol : water and 2-butanone as solvents structure formation of BTA 17 takes places before the BTA 13 can self-assemble. And the other way around using 1-propanol as solvent system. Additionally, the results of the clear and cloud points investigations are comprised in **Table 4.1**.

Table 4.1: Clear and cloud points of BTA 17 and BTA 13 in selected solvents and solvent mixtures as determined with a Crystal16[®] System from Technobis™ via turbidity detection.

Solvent	BTA 13	BTA 17
	Clear point / cloud point (°C)	Clear point / cloud point (°C)
1-propanol	48 / 37	~20 / n.d.
1-propanol : water (3 : 2(w/w))	28 / 17	67 / 62
2-butanone	~20 / n.d.	27 / 10

¹)Clear point determined upon heating with a rate of 0.5 K/min under stirring with 600 rpm. BTA concentration was 0.5 wt.-%.

²)Cloud point determined upon cooling with a rate of 0.5 K/min under stirring with 600 rpm. BTA concentration was 0.5 wt.-%.

³) not determined

4.2 Multicomponent self-assembly to core-shell fibers

Proposed multicomponent self-assembly processes are schematically shown in **Figure 4.7**, which are mainly considered in this work. The preparation of such structures is performed on the basis of established standard procedures at the work group of the Macromolecular Chemistry I at the University of Bayreuth. The corresponding self-assembly process as well as the experimental features are shown in **Figure 3.22** in chapter 3.3. For the co-self-assembly, a solution of two fully dissolved components, e.g. BTA 13 and 17, at elevated temperatures was dropped on a silicon wafer or a glass slide (**Figure 4.7 A**). Self-assembly takes place upon evaporation of the solvent and cooling of the system. Considering the solvent-dependent findings shown before, one component is assumed to assemble into a fibrous structure (**Figure 4.7 B**) before the self-assembly of the second component takes place. Potentially it may be assumed that both components self-assemble individually, resulting in either self-sorted structures (**Figure 4.7 C.1**) or in a fibrous structure (**Figure 4.7 C.2**) where the surface of the initially formed self-assembled structure acts as nucleation site for the second component. Thus, the latter may result in core-shell like structures as shown in (**Figure 4.7 C.2**). After complete drying and depending on the specific self-assembly behavior in solution, both the self-sorted structures (**Figure 4.7 D.1**) and the core-shell fibers (**Figure 4.7 D.2**) can be examined.

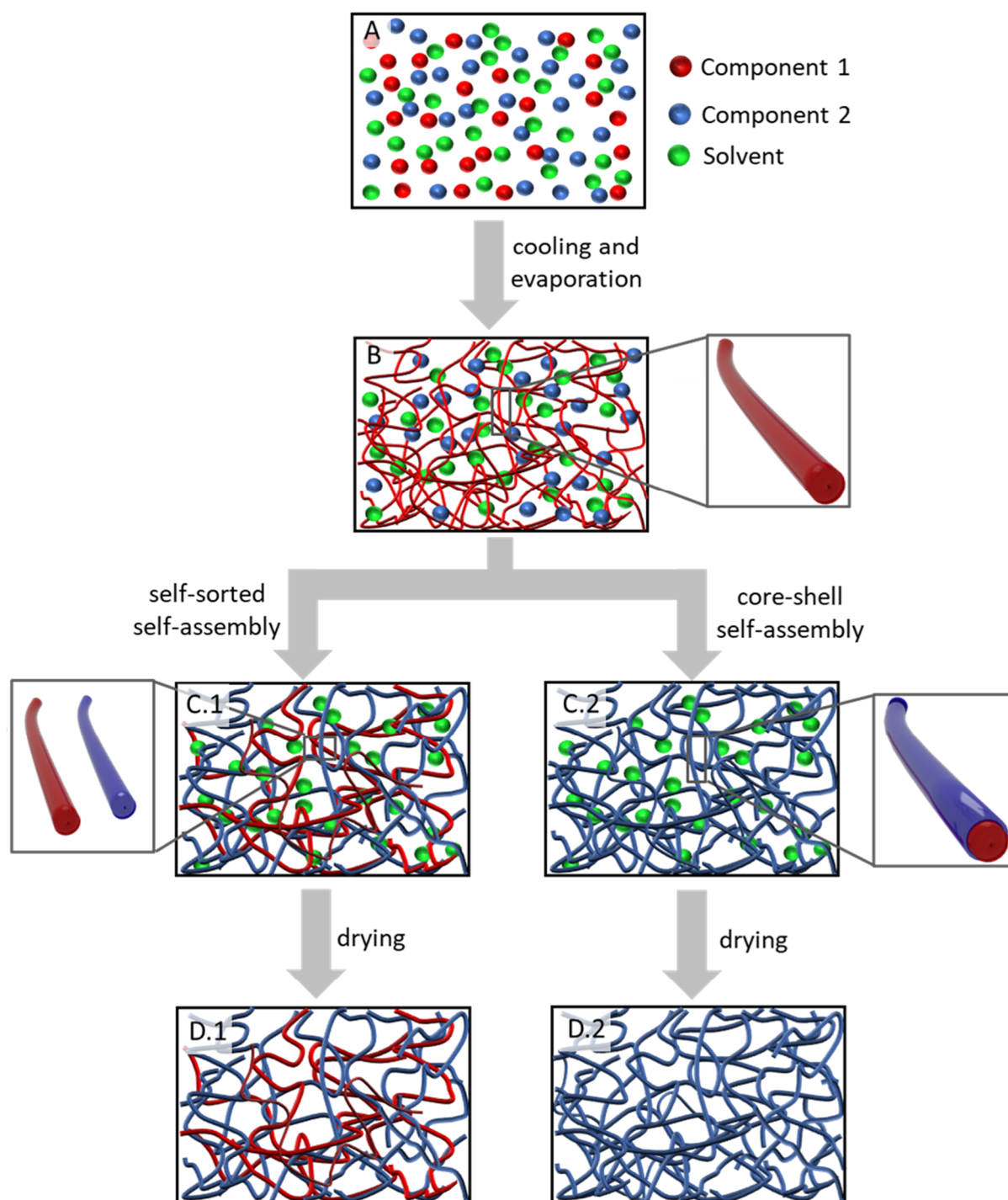


Figure 4.7: Schematic representation of multicomponent self-assembly processes. **A:** Two components (component 1: red and component 2: blue dots) are fully dissolved in selected solvents (green dots) at elevated temperatures. **B:** Upon cooling and evaporation of the solvent, self-assembly of component 1 is initiated first. Upon further cooling and evaporation, two different self-assembly processes may take place. On the one hand (**C.1**), the second component could assemble independently of the first, so that self-sorted structures are formed, red and blue fibers lie next to each other. On the other hand (**C.2**) self-assembly of component 2 is initiated at the surface of a component 1 fiber (red fiber), resulting in a core-shell superstructure (blue fiber). After complete drying, self-sorted (**D.1**) or core-shell (**D.2**) superstructures can be isolated.

4.2.1 Multicomponent self-assembly from 1-propanol

To provide evidence for the conceptual approach shown in **Figure 4.7**, the multicomponent self-assembly of a BTA 17 and BTA 13 in a molar ratio of 3:2 from 1-propanol was investigated first. Therefore, BTA 17 and BTA 13 were dissolved in the respective molar ratio at a total concentration of 0.5 wt.-% at 60 °C. The structures formed via multicomponent-assembly were investigated by DSC and FTIR-Spectroscopy. Furthermore, the structures are visualized microscopically by methods such as Raman coupled light microscopy and SEM-EDX investigations.

Thermal properties of single- and multicomponent assembled structures

In the following, the single components and the co-assembled samples prepared from different solvent systems will be investigated by means of DSC measurements. Only the first melting curve of the samples will be investigated because BTA 13 decomposes upon melting (see chapter 3.2.1). Furthermore, the second melting curve are expected to feature the co-assembly behavior as it may be obtained from bulk, which is probably different from the findings obtained after the self-assembly from solution. The melting peaks of the co-assembled samples provide a first evidence if the two building blocks were randomly arranged within single columns or if they were assembled individually. If the co-assembled samples only have one melting peak, it can be assumed that the two BTAs assembled together in one column. If the samples have two melting peaks, they probably self-assembled separately.

The resulting heating curves of the DSC measurements of the co-assembled sample (BTA 17 : BTA 13 (3 : 2 molar ratio)) and the neat BTAs 17 and 13 assembled from 1-propanol are shown in **Figure 4.8**.

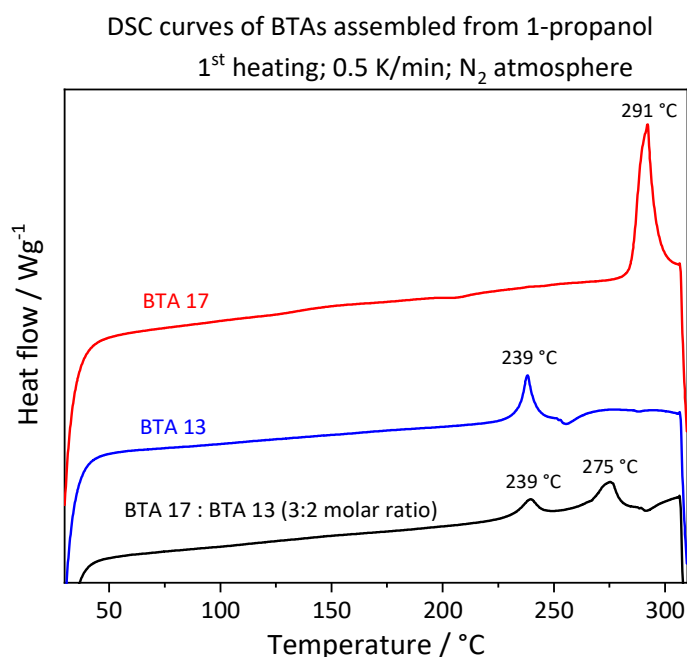


Figure 4.8: DSC curves of the first heating of self-assembled structures of BTA 17 (red), BTA 13 (blue) and a mixture of BTA 17 and BTA 13 (black) prepared from 1-propanol.

In the case of the co-assembled sample, the first melting peak appeared at 239 °C. This value is in very good agreement with the melting peak of neat BTA 13 assembled from 1-propanol. The second melting peak in the co-assembled sample appeared at 275 °C. The melting temperature of neat BTA 17 was found at 290 °C. Thus, the second melting peak in the multicomponent assembled sample was 15 °C lower than the melting temperature of BTA 17 assembled from 1-propanol. One potential interpretation is that a rather small amount of BTA 13 is incorporated into the BTA 17. Another potential interpretation is that the previously molten BTA 13 might act as solvent or plasticizer for BTA 17 and thus the melting temperature of the second component might be decreased. The results of the DSC measurement show that the two used components for the co-self-assembly process most likely did not arrange randomly within the same columnar structure due to the appearance of two individual melting points with a temperature difference of 36 °C. This means that the used BTAs assembled in individual columns consisting only of one of the components. However, it cannot be distinguished between a self-sorted system or a core-shell system.

FTIR-Spectroscopic studies of the self-assembled structures

In the following, the different co-assembled samples were investigated with the help of a FTIR-spectrometer in ATR mode. The spectra were recorded in the wavenumber range of 650 cm^{-1} to 4000 cm^{-1} and the vibrations of the multicomponent samples were compared with samples of the neat compounds.

In **Figure 4.9**, the FTIR-spectra of the multicomponent sample and the neat BTA 13 and 17, all samples prepared from 1-propanol, are shown.

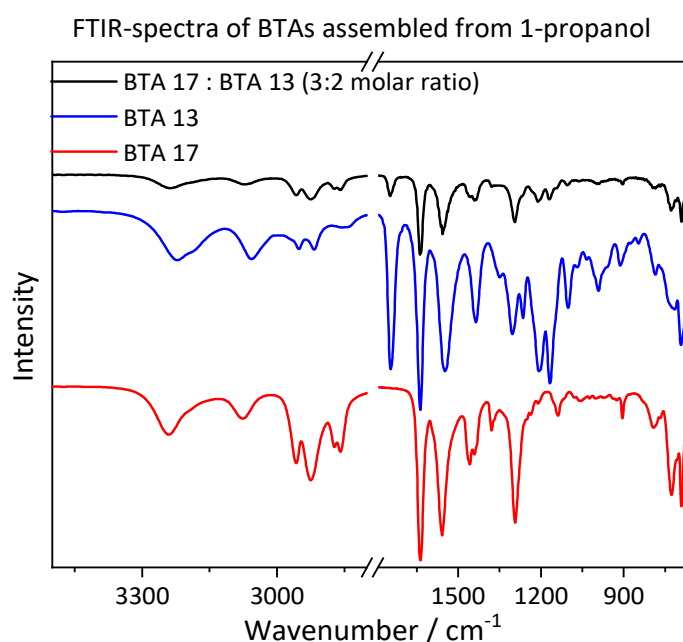


Figure 4.9: FTIR-Spectra of BTA 17 (red curve), BTA 13 (blue curve) and BTA 17 : BTA 13 (3 : 2 mol-%) (black curve) assembled from 1-propanol.

Based on the FTIR measurements it can be seen that the spectra of the co-assembled sample look very similar to the spectra of BTA 13. The vibration found at 1740 cm^{-1} is characteristic for ester groups due to the methyl ester of the methionine group, which are present in the periphery of BTA 13. This characteristic vibration also appears in the investigated co-assembled sample. Also, in the range of the fingerprint area with wavenumbers of 1500 cm^{-1} to 650 cm^{-1} the vibrations of BTA 13 are nearly the same as those of the assembled BTA-mixture. Moreover, vibrations which may be assigned to BTA 17 are present e.g. in the region of 1450 cm^{-1} , however to a smaller extent as it may be probably expected considering the molar ratio of the two components. In this context one has to note that FTIR-spectroscopy scans the surface of an object depending on the penetration depth of the method. Thus, it can be assumed that on or close to the surface, the objects mainly consist of the compound BTA 13. Moreover, as mentioned in chapter 3.2.2, based on characteristic vibrations for columnar stacking of BTAs these values provide evidence whether the compounds are present in a columnar crystalline arrangement or one or both crystals are deposited in another crystalline arrangement or an amorphous manner. It was found that the Amide II and Amide A vibrations associated with a columnar stacking typically appear at 1560 cm^{-1} and 3240 cm^{-1} . BTA 13 and BTA 17 as well as the co-assembled sample show these characteristic vibrations. Thus, it can be claimed that the co-assembled sample also has a columnar structure regardless which of the two multicomponent morphologies is present.

Analysis of the co-assembled structures with Raman- and EDX-spectroscopy

All co-assembled structures were analyzed with Raman- and EDX-spectroscopy. Thus, these methods are explained in more detail in this section. The samples described above were investigated with the help of a light microscope coupled with Raman-spectrometer from WiTec®. This confocal microscope allows to investigate the sample via Raman spectroscopy with spatial resolution. Consequently, Raman spectral imaging can be performed, where the acquisition of a complete Raman spectrum at every image pixel is possible. False color images allow to show in a convenient manner where the single components in the sample appear.

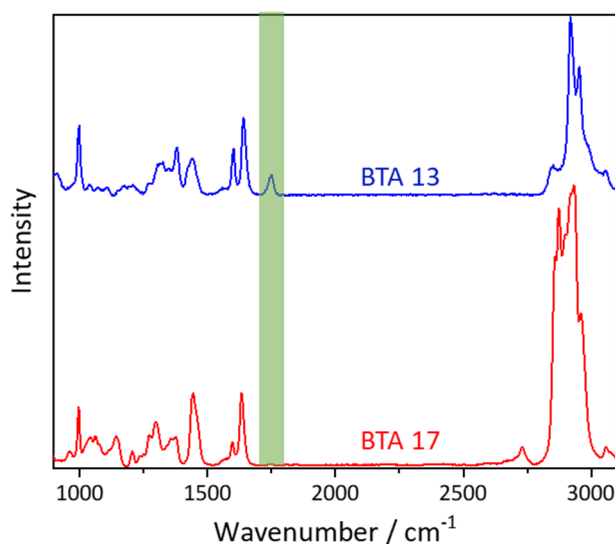


Figure 4.10: Raman spectra of BTA 13 (blue) and BTA 17 (red). In the case of BTA 13, the vibration at 1750 cm^{-1} of the ester group can be clearly detected.

For the detection of the individual components with Raman-spectroscopy, the spectra of both BTAs have to be distinguished and compared. The two Raman spectra of the neat BTAs shown in **Figure 4.10** feature a significant difference mainly in the vibration located at 1750 cm^{-1} . This vibration only appears for BTA 13 because it is characteristic for methionine ester groups. In areas of the spatially resolved images, where BTA 13 is present, the characteristic vibration for the ester will appear. These areas will be colored blue in the following false color images. Areas where only BTA 17 can be detected will be colored red.

Figure 4.11 shows exemplarily light microscopic images of the multicomponent self-assembly of BTA 17 and BTA 13 in a molar ratio of 3:2 from 1-propanol.

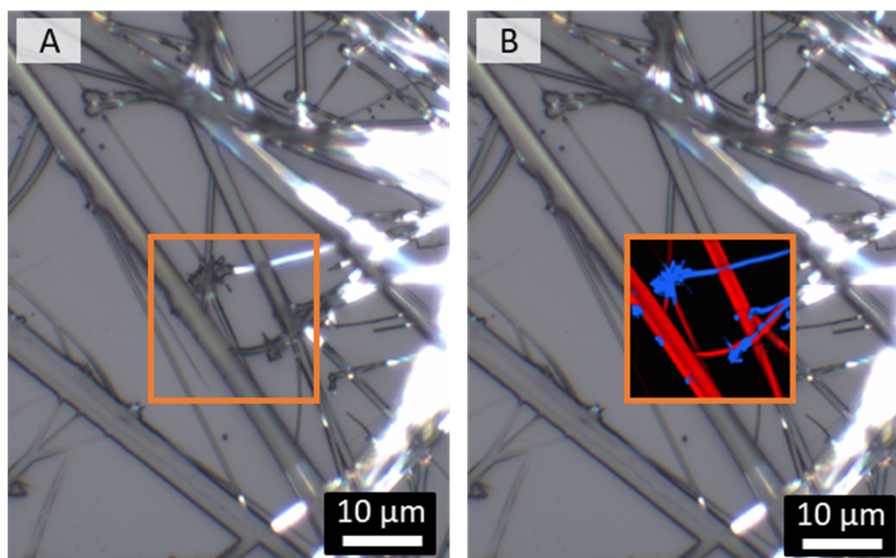


Figure 4.11: Microscopic analysis of self-assembled fibers of BTA 17 and BTA 13 (3 : 2 molar ratio) from 1-propanol with a BTA-concentration of 0.5 wt.-% at a starting temperature of $70\text{ }^{\circ}\text{C}$. **A:** Light microscopic image of self-assembled fibers and **B:** the same microscopic image including a false color section as determined by confocal Raman-spectroscopy. Red colored structures represent BTA 17. Blue colored structures represent BTA 13.

In **Figure 4.11 B**, the corresponding false color images of the Raman imaging are shown as an overlay to the light microscopy image.

According to the false color image, the two BTAs seem to assemble in a self-sorted manner from 1-propanol. Supramolecular fibers which are only colored red consist of BTA 17. The fibers next to those are blue colored and consist of BTA 13. These fibers seem not to influence the formation of the other BTA fibers during the self-assembly process. Moreover, BTA 13 seems to assemble specifically in a given area and feature a cluster-like fibrous morphology.

Another imaging method to distinguish between the two BTAs is SEM coupled with EDX spectroscopy. Here, the two used compounds can be easily differed by the detection of the specific energy of the X-rays of the sulfur atoms of BTA 13. Thus, areas containing sulfur atoms can be detected and by using the mapping mode, false color images highlighting the structures containing BTA 13 can be achieved.

First, SEM images of the neat aliphatic 1,3,5-benzenetrisamide (BTA 17), the neat methionine containing BTA (BTA 13) and the BTA mixture assembled from 1-propanol are compared in **Figure 4.12**. On the right side of the figure, the corresponding fiber diameter histograms are shown. For the fiber diameter histograms at least 150 individual fibers were measured.

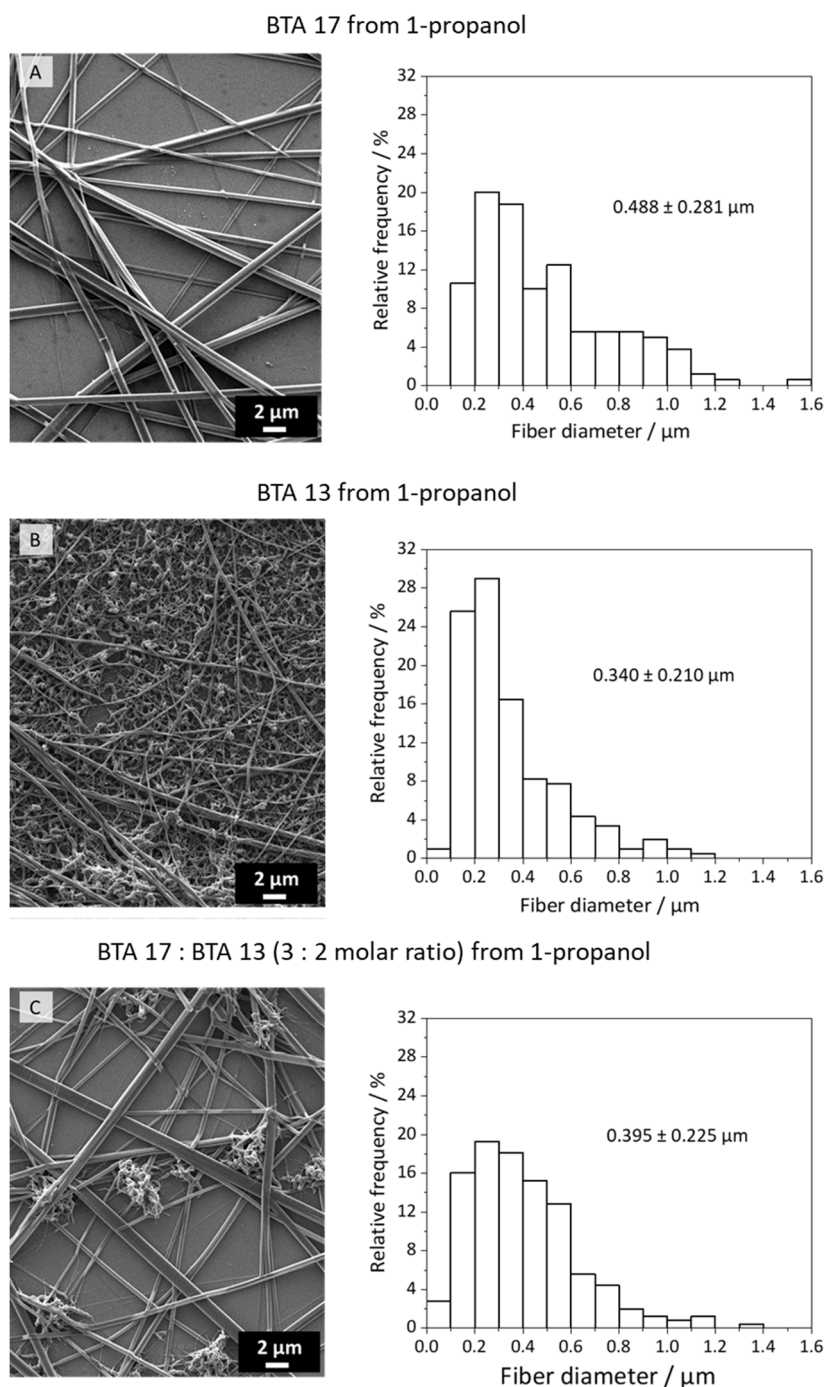


Figure 4.12: SEM images of self-assembled structures of BTA 17 (A), BTA 13 (B), and BTA mixture of BTA 17 and BTA 13 (3 : 2 molar ratio) (C) and the corresponding fiber diameter histograms. Prepared from 1-propanol with a BTA-concentration of 0.5 wt.-% at a starting temperature of 70 °C. For each histogram at least 150 fibers were used.

As it can be seen in **Figure 4.12 A**, BTA 17 formed homogeneous supramolecular fibers assembled from 1-propanol. In general, these fibers appear to be comparable stiff and feature a very long fiber length. Moreover, some fibers show kinks and have a hexagonal like shape. The mean fiber diameter is about 490 nm with a rather broad fiber diameter distribution as shown in the fiber diameter histogram.

In contrast, the fibers obtained after the self-assembly of BTA 13 are less homogeneous in shape than those assembled from BTA 17. In the SEM image, some long and thicker fibers are present

accompanied by many thin short fibers. The longer fibers have a slightly twisted shape. The fiber diameter histogram shows that mainly small fibers with an average fiber diameter of about 340 nm were formed. We note that to a small extent, fibers with a diameter of 1 μm were found as well.

The co-assembled sample in **Figure 4.12 C** shows in general two types of self-assembled structures. There are some thicker long fibers. These fibers are very similar to the fibers formed from BTA 17. Next to the long fibers, there are spots with bundles of small-shaped objects. These structures seem to have a slightly twisted shape and they are very similar to the objects formed from BTA 13. It can be claimed that the long fibers consist of the aliphatic BTA 17 and the small objects are formed from the sulfur-containing BTA 13. This assumption agrees with the results of the Raman spectroscopic investigations discussed before. The resulting average mean fiber diameter of the co-assembled structures with 395 nm lies between the diameters of the two neat components. The two BTAs obviously do not influence each other during the self-assembly process using these conditions.

Finally, these co-assembled sample were investigated via EDX-spectroscopy to verify the findings discussed above.

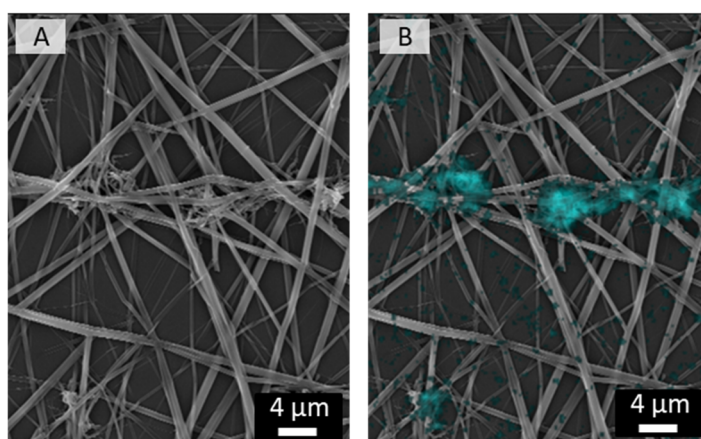


Figure 4.13: Microscopic analysis of self-assembled fibers of BTA 17 and BTA 13 (3 : 2 molar ratio) from 1-propanol with a BTA-concentration of 0.5 wt.-% at a starting temperature of 70 °C. **A:** SEM image of the self-assembled fibers. **B:** Corresponding false color SEM image. The turquoise colored areas represent sulfur atoms as detected with EDX-spectroscopy.

In **Figure 4.13** the investigated SEM image (**A**) and the corresponding false color image (**B**) are shown. Only some areas are colored turquoise which represents sulfur atoms. In these areas, mainly thin fibers are present. The long and thicker fibers are very similar to the morphology of neat BTA 17 prepared from 1-propanol and seem not to contain sulfur indicating that these fibers in fact consist of BTA 17. The small structures, which contain the sulfur atoms also look very similar to the structures formed from BTA 13 self-assembled from 1-propanol (**Figure 4.13 B**). These results are in agreement with the Raman-images shown before. With both methods, the BTAs were detected separately from each other. Thus, both methods provide evidence for a self-sorted system as discussed above.

In the following chapters, the findings of the with Raman spectroscopy and EDX spectroscopy are discussed together.

4.2.2 Multicomponent self-assembly from 1-propanol/water

Similarly to the samples before, multicomponent self-assembled structures of the same BTA mixture (BTA 17 and BTA 13, molar ratio 3:2) but from 1-propanol : water (3:2(w/w)) were prepared and investigated in the same manner.

Thermal properties of single- and multicomponent assembled structures

In **Figure 4.14**, the DSC-curves of the first melting of the samples self-assembled from 1-propanol : water (3:2(w/w)) are shown. Likewise before, the first melting point for the multicomponent assembled sample is nearly at the same value as the neat BTA 13. In both cases, the melting point appears at about 235 °C or 238 °C, respectively. The second melting peak is assigned to the melting point of the BTA 17, which is reduced from 289 °C to 270 °C compared to the neat BTA 17. The two melting peaks indicating that two individual species of highly ordered self-assembled supramolecular objects were present in the sample. Thus, co-assembled structures, which are distributed in a statistical manner in the same column are ruled out in this situation as well.

DSC curves of BTAs assembled from 1-propanol : water (3 : 2 (w/w))
1st heating; 0.5 K/min; N₂ atmosphere

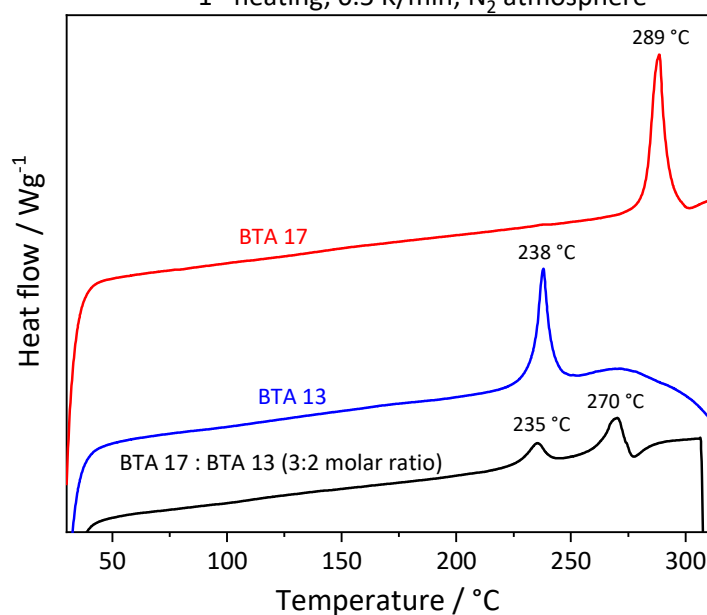


Figure 4.14: DSC curves of the first heating of self-assembled structures of BTA 17 (red), BTA 13 (blue) and a mixture of BTA 17 and BTA 13 (black) prepared from 1-propanol : water (3:2(w/w)).

FTIR-Spectroscopic studies of the self-assembled structures

Figure 4.15 shows the FTIR-spectra of the self-assembled neat and multicomponent samples prepared from 1-propanol : water (3:2(w/w)). Again, the multicomponent assembled sample shows the characteristic vibration for the ester group of BTA 13 at 1740 cm⁻¹. Moreover, vibrations of the BTA 17 can be detected at 1450 cm⁻¹.

As mentioned before FTIR-spectroscopy provide also evidence for columnar staking based on characteristic vibrations. It can be also claimed that the co-assembled sample has a columnar structure even if the two building blocks might assemble individually.

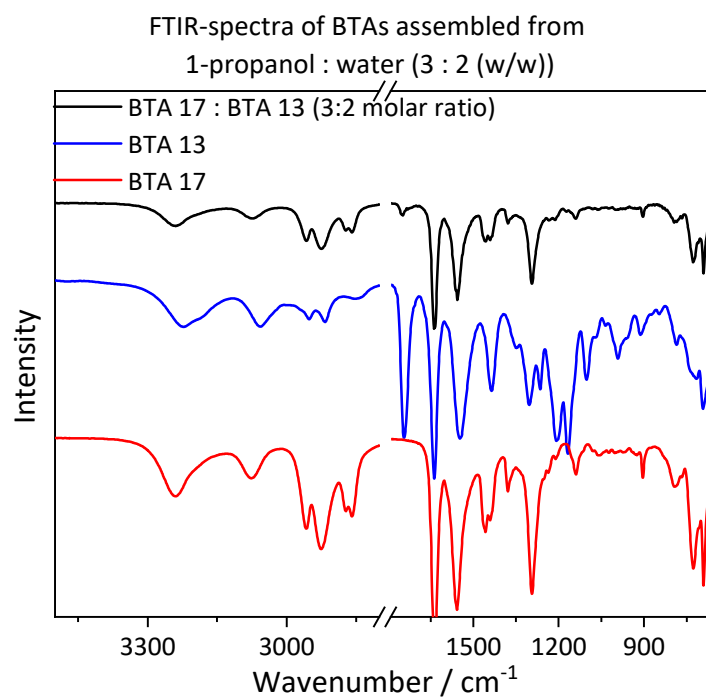


Figure 4.15: FTIR-Spectra of BTA 17 (red curve), BTA 13 (blue curve) and BTA 17 : BTA 13 (3 : 2 molar ratio) (black curve). Compounds were self-assembled from 1-propanol : water (3:2(w/w)).

Analysis of the co-assembled structures with EDX- and Raman-spectroscopy

The isolated structures of these supramolecular samples assembled from 1-propanol : water (3:2(w/w)) were eventually investigated by SEM; EDX and Raman coupled light microscope.

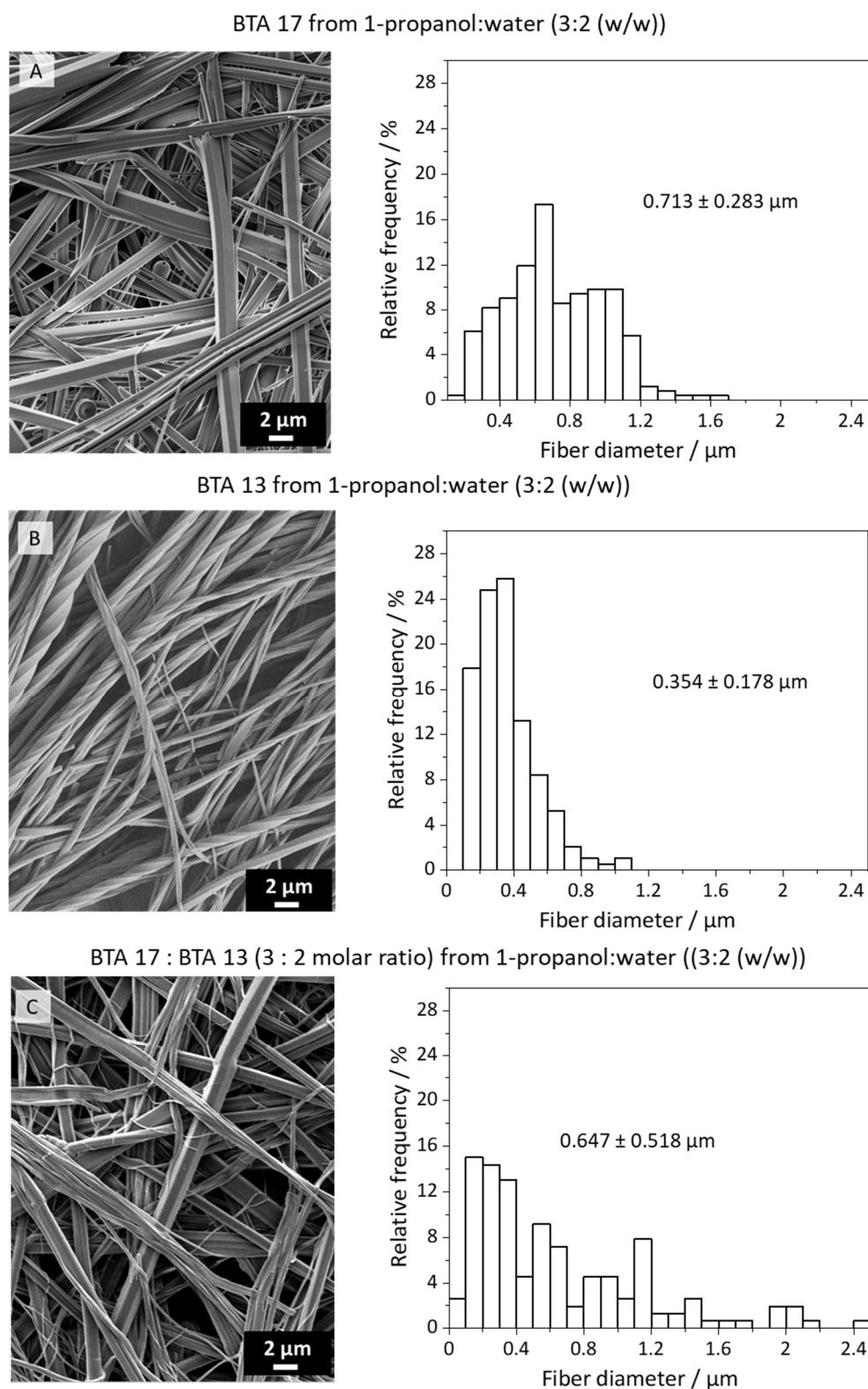


Figure 4.16: SEM images of self-assembled structures of BTA 17 (A), BTA 13 (B), and BTA mixture of BTA 17 and BTA 13 (3 : 2 molar ratio) (C) and the corresponding fiber diameter histograms. Prepared from 1-propanol : water (3 : 2 (w/w)) with a BTA-concentration of 0.5 wt.-% at a starting temperature of 70 °C. For each histogram at least 150 fibers were used.

In **Figure 4.16**, the SEM-images and the corresponding fiber diameter histograms of self-assembled BTA 17, BTA 13 and the BTA-mixture (BTA 17 : BTA 13 (3 : 2molar ratio)) from 1-propanol : water (3:2(w/w)) are shown. In all three cases, supramolecular BTA fibers can be detected. BTA 17 assembled into relatively thick fibers, which have in some cases a hexagonal shape. Next to these thicker fibers, some small fibers can be seen. In some cases, little cracks in the fibers can be detected (**Figure 4.16 A**). As it can be seen in the corresponding fiber diameter histogram, the formed fibers have a relatively big fiber diameter of about 710 nm. The fibers formed from BTA 13 have a more homogenous shape than the fibers obtained from the self-assembly of BTA 17. The BTA 13-fibers have in nearly all cases a twisted shape. Here, also some cracks can be detected (**Figure 4.16 B**). In this case, the fiber diameter distribution is relatively narrow, the average fiber diameter is about 350 nm.

The fibers formed from the BTA mixture have a less homogeneous shape than the fibers formed from neat BTA 13. There are some thick fibers which have partly a hexagon-like shape. But there are also very thin fibers (**Figure 4.16 C**). At the first glance, the fibers look relatively similar to the fibers of BTA 17 but the small fibers seem to have a slightly twisted form, as it was observed under these conditions for BTA 13 and therefore assigned to this component. This leads to the conclusion that within this sample the thick fibers consist of BTA 17 and the thin fibers of BTA 13. Here, the resulting fiber diameter histogram shows a very broad distribution. The mean fiber diameter is about 650 nm which is between the two neat self-assembled samples.

Since these results provide no clear picture, a more detailed picture can be obtained by the SEM image with the corresponding false color image of the EDX mapping measurement and the light microscopic image with the corresponding false color Raman image as shown in the following in the **Figure 4.17**.

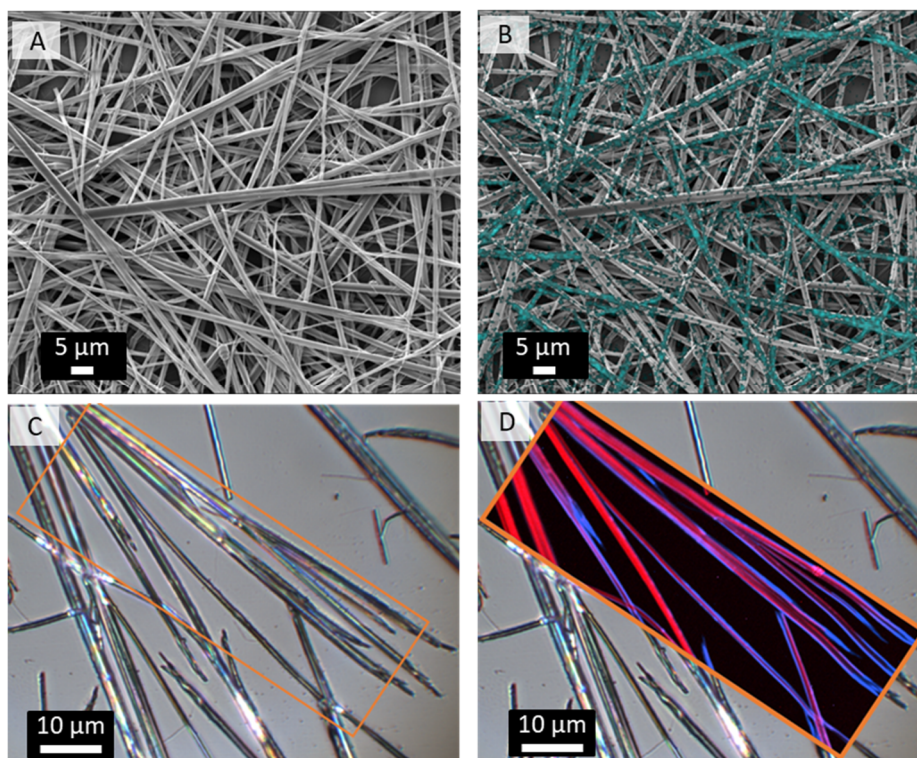


Figure 4.17: Microscopic analysis of self-assembled fibers of BTA 17 and BTA 13 (3 : 2 molar ratio) from 1-propanol : water (3:2 (w/w)) with a BTA-concentration of 0.5 wt.-% at a starting temperature of 70 °C. **A:** SEM image of the self-assembled fibers. **B:** Corresponding false color SEM image. The turquoise colored areas represent sulfur atoms as detected with EDX-spectroscopy. **C:** Light microscopic image of self-assembled fibers and **D:** the same microscopic image including a false color section as determined by confocal Raman-spectroscopy. Red colored structures represent BTA 17. Blue colored structures represent BTA 13.

The false color image of the co-assembled sample resulting of the EDX mapping is shown in **Figure 4.17 B**. It can be seen that most of the BTA-fibers were colored. However, it might be possible that not all supramolecular fibers contain sulfur. It has to be mentioned that the local resolution of the EDX varies with the size of the electron beam interaction volume. As a result, areas, where no functional groups are present, may appear colored as well. On the other hand, areas, where sulfur is present, may not be colored due to a fairly small signal intensity recorded during the EDX-measurement.

The false color image in **Figure 4.17 D** shows the results of the Raman imaging. In the sample, the two used BTAs can be detected and distinguished. Interestingly, the obtained results are different from those findings found previously. The blue colored areas surround the red colored fibers. Thus, the two BTAs obviously form a core shell structure from 1-propanol : water (3:2 (w/w)) whereas BTA 13 forms the shell and the BTA 17 the core. This finding goes in lines with the solubility studies. BTA 17 assembles in this solvent system at a temperature of about 60 °C. BTA 13 assembles at much lower temperatures at about 20 °C. In this situation, BTA 17 is assumed to act as nucleation sites for the BTA13 fiber growth. This is the first example in this work where BTA core-shell fibers were successfully prepared by using selected self-assembly conditions.

4.2.3 Multicomponent self-assembly from 2-butanone

Finally, a third system was studied, namely, the multicomponent self-assembled structures of the BTA mixture (BTA 17 and BTA 13, molar ratio 3:2) in 2-butanone.

Thermal properties of single- and multicomponent assembled structures

The single components and the co-assembled samples prepared from 2-butanone were investigated by means of DSC measurements. As discussed before, only the first melting curve of the samples will be considered. **Figure 4.18** shows the heating curves of the DSC measurements for the neat components and co-assembled sample prepared from 2-butanone. The blue curve represents the first heating curve of neat BTA 13 which has a melting temperature of about 232 °C. The first heating curve of neat BTA 17 is represented by the red curve and show a melting temperature at 287 °C. As it can be seen, the black curve, which represents the first heating of the co-assembled sample has two melting peaks. The first peak appears at 234 °C and the second appears at 272 °C. The first peak is assigned to the melting of BTA 13, since it has nearly the same melting temperature as the neat compound. The second peak is assigned to the melting peak of BTA 17, which appears at 272 °C, about 15 °C lower than in the neat component. Like discussed before, a rather small amount of BTA 13 may be incorporated into the supramolecular structure of BTA 17 or the previously molten BTA 13 might act as solvent or plasticizer for BTA 17. The results of the experiment can be interpreted that the two supramolecular building blocks do not build in one column from 2-butanone. However, they feature a highly ordered structure due to the presence of two melting peaks.

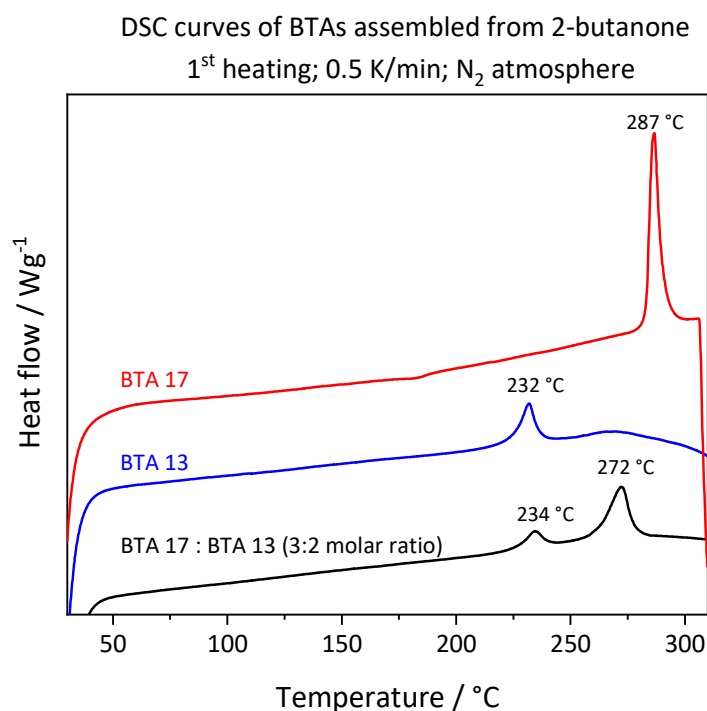


Figure 4.18: DSC curves of the first heating of self-assembled structures of BTA 17 (red), BTA 13 (blue) and a mixture of BTA 17 and BTA 13 (black) prepared from 2-butanone.

FTIR-Spectroscopic studies of the self-assembled structures

In **Figure 4.19**, the FTIR spectra in a wavenumber range from 650 cm^{-1} to 4000 cm^{-1} of the dried samples are shown. The vibrations of the multicomponent samples were compared with samples of the neat compounds. It can be seen that the co-assembled sample shows the characteristic vibration for the ester group of the BTA 13 building block. Moreover, specific vibrations attributed to the BTA 17, for example at 1450 cm^{-1} , appear in the co-assembled spectrum as well. As in the samples discussed before and according to the characteristic vibrations, it can be concluded that the co-assembled sample of both BTAs feature a columnar structure, although no clear statement can be made whether a self-sorted structure or a core-shell structure is present.

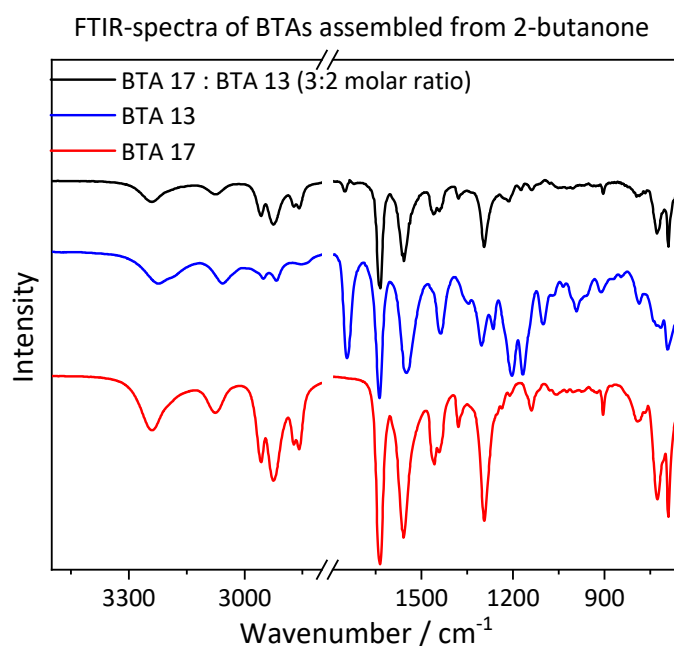


Figure 4.19: FTIR-Spectra of BTA 17 (red curve), BTA 13 (blue curve) and BTA 17 : BTA 13 (3 : 2 molar ratio) (black curve). Compounds were self-assembled from 2-butanone.

Analysis of the co-assembled structures with EDX- and Raman-spectroscopy

The self-assembly behavior of the neat components and the mixtures in the selected solvent systems were investigated with the methods as outlined before and compared to each other in the following. The self-assembly of BTA 13 will be discussed separately because a smaller concentration is required to observe supramolecular structures of dried samples from 2-butanone due to the much smaller fiber diameter of the structures, as described in chapter 3.3. Typically, very small nanostructures at a larger concentration results in the formation of highly dense films, where the nanofibers dimensions cannot be clearly distinguished anymore. Therefore, to investigate the self-assembly behavior of BTA 13 from 2-butanone, the BTA concentration was decreased in a way, where the lower concentration results in a decreased number of supramolecular objects avoiding a very densely packed fiber morphology. It was found that a solution with 0.05 wt.-% of BTA 13 in 2-butanone after full dissolution and self-

assembly upon cooling and evaporation of the solvent was suitable for SEM investigation of the morphology. The corresponding SEM images of the dried samples are shown in **Figure 4.20**.

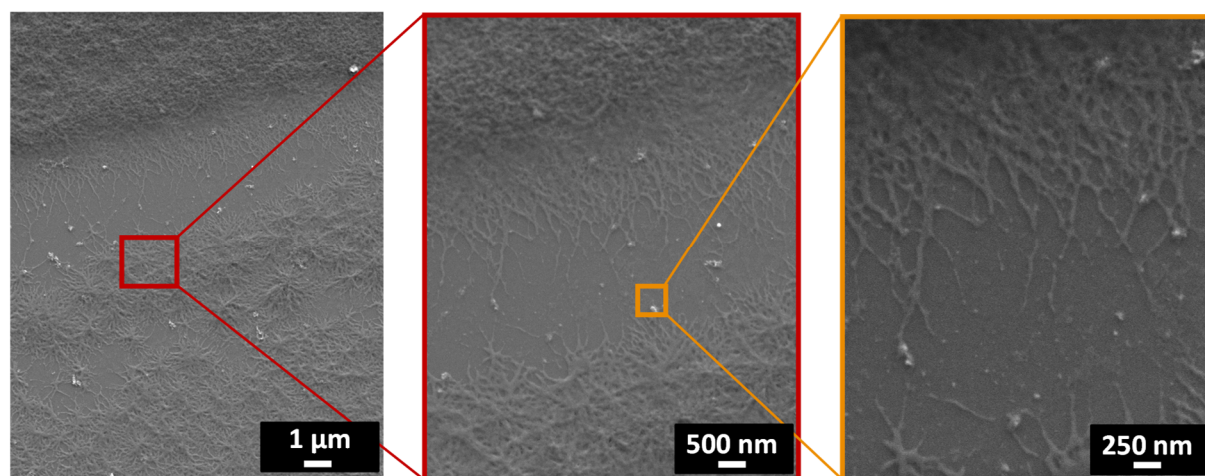


Figure 4.20: SEM images with different magnifications of BTA 13 self-assembled from 2-butanone at a concentration of 0.05 wt.-%. Left 5000x; middle 10.000x, right 20.000x. The BTA nanofibers exhibit fiber diameters between 40 nm and 70 nm.

In this case, BTA 13 formed supramolecular nanofibers with an approximate fiber diameter of 40 nm to 70 nm. These BTA nanofibers can be seen in **Figure 4.20** on the right side at a magnification of 20.000x. At lower magnifications the fibers can still be hardly detected, due to the formation of a film-like structure consisting of the BTA. With this preparation method at a BTA-concentration of 0.05 wt.-%, it was possible to visualize that BTA 13 assembled into very thin supramolecular nanofibers, which in turn suggests that the film-like structure at a BTA-concentration of 0.5 wt.-% consists of many very small supramolecular nanofibers.

In **Figure 4.21**, the SEM images of self-assembled neat BTA 17 (**A**), neat BTA 13 (**B**) and BTA 17 : BTA 13 (3 : 2 molar ratio) (**C**) from 2-butanone and a concentration of 0.5 wt.-% are shown. On the right side of the figure, the corresponding fiber diameter histograms are shown. For the histograms at least 150 individual fibers were measured.

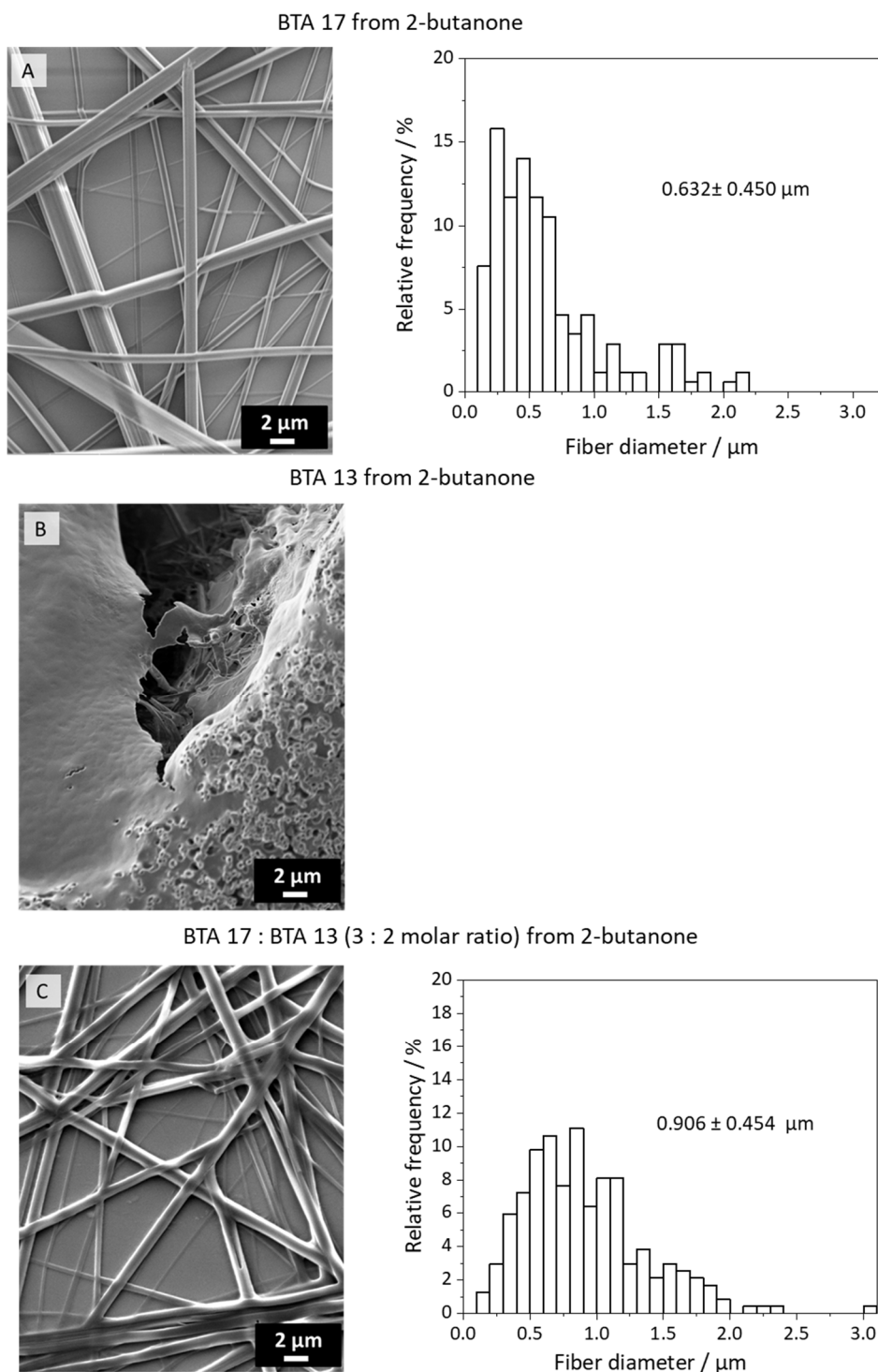


Figure 4.21: SEM images of self-assembled structures of BTA 17 (A), BTA 13 (B), and BTA mixture of BTA 17 and BTA 13 (3 : 2 molar ratio) (C) and the corresponding fiber diameter histograms. Prepared from 2-butanone with a BTA-concentration of 0.5 wt.-% at a starting temperature of 70 °C. For each histogram at least 150 fibers were used.

As outlined before, no supramolecular structure can be clearly detected and evaluated in the case of BTA 13 at this concentration. In contrast, the supramolecular fibers formed from BTA 17 can be observed, which feature a slightly inhomogeneous diameter distribution. The average mean fiber diameter is about 630 nm. The fiber diameter distribution of the co-assembled sample has a more

Gaussian-shape than the histogram of BTA 17 featuring a mean fiber diameter of the co-assembled of 900 nm. This value is about 270 nm larger than the diameter of the fibers formed from the neat BTA 17, although the overall morphology of the fibers in both samples looks very similar.

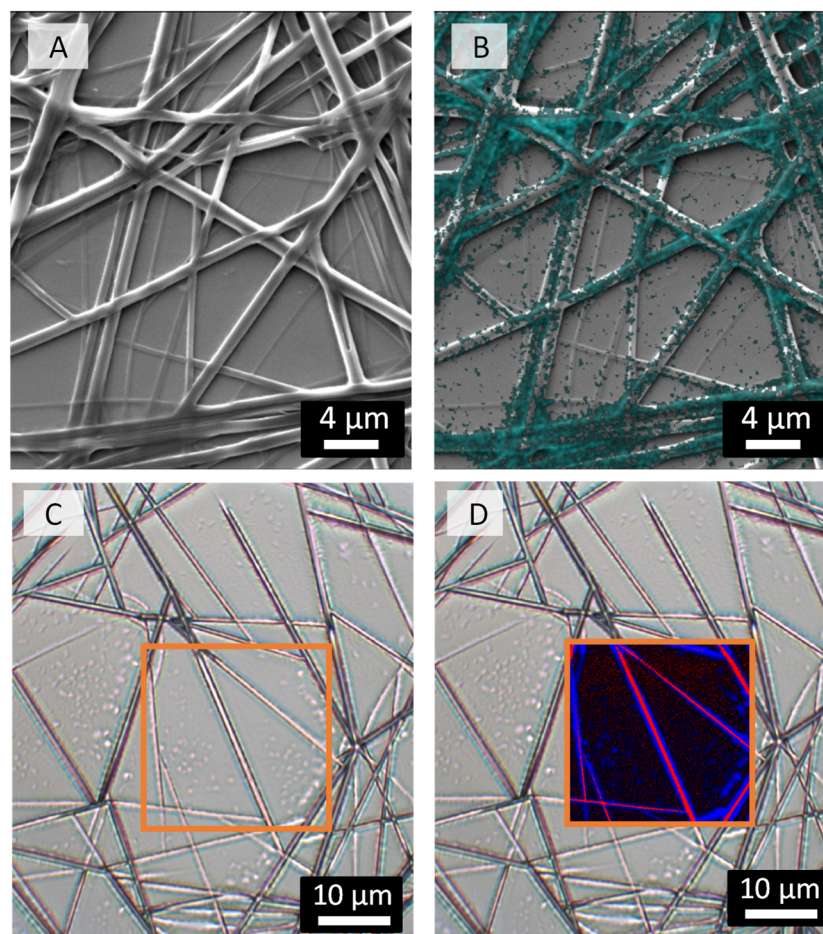


Figure 4.22: Microscopic analysis of self-assembled fibers of BTA 17 and BTA 13 (3 : 2 molar ratio) from 2-butanone with a BTA-concentration of 0.5 wt.-% at a starting temperature of 70 °C. **A:** SEM image of the self-assembled fibers. **B:** Corresponding false color SEM image. The turquoise colored areas represent sulfur atoms as detected with EDX-spectroscopy. **C:** Light microscopic image of self-assembled fibers and **D:** the same microscopic image including a false color section as determined by confocal Raman-spectroscopy. Red colored structures represent BTA 17. Blue colored structures represent BTA 13.

In **Figure 4.22**, the SEM image (**A**) and the corresponding false color image of the EDX mapping measurement (**B**) as well as the light microscopic image (**C**) and the corresponding false color Raman image (**D**) of the co-assembled sample are shown.

The turquoise areas in the false color image in **Figure 4.22 B** show those spots where sulfur atoms were detected during the EDX-mapping process. The electron beam interaction volume can have a diameter of 100 nm up to 1 μm and thus, on some spots sulfur might be detected but the sulfur lies just next to this area and emitted the characteristic X-Rays. In this way, the signals in the areas without fibers can be explained. But it can be seen that on nearly all fibers turquoise dots are present. These colored dots are mainly located on the fibers and only partly in areas without fibers. Thus, it can be concluded that

the co-assembly with both BTAs led to a homogeneous fiber morphology, where the larger supramolecular fibers of the BTA 17 nearly contain all sulfur.

From the false color image of the Raman imaging in **Figure 4.22 D**, it can be seen that the BTAs assemble indeed into core-shell fibers. In this sample, the core of the formed structures is colored red resembling the aliphatic BTA 17. The edges of the supramolecular fibers are colored blue, which corresponds to the characteristic signals of BTA 13. Thus, it can be claimed that the assembly from 2-butanone leads to core-shell fibers with a sulfur-containing shell.

This self-assembly behavior may be explained with the results obtained from the clear and cloud points of the solubility investigation of the single components. Here it was found that BTA 17 assembles from a hot solution of 2-butanone at a temperature of 10 °C. Contrary, BTA 13 does not assemble at the investigated concentration and temperatures. In case of the mixture of both BTA, first BTA 17 will start to self-assemble and subsequently BTA 13 assembles on the formed supramolecular structures of BTA 17, which act as nuclei. Since BTA 13 forms very thin supramolecular fibers from 2-butanone, the core-shell fibers obtained from the BTA mixture, comprises a core consisting of relatively thick fibers of BTA 17 and a smooth shell consisting of thin fibers of BTA 13.

4.3 Adsorption of metal ions on supramolecular core-shell fibers from aqueous solution

4.3.1 Preparation of mechanically stable composites with supramolecular core-shell fibers

The following experiments were performed and evaluated at the DWI- Leibniz Institute for Interactive Materials at the RWTH Aachen under the supervision of Dr. H. Thomas. In particular, for these experiments the synthesized BTA 13 and BTA 17 were used and the aforementioned evaluated self-assembly protocols were the basis for these experiments and modified and adopted to the specific composite system as outlined below. The experiments were conducted and evaluated in the course of a joint project of the “*Arbeitsgemeinschaft industrieller Forschungsvereinigungen*” (AiF). The approach and parts of the results of this chapter are already published in a joint publication in the journal of *Technische Textilien*.^[180]

For the preparation of the microfiber-nanofiber-composites, this part of the work focusses on previously gained knowledge. As demonstrated in earlier works at our department, Misslitz et. al. and Weiß et al. showed that scaffolds or support structures such as nonwovens can be beneficially combined with supramolecular fibers by using an *in-situ* preparation approach for the formation of the supramolecular nanofibers within the support structure.^[102,106]

Here, also a nonwoven was used to produce a functional supramolecular fiber-microfiber composite with co-assembled 1,3,5-benzenetrisamide fibers. The major challenge is in contrast to the aforementioned work, the introduction of functional supramolecular nanofibers and in particular the use of core-shell structures. The preparation of such a composite is shown schematically in **Figure 4.23**. With the help of the functional groups of the supramolecular nanofibers, these composites should be used to immobilize metal ions from an aqueous solution. As shown previously (chapter 3.4), metal nanoparticles can be adsorbed with the BTA 13 shell structure. Another feature is that BTA 17 as core structure provide a non-functional supramolecular nanofiber, which is mechanical robust.

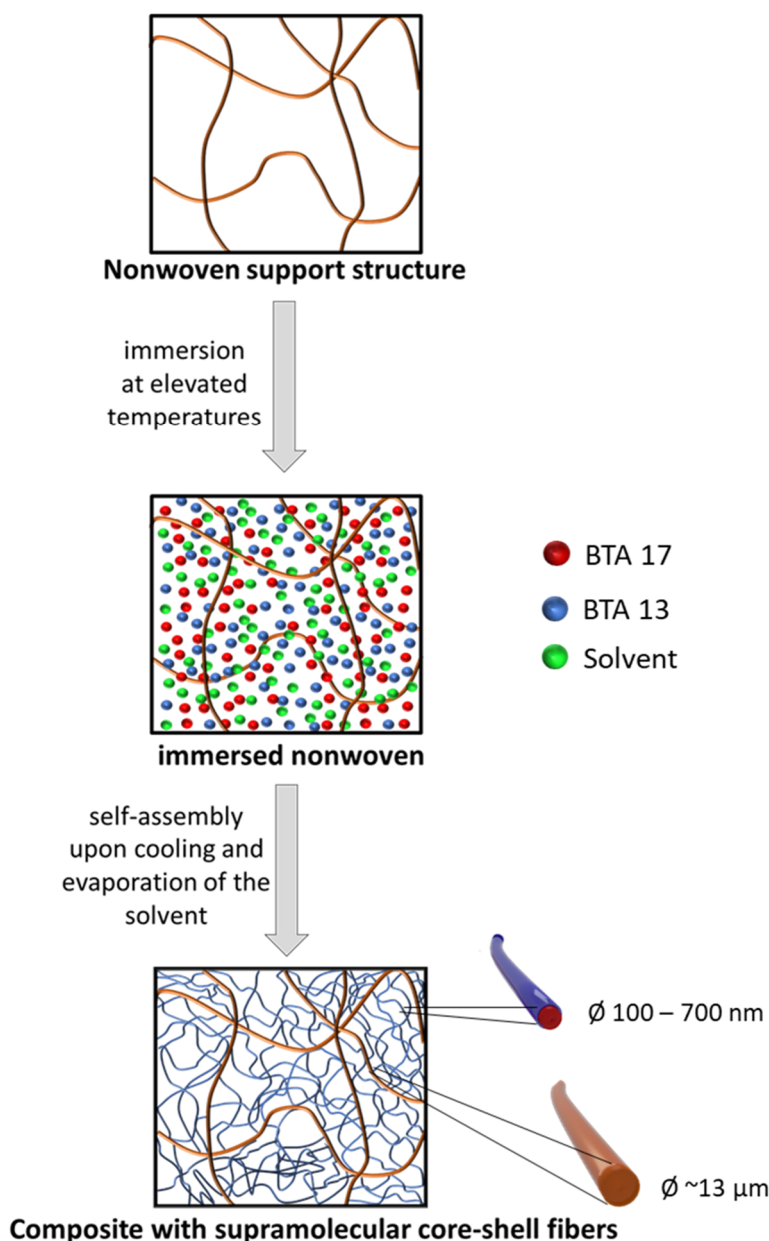


Figure 4.23: Schematic representation of the preparation of supramolecular fiber-microfiber composites. First, the nonwoven is dipped into a BTA-solution at elevated temperatures. The fabric soaked with BTA solution is dried at room temperature lying horizontally (brown lines: fibers of the fabric; red dots: aliphatic 1,3,5-benzenetrisamide molecules; blue dots: sulfur containing 1,3,5-benzenetrisamide molecules; green dots: solvent molecules). By cooling and evaporation of the solvent, the self-assembly process is initiated and supramolecular nanofibers are formed in the carrier fabric (blue lines: supramolecular core-shell fibers).

The basic preparation process to produce such nanofiber-microfiber composites, involves the immersions of the nonwoven in a BTA-solution at elevated temperatures for several seconds. This is done to ensure that the scaffold is completely impregnated with BTA-solution. The prepared nonwoven was then air-dried in a horizontal position to ensure a homogeneous self-assembly within the scaffold. At this stage, the solution cools down and at the same time the solvent start to evaporate. Thus, the self-assembly process is initiated and supramolecular fibers were formed inside the fabric.

By using two BTA building blocks and a certain solvent system, co-assembled core-shell fibers can be formed. After the complete drying, the prepared composite can be used for different experiments.

Filter material preparation

From the experimental point of view, a needle felt consisting of PET fibers was used as nonwoven support structure. Subsequently, the BTA-fibers using BTA 13 und BT 17 were assembled from 1-propanol : water (3 : 2(w/w)) mixture. In this context, the PET scaffold material was found to be beneficial, because of its proper polarity allowing for a full wetting behavior with the solvent mixture. Moreover, the PET ester groups might interact with the supramolecular building blocks and thus can act as nuclei. The solvent system 1-propanol : water (3 : 2(w/w)) was chosen because it is known that the functional BTA 13 assembles into supramolecular fibers from this solvent system (see chapter 3.3.3). Moreover, as shown before this solvent system is suitable to achieve core-shell fibers by co-assembly processes (chapter 4.2.2). These supramolecular structures provide functionality in the shell for the adsorption experiments of the metal ions. The ratio of the both BTA 13 and 17 was chosen at the DWI, as a result from different previously performed screening experiments and was selected to be 0.1 wt.-% for BTA 17 and 0.9 wt.-% for BTA 13. Also, an experiment with a mixing ratio of both BTAs with 1 to 1 (w/w) was performed.

In **Figure 4.24**, a photographic image of the composite and corresponding SEM images of the functional-supramolecular-fiber-microfiber-composite are shown. This composite was prepared from 0.9 wt.-% BTA 13 and 0.1 wt.-% BTA 17 from 1-propanol : water (3:2 w/w) at 50 °C. The immersion time of the nonwoven was 60 seconds. As it can be seen, a dense supramolecular fiber network was formed inside the scaffold. The fibers seem to be relatively homogeneous in shape. These composites were used for the following adsorption experiments.

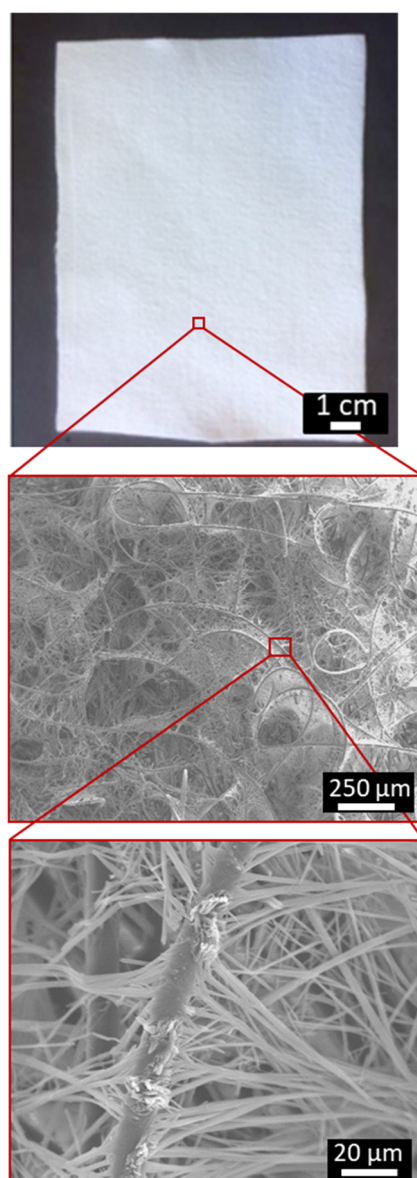


Figure 4.24: Photographic image of the prepared needle-felt PET nonwoven on the top and SEM images with different magnifications of the supramolecular functional-fiber-microfiber-composite below.

Filter device preparation

In general, a filter material is often not used as such, but adopted to fit the filter cartridge and cartridge geometry. For the adsorption experiments in a continuous flow process, two considerations with respect to the filter cartridge and the stream flow lines were made: i) In an easy to prepare setup configuration, the nonwoven sheet comprising the composite filter material with a size of 100 x 150 mm was simply rolled up and put into the filter cartridge with a height of 100 mm and a diameter of 20 mm or ii) defined round pieces of the nonwoven sheet comprising the composite filter material was punched fitting the diameter of 47 mm of the 3D-printed cartridge. By this, 15 layers were put on each other to achieve the filter device. Particular, the latter setup provides the opportunity to guide the flow of a liquid through the filter medium in a more appropriate manner due to the more compact design.

Figure 4.25 shows schematically the two applications of the composite used in this thesis for the adsorption of metal ions.

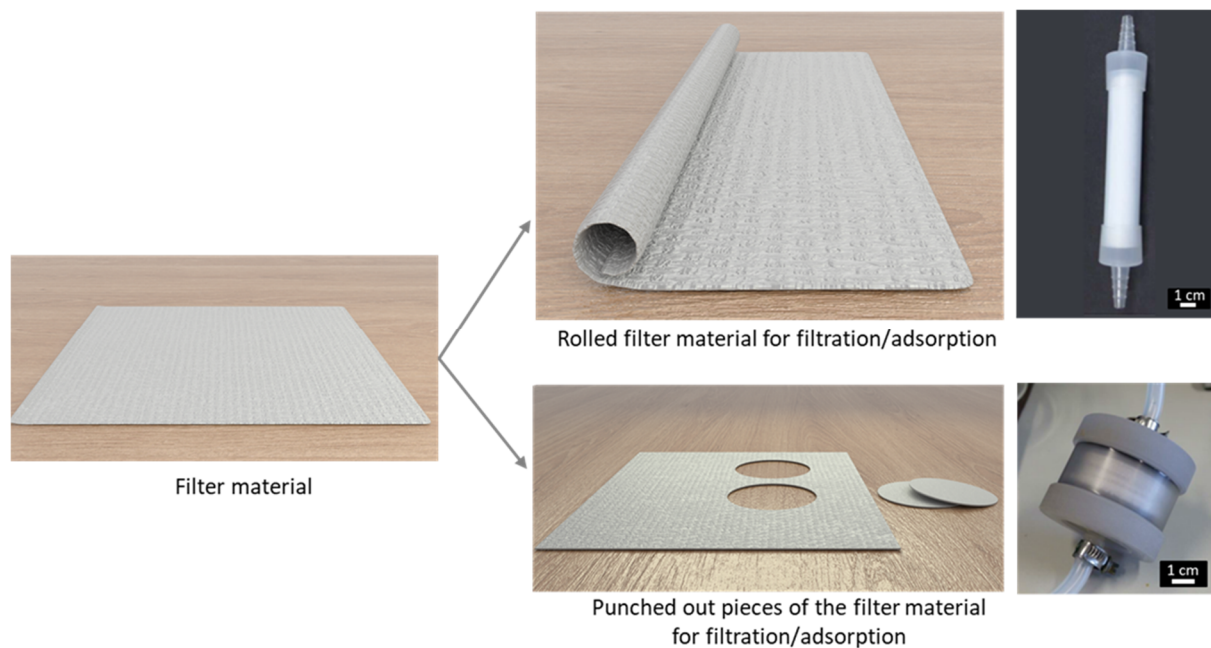


Figure 4.25: Schematic representation of the further processing methods of the composite for the filtration/adsorption of metal ions. On the one hand the composite can be rolled and used in this rolled form on the other hand, pieces of the composite can be punched out and stacked for further use.

4.3.2 Adsorption of metal ions on the composite

For the adsorption experiments of different metal ions were selected such as gold, silver, platinum and mercury. For the majority of the experiments, mainly gold ions were used, because of the straightforward use to the HAuCl_4 solution and the detection of the metal ions or the reduced AuNP. In a first set of experiments a filter holder with rolled up filter material in the geometry as described above was used and evaluated. In **Figure 4.26**, the used composite in the respective filter holder and the used filtration set-up are shown as photograph.

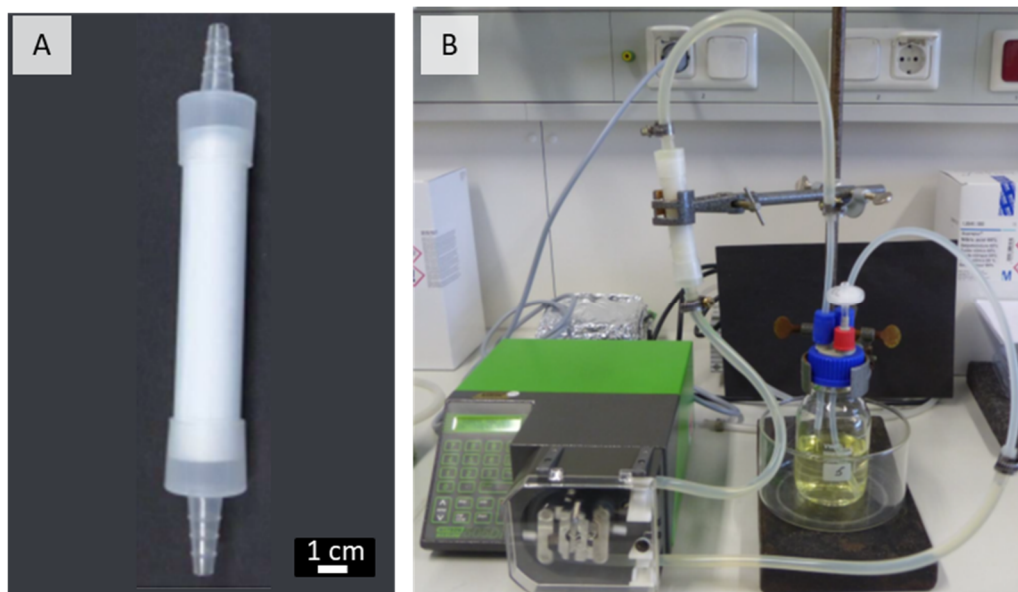


Figure 4.26: **A:** Cartridge equipped with the rolled composite based on supramolecular nanofibers of BTA 17 and BTA 13 (1 : 9 w/w) and the needle felt (PET) with a size of 100 x 150 mm and a medium capacity height of 100 mm. **B:** Photograph of the filtration set-up. A peristaltic pump with a flow rate of 200 mL/min was used to circulate the metal ion solution through the filter unit. For the adsorption experiments, 200 mL of the metal ion solution were placed in the reservoir.

Here the setup for the filtration experiments comprises a peristaltic pump, filter unit and a reservoir with metal ion solution. The peristaltic pump was used to circulate the metal ion solution with a flow rate of 200 mL/min through the filter unit. Inside the reservoir, 200 mL of the solution were placed. Typically, the tests were performed over a period of 24 h. Within this period, solutions were taken after defined time intervals (0.5 h, 1 h, 1.5 h, 2 h, 3 h, 4 h, 5 h, 6 h, 7 h, 8 h and 24 h) and investigated to determine the metal content. The content of metal ions was investigated with the help of an ICP-AES device.

To determine the adsorption behavior of Au^{3+} ions, HAuCl_4 solutions in water at a pH-value of 7 were investigated. The concentration was set to be approximately 20 mg of gold per 1 g of the used textile-composite. In **Figure 4.27**, the graphs of the gold ion adsorption of two individual experiments with similar conditions are shown. For one experiment, 21.3 g of the composite at an Au^{3+} concentration of 457 mg/L were used (red curve in **Figure 4.27**) and for the other one, 42.8 g of the composite at an

Au^{3+} concentration of 859 mg/L (black curve in **Figure 4.27**) were used. The individual measuring points are shown as symbols and the solid lines act as guide to the eye.

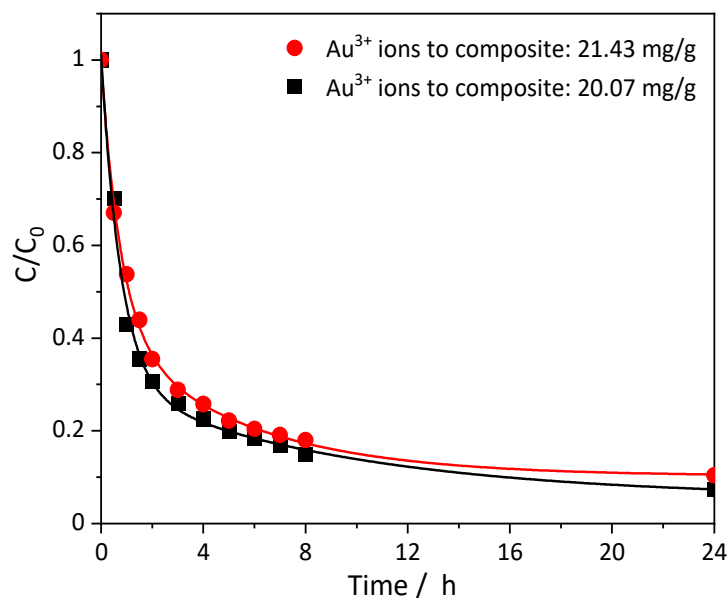


Figure 4.27: Absorptivity of Au^{3+} ions on two individual composites within a period of 24 h demonstrating reproducibility. The aqueous Au^{3+} ion concentrations were selected to match a concentration of approximately 20 mg Au to 1 g composite (red: 21.43 mg/g; black: 20.07 mg/g). Solid lines represent a guide to the eye. The composites were prepared by immersing a needle felt (PET) in a solution of 1-propanol : water (3:2 (w/w)) with BTA 17 and BTA 13 (1 : 9 w/w) for 60 seconds.

The solid lines represent a guide to the eye and found for both experiments to be very close to each other. The data points of the red graph are slightly higher than those of the black graph. This can be explained by the fact that for the first experiment with 21.43 mg of Au^{3+} per 1 g of the textile-composite, a higher gold concentration was applied. For the black curve, the concentration was 20.07 mg/g (gold/composite). Thus, for the latter experiment more functional supramolecular fibers were available during the adsorption experiment with respect to the initial gold concentration. Nevertheless, the similarity of the results suggests that of both experiments feature a high reproducibility and more important the composites are capable of absorbing a high amount of gold. Thus, the adsorption capacity was investigated dependent on the used amount of BTA fiber-microfiber composite. Therefore, a gold ion solution with a concentration of 860 mg/L was used. To study a difference in the capacity capability, composites with a weight of 19.6 g and 42.8 g, respectively, were used differing by a factor of 2. The resulting absorptivity are shown in **Figure 4.28**.

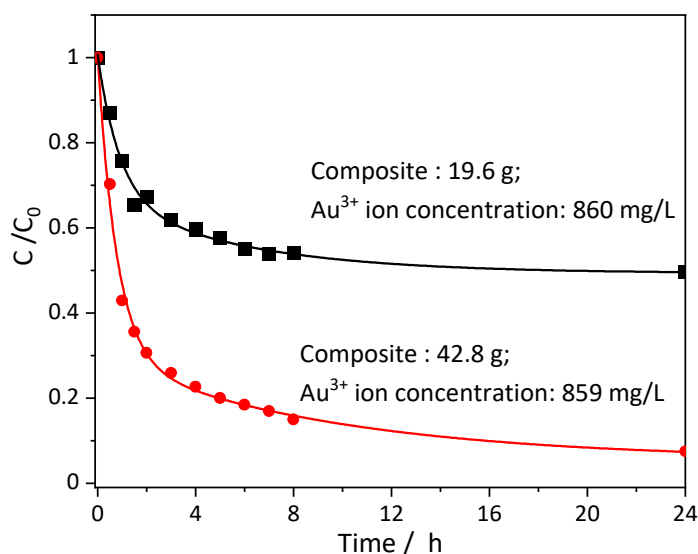


Figure 4.28: Absorptivity of Au^{3+} ions on two individual composites within a period of 24 h demonstrating the dependence of the amount of composite on the adsorption. The Au^{3+} ion concentrations were approximately 860 mg/L in water. The weight of the composites was 19.6 g (black) and 42.8 g (red), respectively. Solid lines represent a guide to the eye. The composites were prepared by immersing a needle felt (PET) in a solution of 1-propanol : water (3:2 (w/w)) with BTA 17 and BTA 13 (1: 9 (w/w)) for 60 seconds.

The red data points representing the experiment with the amount of 19.6 g of composite. It shows after an adsorption time of 24 h, that the composite adsorbed about 50 % of the initial amount of gold. Here, the adsorptivity of the composite, might be reached after 8 h. In contrast, the adsorption velocity and the adsorption efficiency of the experiment with double amount of the composite, i.e., 42.8 g of the composite were much higher. Here, about 92 % of the initial gold ions were adsorbed. Full capacity might be reached after 24 h. These experiments showed that the used amount of composite has a huge influence on the adsorption velocity and the efficiency of the adsorption of the metal ions.

In another series of experiments, a composite was used multiple times to adsorb gold ions from a solution. Here, the Au^{3+} ion concentrations were selected to match a concentration of approximately 5.1 mg of Au to 1 g of the composite for each cycle. For every cycle, the solution was circulated for 120 min. The circulation flow rate was set to 200 mL/min.

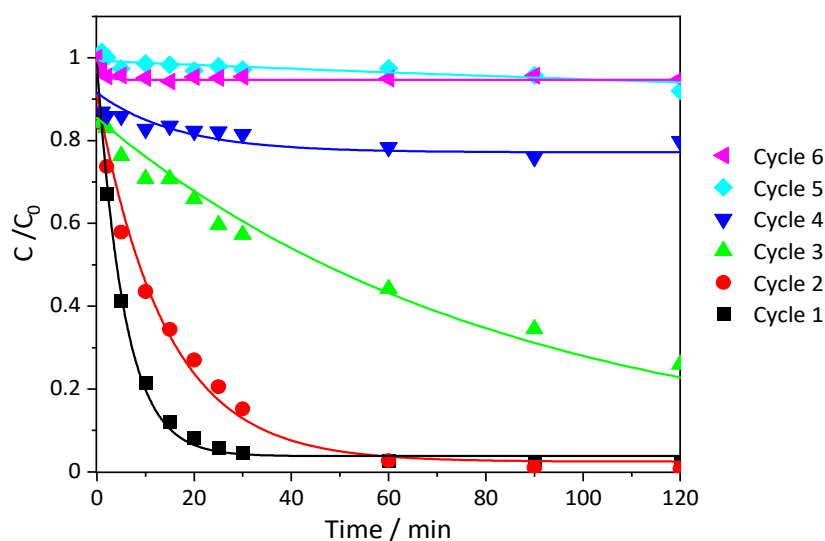


Figure 4.29: Absorptivity of Au^{3+} ions on a single composite within a period of 120 minutes. Each cycle represents an absorptivity measurement with a fresh Au^{3+} ion solution using the same composite demonstrating its adsorption capacity. The Au^{3+} ion concentrations were selected to match a concentration of approximately 5.1 mg Au^{3+} to 1 g composite. Solid lines represent a guide to the eye. The composites were prepared by immersing a needle felt (PET) in a solution of 1-propanol : water (3 : 2 (w/w)) with BTA 17 and BTA 13 (1 : 9 (w/w)) for 60 seconds.

The graphs in **Figure 4.29** show the time-dependent absorptivity of each cycle. In the first two cycles, the whole amount of the gold was adsorbed from the solution. However, the adsorption velocity for the second cycle (red graph) was already slower than for the first one (black graph). Within the investigated time period, not all gold ions could be adsorbed in the third cycle (green graph) because a closer look reveals that a plateau has not yet reached. In the fourth cycle (dark blue graph) only 21 % of the gold ions were adsorbed. In the fifth (light blue graph) and sixth (magenta graph) cycle only 8 % and 5 % of the gold ions were immobilized in a period of 2 h, respectively. Demonstrating that the maximum load capacity of the used composite was reached.

These experiments showed that one composite could be used multiple times for the immobilization of metal ions from an aqueous solution. In total, 15.8 mg of gold can be adsorbed per gram of textile composite material revealing a quantitative number of the loading capacity of these composites which can be calculated to be 1.6 % of the whole used filter material. The loading capacity of the functional supramolecular nanofibers should be much higher due to the low nanofiber content in the composite filter material.

To investigate the influence of the BTA 13 content in the co-assembled fibers in more detail on the adsorption performance, experiments were performed comprising composites which were prepared from a solution with a BTA mixture of BTA 17 and BTA 13 in a weight ratio of 1 to 1. Thus, the amount of the BTA 13 was reduced significantly. Which allows for a comparison with a previously performed experiment featuring composites with a weight ratio of BTA 17 and BTA 13 of 1 to 9. The Au^{3+}

concentration for the composite prepared from the BTA mixture with the 1 to 1 ratio was 463 mg/L and for the composite prepared with a BTA ratio of 9 to 1, the gold concentration was 457 mg/L. The resulting graphs and solid lines as guide to the eye are shown in **Figure 4.30**. The black curve corresponds to the experiment with the BTA fibers with a 1 to 1 ratio. The red curve corresponds to the experiments with the previously used composite with a higher content of sulfur-containing BTA 13. It can be clearly seen that the adsorption velocity and the adsorption performance of the sample prepared from BTA 13 and BTA 17 (1 : 1(w/w)) were much lower than those of the sample with a higher ratio of BTA 13 and BTA 17 (9 : 1(w/w)). The composite prepared with BTAs in an equal weight ratio reduced the gold content in the solution by 61 %. The composite with the BTA-fibers with a mixing ratio of 9 to 1 (BTA 13 to BTA 17) adsorbed about 90 % of the gold ions in the same time. At the first glance these experiments show that the used content of functional BTA for the formation of supramolecular fibers inside the nonwoven has a great influence on the resulting adsorption performance of the prepared composites. However, the content of BTA 13 was reduced by an order of 9 and the adsorption capacity was only reduced by 30 %. Also, the adsorption capacity of the composites is reached after 8 h in both experiments. This gives an indication that similar nanofibers, probably core-shell fibers, were formed in both cases. Furthermore, it seems that the adsorption capacity of the composites does not depend linearly on the amount of BTA 13 used.

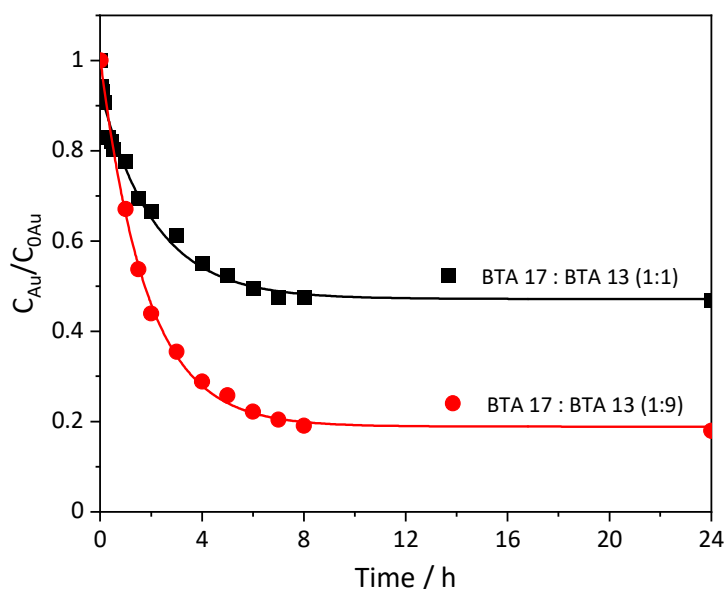


Figure 4.30: Absorptivity of Au^{3+} ions on two individual composites with different composition of supramolecular building blocks within a period of 24 h demonstrating the influence of the BTA 13 content. The Au^{3+} ion concentrations were selected to match a concentration of approximately 21 mg Au to 1 g composite. Solid lines represent a guide to the eye. The composites with different composition of supramolecular building blocks were prepared with BTA 17 and BTA 13 in a weight ratio of 1:9 (red) and 1:1 (black) by immersing a needle felt (PET) in a solution of 1-propanol : water (3:2 (w/w)) for 60 seconds, respectively.

Besides the adsorption of gold ions, the adsorption of other precious or serious metal ions such as silver, platinum and mercury were investigated using the functional supramolecular fiber polymer fiber composites. Here, composites equipped with BTA fibers in a weight ratio of 1 to 9 were used (BTA 17 to BTA 13). All metal ion solutions had the same molar concentration. All adsorption conditions were the same as used in the previous experiments. The individual metal-containing solutions were circulated with a flow rate of 200 mL/min for 24 h. In **Figure 4.31**, the resulting absorptivity of the first 500 minutes are shown, because a further change in the metal absorption after that time was not detected.

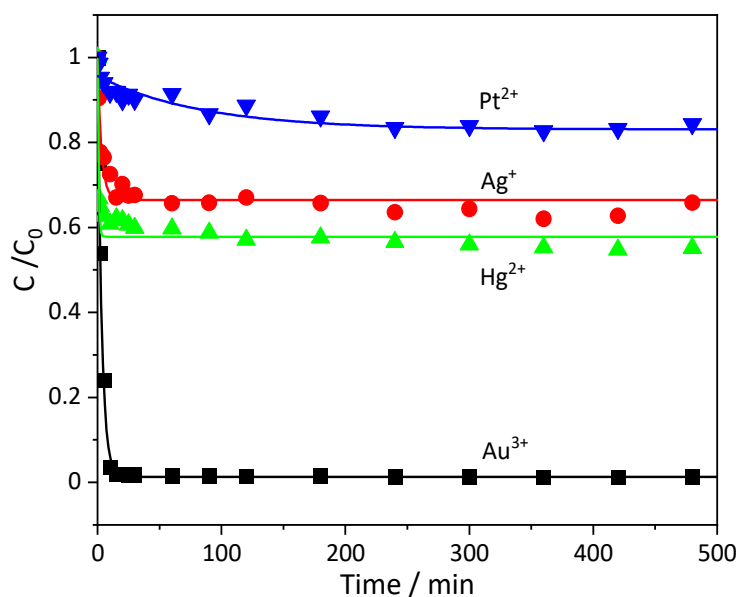


Figure 4.31: Absorptivity of different metal ions such as Au³⁺ (black curve), Ag⁺ (red curve), Hg²⁺ (green curve) and Pt²⁺ (blue curve), with individual composites demonstrating the adsorption selectivity with respect to different metal ions (for clarity shown within a period of 500 min, experiment was performed over a period of 24 h). Solid lines represent a guide to the eye. The individual metal ion concentrations were selected to match a concentration of approximately 0.11 mol Au³⁺ to 1 g composite for an equimolar ratio. The composites were prepared by immersing a needle felt (PET) in a solution of 1-propanol : water (3:2 (w/w)) with BTA 17 and BTA 13 (1 : 9 w/w) for 60 seconds.

As it can be clearly seen in **Figure 4.31**, the gold ions were adsorbed with a very high efficiency. Here, the metal concentration in the solution decreased very quickly and almost all gold ions were adsorbed by the functional supramolecular fiber composites. Moreover, the functional fibers adsorbed the mercury ions with a reasonable efficiency but lower capacity. Here, about 56 % of the metal ions were adsorbed from the functional 1,3,5-benzotrisamide fibers during the time of the experiment being significantly lower than the maximal absorptivity of gold ions. The graph of the adsorption of silver ions looks similar to the graph of mercury but here also less ions were adsorbed with the sulfur groups of BTA 13. The adsorption efficiency was about 30 %. The absorptivity with respect to the platinum ions

were very low. Only 20% of the metal ions from the solution were immobilized at its best on the functional BTA fibers and the time to deposit the metal is significantly elongated. In **Table 4.2**, the results of the absorption experiments are shown summarized.

Table 4.2: Comparison of the absorption efficiency of different metal ions on the composite filter media after 24 h.

	Au³⁺	Hg²⁺	Ag⁺	Pt²⁺
Amount of filter media [g/L]	21.0	21.2	20.6	21.1
Initial metal concentration [mg/L]	105	121	60	114
Adsorbed metal concentration on composite[mg/L]	104	68	18	23
Efficiency (24 h) [%]	99	56	30	20

These results demonstrate that the adsorption capacity is highly selective depending on the metal ions to be adsorbed. Obviously, the metal ions are adsorbed by the functional BTA fibers in the following sequence under the given experimental conditions: Au³⁺ >> Hg²⁺ > Ag⁺ > Pt²⁺. Probably, the adsorption efficiency may be varied to some extent by changing the conditions of the experiment. For instance, the pH-value or the temperature may have an influence on the adsorption capability of the metal ions. The promising efficiency demonstrated by these experiments also suggests that, for real life applications, the filter holder may be improved to increase and improve the adsorption efficiency. Furthermore, the adsorption time to immobilize the metal ions in solution could be increased. Also, another approach may include the use BTAs with other functionalities in their periphery.

To account for some of these issues, the filtration set up was optimized to further increase the adsorption efficiency. For this, a 3D-printed filter holder was created in which 15 round pieces with a diameter of 47 mm of the composite were placed in a stacked geometry improving the flow through the filter medium and accessible filtration area.^[180] A photograph of the new filter holder equipped with the composites is shown in **Figure 4.32 A** and modified filtration set up is shown in **B**.

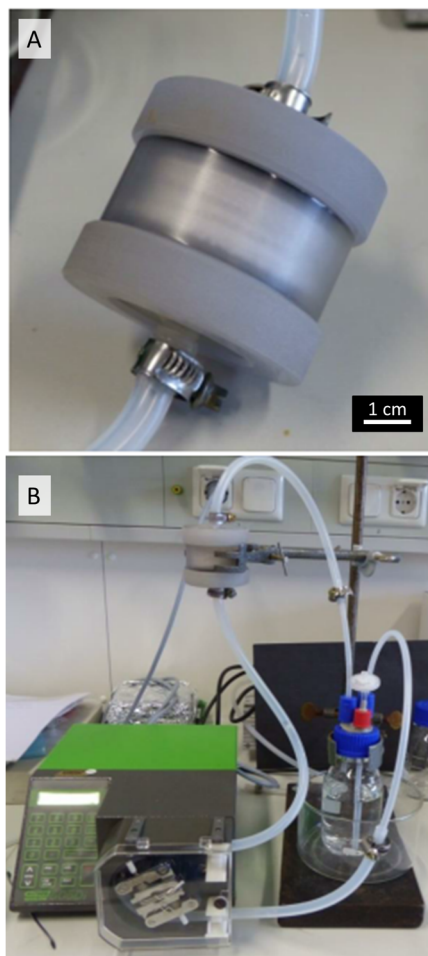


Figure 4.32: **A:** Photograph of the 3D-printed filter holder with an inner diameter of 47 mm, equipped with 15 round punched and horizontally stacked sheets of composites. **B:** Photograph of the filtration set-up. A peristaltic pump with a flow rate of 200 mL/min was used to circulate the metal ion solution through the filter unit. For the filtration experiments, 200 mL of the metal ion solution were placed in the reservoir.

With this 3D printed filter holder an experiment was performed to compare the adsorption efficiency of the modified set-up with the older one. To validate the improvement, experiments with the different filter holder designs were performed. In the case of the new filter holder design, a gold ion solution with a concentration of 877 mg/L was used similar as described before. The amount of the composite related to the investigated volume of Au^{3+} ion solution was 41.9 g/L. As reference, the former filter holder design was used with the same composition of the composite. For the experiment, an Au-concentration of 859 mg/L and a textile amount related to the volume of Au^{3+} ion solution of 42.8 g/L were used. Both adsorption experiments were performed over 24 h and the metal solution was pumped with a flow rate of 200 mL/min. The resulting graphs are shown in **Figure 4.33**. It shows that the adsorption velocity with the new design is much faster compared to the former design. After about 100 minutes nearly all of the gold ions were adsorbed with the new design and an adsorption efficiency of 99.9 % was reached. In case of the experiment with the old filter holder it was not possible to adsorb all of the metal ions during the investigated time interval, resulting in an efficiency of 92.6 %

of the initial gold. This experiment shows the significant influence of the experimental set up. Demonstrating that still a significant improvement can be found.

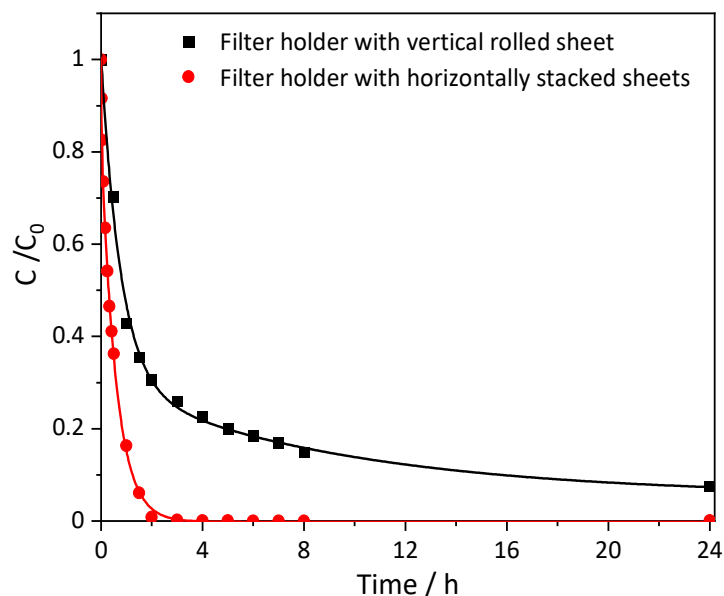


Figure 4.33: Absorptivity of Au^{3+} ions within a period of 24 h using two different filter holders demonstrating the influence of the filter geometry and the composite orientation. Black: Cartridge with a vertically rolled sheet of composite. Red: 3D-printed filter holder equipped with 15 round punched and horizontally stacked sheets of composites. Both Au^{3+} ion concentrations were selected to match a concentration of approximately 21 mg Au to 1 g composite. Solid lines represent a guide to the eye. The composites were prepared by immersing a needle felt (PET) in a solution of 1-propanol : water (3:2 (w/w)) with BTA 17 and BTA 13 (1 : 9 (w/w)) for 60 seconds.

4.4 Conclusion

This chapter described within two main sections the investigation and characterization of the multicomponent-assembly process of two BTA molecules from different solvent systems (1-propanol; 1-propanol : water (3 : 2(w/w)) and 2-butanone). Furthermore, the application of these multicomponent-assembled structures to immobilize metal ions from an aqueous solution was shown. In the first part, the self-assembly behavior of the mixtures of two chemically different BTAs was investigated by means of DSC, FTIR-spectroscopy, SEM, EDX-spectroscopy and Raman-imaging-spectroscopy. In particular, it could be shown that the multicomponent-self-assembly behavior strongly depends on the used solvent system. For instance, using 1-propanol as solvent for the co-assembly process, the used supramolecular building blocks assembled in a self-sorted manner. This means that the aliphatic BTA 17, self-assembles individually into long fibers and the sulfur-containing BTA 13 into small fiber-like structures. In contrary to that, using the alcoholic water mixture 1-propanol : water (3 : 2(w/w)), core-shell fibers with a functional sulfur-containing shell and an aliphatic core were formed. All data suggest that both compounds are present in self-assembled structures. Thus, in this situation, one can assume that BTA 17 acts as an epitaxial surface for the self-assembly of the BTA 13. In a similar manner, this BTA-mixture formed uniform supramolecular core-shell fibers from 2-butanone. The core of these structures consists of the aliphatic BTA 17 and the shell of the sulfur containing BTA 13. Thus, by using 2-butanone or 1-propanol : water (3 : 2(w/w)), novel co-assembled core-shell structures could be formed. The so formed fibers have their functional groups on the fiber surface and therefore could be used for different applications.

In the second part, the previously gained knowledge was used to produce BTA-fiber-microfiber-composites to immobilize metal ions from aqueous solutions.

It could be shown that the produced composites have a high adsorption efficiency and capacity of gold (III) ions. It was possible to adsorb 99.9 % of the immersed gold ions in a period of 24 h. Also, experiments were performed with a changed ratio of the two used 1,3,5-benzentrisamides. The quantity of sulfur-containing BTA shows an influence on the adsorption behavior of the prepared composites. With a higher sulfur content, the adsorption efficiency was increased. However, the adsorption capacity is not linearly dependent on the amount of BTA 13. At least, other metal ions were adsorbed on the functional BTA fibers and their adsorption properties were investigated. It could be shown that the tendency to absorb metal ions significantly decreases from Au^{3+} , Hg^{2+} , Ag^+ to Pt^{2+} demonstrating the high selectivity of the system.

5 Sand–supramolecular nanofiber composites for the filtration of bacteria from water

5.1 Water treatment of polluted water

As described in many studies, such as the United Nations World Water Development Report, one of the main causes of waterborne infections is the use of impure, bacterially contaminated water for food preparation.^[1] One major goal of the United Nations Agenda report for sustainable development 2030 is “the access to safe and affordable clean drinking water for all”.^[16] Consequently, there are numerous different approaches to tackle these issues.^[5,9,17,19,181–184] Till date, one inexpensive and fast treatment of water is based on the use of reactive chemical compounds, which makes large quantities of water drinkable. A common technique is chlorination, e.g. by treatment with hypochlorite, to remove pathogenic germs from water. Another technique is the purification with ozone-based components. Only small amounts of the chemical reduce the number of microbes significantly. However, among environmental concerns in general, the disinfection of water with chloride or ozone leads to byproducts which can be cancerogenic for human beings.^[184,185]

In contrast to central large volume and low-cost water treatment solutions named before, specific decentral individual solutions, so-called point of use (POU) solutions are in use. An example for POU method for purification of water is the use of so-called “bio-sand” filters. These filter units are built up in a relatively simple and straightforward way. Often a housing of concrete is filled with a large amount of sand material. Over a period of around two weeks or more, a biofilm establishes inside the filter which is essential to reach the maximum filtration efficiency with respect to remove pathogens from water.^[18–20] Such bio-sand filters are utilized, for example in households as POU devices.^[184,186] Another example for commercially available POU water filters are systems from LifeStraw® or wateroam. Both systems utilize a membrane to remove pathogens from water with a high efficiency. The LifeStraw® is a hand-held device and works with hollow fiber membranes to remove contaminations from the water stream.

Considering water-related filtration issues in general, the different sizes of contaminations in water are shown in **Figure 5.1**. Additionally, the respective filtration technologies are shown to remove the contaminates with specific sizes. For example, bacteria cells have approximately a size between 10^{-7} and 10^{-5} meters, in other words ranging from a few hundred nanometers to a few micrometer.^[187] For the removal of larger bacterial cells, depth filtration is a suitable tool to remove smaller-sized bacteria microfiltration. Microfiltration removes particles with a size of $0.04\ \mu\text{m}$ to $1\ \mu\text{m}$ by using hollow fibers membranes for example.^[188] Consequently, a method that bridges both filtration techniques is desirable to remove all sizes of bacterial cells.

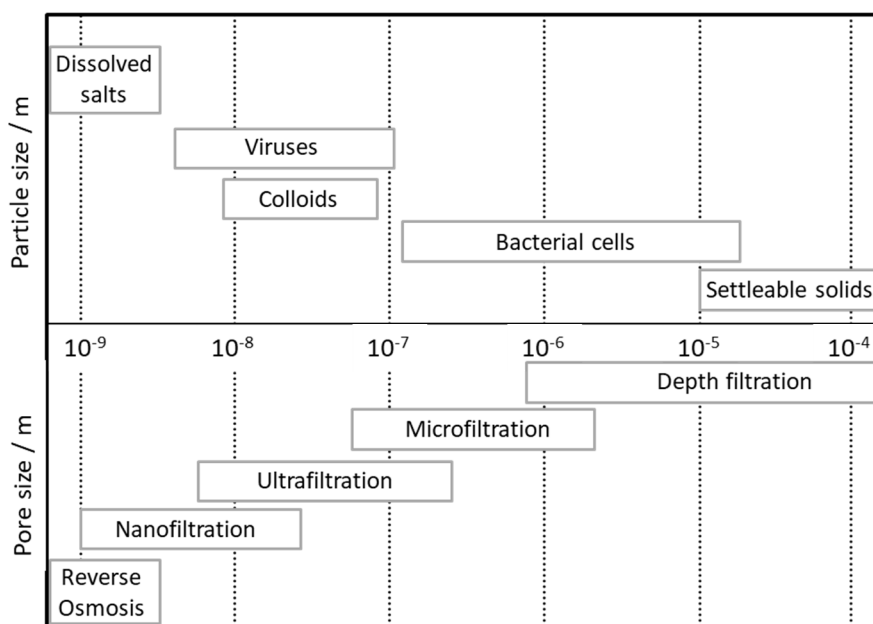


Figure 5.1: Size of water contaminations and pore size of filtration technologies. [adapted from [ref.^[187]]]

Nanomaterials as antibacterial components

In the search for filter devices with improved filtration efficiencies and high filtration volumes, research is dedicated to develop novel techniques including nanomaterial-based filtration systems. These nanomaterials include carbon nanotubes, fullerenes or different metal (oxide) nanoparticles such as TiO_2 , Al_2O_3 , Cu and Ag.^[189,190]

Especially silver nanoparticles (AgNPs) were investigated intensively due to their well-known antibacterial properties due to the release of Ag^+ -ions from the particles.^[191–195] Ag^+ -ions deteriorate the permeability of the bacterial cell membrane and can also damage the DNA of the bacteria. Additionally, they are known for the formation of reactive oxygen species which can also destroy the cell membrane. Furthermore, AgNPs may feature antiviral effects.^[190,196–198] Therefore, silver nanoparticles were also used in different studies as antifouling agents for membrane filtration applications.^[190] They prevent the formation of a film consisting of microorganisms which potentially decrease the function and performance of a membrane filter.^[196] The studies showed that the membranes equipped with silver disinfect water flows contaminated with 10^6 colony forming units (CFU)/mL of *E. coli* bacteria. In other studies, polyurethane foams or silica gels were equipped with silver nanoparticles. These foams or gels were used as filter medium for contaminated water and could also reduce the number of CFU to zero.^[199–201] In all these techniques, the nanoparticles have to be immobilized because the consequences of accumulation of silver nanoparticles in nature is not fully investigated.^[199–201] However, there are some studies which showed a disadvantageous effect of silver nanoparticles in sewage treatment plants as useful bacteria can be killed.^[202]

Conceptual approach based on supramolecular nanofibers and sea sand composites

In previous work by Daniel Weiß of our research group, the concept of supramolecular nanofiber sea sand composites was developed to create a high efficient sand filter device.^[37] These filter elements should combine depth and micro-filtration due to the *in situ* incorporation of nanofibers. The formed supramolecular fibers built a network between the individual sand grains and between the grains and the wall of the cartridge. In **Figure 5.2** such a prepared filter is shown schematically in comparison with a filter without supramolecular nanofibers. Conceptually, the nanofiber networks between the sand grains create a much denser filter than a filter with a pure sand fill as the filtering element. Also note, the filtration efficiency of the neat sand filter relies on an established biofilm.

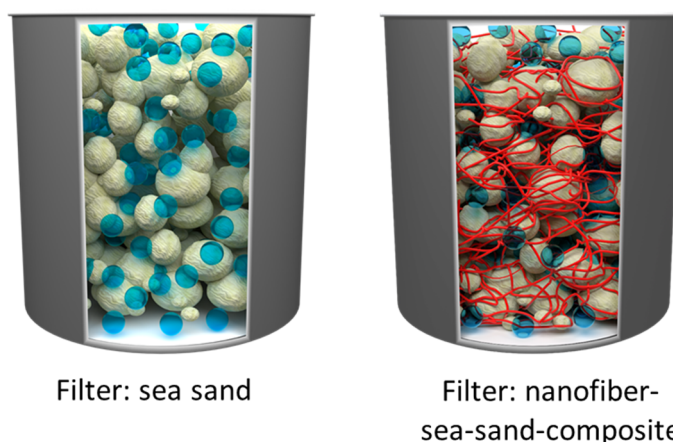


Figure 5.2: Schematic representation of the filter element with neat sea sand as filtration media (left side) and the *in-situ* prepared filter element with a supramolecular nanofiber-sea-sand-composite (right side). Light spheres represent water and red lines represent the supramolecular nanofibers.

Such nanofiber-sea sand filter elements as shown in **Figure 5.2** (right) were used in previous work at the chair of the Macromolecular Chemistries 1 to filtrate *E.coli* bacteria from a water flow with a high efficiency. But inside of these filters, a bacteria population could remain and grow after the filtration process due to the fact that there is no antifouling agent.^[37]

The aim of this chapter is the development of a novel water filter unit with antibacterial and antifouling properties based on the preparation conditions of the work of Daniel Weiß. Therefore, granular fillings consisting of sea sand will be equipped with functional supramolecular nanofibers. With the help of these functional supramolecular nanofibers, silver nanoparticles with their antibacterial properties will be immobilized on the fiber surface. The schematic preparation of such filter elements is shown in **Figure 5.3**.

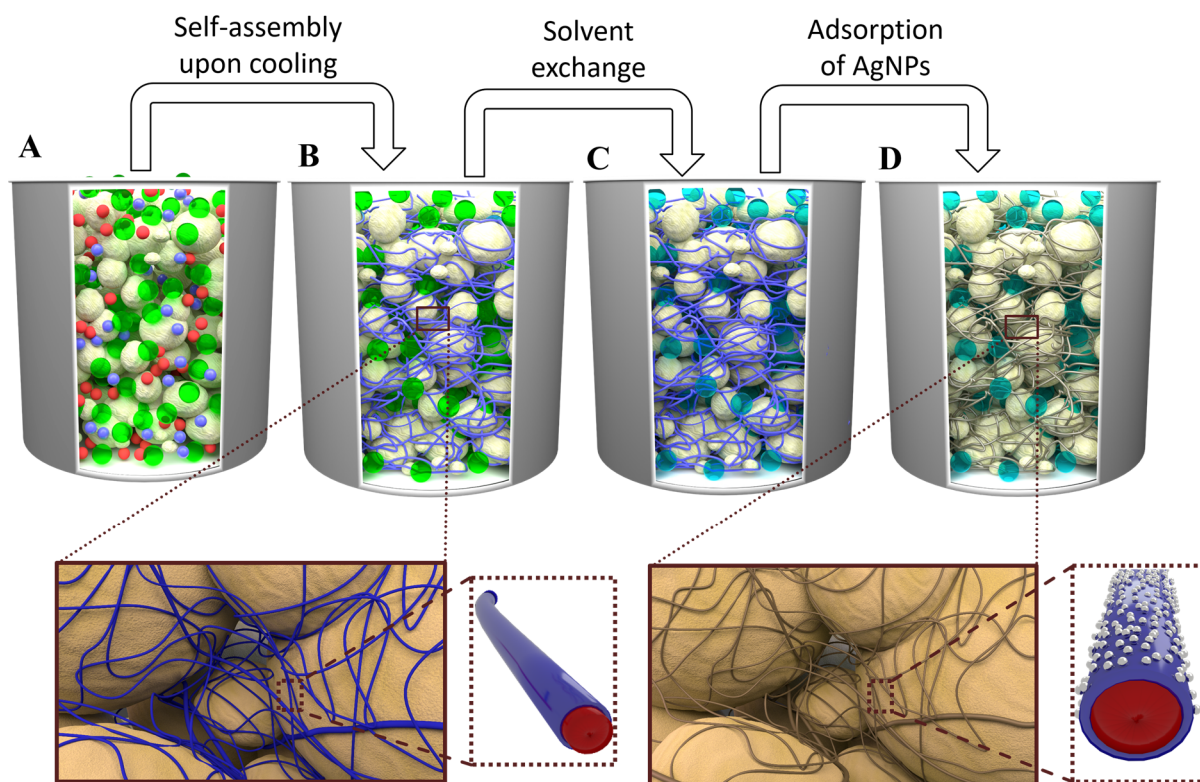


Figure 5.3: Schematic representation of the *in-situ* preparation process of co-assembled supramolecular filter-sea-sand-composites. **A:** A container filled with a defined amount of sea sand is immersed into a clear BTA-mixture solution at elevated temperatures until the sand is fully soaked (red spheres: aliphatic BTA; blue spheres: functional BTA; green spheres: solvent). **B:** The system is cooled down to induce the *in-situ* formation of supramolecular nanofibers within the voids of the granulate material. At first, the aliphatic BTA forms supramolecular fibers. Subsequently, the functional BTA starts to assemble on the fibers of the aliphatic BTA. Thus, core-shell fibers can be formed (blue lines: core-shell fibers). A schematic representation of such a core-shell fiber is shown on the bottom side of the sketch. **C:** The solvent is exchanged with a non-solvent like water (light transparent blue spheres: non-solvent). **D:** Silver nanoparticles (AgNP) can be adsorbed on the surface of functional supramolecular fibers. These AgNPs are immobilized on the surface of the fibers (bronze lines: fibers with AgNPs). A schematic representation of such a core-shell fiber with adsorbed AgNPs is shown on the right side of the sketch. The wet composite can be used for different filtration applications.

Consequently, the preparation of such a device differs also from the aforementioned approach as schematically depicted in **Figure 5.3 A**. Here, the sea sand is immersed in a clear BTA-solution at elevated temperatures where the BTAs are dissolved completely until the whole sand is soaked. Subsequently, the system is cooled down very quickly using a cooling bath. During the cooling process, the supramolecular building blocks are not soluble anymore and the self-assembly process takes place upon cooling. Thus, supramolecular fibers are formed *in-situ*. The formed BTA-fibers grow between the individual sand grains and form a supramolecular nanofiber network. In case of a co-assembly system, at first the BTA with the lower solubility self-assembles. Subsequently, the second BTA starts to self-assemble. The previously formed BTA fibers can act as nucleation points and thus, core-shell fibers can be formed (**Figure 5.3 B**). Because of the rapid cooling, it is assumed that many nuclei and thus many supramolecular fibers are formed.

In the next preparation step, the used solvent will be exchanged with the non-solvent water. During this process, the formed supramolecular fibers will not be damaged (**Figure 5.3 C**). The so prepared filter unit will be used in the wet state for different experiments. It is possible to equip the formed functional BTA fibers with silver nanoparticles to create a filter unit with antibacterial properties (**Figure 5.3 D**).

5.2 Supramolecular sea sand nanofiber composites for filtration

5.2.1 Components and preparation of sand-nanofiber composites as filter media

In the following, the preparation of composites for water filtration will be described in more detail. As cartridge, a chemically inert container consisting of isotactic polypropylene (iPP) was used as shown in **Figure 5.4 A**. The bottom of the container was perforated with a needle with a diameter of 0.9 mm. An example of such a perforated bottom is shown in **Figure 5.4 B**.

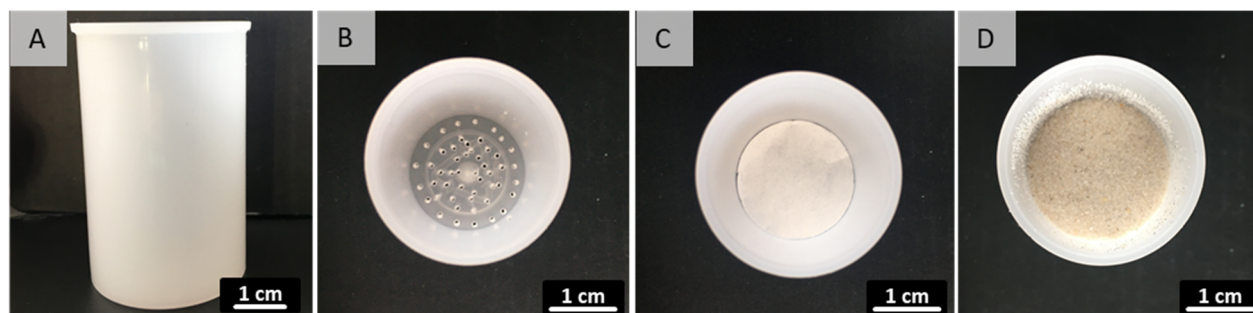


Figure 5.4: Photographic image of **A**: The used plastic container, **B**: The perforated bottom of the container, **C**: The filter paper on the bottom of the cartridge and **D**: The cartridge filled with 25 g sea sand.

Then, the bottom of the cartridge was covered with a previously punched cellulose filter paper (ROTILABO® Typ 601A) with an inner diameter of 30 mm (**Figure 5.4 C**). The filter paper has a retention range of 5 μm to 13 μm preventing the sea sand particles to pass the cartridge but has otherwise no significant effect on the filtration process. The so prepared cartridge was equipped with 25 g sea sand which resulted in a filling height of about 60 % (**Figure 5.4 D**). SEM images of the used sand grains, which have a diameter of about 0.3 mm are shown in **Figure 5.5**. As they have a relatively rough surface, the individual sand grains can interlock and increase the stability of the neat granular filling. Potentially such rough surfaces are beneficial for the formation of supramolecular nanofiber networks allowing the sand grains to remain in their initial position.

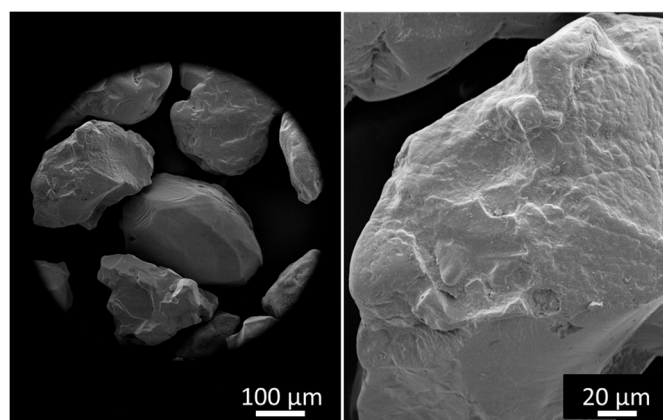


Figure 5.5: SEM images of the used sea sand. Left an overview image and right a detailed image.

For the preparation of the filter units, the functional sulfur-containing BTA 13 and the aliphatic BTA 17 were used (see **Figure 5.6**). BTA 17 is based on trimesic acid and peripheral aliphatic 2-ethylhexyl side

groups. The periphery of the second BTA, BTA 13, consists of a modified amino acid methionine. These BTAs carry different functional groups in the periphery. The supramolecular building blocks will be partly used individually and in combination to prepare sea sand-nanofiber composites.

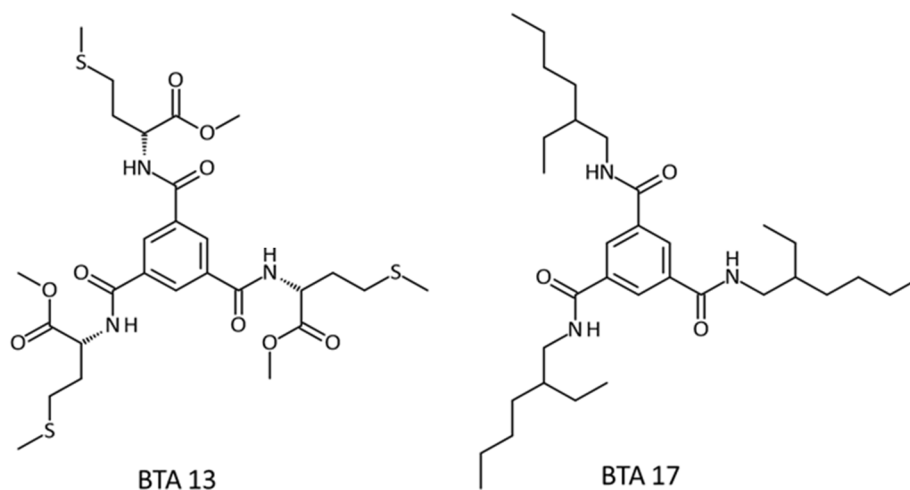


Figure 5.6: Chemical structure of the used BTAs. Left the L-methionine containing BTA 13 and right the aliphatic BTA 17 with 2-ethylhexyl side groups.

The concept of the functional supramolecular-fiber-sea-sand-composites preparation is shown before in **Figure 5.3**. The individual steps for the preparation of functional supramolecular-fiber-sea-sand-composites equipped with silver nanoparticles for antibacterial properties are shown schematically in **Figure 5.7**. A plastic container used as cartridge (see **Figure 5.4**) and filled with 25 g of sea sand is immersed in a clear fully dissolved BTA solution at elevated temperatures. For this purpose, the cartridge is immersed in the hot solution without allowing any parts of the BTA solution to flow into the filter cartridge from above. After the entire sand is soaked with the solution, the plastic container is placed in a suitable bag and stored in an isopropanol dry ice bath at $-79\text{ }^{\circ}\text{C}$ for 30 minutes. Meanwhile, supramolecular fibers are formed upon cooling of the system. These supramolecular fibers can form a dense nanofiber network between the sand grains and the wall of the cartridge. After removing the filter unit from the cooling bath, the solvent is exchanged with a non-solvent, such as water. In the case that functional supramolecular nanofibers have been formed, they can be equipped with antimicrobial silver nanoparticles in a subsequent step. Therefore, a silver nanoparticle suspension is flushed through the filter element and after a short period of time the elements are flushed with water to remove excess AgNP suspension. The filter elements prepared in this way can be used in the wet state for various filtration experiments.

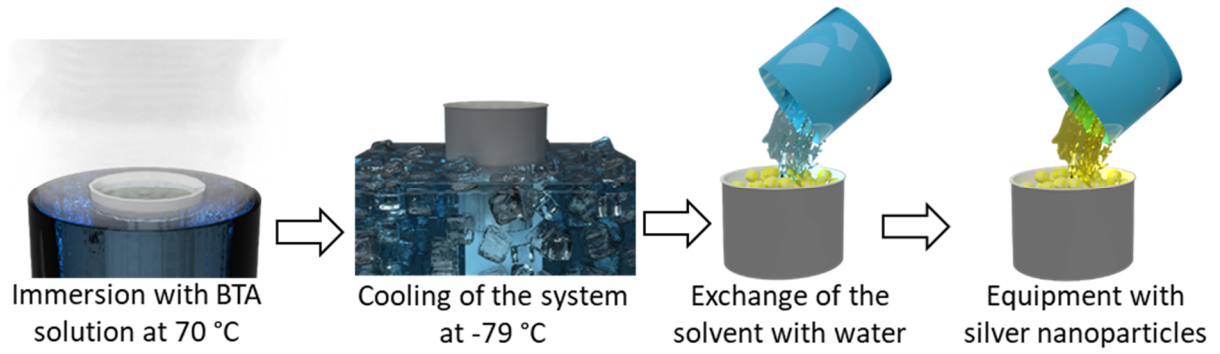


Figure 5.7: Schematic representation of the *in-situ* preparation process of co-assembled supramolecular filter-sand-composites. The cartridge is immersed in a BTA-solution at elevated temperature until the whole sand is soaked with the solution. Thereafter, the filter unit is cooled at -79 °C for 30 min. Subsequently, the solvent is exchanged with water and in the last step, the filter is flushed with a silver nanoparticle suspension. Preparation parameters: Solvent: 2 butanone, BTA concentration: 1.5 wt. %, immersion temperature: 70 °C, cooling temperature: -79 °C, cooling time: 30 min, non-solvent: water, total mass of granulate material: 25 g.

5.2.2 SEM-Characterization of the sea sand nanofiber composites

By various screening experiments it could be shown that such sea sand nanofiber composites could not be prepared with neat functional BTA 13 alone because it does not completely self-assemble from the selected solvent and was still in part dissolved at the applied conditions (see also solubility studies in chapter 3.3.2). Upon further adopting the self-assembly conditions, it did only form very thin supramolecular nanofiber as it was already demonstrated in chapter 4.2. However, such thin and short fibers are not applicable to achieve a mechanically stable and robust composite. Therefore, the composites were prepared by using mixtures of BTA 13 and BTA 17. Composites with neat BTA 17 were prepared as reference material in a similar way as described by Weiss.^[37] In a general procedure, the BTAs were dissolved in 2-butanone to yield a total BTA content of 1.5 wt.-%. The composites were prepared with a BTA solution at 70 °C which assures a complete solubility of the building blocks. The immersed samples were cooled down in an isopropanol dry ice bath (-79 °C) for 30 minutes. Subsequently, the solvent was exchanged with 200 mL of water. In case of co-assembled samples, a molar mixture of BTA 17 and BTA 13 with a ratio of 3 to 2 and 1 to 1 was used.

For SEM-characterization purpose, the composites were completely dried. Then, the cartridge was turned upside down and the granular filling with the supramolecular nanofibers was tapped out of the plastic housing. The optical appearance of the released granular material composites serves already as a first simple indication for the presence of mechanically robust nanofibers based on the extent of the shape persistence of granular matter of the cartridge (**Figure 5.8**). Subsequently, the composites were investigated by means of SEM. In order to investigate a representative sample to evaluate the formation of a supramolecular fiber network between the sand grains, a small part was taken from the middle of the composite.

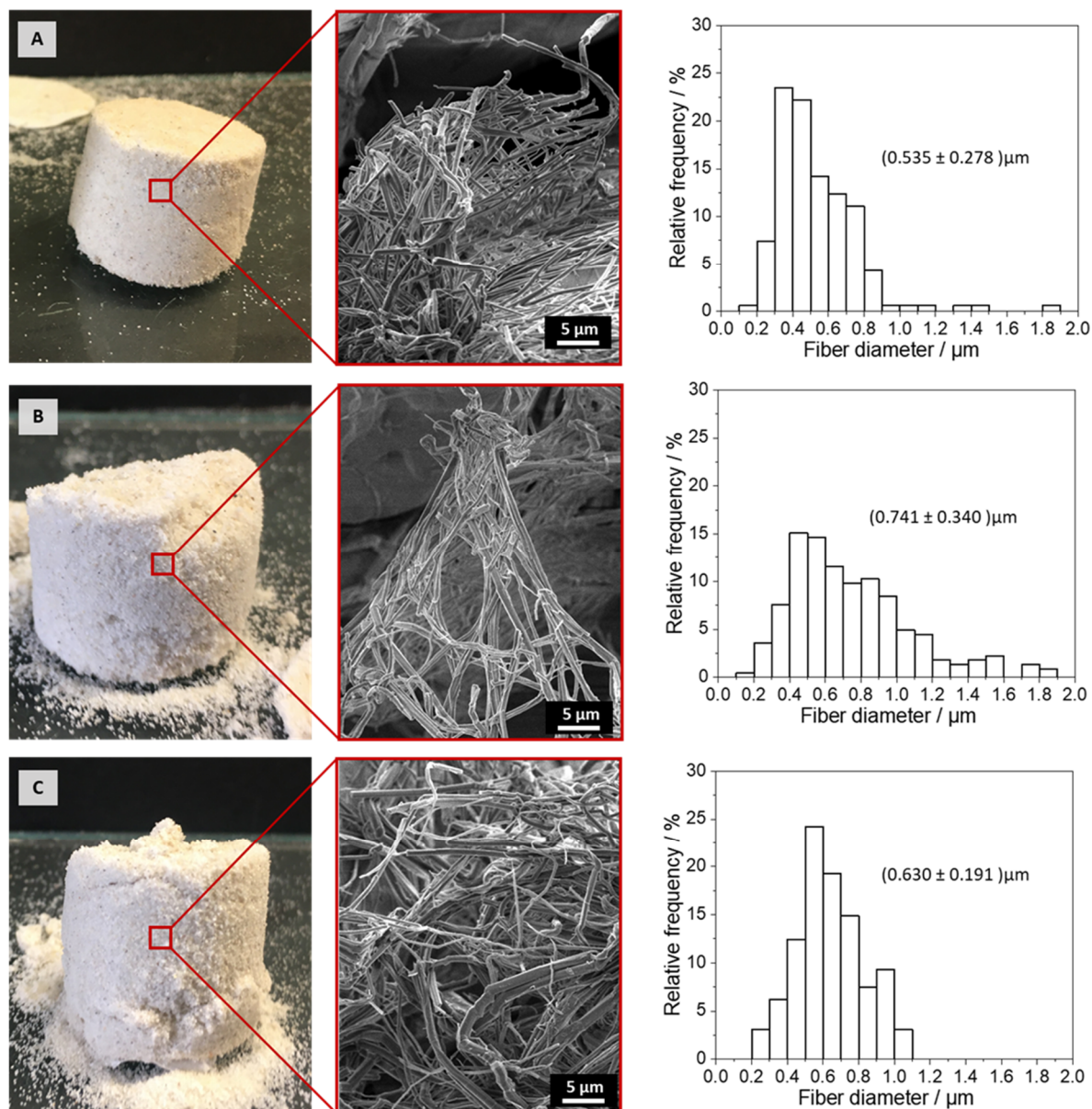


Figure 5.8: Photographic images of different composites after turning the cartridges upside down. In the middle, the corresponding SEM images of the fiber network inside the composites are shown. **A:** Composite prepared with BTA 17. **B:** Composite prepared with BTA 17 : BTA 13 in a molar ratio of 3 : 2. **C:** Composite prepared with BTA 17 : BTA 13 in a molar ratio of 1 : 1. On the right side the corresponding fiber diameter histogram are shown. For the histograms at least 150 individual fibers were counted. Solvent: 2-butanone; BTA-concentration: 1.5 wt.-%; Immersion temperature: 70 °C; Cooling temperature: -79 °C; Cooling time: 30 min; Non-solvent: water; Total mass of the sand: 25 g.

In detail, the photographic images on the left side of **Figure 5.8** show all sea sand BTA-fiber composites after they were turned upside down. In all cases, the sea sand-composites still keep their form. The network formed between the sand grains seem to stabilize the structure. The shape persistence seems to decrease with increasing amount of BTA13. All results can be regarded as an indication that a supramolecular fiber network must be formed during the self-assembly process.

In all investigated cases, the SEM images (**Figure 5.8**) show the formation of supramolecular networks between individual sand grains. It also seems that the BTA fibers are fixated on the surface of the sand grains and grow from there to another grain. In the first glance, the network and the BTA fibers in all samples look very similar.

A closer look at the fiber diameter histograms on the right side of the **Figure 5.8** reveals that the fiber diameter distribution of BTA 17 is rather broad but most fibers had a diameter in the range of 0.2 μm to 1.0 μm . Based on the histogram an average diameter of 535 nm was determined. The co-assembled fibers formed from BTA 17 and BTA 13 in a molar ratio of 3 to 2 show an average fiber diameter of 741 nm. Apart from the slightly increased average fiber diameter, the fiber diameter distribution is also comparable broad. Nevertheless, a dense supramolecular fiber network was formed. The sample prepared from BTA 17 and BTA 13 with a molar ratio of 1 to 1 had a mean fiber diameter of 630 nm. The distribution of the fiber diameter is relatively narrow.

To sum up, it could be seen that the samples with co-assembled fibers have a thicker mean fiber diameter than the sample prepared with the aliphatic BTA. This phenomenon may be attributed to the formation of core-shell fibers. Furthermore, the formed supramolecular nanofibers inside the granular fillings are homogeneous in shape. These fibers and fiber networks should be capable for filtration applications.

5.2.3 Investigation of the sea sand nanofiber composites stability at various water-flow conditions

Apart from the visual inspection and SEM investigation, a more representative stability test with respect to the nanofibers in the sea sand composites was performed with the help of a custom-made filter set-up (**Figure 5.9**) under continuous flow conditions. For this, the filter test rig was equipped with a Knauer HPLC pump which can ensure a flow rate between 100 mL/min and 1000 mL/min. Moreover, the pressure before and after the filter unit was detected. For the experiment, the respective nanofiber sea sand composites were placed in the holder for the filter units. Subsequently, clean water without any particles was pumped through the cartridge with a flow rate of 500 mL/min while the differential pressure was determined with the help of the two pressure sensors before and after the filter unit.

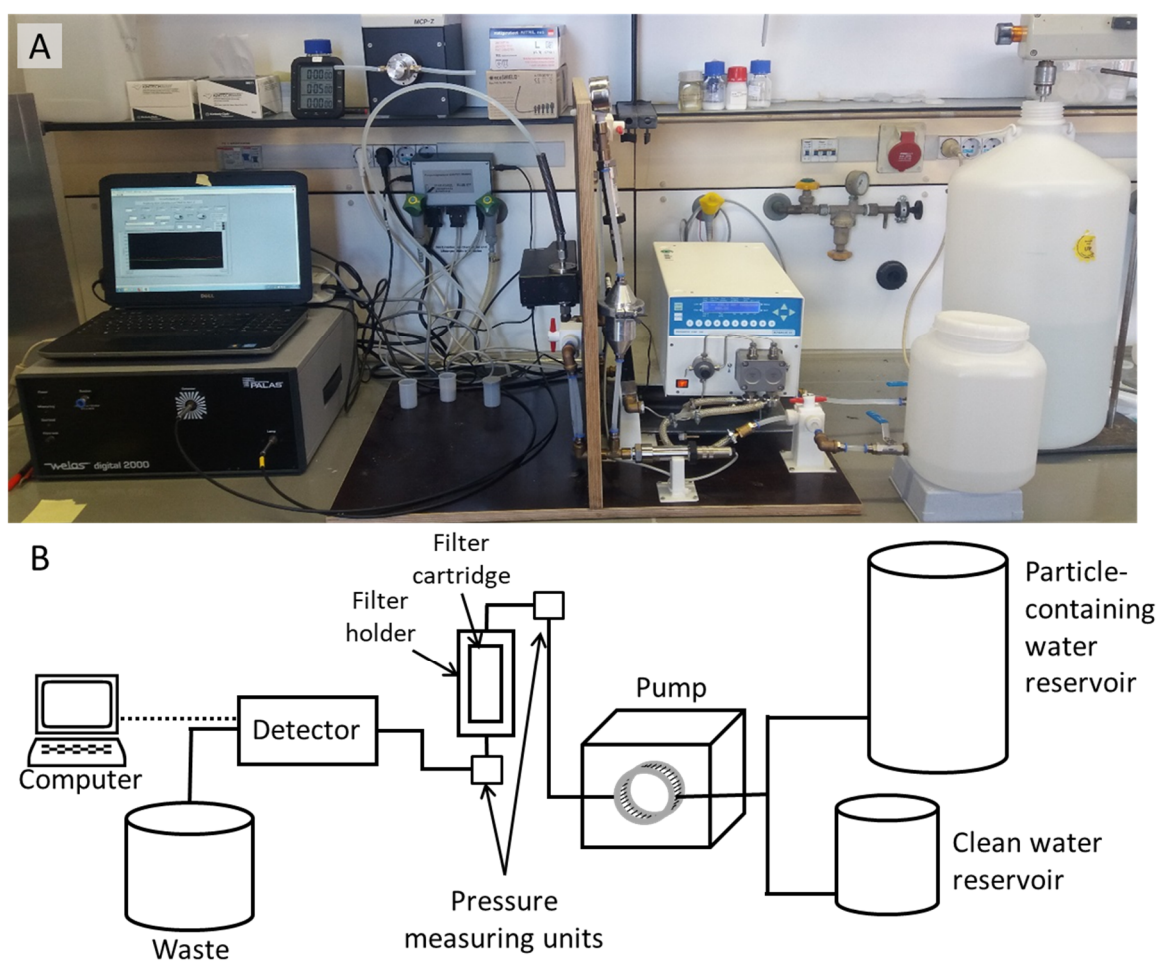


Figure 5.9: **A:** Photographic image of the custom-made water filtration set-up. **B:** Schematic illustration of the essential parts of the set up comprising a reservoir with clean water and water containing particles; a HPLC-Pump which can ensure a flow rate between 100 mL/min and 1000 mL/min; pressure measuring units to detect the differential pressure drop; a filter holder with a filter cartridge inside: a detector (WELAS 2000[®] detector of Palas[®] can detect particles in a range of 0.6 μm to 29 μm which is only used for filtration experiments) and a computer system.

All in following graphs are exemplary for a measurement series of at least three individual samples for each BTA system used. For every individual investigated systems, the results were very similar.

As a primary reference experiment, a cartridge filled with neat sand was investigated over a period of 30 min to evaluate the applied differential pressure and the resulting data are shown in **Figure 5.10**.

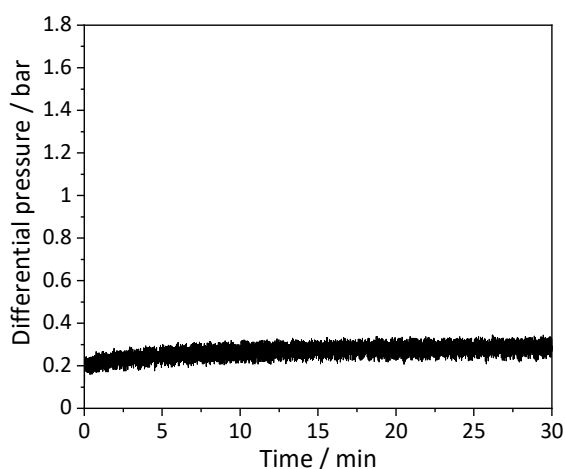


Figure 5.10: Graph of the measured differential pressure of a cartridge filled with 25 g neat sea sand. The flow velocity was 500 mL/min. Measured over a period of 30 min.

It can be seen that the graph rises slightly at the beginning. After about 2 minutes it has reached its maximum of about 0.2 bar. Then, the value of the differential pressure remains constant. Since there was no significant change during the course of the experiment, it was stopped after 30 min.

Next, a composite equipped with BTA 17 was investigated. In **Figure 5.11 A** the differential pressure of the sample over a duration of 50 min is shown.

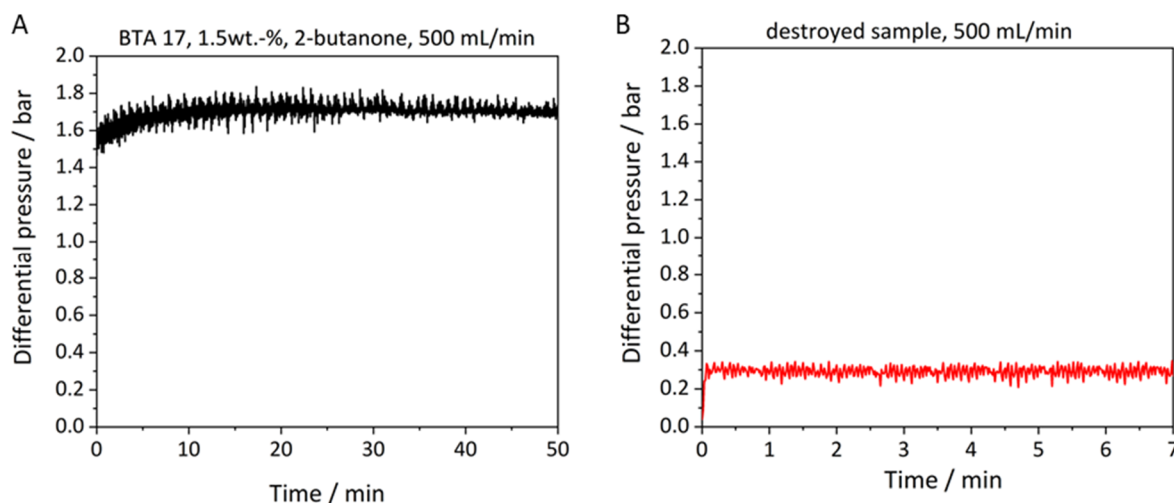


Figure 5.11: A: Differential pressure of an intact sample in a time interval of 50 min. **B:** Differential pressure of a sample with destroyed fiber network. Sample preparation: BTA 17, Solvent: 2-butanone; BTA-concentration: 1.5 wt.-%; Immersion temperature: 70 °C; Cooling temperature: -79 °C; Cooling time: 30 min; Non-solvent: water; Total mass of the sand: 25 g. Testing conditions: Flow rate: 500 mL/min.

It can be seen that after a small increase in the beginning, the differential pressure also stays constant, however, at a pressure drop of approximately 1.7 bar over the whole period of time of the experiment.

This means that the network inside the granular filling was stable against the applied pressure. The graph in **Figure 5.11 B** shows the differential pressure of a sample with a destroyed supramolecular fiber network. For this, the granular matter within the sample was stirred with a spatula before starting the experiment, which destroys the nanofiber network. Now, the differential pressure is significantly lower than before destroying the fibers and at a similar value than the sample with neat sand. This demonstrates that the comparable large difference in the pressure drop of the composite and the reference is solely attributed to the presence of an intact network in the previous experiment.

Finally, the stability of different composites with co-assembled supramolecular fibers will be investigated. In **Figure 5.12**, the graphs of a sample prepared with BTA 17 and BTA 13 in a molar mixing ratio of 3 to 2 are shown.

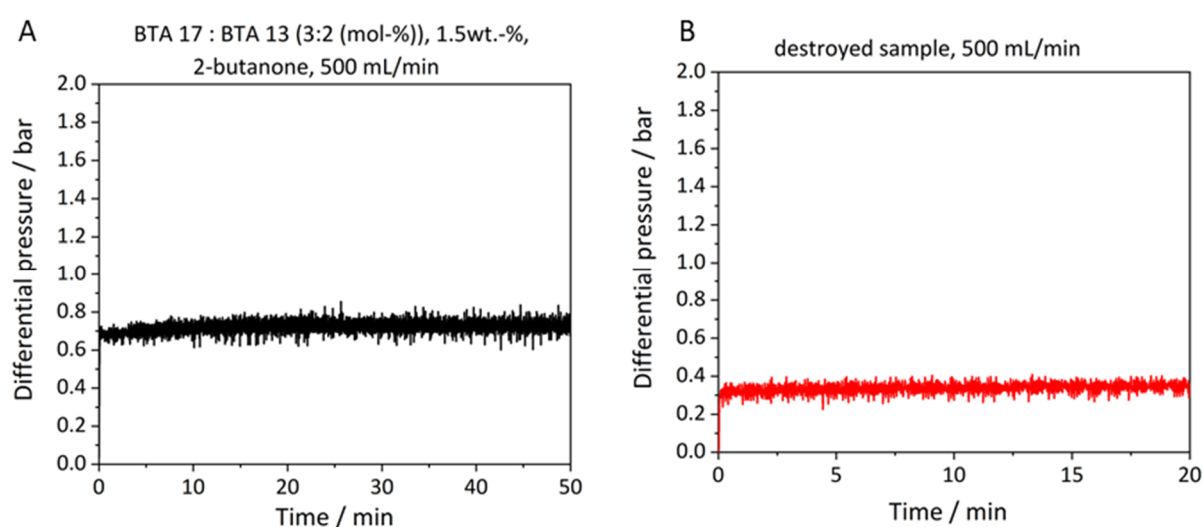


Figure 5.12: **A:** Differential pressure of an intact sample in a time interval of 50 min. **B:** Differential pressure of a sample with destroyed fiber network. Sample preparation: BTA 17 : BTA 13 (3 : 2 molar ratio), Solvent: 2-butanone; BTA-concentration: 1.5 wt.-%; Immersion temperature: 70 °C; Cooling temperature: -79 °C; Cooling time: 30 min; Non-solvent: water; Total mass of the sand: 25 g. Testing conditions: Flow rate: 500 mL/min.

Figure 5.12 A shows that the differential pressure was constantly at about 0.7 bar. As no significant reduction in pressure drop could be observed during the experiment, it is concluded that the supramolecular fiber network remains intact. In **Figure 5.12 B**, the graph of the sample with the mechanically destroyed network by stirring the composite is shown. Here, the differential pressure has a value of approximately 0.3 bar, which is significantly lower than the pressure of the intact sample and has a similar value like the sample with neat sand.

Ultimately, the recorded pressure drops of a composite prepared with BTA 17 and BTA 13 in a molar mixing ratio of 1 to 1 are shown in **Figure 5.13**.

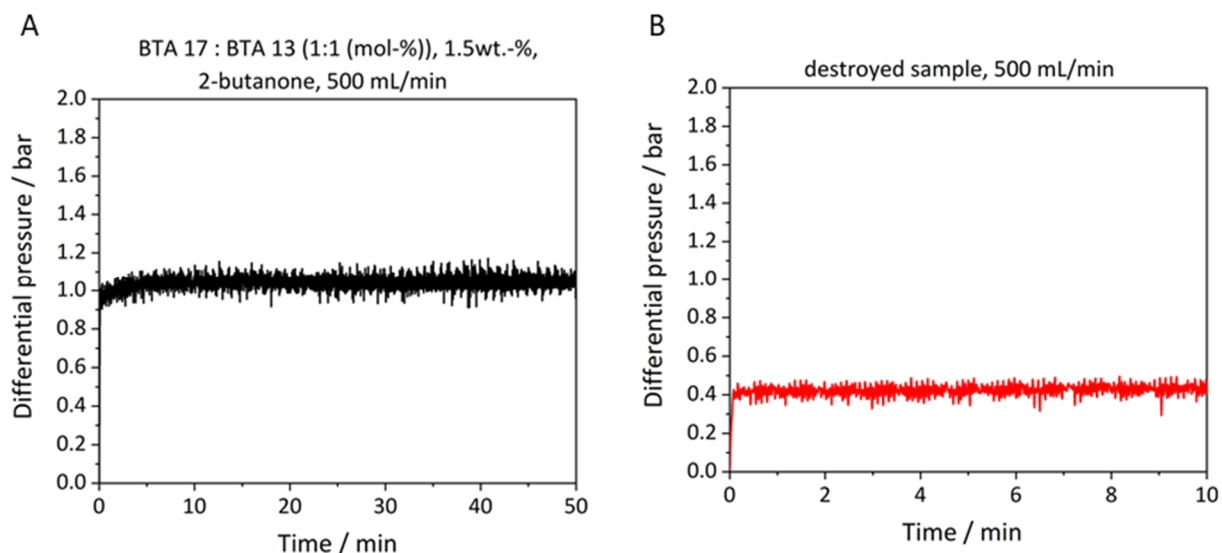


Figure 5.13: **A:** Differential pressure of an intact sample in a time interval of 50 min (black line). **B:** Differential pressure of a sample with destroyed fiber network. Sample preparation: BTA 17 : BTA 13 (1 : 1 molar ratio), Solvent: 2-butanone; BTA-concentration: 1.5 wt.-%; Immersion temperature: 70 °C; Cooling temperature: -79 °C; Cooling time: 30 min; Non-solvent: water; Total mass of the sand: 25 g. Testing conditions: Flow rate: 500 mL/min.

Similarly, this composite sample with intact nanofibers features an average differential pressure of 1.0 bar. Likewise, the samples investigated before, the value of differential pressure stays constant over the whole period of time of the experiment. **Figure 5.13 B** shows the graph of a mechanically destroyed sample. The measured differential pressure here was about 0.4 bar. This value is a little bit higher than the value of the reference sample without supramolecular fiber network but it is still very similar. Although this slight difference cannot be explained with certainty, potential explanations comprise (i) an incomplete destruction of the fiber network, (ii) fiber fragments that form a layer of fibers, which may be collected at the filter paper at the bottom of the cartridge and therefore contribute to the differential pressure and (iii) preparation related issues.

Notably, in all graphs of the composite and the destroyed composites a clear trend can be seen with respect to the difference of both differential pressures of the samples presented before. This difference is calculated to 0.4 and 0.6 bar for the co-assembled composites. The reference composite with the aliphatic nanofibers shows the highest difference with 1.3 bar representing a clear contribution of the nanofiber network.

To sum up, all investigated composite samples were very stable applying significant harsh conditions with a continuous flow rate of 500 mL/min. It can be noted that these measurements can also be performed at much higher flow rates such as 800 to 1000 mL/min. However, the custom-made set-up was not suitable at this high flow rates, as there were issues regarding leak tightness due to the higher pressures. Nevertheless, composites were able to withstand these pressures and flow rates without damaging. During these measurements, the differential pressures drops remain constant over the whole period of time. Samples with destroyed supramolecular fiber networks showed significantly

lower differential pressures, which were very close to those of the neat sea sand reference samples. These findings provide a strong indication that the BTA-fibers inside the networks remain highly stable under these conditions.

5.3 Filtration with sea sand nanofiber composites

5.3.1 Filtration experiments of polymer model particles

Bacteria can be regarded as micrometer-sized particles. In view of filtration, a device that combines the properties of in depth and microfiltration (see **Figure 5.1**) is expected to be highly beneficial for this purpose. To evaluate the general function of the composite in view of filtration of small particles in the micrometer range, the filtration efficiency of selected functional sand–supramolecular nanofiber composites was investigated employing a model system. As model system for the filtration tests suitable for high throughput procedures on a lab scale, a suspension of non-harmful small polystyrene (PS) microparticles with a defined diameter of 1.1 μm was used. The dimensions of these polymer particles are in the range of small-sized bacteria.^[187] In **Figure 5.14**, SEM images of the used PS latex particles are shown.

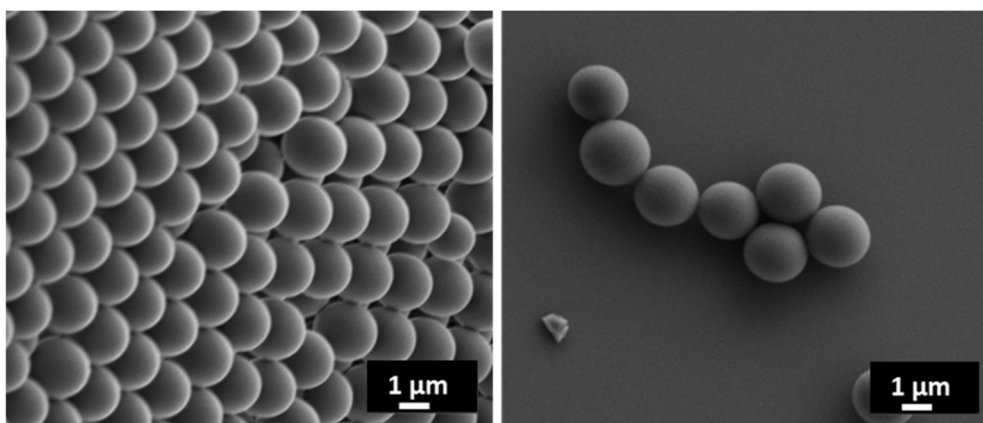


Figure 5.14: Polystyrene latex particles with a diameter of 1.1 μm . These particles were used as model system for the filtration tests.

For these experiments, the same custom-made water filtration set-up was used as shown in **Figure 5.9**. 25 μL of a 10 wt.-% PS-latex suspension were added to approximately 25 L of clean water. This level of dilution represents the maximum useful concentration of particles, which can be monitored without overloading the detector, Welas 2000[®]. At the beginning of each experiment, each installed filter device containing the sea sand-nanofiber-composite was flushed with at least 250 mL clean deionized water to remove any potential contaminants and also air bubbles in the system which probably influence the detector. For a typical measurement, the flow rate was set to 500 mL/min for a duration of 5 minutes resulting in a total filtration volume of 2.5 L of the PS microparticle suspension. The particles passing the filter device and the pressure before and after the filter unit were monitored during the entire time of the experiment.

To calculate the filtration efficiency of the used filter units, for every set of filtration experiment, background measurements were recorded in which the number of particles was determined without a filter unit being installed in the filter test rig.

As reference experiment, the filtration performance of cartridges filled with neat sea sand was conducted and evaluated. These experiments were performed with the same particle batch suspension. The resulting graph is shown in **Figure 5.15**. The dashed green line represents the counted polystyrene particles with neat sand in the filter cartridge and the black graph the background measurement. As both measurements were performed with the same batch suspension and conditions, the integral features the same number of particles. Both graphs are almost identical featuring a maximum of counted particles. This demonstrates that the neat sand and the filter paper on the bottom of the cartridge do not have any filtration effect at the chosen conditions.

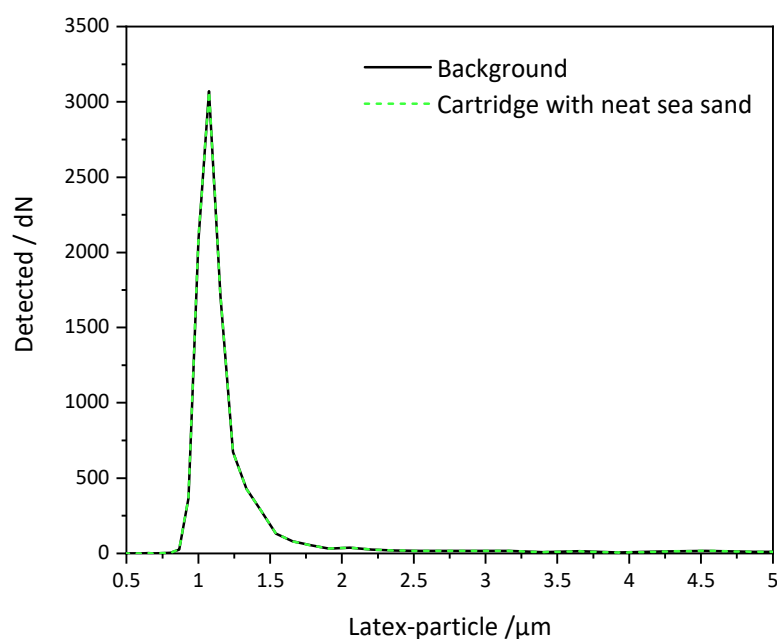


Figure 5.15: Particle size distribution of the measured particles of the polystyrene latex suspension in water. The latex particles have a diameter of $1.1 \mu\text{m}$. The black curve corresponds to the number of measured particles in a volume of 2.5 L without any cartridge inside the filter holder. This value corresponds to the number of particles inside the suspension before the filtration test. The dashed green curve corresponds to the particle size distribution of the experiment with 25 g neat sand inside the cartridge and the filter paper on the bottom of the container. Measuring parameters: Volumetric flow rate: 500 mL/min; Total filtrated volume for each curve: 2.5 L; Filter area: 7.06 cm^2 .

As a further experiment, the BTA-fiber sea sand composite using BTA 17, which was prepared with 1.5 wt.-% BTA in 2-butanone at a self-assembly temperature of $-79 \text{ }^\circ\text{C}$, was used (see **Figure 5.3**). Prior to the filter experiment, 2-butanone was exchanged with 200 mL of water. The result of the performed filtration experiment with 2.5 L of the latex particle suspension is shown in **Figure 5.16 A**. The corresponding background measurement is plotted with a black line.

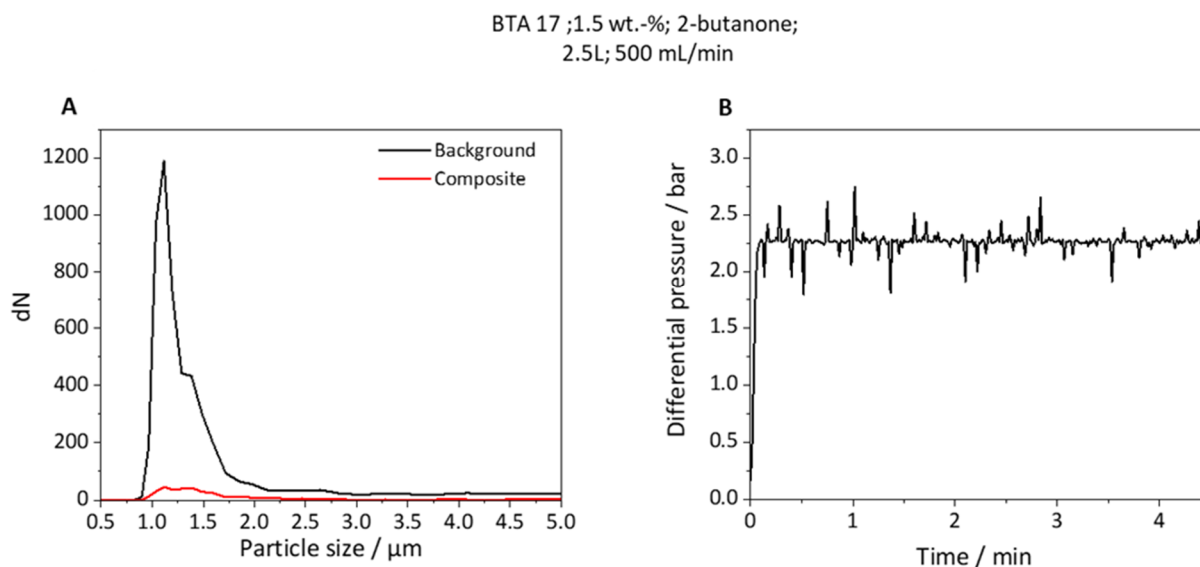


Figure 5.16: **A:** Particle size distribution of the measured particles of the polystyrene latex suspension in water. The latex particles have a diameter of 1.1 μm . The black curve corresponds to the number of measured particles in a volume of 2.5 L without any cartridge inside the filter holder. This value is the number of particles inside the suspension before the filtration test. The red curve corresponds to a filtration experiment with a cartridge equipped with fibers of BTA 17. **B:** Differential pressure of the sample during the experiment. Filter unit preparation parameters: Solvent: 2-butanone; BTA-concentration: 1.5 wt.-%; Immersion temperature: 70 $^{\circ}\text{C}$; Cooling temperature: -79 $^{\circ}\text{C}$; Cooling time: 30 min; Non-solvent: water; Total mass of the sand: 25 g. Measuring parameters: Volumetric flow rate: 500 mL/min; Total filtrated volume for each curve: 2.5 L; Filter area: 7.06 cm^2 .

This supramolecular nanofiber-sea-sand-composite exhibits a very good filtration efficiency of about 96 % of the particles during the filtration of 2.5 L of the latex suspension (**Figure 5.16 A**). This result shows that the fiber network formed *in situ* between the sand grains has a very good ability to reduce the amount of micro-sized pollutants in water.

During the filtration experiment, the differential pressure before and after the cartridge was measured in the same way as demonstrated during the stability experiments before. The measured differential pressure was found to be constant at about 2.25 bar (**Figure 5.16 B**). Since the differential pressure does not increase during the period of filtration, a clogging of the filter due to the formation of a filter cake is not observed. This means that the supramolecular fiber network was stable during the experiment but also that the capacity of the filter was not reached.

Finally, experiments revealing the filtration performance of a composite prepared with a BTA-mixture consisting of BTA 17 and BTA 13 in a molar ratio of 3 to 2 were performed. The results regarding the particle retention and the differential pressure are shown in **Figure 5.17**.

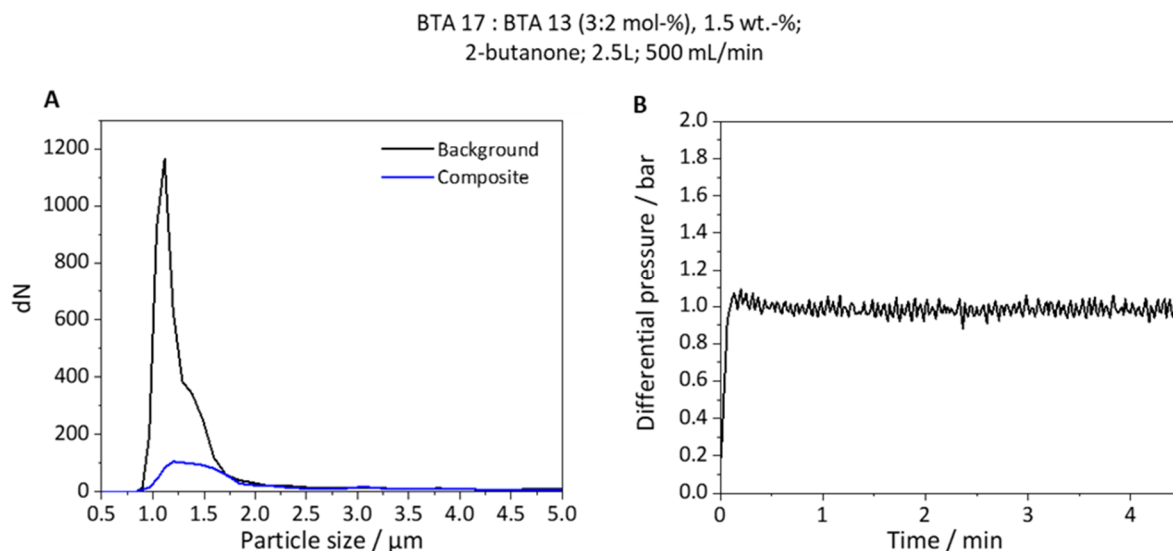


Figure 5.17: **A:** Particle size distribution of the measured particles of the polystyrene latex suspension in water. The latex particles have a diameter of $1.1\mu\text{m}$. The black curve corresponds to the number of measured particles in a volume of 2.5 L without any cartridge inside the filter holder. This value is the number of particles inside the suspension before the filtration test. The blue curve corresponds to the filtration experiment with a cartridge equipped with fibers of BTA 17 : BTA 13 in a molar ratio of 3 to 2. **B:** Differential pressure of the sample measured during the filtration experiment. Filter unit preparation parameters: Solvent: 2-butanone; BTA-concentration: 1.5 wt.-%; Immersion temperature: $70\text{ }^{\circ}\text{C}$; Cooling temperature: $-79\text{ }^{\circ}\text{C}$; Cooling time: 30 min; Non-solvent: water; Total mass of the sand: 25 g. Measuring parameters: Volumetric flow rate: 500 mL/min; Total filtrated volume for each curve: 2.5 L; Filter area: 7.06 cm^2 .

Figure 5.17 A, shows the detected particles for the experiment with the composite in the filter cartridge (blue curve) and the corresponding background measurement (black curve). It can be clearly seen that the maximum of the size distribution is significantly reduced. The investigated filter unit showed a slightly lower filtration efficiency of about 90 % as the composite made with BTA17 (96 %). Likewise before, the number of PS-particles could be strongly reduced.

In a similar manner, the differential pressure remains constant but features a lower value of 1.0 bar. This difference is consistent with the stability test and is attributed to a stable, but different fiber network.

However, in contrast to the composite with BTA 17, this composite featuring co-assembled supramolecular fibers with peripheral functional groups is proposed to immobilize silver nanoparticles which feature antibacterial properties and therefore are expected to feature an improved performance in the filtration of bacterial suspensions.

5.3.2 Deposition of silver nanoparticles on functional supramolecular nanofiber

As demonstrated in chapter 3.4, supramolecular nanofibers comprising sulfur-containing BTAs exhibit the potential to immobilize AgNPs. Moreover, composites comprising nonwovens and co-assembled functional BTA nanofibers can immobilize metal ions, in particular Au^{3+} with high efficiency (see chapter 4.3). Consequently, in this chapter the adsorption capabilities of different prepared BTA-fiber-sea-sand-composites with respect to AgNPs were investigated. In particular, it is aimed to immobilize AgNPs from a suspension on the surface of the supramolecular fibers inside of the cartridges and therefore to provide the opportunity to yield a filter unit with antibacterial properties. Such a system is highly beneficial for the filtration of bacterial suspensions because it combines particle retention capabilities with antibacterial and antifouling properties and thus extends the lifetime of a filter device. For these experiments, silver nanoparticle suspensions were synthesized according to the literature-known procedure of Li et al. and Rashid et al., which is based on the reduction of silver nitrate with citrate.^[203,204] A photograph of a successfully prepared yellowish suspension is provided in **Figure 5.18 A**. In **Figure 5.18 B**, a SEM image of the synthesized silver nanoparticles is shown. These nanoparticles are mainly spherical in their shape.

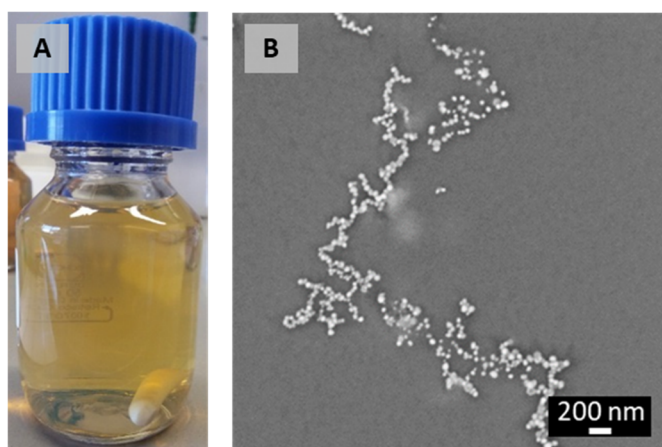


Figure 5.18: **A:** Photographic image of a silver nanoparticle suspension. The suspension has a yellowish color. **B:** SEM image of synthesized silver nanoparticles with spherical shape with an average diameter of 60 nm. Upon evaporation, the spherical AgNPs tend to agglomerate.

Subsequently, experiments to immobilize the AgNPs within the composite were performed in a very simple and straightforward manner as depicted in **Figure 5.19**. For this, the cartridge with a supramolecular fiber-sea-sand-composite was placed inside the filter holder. The composite was dried before the experiment in order to prevent dilution of the nanoparticle suspension. The holder was closed with its cap, which was equipped with a luer-lock connection. Then, 20 mL of the silver nanoparticle suspension were flushed through the composite with help of a syringe. The filtrate was captured in a vessel. Afterwards, the composite was flushed with 100 mL of clean water to remove non-immobilized AgNPs. The flushed water was captured in a separate vessel. All of the used composites were prepared as described before.

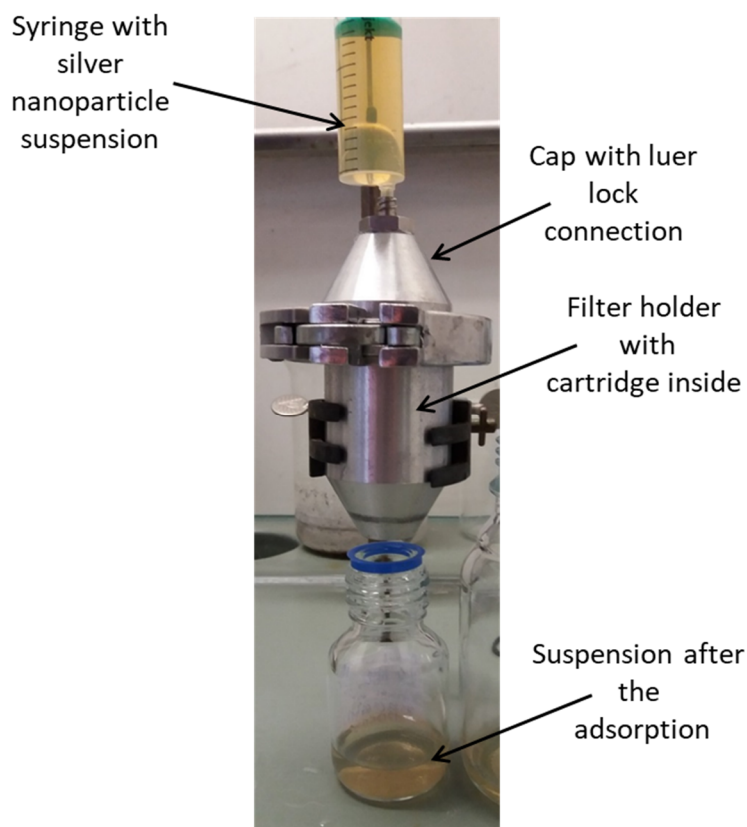


Figure 5.19: Photograph of the experimental setup for the adsorption of silver nanoparticles on the supramolecular fibers in a cartridge. After passing the filter unit, the suspension in this experiment maintains the yellowish color indicating that no immobilization of the AgNPs has taken place.

As a first reference experiment, an adsorption experiment was performed with a composite containing a supramolecular fiber network of BTA 17. These fibers do not have any functional group. As it can be seen in **Figure 5.20 A**, the AgNP suspension which was captured after the filter unit had nearly the same color like the initial suspension as it was expected. To quantify this result, i.e. the capability to immobilize AgNPs, absorption measurements were performed. Comparing the UV/Vis spectra of the same suspension before and after the immobilization experiment allows to evaluate these findings by comparing the maxima. The UV/Vis spectra in **Figure 5.20 B** show that the two graphs are almost identical. Thus, no silver nanoparticles were adsorbed during the experiment.

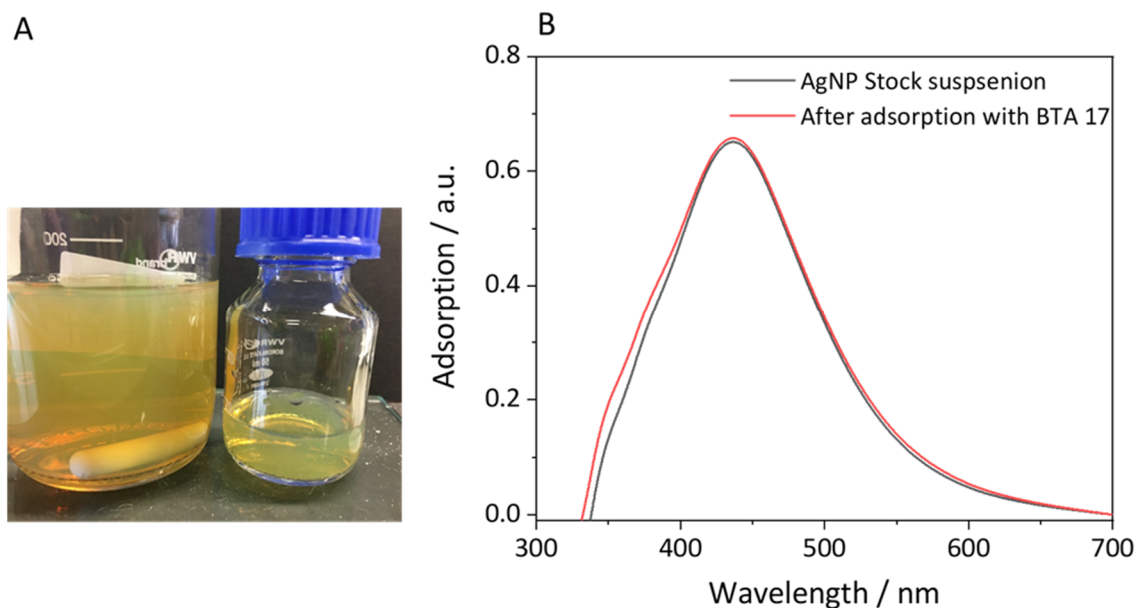


Figure 5.20: A: Photograph of the used silver nanoparticles suspension (left) and the suspension after the adsorption experiment (right). B: UV/Vis-spectra of the used silver nanoparticle suspension (black curve) and the suspension after the adsorption experiment (red curve). Filter unit preparation parameters: BTA-system: BTA 17 Solvent: 2-butanone; BTA-concentration: 1.5 wt.-%; Immersion temperature: 70 °C; Cooling temperature: -79 °C; Cooling time: 30 min; Non-solvent: water; Total mass of the sand: 25 g. AgNP-suspension volume: 20 mL.

Next, the same adsorption experiment was performed with a composite prepared with BTA 17 : BTA 13 in a molar ratio of 3 : 2. In **Figure 5.21**, a photograph of the suspension before and after the adsorption experiment and the corresponding UV/Vis-spectra are shown. **Figure 5.21 A** shows that the captured suspension in the small vessel has a less intensive color than the used AgNP-suspension in the bigger vessel. **Figure 5.21 B** shows the UV/Vis-spectra of the used silver nanoparticle suspension (black) and the captured suspension after the adsorption experiment (blue) demonstrating that a retention of the AgNPs has taken place. Determination of the ratio of both maxima ($\text{Max}_{\text{filtrate}}/\text{Max}_{\text{stock solution}}$) yielded an absorption efficiency of about 65 % of the silver nanoparticles.

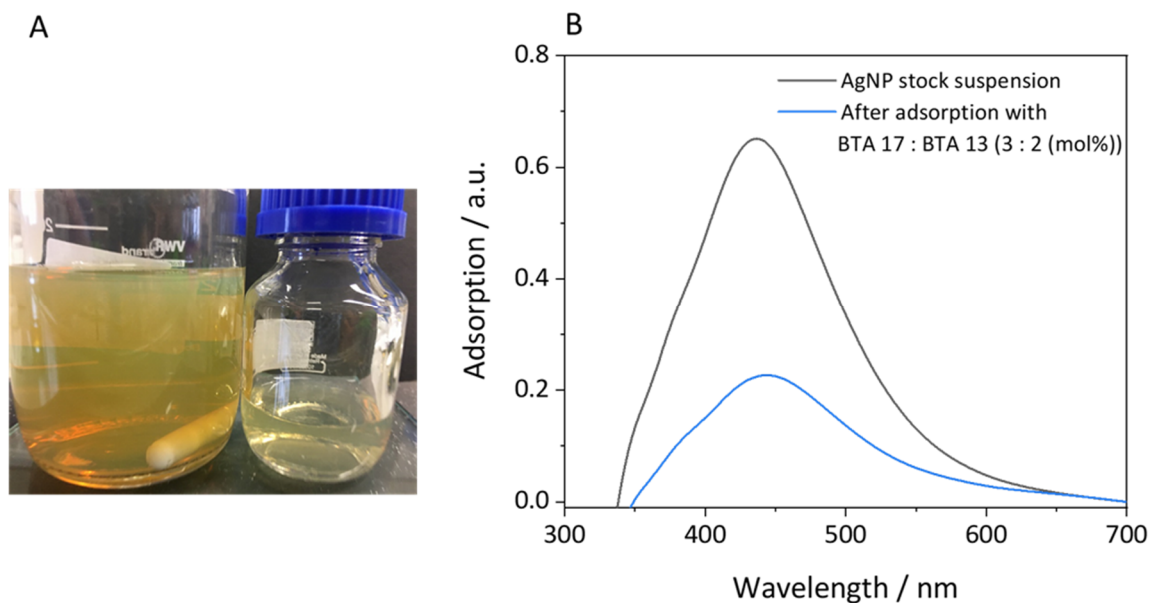


Figure 5.21: **A:** Photograph of the used silver nanoparticles suspension (left) and the suspension after the adsorption experiment (right). **B:** UV/Vis-spectra of the used silver nanoparticle suspension (black curve) and the suspension after the adsorption experiment (blue curve). Filter unit preparation parameters: BTA-system: BTA 17 : BTA 13 (3 : 2 molar ratio) Solvent: 2 -butanone; BTA-concentration: 1.5 wt.-%; Immersion temperature: 70 °C; Cooling temperature: -79 °C; Cooling time: 30 min; Non-solvent: water; Total mass of the sand: 25 g. AgNP-suspension volume: 20 mL.

Moreover, the adsorption experiments performed with composites prepared with BTA 17 : BTA 13 in a molar ratio of 1 to 1 were investigated. This ratio was selected due to the promising results shown chapter 4.3, where it was shown that the adsorption efficiency depends on the used amount of functional BTA.

In **Figure 5.22**, the photograph of the used nanoparticle suspension and the suspension after the adsorption (**A**) and the corresponding UV/Vis spectra (**B**) are shown. The suspension after passing the composite is nearly colorless and only a light yellowish color can be seen. Also, the UV/Vis spectra show that the silver nanoparticle content of the filtrated suspension was decreased resulting in a calculated adsorption efficiency of 96 %.

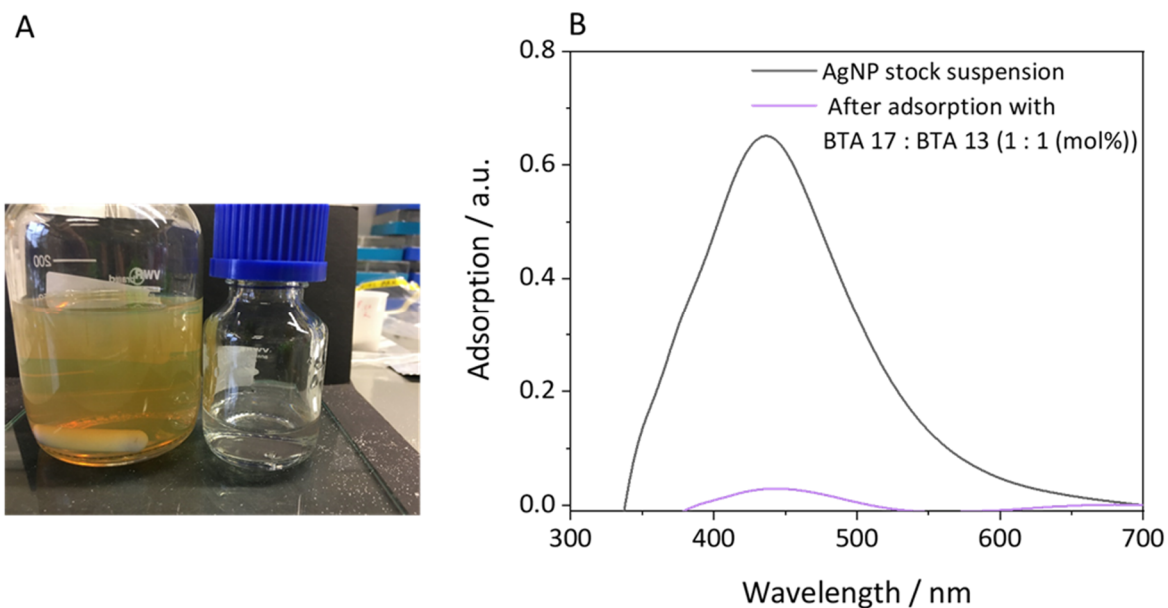


Figure 5.22: **A:** Photograph of the used silver nanoparticles suspension (left) and the suspension after the adsorption experiment (right). **B:** UV/Vis-spectra of the used silver nanoparticle suspension (black curve) and the suspension after the adsorbed experiment (purple curve). Filter unit preparation parameters: BTA-system: BTA 17 : BTA 13 (1 : 1 molar ratio) Solvent: 2 -butanone; BTA-concentration: 1.5 wt.-%; Immersion temperature: 70 °C; Cooling temperature: -79 °C; Cooling time: 30 min; Non-solvent: water; Total mass of the sand: 25 g. AgNP-suspension volume: 20 mL.

Finally, to provide a further evidence that the composite with supramolecular functional nanofibers are beneficial to immobilize AgNPs, such samples were investigated by SEM and EDX. For this, the composite containing supramolecular fibers of BTA 17 and BTA 13 (1 : 1 molar ratio) equipped with nanoparticles was selected and a sample was taken from the middle of the composite. The obtained micrograph and the corresponding EDX spectrum are shown in **Figure 5.23**. On the surface of such fibers silver nanoparticles (**Figure 5.23 A**, Position 2) can be detected, which have an irregular shape. Obviously, these nanoparticles strongly tend to agglomerate during the deposition process. The EDX spectrum of point 2 was chosen as an example and the element silver can be verified which appears at about 3.3 keV. This investigation proved that the silver nanoparticles were adsorbed inside the prepared granular fillings.

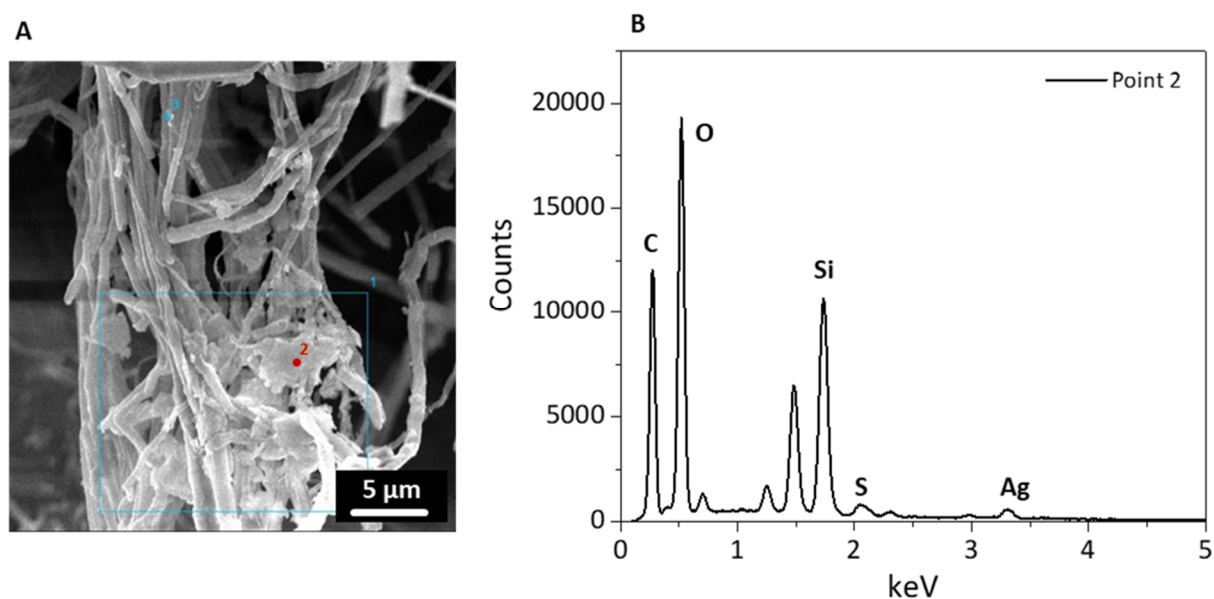


Figure 5.23: **A:** SEM image of supramolecular fibers equipped with silver nanoparticles. The areas for the EDX-measurement are marked. **B:** Corresponding EDX-spectrum of point 2. This position was chosen as an example. Filter unit preparation parameters: BTA-system: BTA 17 : BTA 13 (1 : 1 molar ratio) Solvent: 2-butanone; BTA-concentration: 1.5 wt.-%; Immersion temperature: 70 °C; Cooling temperature: -79 °C; Cooling time: 30 min; Non-solvent: water; Total mass of the sand: 25 g. Ag nanoparticle suspension volume: 20 mL.

In summary, it could be shown that sulfur-containing BTAs are suitable to adsorb AgNPs and the adsorption efficiency depends on the amount of the sulfur-containing BTA. With increasing BTA 13 content, the immobilization of AgNPs becomes more efficient. These results show that it is possible to equip the functional supramolecular fibers inside a granular filling with silver nanoparticles in a simple and straightforward way. In contrast, non-functional BTAs are not capable of adsorbing silver nanoparticles under these conditions.

5.3.3 Filtration of *E.coli* bacteria

Finally, the supramolecular fiber-sea-sand-composites were evaluated in view of their filtration capabilities to remove bacterial contaminants from aqueous media. In particular, emphasis was given on the filtration of suspensions comprising *E.coli* bacteria (DSM No.: 498). These experiments were performed at the DWI Leibniz Institute for Interactive Materials at the RWTH Aachen. For this, sea-sand-composites were prepared with supramolecular fibers of BTA 17 and BTA 13 in a molar ratio of 3 to 2 due to the promising results of the previous filtrations experiments. This also includes their high potential to adsorb silver nanoparticles which introduces an additional antibacterial effect leading to an improved filtration effect of living bacteria as well as an improvement in period of usage and storage of the filter media.

For the filtration experiments, various sea-sand-composite systems were investigated. First of all, filtration cartridges containing neat sea sand without supramolecular fibers were tested. These cartridges were equipped with a filter paper on the bottom and were filled with 25 g sea sand. The filter paper with a pore size of 5 μm does not contribute to the filtration of bacteria in a significant manner. Furthermore, composites with functional supramolecular nanofibers were prepared as it was described in chapter 5.3.2. The overall concentration for both BTAs in the solution for the preparation of the composite was 1.5 wt.-%. After the composite preparation, a soxhlet-extraction of such fiber sea sand composites was performed, yielding a total 1,3,5-benzenetrisamide amount of about 85 mg inside each cartridge. Consequently, the sea sand composite consists of only 0.3 wt.-% of supramolecular nanofibers.

As main filtration devices apart from the reference devices, silver nanoparticles were immobilized on the supramolecular nanofibers in the composites. To equip the composites with AgNPs, they were flushed with a silver nanoparticle suspension as described in chapter 5.3.2. A photograph of the silver nanoparticle suspension (**A**) and a SEM image of the nanoparticles (**B**) as well as the corresponding UV/Vis spectrum (**C**) are shown in **Figure 5.24**. Deposition of silver nanoparticles was performed by flushing 25 mL of the suspension through the cartridge. Afterwards, the system was flushed with about 200 mL of water to remove potentially non-adsorbed particles.

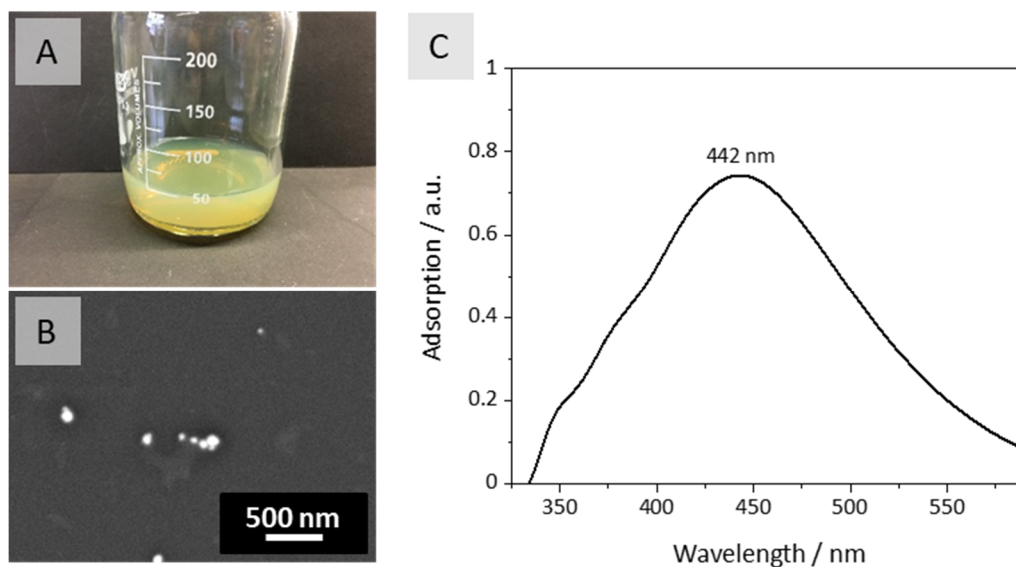


Figure 5.24: **A:** Photograph of the used silver nanoparticle suspension. **B:** SEM image of the silver nanoparticles. **C:** UV/Vis-spectra of the silver nanoparticle suspension. The maximum was at a wavelength of 442 nm.

Filtration set-up for the removal of bacterial contaminants

To evaluate the efficiency of the filtration of bacteria contaminants, a setup comprising a peristaltic pump, a reservoir with the bacterial suspension, the filter cartridge holder and a sterile vessel for the collected aqueous media was used. For the experiments, a flow rate of 60 mL/min was selected. In this way, 60 mL of the bacteria suspension were pumped through the individual filter units which were placed inside the custom-made filter holder within a minute. The filtrate was caught in a vessel and was analyzed afterwards. A photographic image of the filtration set-up is shown in **Figure 5.25**.

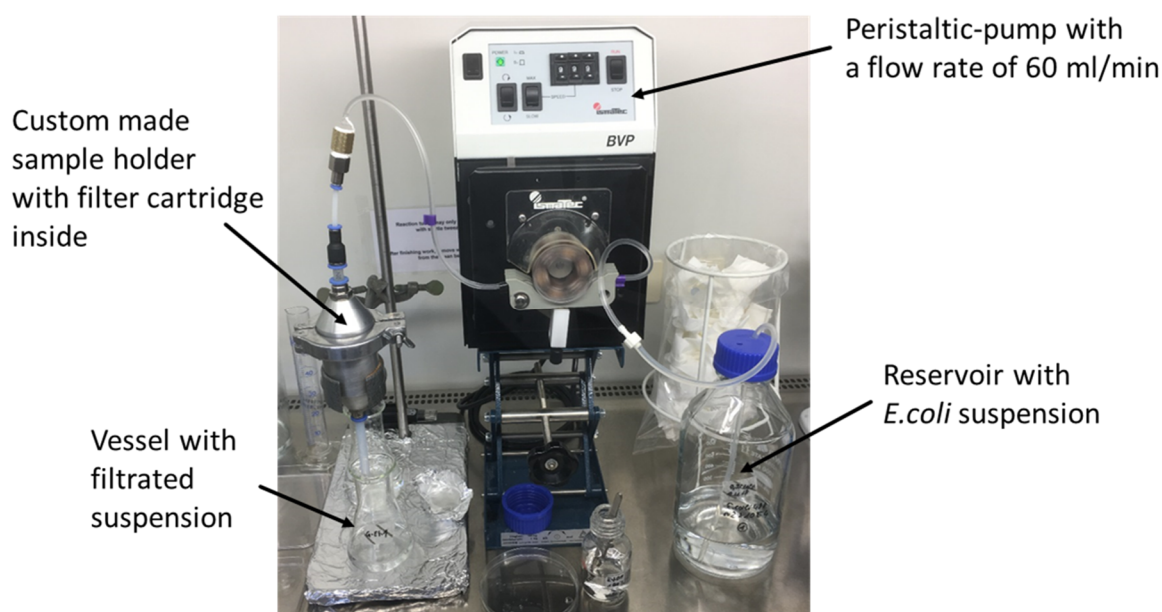


Figure 5.25: Photographic image of the used filtration set-up for the bacteria filtration. A peristaltic pump was used to pump the bacteria suspension through the filter unit. The filtrate was captured in a vessel.

For a detailed evaluation, different tests were performed. First of all, the prepared samples were examined for their sterility. Therefore, the samples were flushed with a 0.9 wt.-% NaCl-solution. This solution was investigated for the formation of new bacteria colonies for a duration of 18 h. The samples include cartridges filled with neat sea sand, sand BTA fiber-composites and sand BTA fiber-composites with silver nanoparticles. In none of them colony forming units (CFU) could be detected, demonstrating that all used samples were sterile and free from germs, which might be accidentally introduced.

The filtration experiments were performed with two *E.coli* suspensions comprising a concentration of 10^3 CFU/mL and 10^4 CFU/mL. This means that one milliliter of the suspension contains 1000 or 10,000 colony forming units, respectively.

In all cases, the composites were investigated before and after the experiments to check visually that no formation of cavities between the wall of the container and the granular filling has taken place.

Figure 5.26 shows such a cartridge before the filtration experiment. Typically, in a case of failure, the cavities appear as a bright vertical line.

In order for comparison, the filtration experiments with bacteria suspensions were performed in the same manner. First of all, the filter unit was flushed with 60 mL of the corresponding *E.coli* suspension at a flow rate of 60 mL/min. Thus, any possible contamination should be removed. This filtrate was subsequently discarded. Then, approximately 60 mL of the *E.coli* suspension was filtered and the filtrate was captured in a sterile vessel. For the evaluation of the germ growth, the as received filtrate and a diluted filtrate in a ratio of 1 : 4 with clean water were used. From each of these filtrates, 50 μ L were placed on three individual spots of an agar plate and were incubated at 32 °C for 18 h. Apart from these incubation experiments, the filtration efficiency was also evaluated by the detection of the optical density. Therefore, 20 μ L of each filtrate were added to 180 μ L of a nutrient solution. This solution was placed in a well plate. During a period of 20 h, the optical density was analyzed every 30 minutes at a wavelength of 612 nm. Between the absorption measurements, the solution was steadily shaken at a constant temperature of 37 °C.

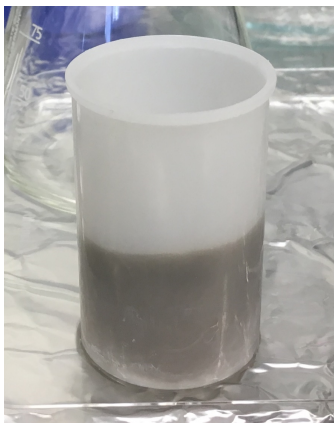
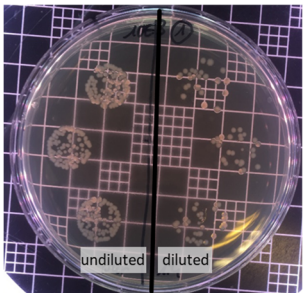
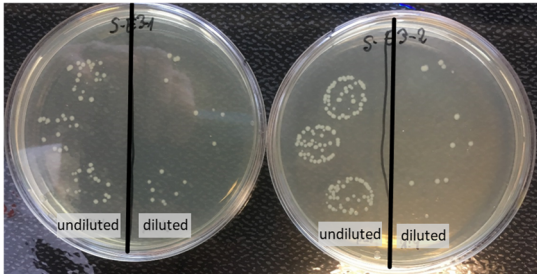
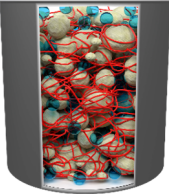
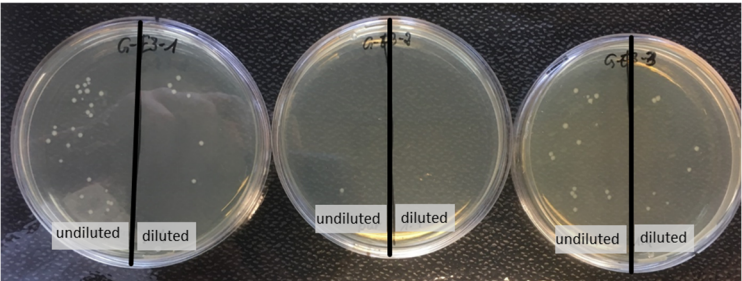
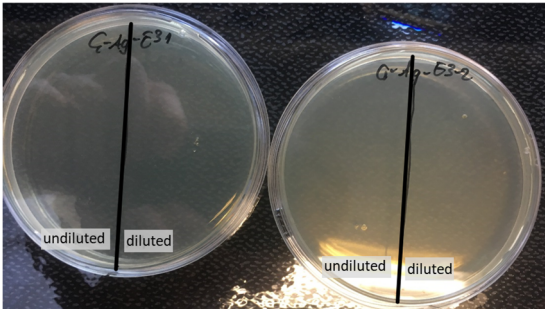


Figure 5.26: Photographic image of a prepared BTA fiber-sea sand composite before the filtration experiment. No cavities can be seen between the wall of the container and the composite.

The results of the bacteria filtration experiments are shown and discussed in detail in the following and are listed in **Table 5.1**.

At first, the used bacteria suspension was investigated as reference experiment. A small amount, 50 μL , of the suspension was placed on an agar-agar plate on three individual locations. Since it is expected that a large number of colonies were formed in undiluted suspension, three drops of a diluted bacteria suspension (1 : 4) were also put on three individual spots of the same agar-agar plate. A photographic image of this prepared agar-agar plate after the incubation of 18 h is shown in **Table 5.1**. On the left side of the plate (undiluted samples) a large number of colonies can be seen, which partly grow together. So, it is impossible to count the single colonies, which were formed. On the right side, the colonies formed from the diluted suspension, single colonies can be detected and counted. Consequently, the diluted incubated set was used as reference value for the filtration experiments.

Table 5.1: Overview of the filtration results with different systems. Also, the reference experiment with no filter unit is given. The middle column shows photographs of agar-agar-plates after an incubation time of 18 h at 32 °C. On the left side of the agar-agar-plates, three drops of the undiluted bacteria suspension or filtrate were placed at different locations. On the right side of the plates, three drops of a diluted suspension (1 : 4) were dropped on three different areas. The used undiluted bacteria concentration was 10^3 CFU/mL.

Filter	Incubated agar-agar plates after 18 h	Filtration efficiency
reference		no efficiency
Sea-sand 		83.7 % ($< \log 1$)
nanofiber-sea sand-composite 		96.9 % ($> \log 1$ to $< \log 2$)
nanofiber-sea sand-composite +AgNP 		100 %

For the first filtration experiment, cartridges filled with 25 g sea sand were used and their filtration performance was investigated. The experiments were performed as described above. A volume of 60 mL of the bacteria suspension was passed through each filter unit and the collected filtrate was investigated by means of incubation test on agar-agar-plates. In **Table 5.1** third row exemplarily two agar-agar plates prepared with the filtrates of two experiments are shown.

In both cases, undiluted and diluted, there are still very large numbers of colony forming units in the filtrate after passing the filter units, which were simply filled with neat sea sand and a filter paper on the bottom of the container. After counting of the single colonies, it could be calculated that a filtration efficiency of 84 % was achieved with this system. Such a filtration efficiency is regarded as insufficient in microbiological studies. In microbiological terms, this filtration efficiency is too low for a relevant application due to the fact that too many colonies will be formed after a short period of time in the filtrated water. Note that the reduction in the number of germs that can form a new colony is typically given in logarithmic notation. For instance, a filtration efficiency of 90 % is denoted as $\log 1$, a filtration efficiency of 99 % is denoted as $\log 2$ and so on. This results in a scale smaller than $\log 1$ ($<\log 1$) in this case.

In a further experiment, filter units were prepared as above but with supramolecular co-assembled BTA nanofibers and investigated for their filtration efficiency of *E.coli* bacteria. The agar-agar-plates prepared with the filtrate of these experiments after incubation are shown in the fourth row of **Table 5.1**. The samples pictured there show clearly a different result than the filtration tests with neat sand. The agar-agar-plates on the right and on the left side show some colonies after the incubation time of 18 h. In both cases some bacteria got through the filter and could form new colonies. However, the filtration performance of these samples was much better than filtration with neat sand. The filtration efficiency was determined to be between 95 % and 96 %, which means there is a germ reduction between $>\log 1$ and $<\log 2$. The agar-agar-plate in the middle of the photograph shows nearly no new formed colonies demonstrating visually a high filtration efficiency. Here, the filtration efficiency was determined to be 99.8 %, which corresponds to a reduction between $>\log 2$ and $<\log 3$. This demonstrates that the performance of these filters was increased significantly over an order of magnitude simply by the incorporation of supramolecular fibers inside the granular filling.

Finally, similarly prepared supramolecular sea-sand-nanofiber-composites were subsequently equipped with silver nanoparticles and investigated in view of their filtration and bacteria reduction performance. In this case, the potential reduction of bacteria will not only be a result of the filtration efficiency but also of the antibacterial properties of (nano)silver. Thus, both effects will play an important role. In the fifth row of **Table 5.1**, the agar-agar-plates prepared with the filtrate of these samples are shown. In none of these samples any bacteria colonies were formed. Thus, the bacteria reduction or filtration efficiency is considered to be 100 %. All bacteria of the used suspension with a bacteria concentration of 10^3 CFU/mL were removed by the filter unit or killed by released Ag^+ -ions. This means that these filters are very effective and that the filtration performance was again increased compared to the samples investigated before.

In another set of experiments, all filtration experiments and subsequent incubation analyses were performed with a concentration of 10^4 CFU/mL. Notably, an increase in concentration clearly provides

harsher filtration conditions. Thus, it can be expected that filtration efficiency decreases. For comparison, all averaged data for all three used filters at the different CFU concentrations are summarized in **Figure 5.27**. The data are the result of counting the colonies formed on the agar-agar-plates.

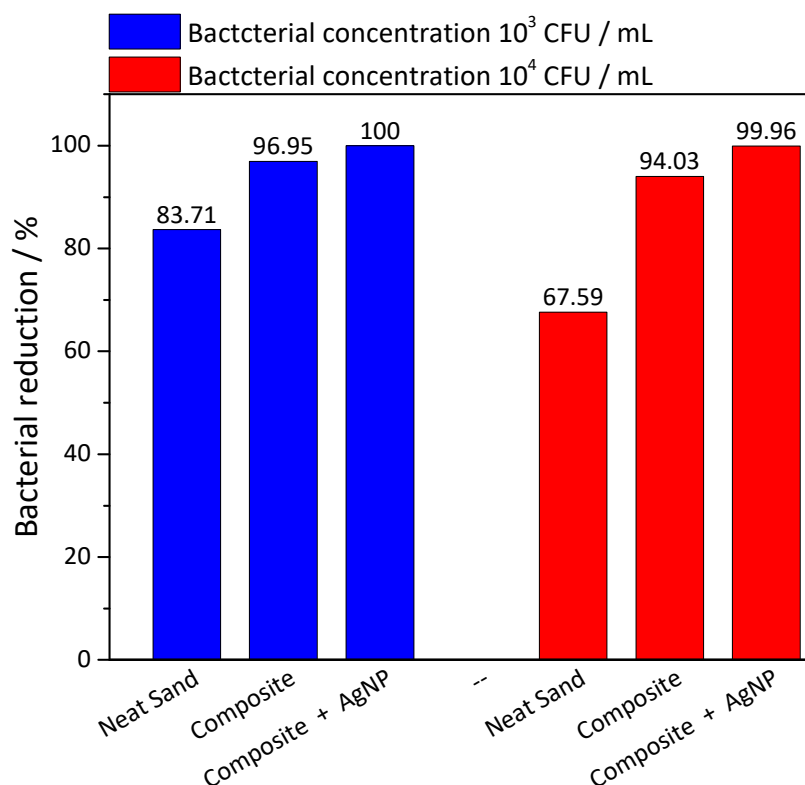


Figure 5.27: Graphical representation of the filtration efficiencies of the different filter units. The efficiencies result from the mean value of the individual measurements which were carried out.

As it can be seen, the filtration efficiency clearly depends on the used bacteria concentration. The filtration efficiency of the tests with a bacteria concentration of 10^3 CFU/mL were unsurprisingly better than those where a bacteria concentration of 10^4 CFU/mL was used. The highest impact can be seen at the samples where the cartridge was filled with neat sand. Here, the efficiency at the higher concentration was about 16 % lower than by using the lower bacteria concentration. Furthermore, a trend can be seen that the filter units with supramolecular fibers have a much better filtration performance than those with neat sand. The sea-sand-nanofiber-composites equipped with silver nanoparticles have in all cases the best bacteria reduction, which is still close to 100 % for 10^4 CFU/mL. Another method to determine the germ filtration efficiency is by time dependent measurement of the optical density (OD) of the filtrates and the stock suspension, as reference. The optical density was determined with the help of a Laser with a wavelength of 612 nm. In contrast to the analysis performed before (incubation of agar-agar plates and counting), this method by using the optical density is much more accurate. In **Figure 5.28**, the diagrams for the measurements of the optical density for the samples investigated with the germ suspension with 10^3 CFU/mL are shown.

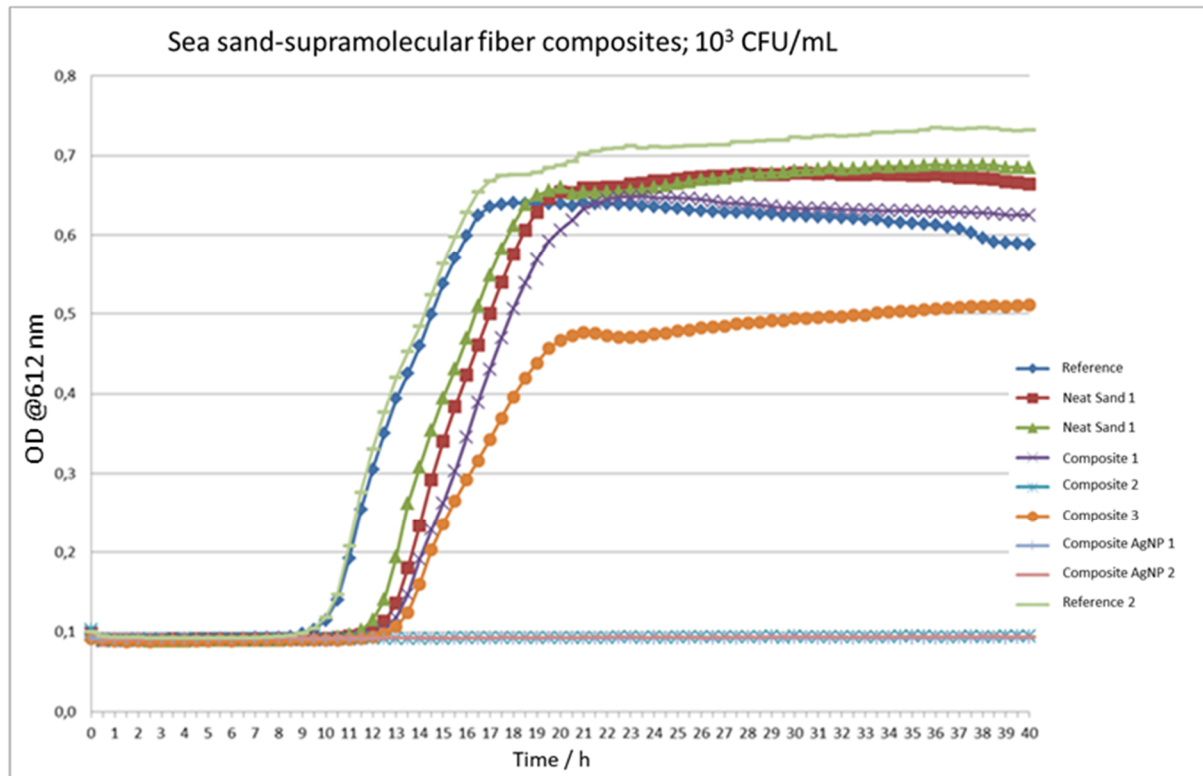


Figure 5.28: Graphs of the optical density of the different samples after the filtration through the different used filter units. Initial bacteria concentration was 10^3 CFU/mL.

The filtrates, which were monitored by the optical density and thus representing the bacteria growth of the different filtrates, are comparable similar for the same kind of composite. The resulting bacterial reductions of all investigated filter units are summarized in **Table 5.2**. The graph of reference sample shown as blue line with dots in **Figure 5.28** shows a strong increase of the optical density up to a value of about 0.7 after 9 h. Similarly, the samples filtrated with neat sand show a relatively fast increase of the optical density. As it was discussed before here the filtration efficiency was relatively low. Considering the results shown in **Table 5.2** the filtration efficiency of the neat sea sand filter units filtrating a bacteria suspension with 10^3 CFU/mL is up to one order of magnitude higher than using a suspension with 10^4 CFU/mL. In the table also, the germ concentration per investigated volume of 60 mL are given. In case of using the lower concentrated suspension, about 10^5 CFUs were used for filtration. By using the higher bacteria concentration, even 10^6 CFUs were used for filtration experiments.

The filtrates of the experiments using sea sand-supramolecular fiber composites show no or only a slight increase in the optical density. As result a high number of bacteria were removed by filtration. As listed in **Table 5.2**, these filter units show a bacteria reduction in the filtrate of greater than log 2 and smaller than log 3 up to an efficiency of 100 % at a lower microbial concentration. These results demonstrate the very good filtration efficiency. By using a higher bacteria concentration, the bacteria

in the filtrate were reduced compared to the stock suspension of $\log 2$ to $>\log 2$ and $<\log 3$. This means that the bacteria concentration was reduced between 99 % and 99.9 %.

The samples filtrated with a composite equipped with silver nanoparticles show no increase in the optical density even after 40 h. Thus, all bacteria were filtrated or also killed by the Ag^+ -Ions demonstrating the benefit of the equipment with silver nanoparticles. As it can be seen in **Figure 5.28**, the reduction of the bacteria at a concentration of 10^3 CFU/mL was 100 %. All germs were filtrated or killed by the released silver ions. The bacteria reduction rate, shown in **Table 5.2**, at the higher investigated bacteria concentration was greater than $\log 4$. This means that more than 99.99 % of the germs were filtrated or killed by the filter unit. These results are still very good and promising for a real-life application.

Table 5.2: Filtration efficiency or bacteria reduction rate of different samples at different bacteria concentrations. The optical density of the individual suspensions was measured every 30 minutes over a period of 20 h at 37 °C. The reduction of the bacteria in the filtrates are given in \log_{10} -steps and in a percentage range.

Analyzed filtrate of filter units with neat sea sand			
Initial germ concentration	Total germ concentration (for 60 mL)	Filtration efficiency in percentage	Filtration efficiency in log notation
CFU/mL	CFU/60 mL	Reduction of the number of bacteria [%]	Reduction of the number of bacteria in \log_{10} steps
2.6×10^3	1.6×10^5	99 to <99.9	2 up to $>2 <3$
2.2×10^4	1.3×10^6	90 to <99	1 up to $>1 <2$
Analyzed filtrate of BTA-fiber-sea-sand-composites			
Initial germ concentration	Total germ concentration (for 60 mL)	Filtration efficiency in percentage	Filtration efficiency in log notation
CFU/mL	CFU/60 mL	Reduction of the number of bacteria [%]	Reduction of the number of bacteria in \log_{10} steps
$2.6/3.5 \times 10^3$	$1.6/2.1 \times 10^5$	<99.9 to 100	$>2 <3$ up to 100 %
2.2×10^4	1.1×10^6	99 to <99.9	2 up to $>2 <3$
Analyzed filtrate of BTA-fiber-sea-sand-composites equipped with AgNPs			
Initial germ concentration	Total germ concentration (for 60 mL)	Filtration efficiency in percentage	Filtration efficiency in log notation
CFU/mL	CFU/60 mL	Reduction of the number of bacteria [%]	Reduction of the number of bacteria in \log_{10} steps
3.5×10^3	2.1×10^5	100 %	100 %
2.6×10^4	1.6×10^6	>99.99	>4

All in all, it could be shown that the cartridges filled with 25 g neat sea sand and a filter paper on the bottom showed the lowest filtration efficiencies. The samples with a supramolecular fiber network inside showed a better filtration performance. Here, dependent on the germ load of the used suspension, 99 % to 100 % of the germs were removed from the aqueous suspension. The best results were achieved with the samples which were equipped with silver nanoparticles. These nanoparticles

themselves have an antibacterial behavior. For these filtration experiments, efficiencies between 99.99 % and 100 % were reached. For all samples, it can be seen that the efficiencies for the experiments with a suspension with 10^3 CFU/mL were better than those with a higher concentration. However, in case of the samples equipped with AgNPS, the difference was relatively small.

5.4 Conclusion

In this part of the work, the self-assembly behavior of different 1,3,5-benzotrisamide systems in a granular filling consisting of 25 g sea sand were extensively investigated. The resulting composites were applied for different filtration application. Such as the high efficiency removal of bacteria from aqueous suspensions.

At first, the prepared composites were investigated for their stability. Therefore, dried samples were investigated, among other things, by means of SEM measurements. Here, it could be shown that dense supramolecular fiber networks between single sand grains were formed. The supramolecular fibers assembled on the surface of those sand grains. By measuring the differential pressure under harsh conditions at a flow rate of 500 mL/min for 50 minutes, the high stability of prepared composites further proofed. The differential pressure stayed constant for all investigated samples indicating a high stability even at differential pressures up to 2 bar. Thus, the formed composites were capable for water filtration experiments.

For orientating filtration experiments, a suspension with polystyrene microparticles with a defined size of 1.1 μm was used as model system. These particles were chosen because their diameter is comparable to the diameter of some bacteria. The investigated samples showed very good filtration efficiencies of 90 % to 96 %.

Composites with functional nanofibers were easy to equip with synthesized silver nanoparticles by flushing a nanoparticle suspension through the filter unit. Depending on the used system up to 90 % of the nanoparticles could be adsorbed. Thus, the filter units got an additional antibacterial behavior. In the last part of the chapter, filtration experiments with *E.coli* bacteria were performed. In contrast to neat sea sand, which did not have a notable filtration performance, the prepared supramolecular fiber-sea-sand-composites showed filtration efficiencies between 99 % and 100 %. As it was expected, the filtration efficiency was a little bit lower at higher bacteria concentrations. It could be shown that composites equipped with silver nanoparticles showed the best bacteria reduction performance. For those samples the efficiency to remove bacteria very high and mostly at 100 %. The germs were hold back by the filter unit or were killed by the released silver ions even at high bacteria concentrations. All in all, the results showed the high efficiency of sand-nanofiber-composites for the filtration of *E.coli* bacteria. By the immobilization of antibacterial AgNPs on the surface of functional nanofibers the efficiency could be further improved to achieve filter units for potential real-life applications.

6 Experimental part

6.1 Materials

Chemicals and solvents

The solvents 1-propanol, 2-butanone and ethyl-L-lactate were purchased from Carl Roth with a purity of 99.99 %. Ethanol was purchased from VWR with a purity of 99.9 %. All chemicals for synthesis were purchased from Sigma Aldrich, TCI, Alfa Aesar and abcr and used with no further purification.

Materials

As filter cartridges for the water filtration, commercially available film cans made of iPP were used. The used sea sand was purchased from Grüssing GmbH and Bernd Kraft GmbH. It was supplied as acid-cleaned and annealed sea sand grains featuring an average grain diameter of 0.3 mm.

6.2 Analytical methods

NMR-Spectroscopy

NMR measurements were performed on a Bruker AC 300 (300 MHz). Approximately 10 mg of the compound were dissolved in ~0.7 mL of a deuterated solvent (DMSO- d_6 , chloroform- d).

FTIR-Spectroscopy

Fourier transform infrared spectroscopic (FTIR) measurements were performed with a PerkinElmer 100 FTIR spectrometer equipped with an ATR sampling accessory. All measurements were performed in a wave number range of 650 cm^{-1} to 4000 cm^{-1} with a resolution of 4 cm^{-1} .

DSC-Measurements

Differential scanning calorimeter (DSC) measurements were performed on a Mettler Toledo DSC 2. In a general procedure, about 5 to 15 mg of the 1,3,5-benzenetrisamides were weighed into 30 μL high pressure crucible pans. Subsequently, the samples were heated under nitrogen at a heating rate of 10 K/min to a temperature above the melting point and cooled down to room temperature at a rate of 10 K/min. Each heating/cooling scan was repeated twice. Between every heating and cooling step, the sample was hold on the reached maximum or minimum temperature for 10 minutes.

TGA-Measurements

Thermogravimetric analysis (TGA) were carried out with a Mettler Toledo TGA/DSC 3+. About 10 mg of the samples were weighed in and heated under a nitrogen atmosphere (60 mL/min) from 30 $^{\circ}\text{C}$ to 700 $^{\circ}\text{C}$ at a heating rate of 10 K/min.

SEM-Investigations

Scanning electron microscopic investigations (SEM) were carried out on a LEO Gemini 1530 FESEM from Zeiss and a FEI Quanta FEG 250. All samples were sputtered with platinum (2.0 nm) under argon atmosphere using a Sputter Coater 208HR (Cressington) before the investigations. For EDX measurements an UltraDry-EDX-Detector (100 mm²) (Thermo Fisher Scientific NS7) was used.

Fiber diameter histograms

The fiber diameters of the supramolecular nanofibers were determined by utilizing AxioVision Software provided by Zeiss. The composites were analyzed at no less than four different positions and at least 150 fibers were considered to generate the nanofiber diameter histograms.

TEM-Measurements

The TEM investigations were carried out at a Jeol JEM-2200FS with an acceleration voltage of 200 kV. The samples were deposited on a carbon coated TEM grid before. Therefore, a drop of the BTA-solution was placed on the grid and the solution was allowed to rest for 20 seconds. The supernatant solvent was subsequently removed with the help of a cellulose filter paper.

Raman coupled light microscope

For the Raman imaging, a WITec alpha300 RA⁺ device was used. For the sample preparation, a molecularly dissolved BTA solution at elevated temperatures was dropped on a glass slide. Supramolecular structures were formed upon cooling and evaporation. Raman spectra were recorded with a 532 nm laser using a high-resolution CCD camera. During Raman-Spectral-Imaging, a complete Raman-spectrum at each pixel was recorded of the previously taken optical microscopic image.

UV/Vis-Spectroscopy

UV/Vis-spectra were recorded with a Jasco V-670 using aqueous suspensions. Polystyrene disposable cuvettes with a capacity of 2.5 mL were used for the measurements. Typically, all measurements were performed in a spectral range from 800 nm to 250 nm with a scanning speed of 1000 nm/min.

Solubility Studies

Solubility of the 1,3,5-benzenetrisamides was investigated with the help of a Crystal16[®] device from Technobis™ by measuring the photo turbidity with a 645 nm laser. These studies were performed simultaneously in four reactors with four chambers each, whereby each reactor can be cooled and heated independently. The maximal useable operating temperature range was from -15 °C to 150 °C.

Metal ion detection

The metal ion concentration during the adsorption tests was determined by ICP-OES (atomic emission spectroscopy with inductively coupled plasma) on a Plasmaquant PQ 9000 Elite from Analytik Jena.

6.3 Synthesis

6.3.1 Synthesis of the peripheral sulfur-containing amine side groups

General synthetic procedure to 2-(alkylthio)ethylamine

The syntheses of the amines for the BTAs 3 to 9 were carried out in a similar manner as described by Kohn et al.^[162] Approx. 7.5 mmol of 2-mercaptoethylamine hydrochloride was added to a solution of 2 eq. (15 mmol) NaOH in 30 mL of methanol. The solution was stirred under an inert gas atmosphere. After the full dissolution of all components, 1 eq. (7.5 mmol) of the respective 1-bromo-alkane was added. The solution was stirred over night at room temperature (approximately 15 h), following by filtration and subsequent removal of the solvent. The crude product was obtained as an oil which was dissolved in diethyl ether and filtrated afterwards. The solvent was removed under vacuum. The obtained oil was purified by vacuum distillation. The product was achieved as colorless oil. The yield of the amines was in a range of 32-74 %.

Synthesis of 2-(isopropylthio)ethanamine

The reaction to 2-(isopropylthio)ethanamine was carried out according to the general synthetic procedure to 2-(alkylthio)ethylamine. The product was obtained as colorless oil in 20 % yield.

Characterization:

¹H-NMR (300 MHz, CDCl₃):

δ (ppm) = 1.3 (d, J = 6.9 Hz, 6 H); 2.65 (t, J = 6.3 Hz, 2 H,); 2.88 (m, 2 H); 7.28 (s, 2H).

Synthesis of 2-(isobutylthio)ethanamine

The reaction to 2-(isobutylthio)ethanamine was carried out according to the general synthetic procedure to 2-(alkylthio)ethylamine. The product was obtained as colorless oil in 49 % yield.

Characterization:

¹H-NMR (300 MHz, DMSO):

δ (ppm) = 0.94 (d, J = 6.6 Hz, 6 H); 1.67 (m, 1 H,); 2.36 (d, J = 6.9 Hz, 2 H); 2.64 (m, 2 H); 2.93 (s, 2 H)

Synthesis of 2-(sec-butylthio)ethanamine

The reaction to 2-(sec-butylthio)ethanamine was carried out according to the general synthetic procedure to 2-(alkylthio)ethylamine. The product was obtained as colorless oil in 31 % yield.

Characterization:

¹H-NMR (300 MHz, DMSO):

δ (ppm) = 0.916 (t, J = 7.3 Hz, 3 H); 1.19 (d, J = 6.9 Hz, 3 H); 1.45 (m, 2 H); 2.49 (m, 2 H); 2.63 (m, 2 H).....

Synthesis of 2-((2-ethylbutyl)thio)ethanamine

The reaction to 2-((2-ethylbutyl)thio)ethanamine was carried out according to the general synthetic procedure to 2-(alkylthio)ethylamine. The product was obtained as colorless oil in 61 % yield.

Characterization:

¹H-NMR (300 MHz, DMSO):

δ (ppm) = 0.83 (t, J = 7.2, 6 H); 1.34 (m, 5 H); 2.46 (m, 4 H); 2.65 (t, J = 6.9, 2 H)

Synthesis of 2-((2-methylbutyl)thio)ethanamine

The reaction to 2-((2-methylbutyl)thio)ethanamine was carried out according to the general synthetic procedure to 2-(alkylthio)ethylamine. The product was obtained as colorless oil in 32 % yield.

Characterization:

¹H-NMR (300 MHz, CDCl₃):

δ (ppm) = 0.91 (t, J = 7.5 Hz, 3 H); 1.00 (d, J = 6.6 Hz, 3 H); 1.23 (m, 1 H); 1.53 (m, 2 H); 1.97 (s, 1 H); 2.37 (m, 1 H); 2.54 (m, 1 H); 2.63 (t, J = 6.3 Hz, 2 H); 2.90 (t, J = 6.3 Hz, 2 H)

Synthesis of 2-(isopentylthio)ethanamine

The reaction to 2-(isopentylthio)ethanamine was carried out according to the general synthetic procedure to 2-(alkylthio)ethylamine. The product was obtained as colorless oil in 76 % yield.

Characterization:

¹H-NMR (300 MHz, DMSO):

δ (ppm) = 0.870 (d, J = 6.6 Hz, 6 H); 1.39 (m, 2 H); 1.62 (m, 1 H); 2.4 (m, 1 H); 2.63 (t, J = 6.9 Hz, 2 H), 3.16 (d, J = 5.4 Hz, 1 H); 3.37 (d, J = 6.9 Hz, 2 H).....

Synthesis of 2-(propylthio)ethanamine

The reaction to 2-(propylthio)ethanamine was carried out according to the general synthetic procedure to 2-(alkylthio)ethylamine. The product was obtained as colorless oil in 50 % yield.

Characterization:

¹H-NMR (300 MHz, DMSO):

δ (ppm) = 0.93 (t, J = 7.5 Hz, 3 H); 1.53 (m, 2 H); 2.45 (m, 4 H); 2.64 (m, 2 H)

Synthesis of L-methyl-2-amino-3-(methylthio)propanoate

For the synthesis of L-methyl-2-amino-3-(methylthio)propanoate, 0.096 mol of thionyl chloride were slowly added to 40 mL of methanol under inert gas and ice cooling. Then, 0.074 mol of S-methyl-L-cysteine were added. The reaction mixture was stirred at room temperature until all solid components

were dissolved. Methanol and thionyl chloride were drawn off and the product was completely dried with a yield of 99%.

$^1\text{H-NMR}$ (300 MHz, DMSO):

δ (ppm) = 2.11 (s, 3 H); 3.02 (d, J = 6.3 Hz, 2 H); 3.36 (s, 3 H); 4.30 (t, J = 5.7 Hz, 1 H); 8.74 (s, 2 H)

Synthesis of 2-Ethyl 4-(Methylthio)-butan-1-amine

Synthesis of (E)-2-ethyl-4-(methylthio)but-2-enenitrile

N-Butyllithium (1.6 M in hexane) and 90 mL THF (99.5 %) were set under argon atmosphere and cooling with a dry ice acetone mixture (-80 °C). Subsequently, diisopropylamine (0.143 mol) in 67.5 mL THF was added slowly dropwise under stirring for 10 minutes. Afterwards, butyronitrile (0.0674 mol) in 67.5 mL THF was added slowly dropwise. The solution was stirred for 45 minutes. Diethylchlorophosphate (97 %, 0.0678 mol) in 67.5 mL THF was added slowly dropwise to the solution. After that, the solution was stirred for 30 minutes. Then, 2-(methylthio)acetaldehyde (0.031 mol) was added and the solution was stirred overnight under cooling. For the work-up, the solution was placed in a separatory funnel and 130 mL water, 40 mL HCl (37 %) and 100 mL DCM were added. The solution was extracted three times with DCM. Afterwards, the DCM phase was dried with sodium sulfate and the solvent was removed after filtration. Subsequently, the solution was purified by liquid chromatography. As eluent hexane : ethyl acetate (20 : 1 and later 10 : 1) was used. The solvent was removed and the product was obtained with a yield of 71 %.

$^1\text{H-NMR}$ (300 MHz, CDCl_3):

δ (ppm) = 1.19 (t, J = 7.5 Hz, 3 H); 2.08 (s, 3 H); 2.26 (m, 2 H) 3.24 (d, J = 8.1 Hz, 2 H); 6.53 (tt, J = 8.1 Hz, 1 H)

Synthesis of 2-ethyl-4-(methylthio)butanenitrile

(E)-2-ethyl-4-(methylthio)but-2-enenitrile (0.035 mol) was placed into a hydrogenation reactor with 5 g of Wilkinson-catalysator, 250 mL benzene and 9 mL ethanol. The reaction was performed under a hydrogen atmosphere with 3 bar pressure and a temperature of 35 °C for more than 72 h. After the hydrogenation step, the solvent was removed. The product was purified by liquid chromatography. As eluent 600 mL hexane : ethyl acetate (20 : 1) and 2 x 800 mL (10 : 1) were used. The solvent was rotary evaporated, 10 mL chloroform were added and removed under vacuum. The product was obtained with a yield of 79 %.

$^1\text{H-NMR}$ (300 MHz, CDCl_3):

δ (ppm) = 1.21 (t, J = 7.5 Hz, 3 H); 1.67 (quint., J = 7.2 Hz, 2 H); 1.84 (m, 2 H); 2.14 (s, 3 H); 2.62 (m, 2 H)

Synthesis of 2-Ethyl 4-(Methylthio)-butan-1-amine

For the synthesis, *2-ethyl-4-(methylthio)butanenitrile* (0.0276 mol) was dissolved in ether and dropped under ice cooling to a LiAlH_4 solution in ether. After the complete addition, the ice bath was removed and the solution was stirred for about 24 h. For the work-up of the product, about 100 mL of a saturated NaOH solution were added to the synthesis solution under ice-cooling. The result is a white solid. 200 ml of a half-molar potassium sodium tartrate solution and 100 ml of water were added to this solid. This solution was extracted four times with ether. The ether phase was washed with brine solution and then dried with sodium sulfate. The ether phase was removed under vacuum. The product was obtained with a yield of 99 %.

$^1\text{H-NMR}$ (300 MHz, CDCl_3):

δ (ppm) = 0.89 (t, $J = 7.5$ Hz, 3 H); 1.37 (m, 2 H); 1.54 (m, 2 H); 1.62 (m, 1 H); 2.11 (s, 3 H); 2.51 (t, $J = 8.1$ Hz, 2 H), 2.66 (d, $J = 5.7$ Hz, 2 H)

6.3.2 Synthesis of 1,3,5-benzenetrisamides*General synthetic procedure to 1,3,5-benzenetrisamides based on 1,3,5-benzenetricarboxylic acid*

In a typical procedure to the 1,3,5-benzenetrisamides, about 3.3 eq of the corresponding amine and a tip of a spatula of dry LiCl were added to 200 mL of tetrahydrofuran (THF) under inert gas. To this solution, dry pyridine or triethylamine (> 4 eq) was added and the solution was cooled to ~ 5 °C. Subsequently, 1 eq. of 1,3,5-benzenetricarboxylic acid trichloride was slowly added. Afterwards, the solution was stirred to complete conversion at ~ 70 °C overnight (approximately 15 h). Product isolation of the solid compounds was carried out by precipitation of the reaction mixture in water under vigorous stirring. The precipitate was filtered off and dried under high vacuum. Customary purification processes included recrystallization or boiling in solvent to achieve the desired product. In general, the product is obtained as a white powder.

Synthesis of N,N',N''-tris[2-(methylthio)ethyl]-1,3,5-Benzenetricarboxamid (BTA 1)

The reaction was carried out according to the general synthetic procedure to BTAs. After recrystallization from methanol, BTA 1 was obtained as white powder in 69 % yield.

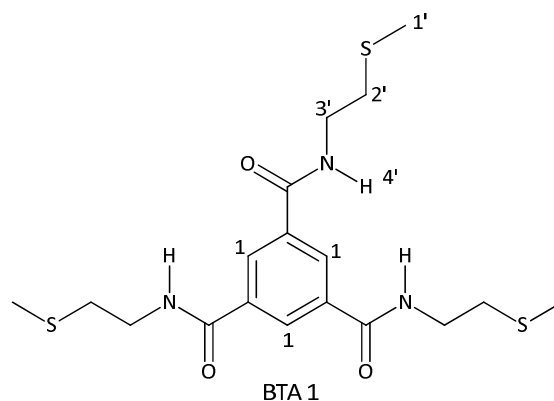


Table 6.1: Used components and amounts for synthesis and work-up.

		Sample weight (molar)
Core	1,3,5-Benzenetricarbonyl trichloride	5 g (0.0548 mol)
Amine	2-(Methylthio)ethylamine	4.41 g (0.0116 mol)
Recrystallization	Methanol	200 mL

Characterization:

¹H-NMR (300 MHz, DMSO, 25 °C):

δ (ppm) = 2.11 (s, 3 H, H_{1'}); 2.67 (t, 2 H, J = 6.6 Hz, H_{2'}); 3.48 (td, 2 H, J = 7.2 Hz, H_{3'}); 8.42 (s, 1 H, H_{4'}); 8.87 (t, 1 H, J = 5.7, H_{4'})

FTIR-Spectroscopy (ATR):

3228 cm⁻¹; 3052 cm⁻¹; 2911 cm⁻¹; 1631 cm⁻¹; 1552 cm⁻¹; 1428 cm⁻¹; 1300 cm⁻¹; 1229 cm⁻¹; 716 cm⁻¹; 689 cm⁻¹

MS:

429 (M⁺) M/z; 355 M/z; 339 M/z; 281 M/z; 265 M/z; 208 M/z; 103 M/z; 74 M/z

DSC-Measurement:

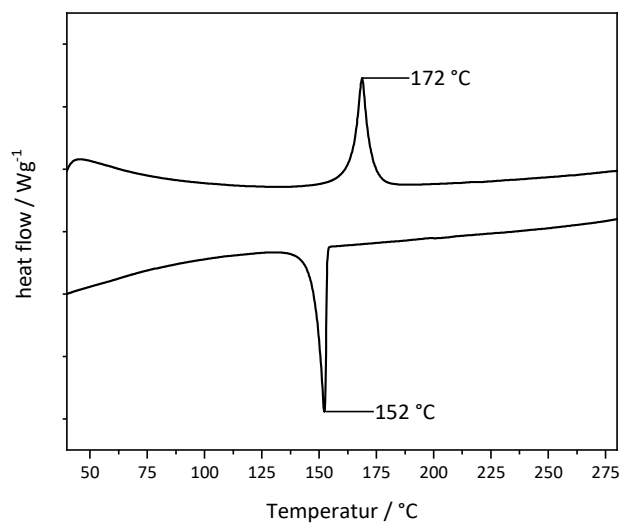


Figure 6.1: DSC heating and cooling scans of BTA 1. DSC data were recorded at a scanning rate of 10 K/min at temperatures ranging from 30 to 275 °C.

Thermogravimetric analysis:

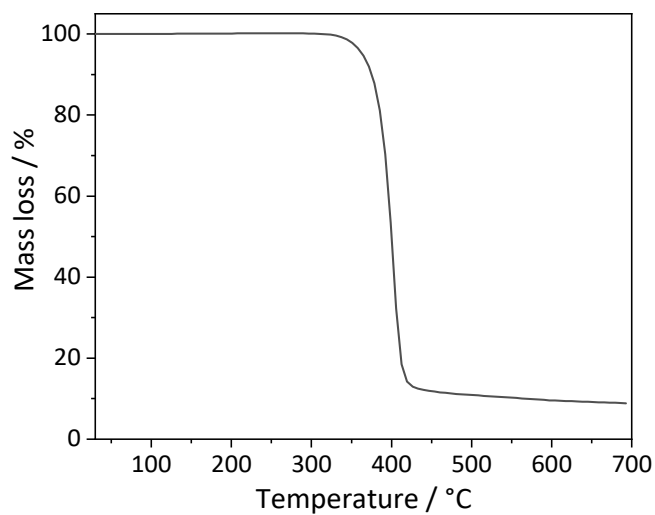


Figure 6.2: Thermogravimetric analysis curve of BTA 1. TGA data were recorded at a scanning rate of 10 K/min under a nitrogen atmosphere at temperatures ranging from 30 °C to 700 °C.

Synthesis of N,N',N''-tris[3-(methylthio)propyl]-1,3,5-benzenetricarboxamid (BTA 2)

The reaction was carried out according to the general synthetic procedure to BTAs. After recrystallization from hexane, BTA 2 was obtained as white powder in 72 % yield.

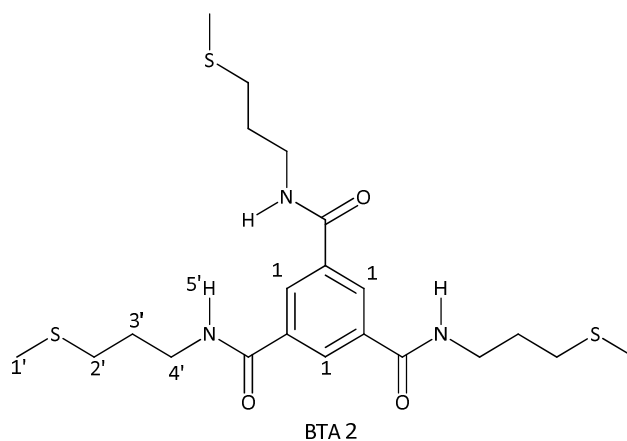


Table 6.2: Used components and key data for the synthesis of BTA 2.

		Sample weight (molar)
Core	1,3,5-Benzenetricarbonyl trichloride	3.5 g (0.0132 mol)
Amine	3-Methylthiopropylamine	4.6 g (0.0437 mol)
Recrystallization	Hexane	200 mL

Characterization:

¹H-NMR (300 MHz, CDCl₃, 25 °C):

δ (ppm) = 1.92 (tt, 2 H, J = 6.9 Hz, H_{3'}); 2.13 (s, 3 H, H_{1'}), 2.59 (t, 2 H, J = 7.05 Hz, H_{2'}), 3.53 (dt, 2 H, J = 5.88, H_{4'}); 7.78 (s, 1 H, H₁) 7.83 (s, 1 H, H_{5'})

FTIR-Spectroscopy (ATR):

3234 cm⁻¹; 3071 cm⁻¹; 2917 cm⁻¹; 1631 cm⁻¹; 1555 cm⁻¹; 1429 cm⁻¹; 1298 cm⁻¹; 1282 cm⁻¹; 1072 cm⁻¹; 690 cm⁻¹

MS:

471 (M⁺⁺) M/z; 456 M/z; 424 M/z; 367 M/z; 340 M/z; 319 M/z; 264 M/z; 207 M/z; 106 M/z; 61 M/z

DSC-Measurement:

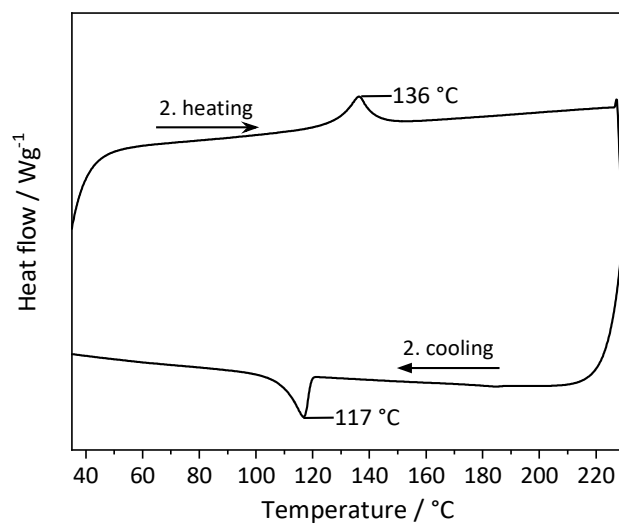


Figure 6.3: DSC heating and cooling scans of BTA 2. DSC data were recorded at a scanning rate of 10 K/min at temperatures ranging from 30 to 230 °C.

Thermogravimetric analysis:

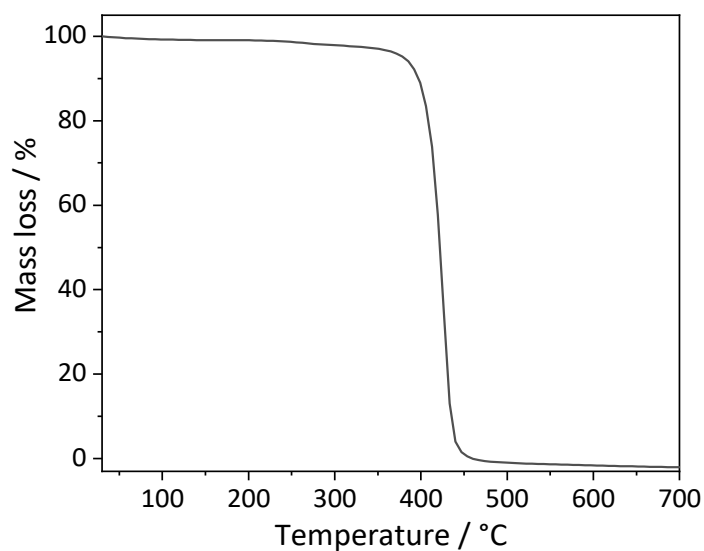


Figure 6.4: Thermogravimetric analysis curve of BTA 2. TGA data were recorded at a scanning rate of 10 K/min under a nitrogen atmosphere at temperatures ranging from 30 °C to 700 °C.

Synthesis of N',N'',N'''-tris(2-(isopropylthio)ethyl)benzene-1,3,5-tricarboxamide (BTA 3)

The reaction was carried out according to the general synthetic procedure to BTAs. BTA 3 was obtained as white powder in 99% yield.

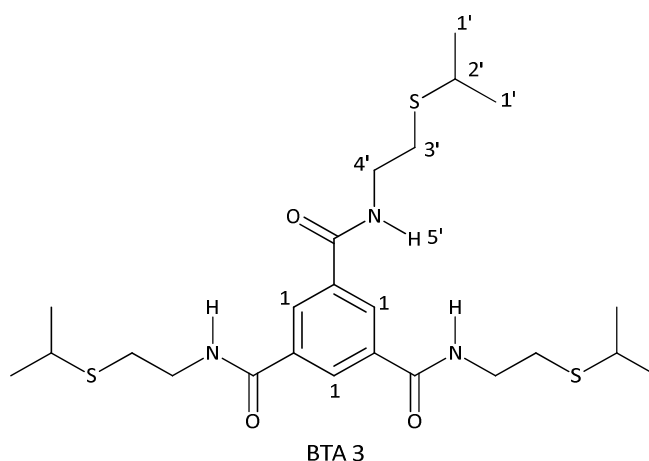


Table 6.3: Used components and key data for the synthesis of BTA 3.

		Sample weight (molar)
Core	1,3,5-Benzenetricarbonyl trichloride	3 g (0.011 mol)
Amine	2-(Isopropylthio)ethanamine	4.5 g (0.038 mol)
Recrystallization	-	-

Characterization:

¹H-NMR (300 MHz, DMSO, 25 °C):

δ (ppm) = 1.22 (t, 6 H, J = 4.32 Hz, H_{1'}); 2.70 (t, 2 H, J = 7.11 Hz, H_{3'}); 3.02 (sep, 1 H, J = 6.66 Hz, H_{2'}); 3.43 (q, 2 H; J = 8.43 Hz, H_{4'}); 8.42 (s, 1 H, H₁); 8.90 (t, 1 H, H_{5'})

FTIR-Spectroscopy (ATR):

3234 cm⁻¹; 3067 cm⁻¹; 2957 cm⁻¹; 1628 cm⁻¹; 1551 cm⁻¹; 1442 cm⁻¹; 1291 cm⁻¹; 1231 cm⁻¹; 728 cm⁻¹; 688 cm⁻¹

MS:

514 (M⁺) M/z; 470 M/z; 439 M/z; 411 M/z; 309 M/z; 235 M/z; 102 M/z; 61 M/z

DSC-Measurement:

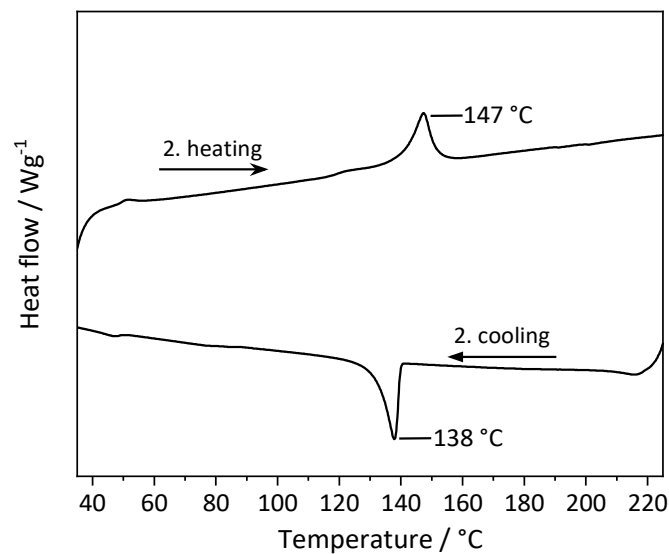


Figure 6.5: DSC heating and cooling scans of BTA 3. DSC data were recorded at a scanning rate of 10 K/min at temperatures ranging from 30 to 230 °C.

Thermogravimetric analysis:

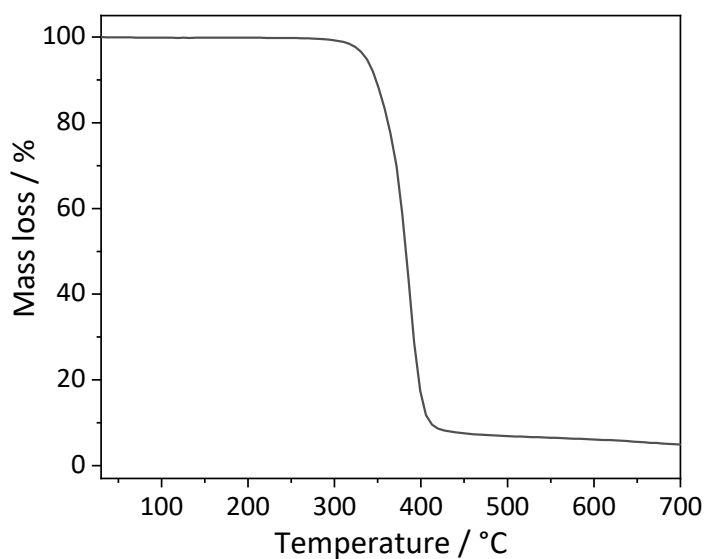


Figure 6.6: Thermogravimetric analysis curve of BTA 3. TGA data were recorded at a scanning rate of 10 K/min under a nitrogen atmosphere at temperatures ranging from 30 °C to 700 °C.

Synthesis of N',N'',N'''-tris(2-(isobutylthio)ethyl)benzene-1,3,5-tricarboxamide (BTA 4)

The reaction was carried out according to the general synthetic procedure to BTAs. BTA 4 was obtained as white powder in 100% yield.

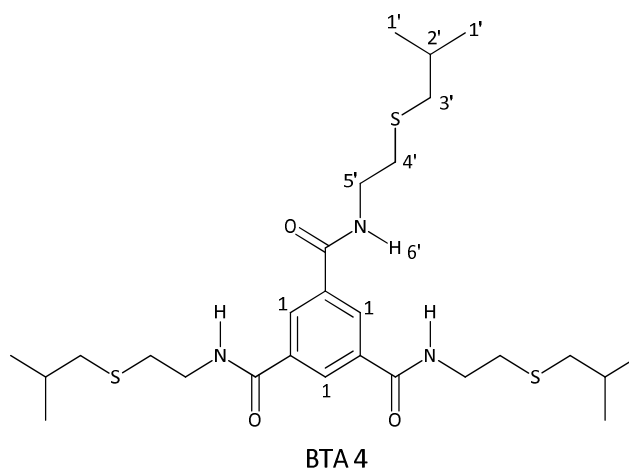


Table 6.4: Used components and key data for the synthesis of BTA 4.

		Sample weight (molar)
Core	1,3,5-Benzenetricarbonyl trichloride	6.8 g (0.025 mol)
Amine	2-(Isobutylthio)ethanamine	11.2 g (0.084 mol)
Recrystallization	-	-

Characterization:

¹H-NMR (300 MHz, DMSO, 25 °C):

δ (ppm) = 0.95 (d, 6 H, J = 6.66 Hz, H_{1'}); 1.76 (t sep, 1 H, J = 7.11 Hz, H_{2'}); 2.45 (d, 2 H, J = 6.87 Hz, H_{3'}); 2.67 (t, 2 H; J = 6.51 Hz, H_{4'}); 3.43 (q, 2 H; J = 6.87 Hz, H_{5'}); 8.42 (s, 1 H, H₁); 8.87 (t, 1 H, H_{6'})

FTIR-Spectroscopy (ATR):

3256 cm⁻¹; 3072 cm⁻¹; 2956 cm⁻¹; 1656 cm⁻¹; 1629 cm⁻¹; 1534 cm⁻¹; 1300 cm⁻¹; 1290 cm⁻¹; 703 cm⁻¹

MS:

555 (M⁺) M/z; 466 M/z; 439 M/z; 323 M/z; 280 M/z; 116 M/z; 101 M/z; 60 M/z

DSC-Measurement:

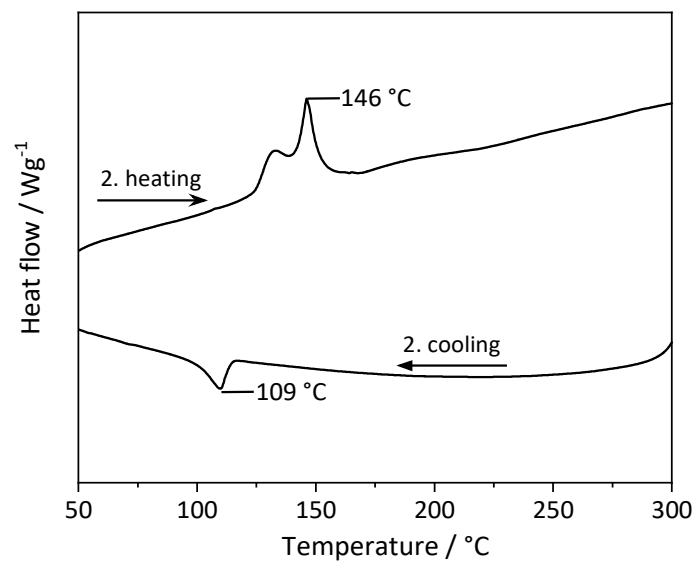


Figure 6.7: DSC heating and cooling scans of BTA 4. DSC data were recorded at a scanning rate of 10 K/min at temperatures ranging from 30 to 300 °C.

Thermogravimetric analysis:

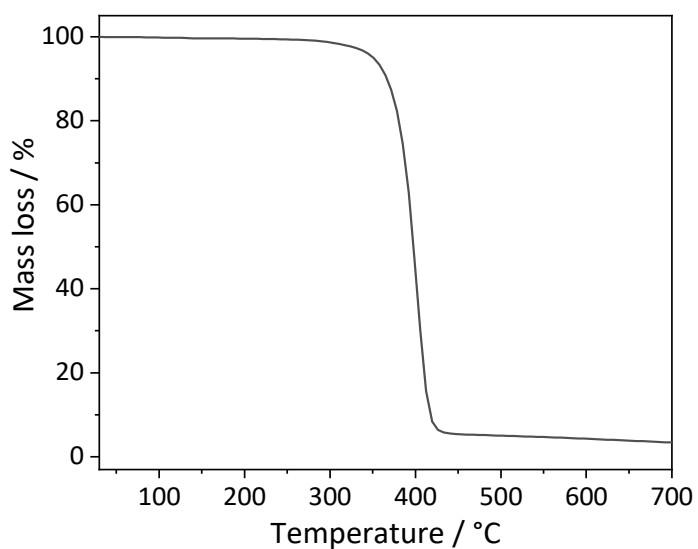


Figure 6.8: Thermogravimetric analysis curve of BTA 4. TGA data were recorded at a scanning rate of 10 K/min under a nitrogen atmosphere at temperatures ranging from 30 °C to 700 °C.

Synthesis of N',N'',N'''-tris(2-(sec-butylthio)ethyl)benzene-1,3,5-tricarboxamide (BTA 5)

The reaction was carried out according to the general synthetic procedure to BTAs. After recrystallization from methanol, BTA 5 was obtained as white powder in 69% yield.

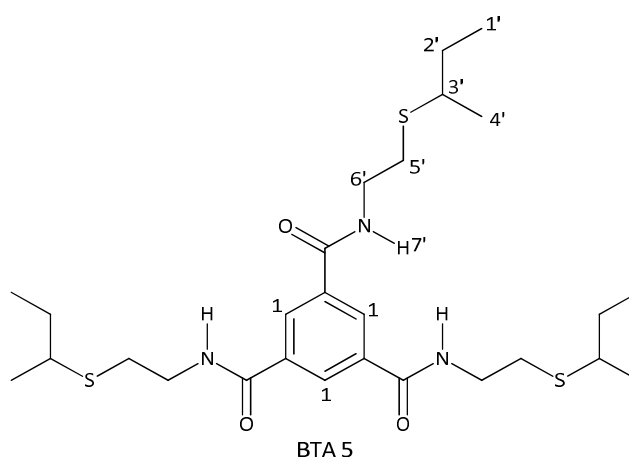


Table 6.5: Used components and key data for the synthesis of BTA 5.

		Sample weight (molar)
Core	1,3,5-Benzenetricarbonyl trichloride	5 g (0.0548 mol)
Amine	2-(Sec-butylthio)ethanamine	4.41 g (0.0116 mol)
Recrystallization	Methanol	200 mL

Characterization:

¹H-NMR (300 MHz, DMSO, 25 °C):

δ (ppm) = 0.92 (t, 3 H, J = 7.41 Hz, H_{1'}); 1.23 (d, 2 H, J = 6.75 Hz, H_{4'}); 1.52 (m, 2 H, H_{2'}); 2.69 (t, 2 H, J = 7.02 Hz, H_{5'}); 2.80 (m, 1 H, H_{3'}); 3.42 (dt, 2 H, J = 8.43 Hz, H_{6'}); 8.42 (s, 1 H, H₁); 8.89 (t, 1 H, J = 5.58 Hz, H_{7'})

FTIR-Spectroscopy (ATR):

3232 cm⁻¹; 3066 cm⁻¹; 2962 cm⁻¹; 1628 cm⁻¹; 1551 cm⁻¹; 1449 cm⁻¹; 1290 cm⁻¹; 1223 cm⁻¹; 689 cm⁻¹

MS:

555 (M⁺) M/z; 498 M/z; 467 M/z; 439 M/z; 323 M/z; 235 M/z; 116 M/z; 60 M/z

DSC-Measurement:

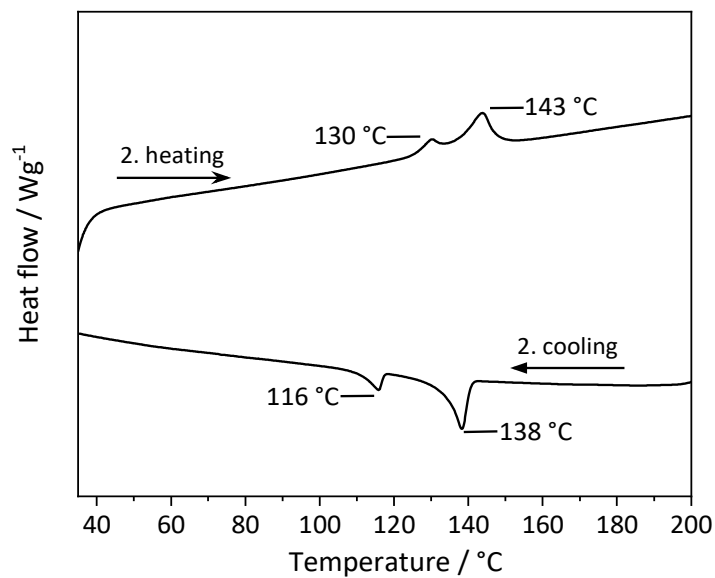


Figure 6.9: DSC heating and cooling scans of BTA 5. DSC data were recorded at a scanning rate of 10 K/min at temperatures ranging from 30 to 200 °C.

Thermogravimetric analysis:

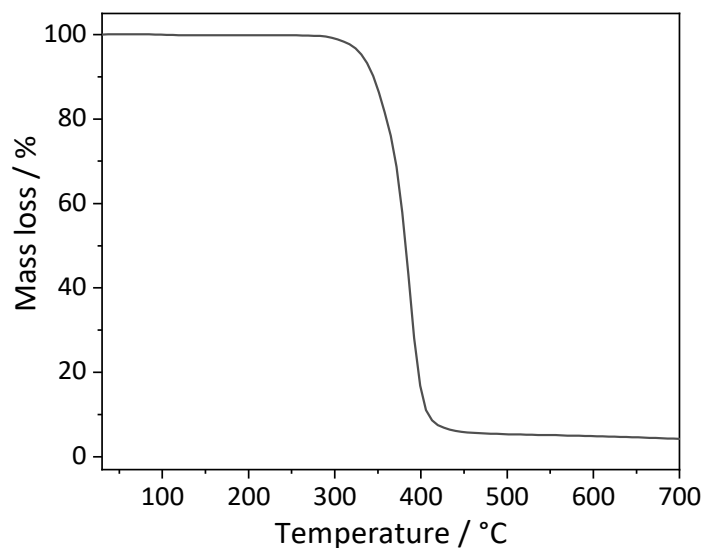


Figure 6.10: Thermogravimetric analysis curve of BTA 5. TGA data were recorded at a scanning rate of 10 K/min under a nitrogen atmosphere at temperatures ranging from 30 °C to 700 °C.

Synthesis of N',N'',N'''-tris(2-((2-ethylbutyl)thio)ethyl)benzene-1,3,5-tricarboxamide (BTA 6)

The reaction was carried out according to the general synthetic procedure to BTAs. After recrystallization from ethanol, BTA 6 was obtained as white powder in 50 % yield.

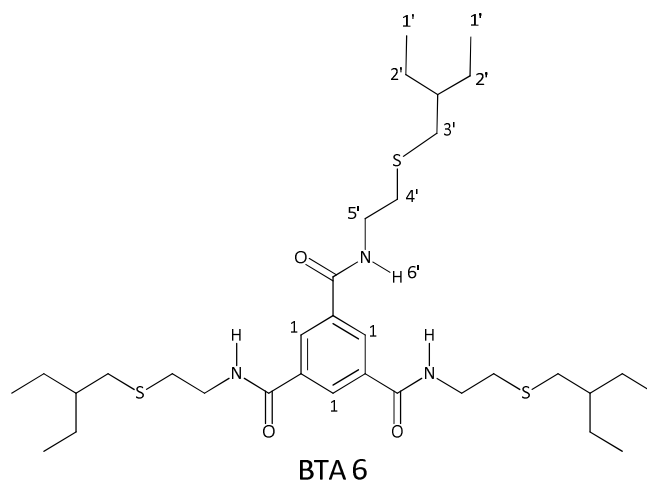


Table 6.6: Used components and key data for the synthesis of BTA 6.

		Sample weight (molar)
Core	1,3,5-Benzenetricarbonyl trichloride	7.5 g (0.028 mol)
Amine	2-((2-Ethylbutyl)thio)ethanamine	15 g (0.093 mol)
Recrystallization	Ethanol	200 mL

Characterization:

¹H-NMR (300 MHz, DMSO, 25 °C):

δ (ppm) = 0.83 (t, 6 H, J = 7.3 Hz, H_{1'}); 1.35 (m, 4 + 1 H, H_{2'+3'}); 2.67 (t, 2 H, J = 7.2 Hz, H_{4'}), 3.05 (dt, 2 H, J = 6.2 Hz, H_{5'}); 8.42 (s, 1 H, H₁); 8.87 (t, 1 H, J = 5.6, H_{6'})

FTIR-Spectroscopy (ATR):

3235 cm⁻¹; 3070 cm⁻¹; 2959 cm⁻¹; 2873 cm⁻¹; 1628 cm⁻¹; 1556 cm⁻¹; 1457 cm⁻¹; 1292 cm⁻¹; 1229 cm⁻¹; 689 cm⁻¹

MS:

640 (M⁺⁺) M/z; 495 M/z; 351 M/z; 144 M/z; 115 M/z; 82 M/z; 40 M/z

DSC-Measurement:

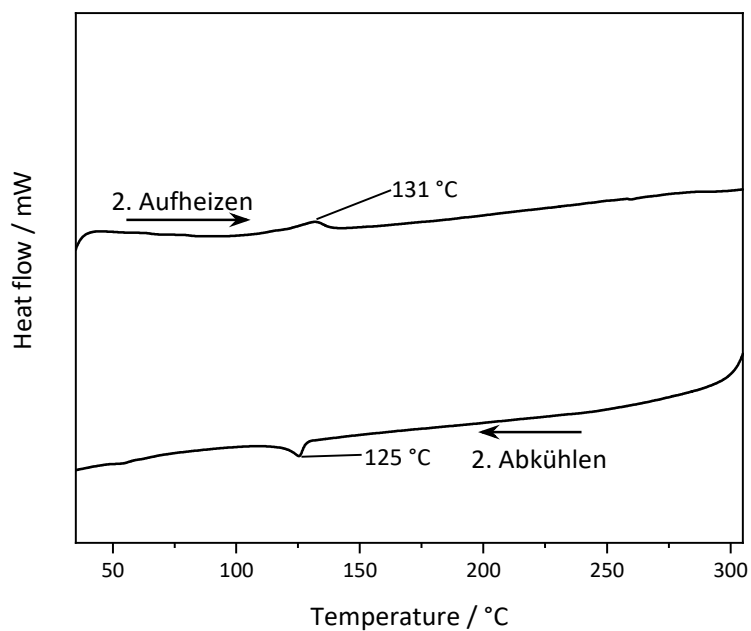


Figure 6.11: DSC heating and cooling scans of BTA 6. DSC data were recorded at a scanning rate of 10 K/min at temperatures ranging from 30 to 300 °C.

Thermogravimetric analysis:

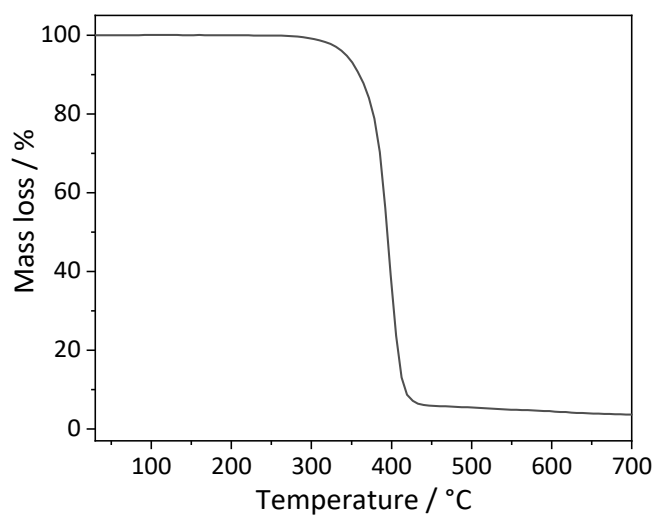


Figure 6.12: Thermogravimetric analysis curve of BTA 6. TGA data were recorded at a scanning rate of 10 K/min under a nitrogen atmosphere at temperatures ranging from 30 °C to 700 °C.

Synthesis of N',N'',N'''-tris(2-((2-methylbutyl)thio)ethyl)benzene-1,3,5-tricarboxamide (BTA 7)

The reaction was carried out according to the general synthetic procedure to BTAs. After recrystallization from methanol, BTA 7 was obtained as white powder in 90 % yield.

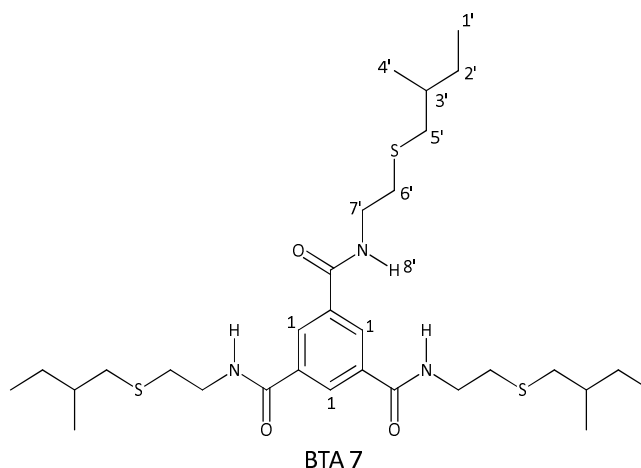


Table 6.7: Used components and key data for the synthesis of BTA 7.

		Sample weight (molar)
Core	1,3,5-Benzenetricarbonyl trichloride	0.8 g (0.0029 mol)
Amine	2-((2-Methylbutyl)thio)ethanamine	1.4 g (0.0095 mol)
Recrystallization	Methanol	10 mL

Characterization:

¹H-NMR (300 MHz, DMSO, 25 °C):

δ (ppm) = 0.85 (t, 3 H, J = 7.4 Hz, H_{1'}); 0.93 (d, 3H, J = 6.6 Hz, H_{4'}); 1.17 (m, 1 H, H_{3'}); 1.50 (m; 2 H, H_{2'}); 2.39 (dd, 1 H, J = 12.7, 7.4 Hz, H_{5'}); 2.57 (dd, 1 H, J = 12.7, 5.8 Hz, H_{5'}); 2.69 (t, 2 H, J = 8.1 Hz, H_{6'}); 3.45 (dt, 2 H, J = 6.1 Hz, H_{7'}); 8.45 (s, 1 H, H₁); 8.92 (t, 1 H, J = 5.6 Hz, H_{1'})

FTIR-Spectroscopy (ATR):

3233 cm⁻¹; 3067 cm⁻¹; 2958 cm⁻¹; 2922 cm⁻¹; 1630 cm⁻¹; 1553 cm⁻¹; 1456 cm⁻¹; 1291 cm⁻¹; 1231 cm⁻¹; 703 cm⁻¹; 689 cm⁻¹

MS:

597 (M⁺) M/z; 467 M/z; 337 M/z; 130 M/z; 70 M/z; 43 M/z

DSC-Measurement:

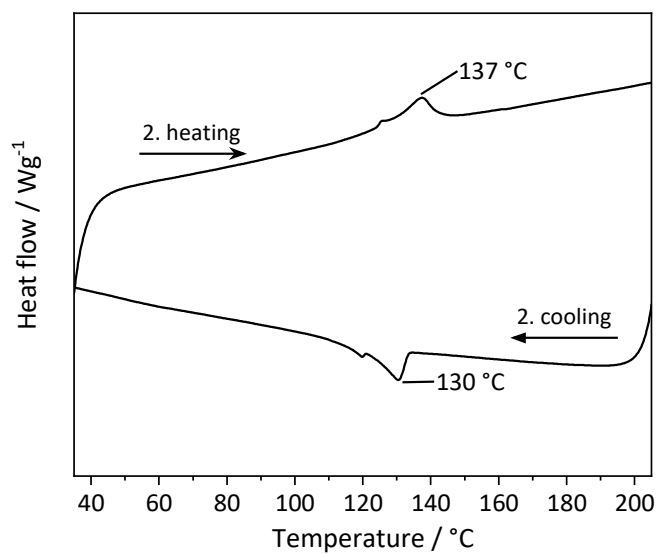


Figure 6.13: DSC heating and cooling scans of BTA 7. DSC data were recorded at a scanning rate of 10 K/min at temperatures ranging from 30 to 210 °C.

Thermogravimetric analysis:

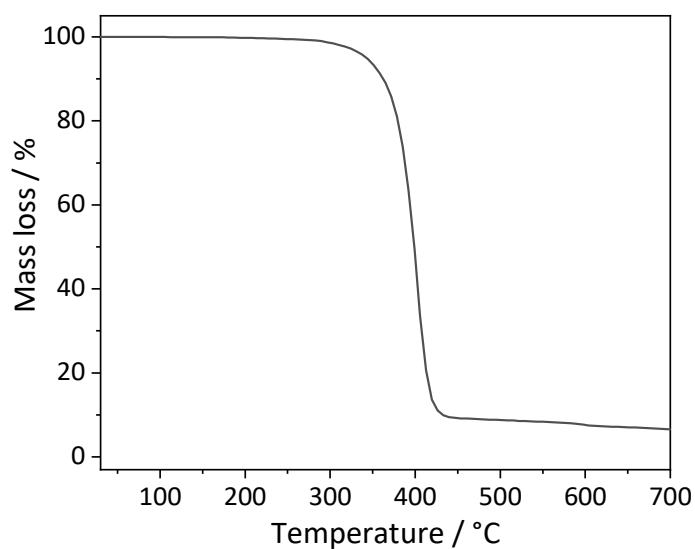


Figure 6.14: Thermogravimetric analysis curve of BTA 7. TGA data were recorded at a scanning rate of 10 K/min under a nitrogen atmosphere at temperatures ranging from 30 °C to 700 °C.

Synthesis of N',N'',N'''-tris(2-(isopentylthio)ethyl)benzene-1,3,5-tricarboxamide (BTA 8)

The reaction was carried out according to the general synthetic procedure to BTAs. After recrystallization from ethanol, BTA 8 was obtained as white powder in 73 % yield.

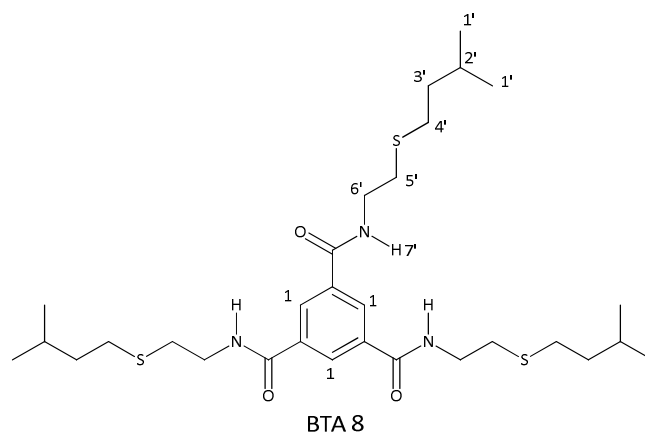


Table 6.8: Used components and key data for the synthesis of BTA 8.

		Sample weight (molar)
Core	1,3,5-Benzenetricarbonyl trichloride	9 g (0.034 mol)
Amine	2-(Isopentylthio)ethanamine	16.4 g (0.111 mol)
Recrystallization	Ethanol	400 mL

Characterization:

¹H-NMR (300 MHz, DMSO, 25 °C):

δ (ppm) = 0.87 (d, 6 H, J = 6.6 Hz, H_{1'}); 1.43 (m, 2 H; H_{3'}); 1.64 (m, 1 H, H_{2'}); 2.55 (m, 2H, H_{4'}); 2.69 (t, 2 H, J = 7.2 Hz, H_{5'}); 3.46 (dt, 2 H, J = 6.1 Hz, H_{6'}); 8.42 (s, 1H, H₁); 8.88 (t, 1 H, J = 5.6 Hz, H_{7'})

FTIR-Spectroscopy (ATR):

3254 cm⁻¹; 3070 cm⁻¹; 2954 cm⁻¹; 1656 cm⁻¹; 1629 cm⁻¹; 1533 cm⁻¹; 1463 cm⁻¹; 1290 cm⁻¹; 1266 cm⁻¹; 702 cm⁻¹

MS:

597 (M⁺) M/z; 4675 M/z; 337 M/z; 130 M/z; 115 M/z; 70 M/z; 43 M/z

DSC-Measurement:

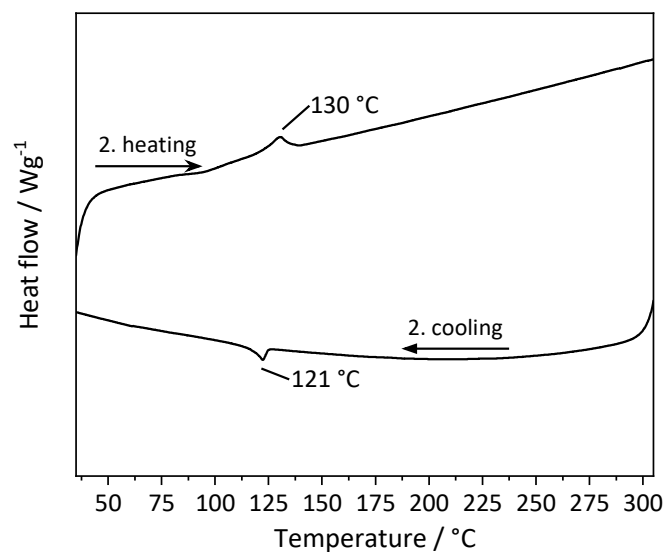


Figure 6.15: DSC heating and cooling scans of BTA 8. DSC data were recorded at a scanning rate of 10 K/min at temperatures ranging from 30 to 300 $^{\circ}\text{C}$.

Thermogravimetric analysis:

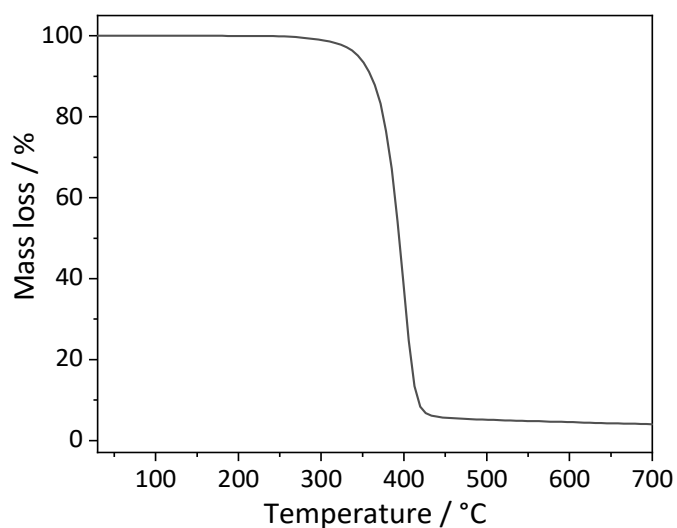


Figure 6.16: Thermogravimetric analysis curve of BTA 8. TGA data were recorded at a scanning rate of 10 K/min under a nitrogen atmosphere at temperatures ranging from 30 $^{\circ}\text{C}$ to 700 $^{\circ}\text{C}$.

Synthesis of N',N'',N'''-tris(2-(propylthio)ethyl)benzene-1,3,5-tricarboxamide (BTA 9)

The reaction was carried out according to the general synthetic procedure to BTAs. After recrystallization from methanol, BTA 9 was obtained as white powder in 79 % yield.

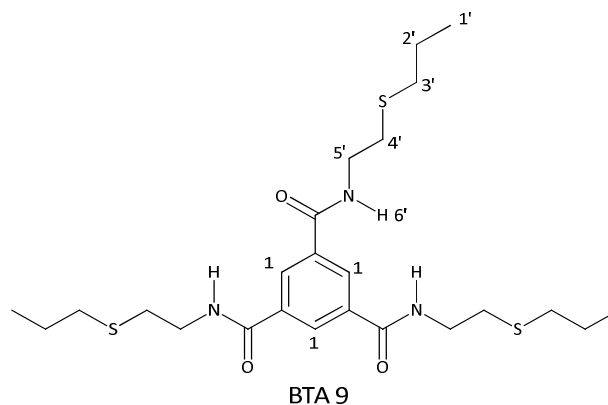


Table 6.9: Used components and key data for the synthesis of BTA 9.

		Sample weight (molar)
Core	1,3,5-Benzenetricarbonyl trichloride	8 g (0.03 mol)
Amine	2-(Propylthio)ethanamine	10.5 g (0.0998 mol)
Recrystallization	Methanol	200 mL

Characterization:

¹H-NMR (300 MHz, DMSO, 25 °C):

δ (ppm) = 0.94 (t, 1 H; J = 7.3 Hz, H_{1'}); 1.57 (qd; 2 H, J = 7.3 Hz, H_{2'}); 2.55 (2 H; J = 7.1 Hz; H_{3'}); 2.69 (t, 2 H, J = 7.5 Hz, H_{4'}); 3.46 (dt, 2 H, J = 6.1 Hz, H_{5'}); 8.42 (s, 1 H, H₁); 8.87 (t, 1 H, J = 5.6 Hz, H_{6'})

FTIR-Spectroscopy (ATR):

3253 cm⁻¹; 3075 cm⁻¹; 2961 cm⁻¹; 1656 cm⁻¹; 1627 cm⁻¹; 1534 cm⁻¹; 1455 cm⁻¹; 1290 cm⁻¹; 705 cm⁻¹

MS:

514 (M⁺) M/z; 411 M/z; 309 M/z; 293 M/z; 208 M/z; 102 M/z; 60 M/z; 43 M/z

DSC-Measurement:

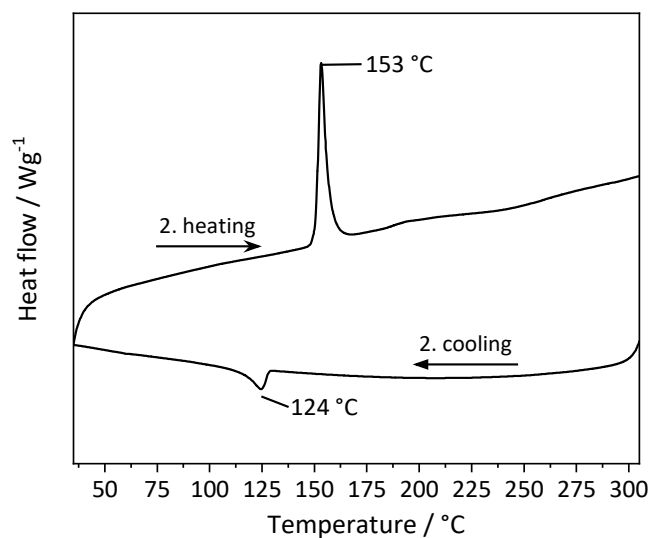


Figure 6.17: DSC heating and cooling scans of BTA 9. DSC data were recorded at a scanning rate of 10 K/min at temperatures ranging from 30 to 310 °C.

Thermogravimetric analysis:

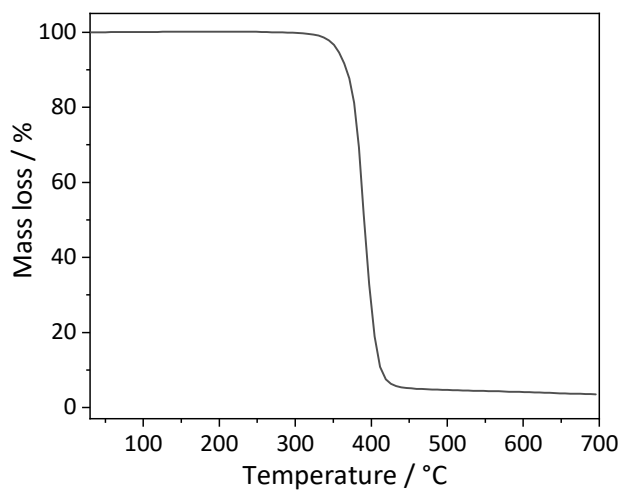


Figure 6.18: Thermogravimetric analysis curve of BTA 9. TGA data were recorded at a scanning rate of 10 K/min under a nitrogen atmosphere at temperatures ranging from 30 °C to 700 °C.

Synthesis of N',N'',N'''-tris(2-ethyl-4-(methylthio)butyl)benzene-1,3,5-tricarboxamide (BTA 10)

The reaction was carried out according to the general synthetic procedure to BTAs. BTA 10 was obtained as white powder in 90 % yield.

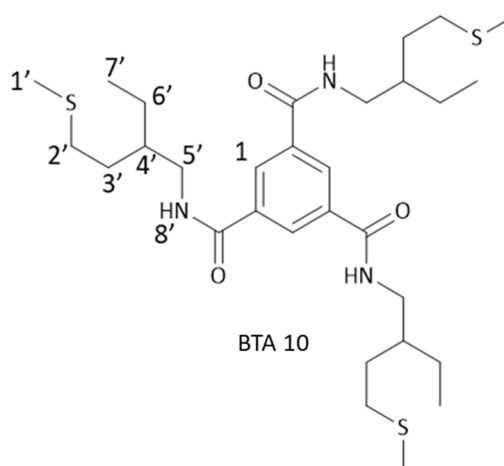


Table 6.10: Used components and key data for the synthesis of BTA 10.

		Sample weight (molar)
Core	1,3,5-Benzenetricarbonyl trichloride	1.9 g (0.0072 mol)
Amine	2-Ethyl-4-(methylsulfanyl)-1-butanamine	3.5 g (0.0238 mol)
Recrystallization	-	-

Characterization:

¹H-NMR (300 MHz, DMSO, 25 °C):

δ (ppm) = 0.89 (t, 3 H, J = 7.4 Hz, H_{7'}); 1.33 (m, 2 H, H_{3'}); 1.53 (m, 2 H, H_{6'}); 1.68 (m, 1 H, H_{4'}); 2.03 (s, 1H, H_{1'}); 2.55 (2 H, H_{2'}); 3.23 (m, 2 H, H_{5'}); 8.37 (s, 1 H, H₁); 8.66 (t, 1 H, J = 5.8 Hz; H_{8'})

FTIR-Spectroscopy (ATR):

3240 cm⁻¹; 3076 cm⁻¹; 2915 cm⁻¹; 1633 cm⁻¹; 1557 cm⁻¹; 1433 cm⁻¹; 1292 cm⁻¹; 726 cm⁻¹; 691 cm⁻¹

MS:

597 (M⁺) M/z; 550 M/z; 451 M/z; 420 M/z; 146 M/z; 130 M/z; 98 M/z; 61 M/z

DSC-Measurement:

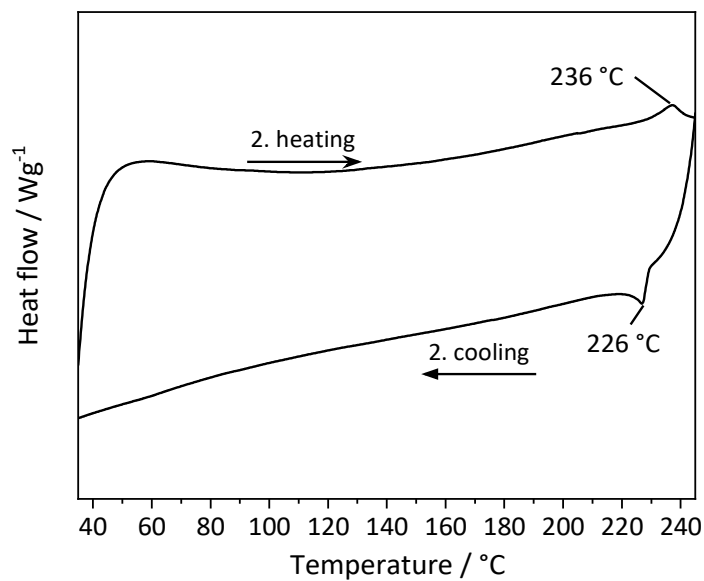


Figure 6.19: DSC heating and cooling scans of BTA 10. DSC data were recorded at a scanning rate of 10 K/min at temperatures ranging from 30 to 250 °C.

Thermogravimetric analysis:

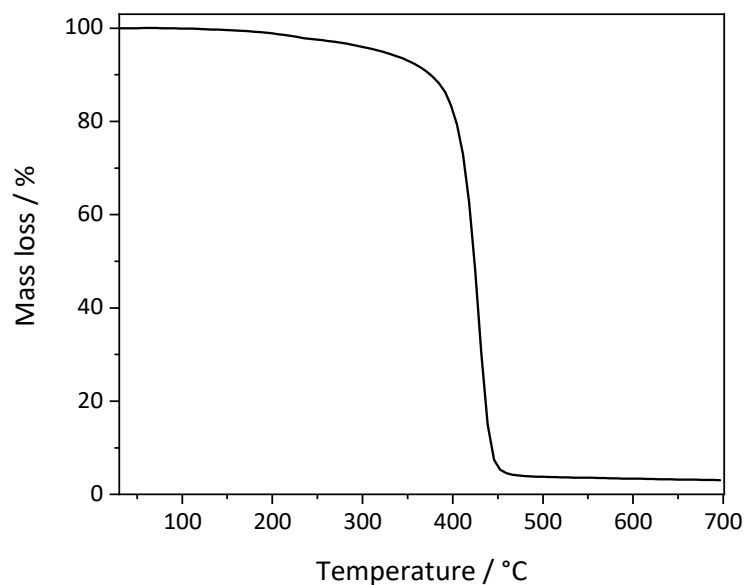


Figure 6.20: Thermogravimetric analysis curve of BTA 10. TGA data were recorded at a scanning rate of 10 K/min under a nitrogen atmosphere at temperatures ranging from 30 °C to 700 °C.

Synthesis of Trimethyl 2,2',2''-(Benzotricarbonyltris(azanediyl))tris(3-mercaptopropanoat) (BTA 11)

The reaction was carried out according to the general synthetic procedure to BTAs. After recrystallization from DMF, BTA 11 was obtained as white powder in 52 % yield.

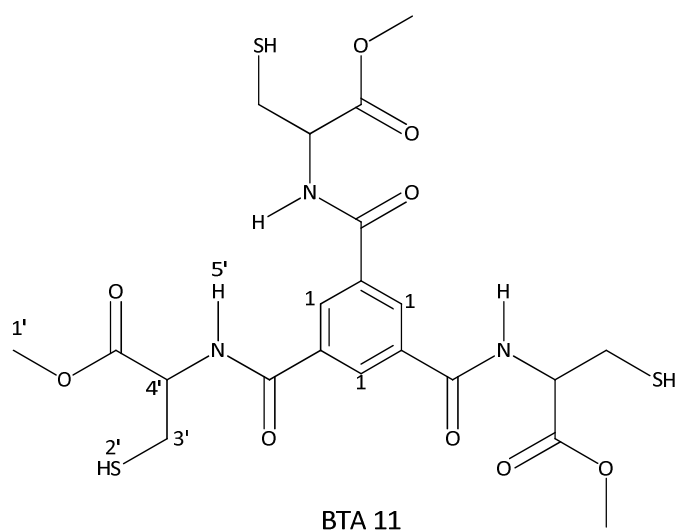


Table 6.11: Used components and key data for the synthesis of BTA 11.

		Sample weight (molar)
Core	1,3,5-Benzenetricarbonyl trichloride	3 g (11.3 mmol)
Amine	L-Cysteine methyl ester hydrochloride	6.4 g (37.3 mmol)
Recrystallization	DMF	10 mL

Characterization:

¹H-NMR (300 MHz, DMSO, 25 °C):

δ (ppm) = 2.72 (t, 1 H, J = 0.75 Hz, H_{2'}); 2.90 (m, 2 H, H_{3'}); 3.68 (s, 3 H, H₁); 4.64 (m, 1 H, H_{4'}); 8.54 (s, 1 H, H₁); 2.75 (d, 1 H, J = 7.56 Hz, H_{5'})

FTIR-Spectroscopy (ATR):

3227 cm⁻¹; 3058 cm⁻¹; 2951 cm⁻¹; 1744 cm⁻¹; 1639 cm⁻¹; 1547 cm⁻¹; 1436 cm⁻¹; 1336 cm⁻¹; 1296 cm⁻¹; 1253 cm⁻¹

MS:

561 (M⁺) M/z; 502 M/z; 484 M/z; 444 M/z; 427 M/z; 309 M/z; 265 M/z; 191 M/z; 76 M/z; 59 M/z

DSC-Measurement:

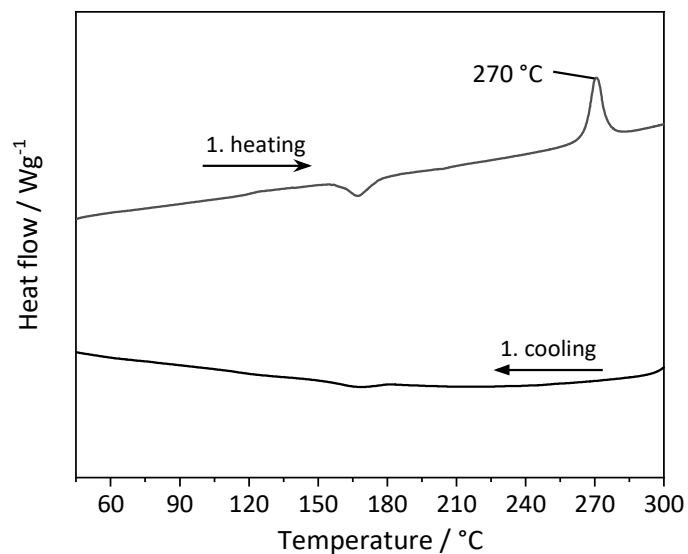


Figure 6.21: DSC heating and cooling scans of BTA 11. DSC data were recorded at a scanning rate of 10 K/min at temperatures ranging from 30 to 310 $^{\circ}\text{C}$.

Thermogravimetric analysis:

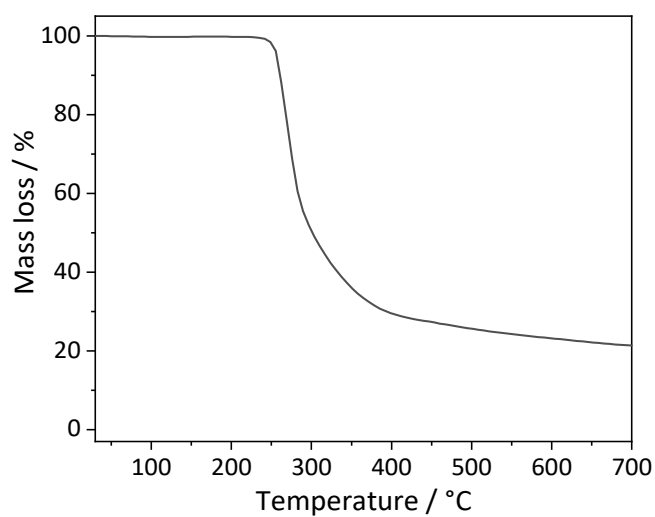


Figure 6.22: Thermogravimetric analysis curve of BTA 11. TGA data were recorded at a scanning rate of 10 K/min under a nitrogen atmosphere at temperatures ranging from 30 $^{\circ}\text{C}$ to 700 $^{\circ}\text{C}$.

Synthesis of (2S,2'S,2''S)-trimethyl 2,2',2''-(Benzotricarbonyltris(azanediyl))tris(3-(methylthio)propanoat) (BTA 12)

The reaction was carried out according to the general synthetic procedure to BTAs. After recrystallization from methanol, BTA 12 was obtained as white powder in 72 % yield.

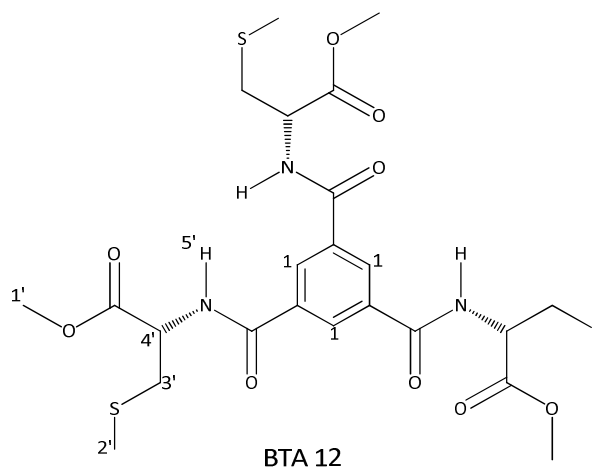


Table 6.12: Used components and key data for the synthesis of BTA 12.

		Sample weight (molar)
Core	1,3,5-Benzenetricarbonyl trichloride	2.89 g (10.9 mmol)
Amine	S-Methyl-L-cysteine-amide	5.37 g (36 mmol)
Recrystallization	Methanol	100 mL

Characterization:

¹H-NMR (300 MHz, DMSO, 25 °C):

δ (ppm) = 2.11 (s, 3 H, H_{2'}); 2.98 (m, 2 H, H_{3'}); 3.68 (s, 3 H, H_{1'}); 4.70 (m, 1 H, H_{4'}); 8.53 (s, 1 H, H₁); 9.28 (d, 1 H, J = 7.71 Hz, H_{5'})

FTIR-Spectroscopy (ATR):

3230 cm⁻¹; 3057 cm⁻¹; 2918 cm⁻¹; 1738 cm⁻¹; 1641 cm⁻¹; 1543 cm⁻¹; 1438 cm⁻¹; 1357 cm⁻¹; 1329 cm⁻¹; 1287 cm⁻¹

MS:

603 (M⁺) M/z; 555 M/z; 544 M/z; 496 M/z; 455 M/z; 339 M/z; 258 M/z; 208 M/z; 132 M/z; 75 M/z

DSC-Measurement:

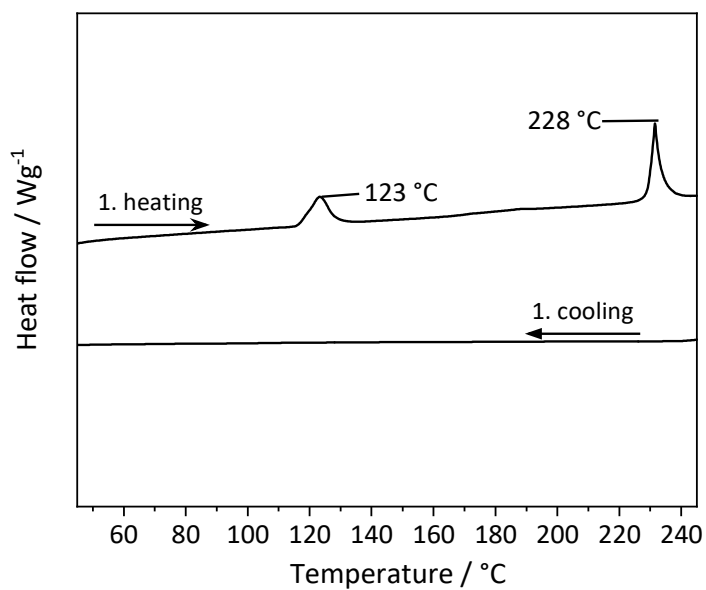


Figure 6.23: DSC heating and cooling scans of BTA 12. DSC data were recorded at a scanning rate of 10 K/min at temperatures ranging from 30 to 250 °C.

Thermogravimetric analysis:

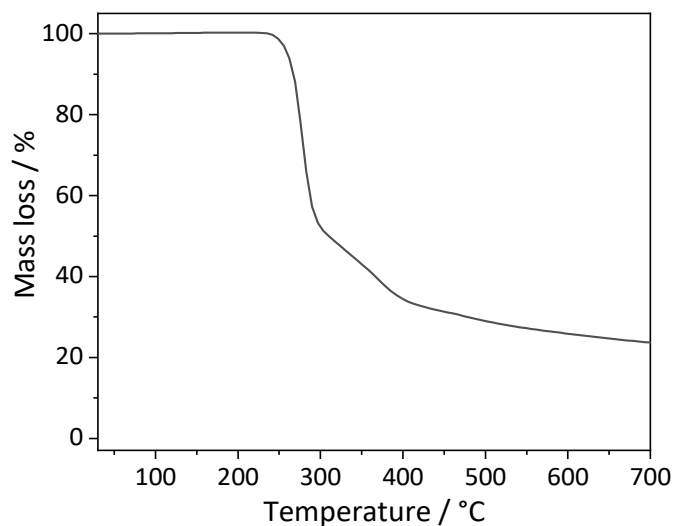


Figure 6.24: Thermogravimetric analysis curve of BTA 12. TGA data were recorded at a scanning rate of 10 K/min under a nitrogen atmosphere at temperatures ranging from 30 °C to 700 °C.

Synthesis of (2S,2'S,2''S)-trimethyl 2,2',2''-(Benzenetricarbonyltris(azanediy))tris(4-(methylthio)butanoat) (BTA 13)

The reaction was carried out according to the general synthetic procedure to BTAs. After recrystallization from methanol, BTA 13 was obtained as white powder in 58 % yield.

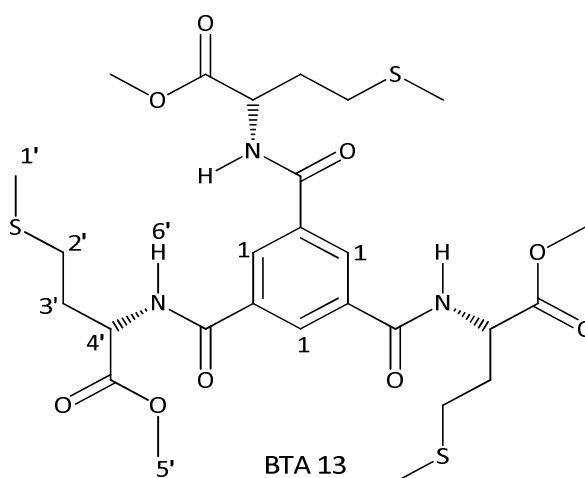


Table 6.13: Used components and key data for the synthesis of BTA 13.

		Sample weight (molar)
Core	1,3,5-Benzenetricarbonyl trichloride	9.7 g (36 mmol)
Amine	L-methioninmethylesterhydrochloride	24 g (120 mmol)
Recrystallization	Methanol	250 mL

Characterization:

$^1\text{H-NMR}$ (300 MHz, DMSO, 25 °C):

δ (ppm) = 2.09 (m, 5 H, $\text{H}_{1'}$, $\text{H}_{2'}$); 2.62 (m, 2 H, $\text{H}_{3'}$); 3.67 (s, 3 H, $\text{H}_{5'}$); 4.62 (m, 1 H, $\text{H}_{4'}$); 8.50 (s, 1 H, H_{1}); 9.16 (d; 1 H, $J = 7.38$ Hz, $\text{H}_{6'}$)

FTIR-Spectroscopy (ATR):

3222 cm^{-1} ; 3056 cm^{-1} ; 2951 cm^{-1} ; 1744 cm^{-1} ; 1635 cm^{-1} ; 1547 cm^{-1} ; 1435 cm^{-1} ; 1302 cm^{-1} ; 1207 cm^{-1} ; 1167 cm^{-1}

MS:

645 (M^{++}) M/z ; 571 M/z ; 536 M/z ; 483 M/z ; 435 M/z ; 376 M/z ; 332 M/z ; 217 M/z ; 164 M/z ; 75 M/z

DSC-Measurement:

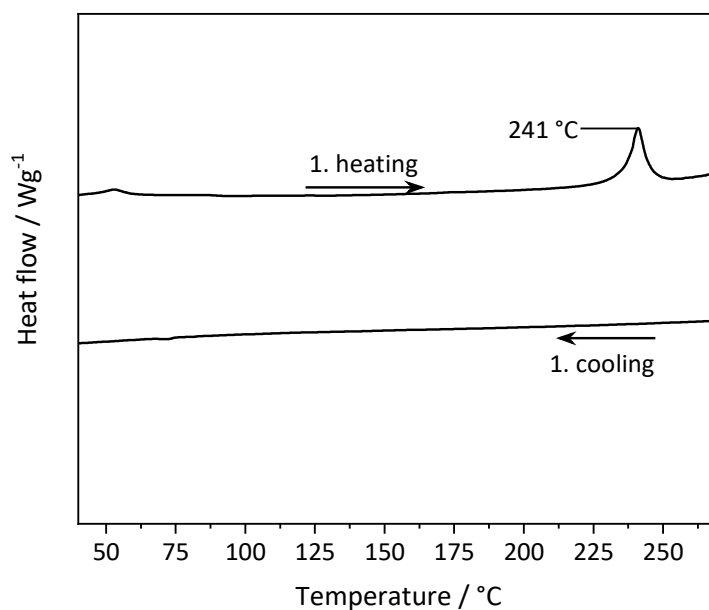


Figure 6.25: DSC heating and cooling scans of BTA 13. DSC data were recorded at a scanning rate of 10 K/min at temperatures ranging from 30 to 260 °C.

Thermogravimetric analysis:

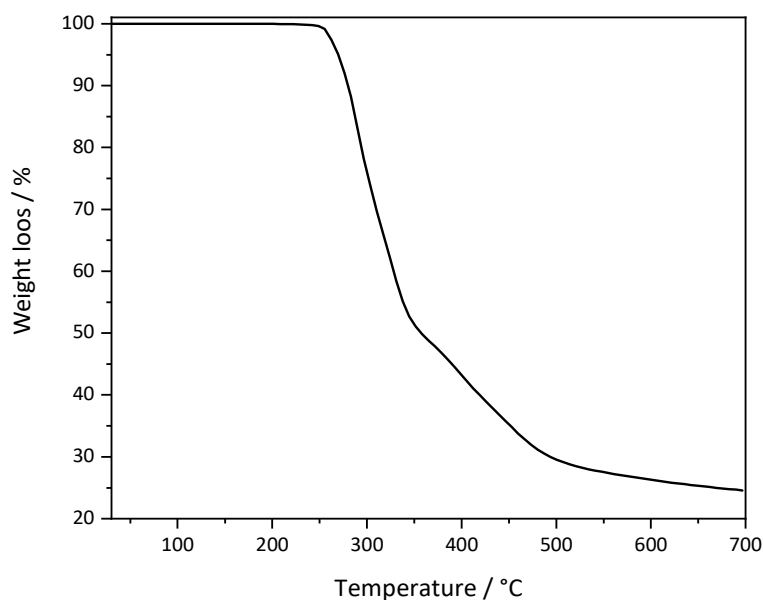


Figure 6.26: Thermogravimetric analysis curve of BTA 13. TGA data were recorded at a scanning rate of 10 K/min under a nitrogen atmosphere at temperatures ranging from 30 °C to 700 °C.

Synthesis of N,N',N''-tris[4-(methylthio)phenyl]-1,3,5-benzenetricarboxamid (BTA 14)

The reaction was carried out according to the general synthetic procedure to BTAs. After recrystallization from DMF, BTA 14 was obtained as white powder in 73 % yield.

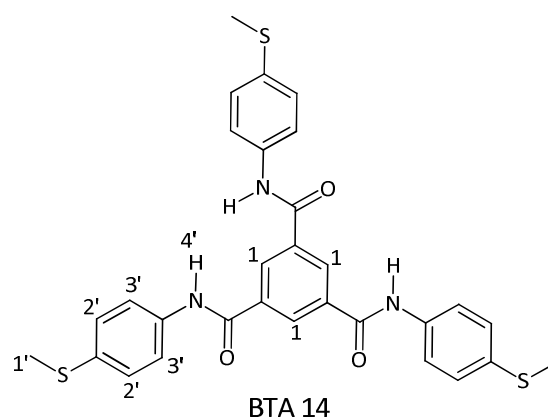


Table 6.14: Used components and key data for the synthesis of BTA 14.

		Sample weight (molar)
Core	1,3,5-Benzenetricarbonyl trichloride	2.88 g (10.8 mmol)
Amine	4-(Methylthio)-aniline	5 g (35.9 mmol)
Recrystallization	DMF	10 mL

Characterization:

¹H-NMR (300 MHz, DMSO, 25 °C):

δ (ppm) = 2.49 (s, 3 H, H_{1'}); 7.30 (d, 2 H, J = 8.91 Hz, H_{2'}); 7.79 (d, 2 H, J = 8.79 Hz, H_{3'}); 8.68 (s, 1 H, H₁); 10.60 (s, 1H, H_{4'})

FTIR-Spectroscopy (ATR):

3362 cm⁻¹; 3269 cm⁻¹; 3107 cm⁻¹; 3064 cm⁻¹; 2921 cm⁻¹; 1667 cm⁻¹; 1590 cm⁻¹; 1581 cm⁻¹; 1508 cm⁻¹; 1493 cm⁻¹

MS:

573 (M⁺) M/z; 435 M/z; 381 M/z; 269 M/z; 241 M/z; 138 M/z; 75 M/z; 36 M/z

DSC-Measurement:

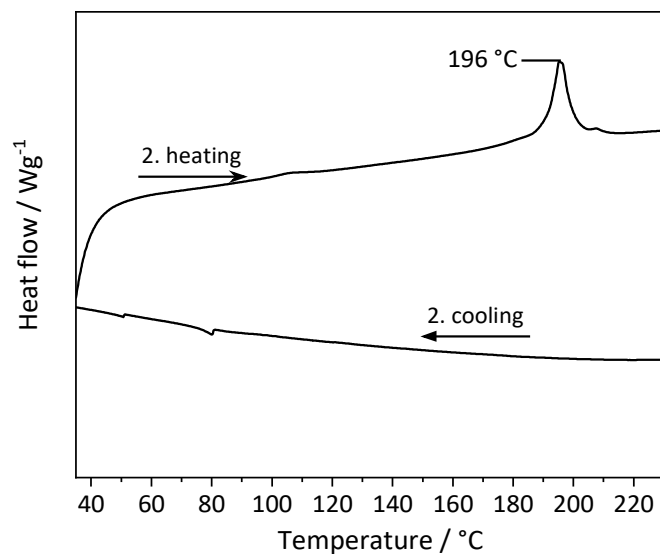


Figure 6.27: DSC heating and cooling scans of BTA 14. DSC data were recorded at a scanning rate of 10 K/min at temperatures ranging from 30 to 230 °C.

Thermogravimetric analysis:

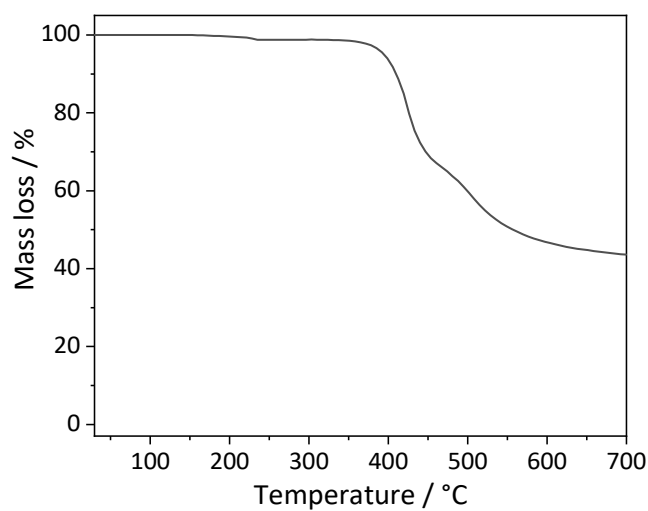


Figure 6.28: Thermogravimetric analysis curve of BTA 14. TGA data were recorded at a scanning rate of 10 K/min under a nitrogen atmosphere at temperatures ranging from 30 °C to 700 °C.

Synthesis of N,N',N''-tris[3-(methylthio)phenyl]-1,3,5-benzenetricarboxamid (BTA 15)

The reaction was carried out according to the general synthetic procedure to BTAs. After recrystallization from DMF, BTA 15 was obtained as white powder in 87 % yield.

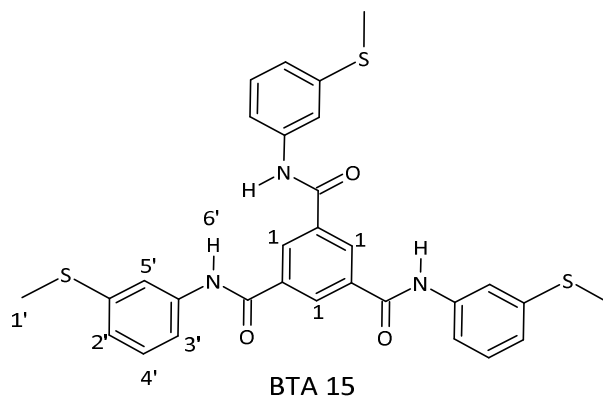


Table 6.15: Used components and key data for the synthesis of BTA 15.

		Sample weight (molar)
Core	1,3,5-Benzenetricarbonyl trichloride	5 g (0.0188 mol)
Amine	3-(Methylthio)-aniline	7 g (0.0622 mol)
Recrystallization	DMF	200 mL

Characterization:

¹H-NMR (300 MHz, DMSO, 25 °C):

δ (ppm) = 2.51 (3 H, H_{1'}); 7.04 (ddd, 1 H, 7.9, 1.8, 0.8 Hz, H_{3'}); 7.34 (dd, 1 H, J = 8.0 Hz, H_{4'}); 7.64 (m, 1 H, H_{2'}); 7.78 (t, 1 H, J = 1.8 Hz, H_{5'}); 8.71 (s, 1 H, H₁); 10.62 (s, 1 H, H_{6'})

FTIR-Spectroscopy (ATR):

3378 cm⁻¹; 3127 cm⁻¹; 3071 cm⁻¹; 2982 cm⁻¹; 2917 cm⁻¹; 1665 cm⁻¹; 1645 cm⁻¹; 1580 cm⁻¹; 1518 cm⁻¹; 1478 cm⁻¹; 1245 cm⁻¹

MS:

573 (M⁺) M/z; 435 M/z; 381 M/z; 269 M/z; 196 M/z; 74 M/z; 44 M/z

DSC-Measurement:

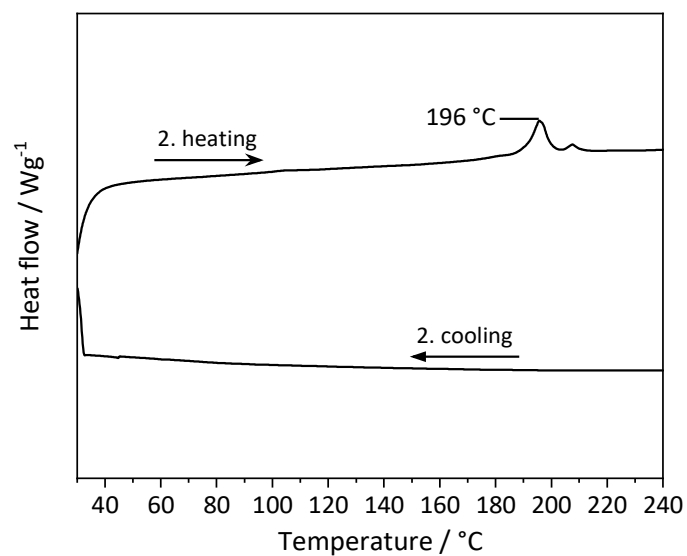


Figure 6.29: DSC heating and cooling scans of BTA 15. DSC data were recorded at a scanning rate of 10 K/min at temperatures ranging from 30 to 250 °C.

Thermogravimetric analysis:

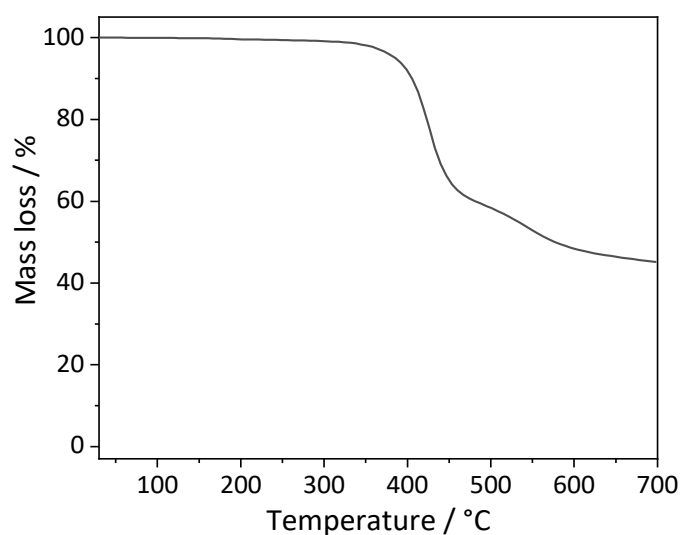


Figure 6.30: Thermogravimetric analysis curve of BTA 15. TGA data were recorded at a scanning rate of 10 K/min under a nitrogen atmosphere at temperatures ranging from 30 °C to 700 °C.

Synthesis of N,N',N''-tris[2-(methylthio)phenyl]-1,3,5-Benzenetricarboxamid (BTA 16)

The reaction was carried out according to the general synthetic procedure to BTAs. After recrystallization from DMF, BTA 16 was obtained as white powder in 90 % yield.

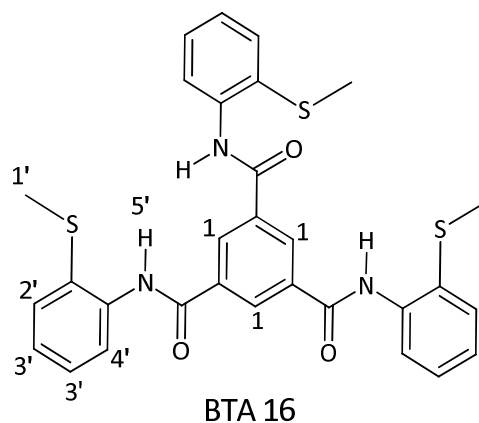


Table 6.16: Used components and key data for the synthesis of BTA 16.

		Sample weight (molar)
Core	1,3,5-Benzenetricarbonyl trichloride	5 g (0.0188 mol)
Amine	2-(Methylthio)-aniline	8.7 g (0.0622 mol)
Recrystallization	DMF	700 mL

Characterization:

¹H-NMR (300 MHz, DMSO, 25 °C):

δ (ppm) = 2.45 (s, 3 H, H_{1'}); 7.25 (td, 1 H, J = 7.5, 1.5 Hz, H_{2'}); 7.34 (td, 1 H, J = 7.5, 1.5 Hz, H_{4'}); 7.40 (m, 2 H, H_{3'}); 8.74 (s, 1 H, H₁); 10.26 (s, 1H, H_{5'})

FTIR-Spectroscopy (ATR):

3203 cm⁻¹; 3021 cm⁻¹; 2921 cm⁻¹; 1645 cm⁻¹; 1520 cm⁻¹; 1470 cm⁻¹; 1295 cm⁻¹; 751 cm⁻¹; 736 cm⁻¹; 675 cm⁻¹

MS:

573 (M⁺) M/z; 526 M/z; 466 M/z; 435 M/z; 381M/z; 296 M/z; 196 M/z; 75 M/z; 45 M/z

DSC-Measurement:

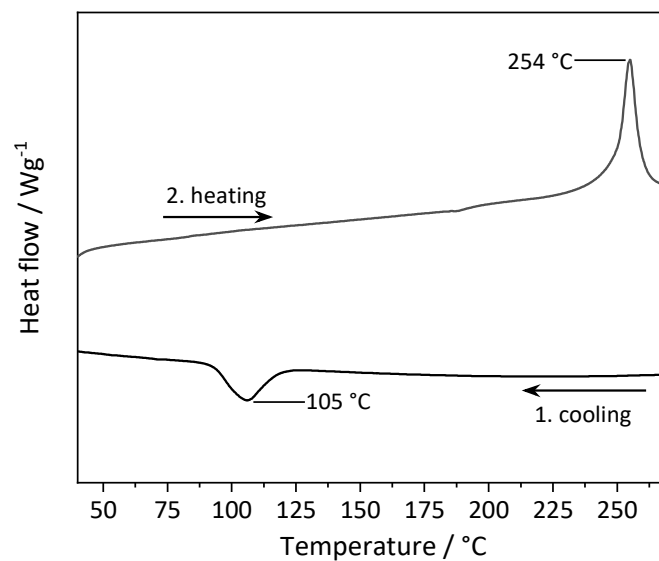


Figure 6.31: DSC heating and cooling scans of BTA 16. DSC data were recorded at a scanning rate of 10 K/min at temperatures ranging from 30 to 260 °C.

Thermogravimetric analysis:

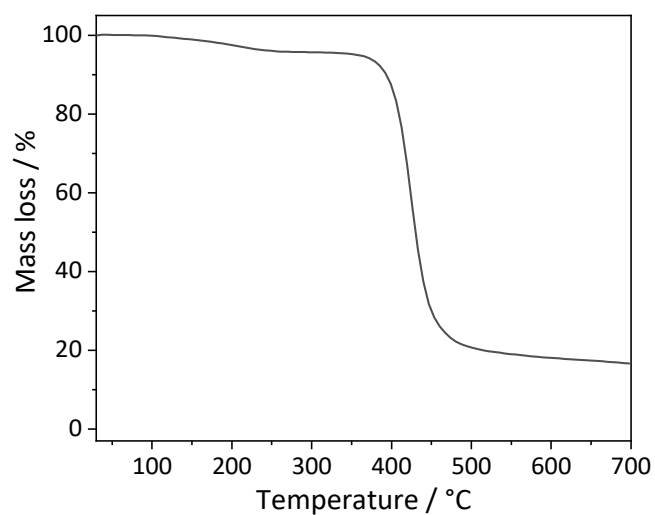


Figure 6.32: Thermogravimetric analysis curve of BTA 16. TGA data were recorded at a scanning rate of 10 K/min under a nitrogen atmosphere at temperatures ranging from 30 °C to 700 °C.

Synthesis of N,N',N''-tris(2-ethylhexyl)benzene-1,3,5-tricarboxamid (BTA 17)

For the reaction, 2-ethylhexylamine was added to trimethyl-1,3,5-benzenetricarboxylate. This mixture was stirred at 125 °C for approximately 15 h. The reaction mixture was cooled down to 20 °C. After recrystallization from acetone, BTA 17 was obtained as white powder in 67 % yield.

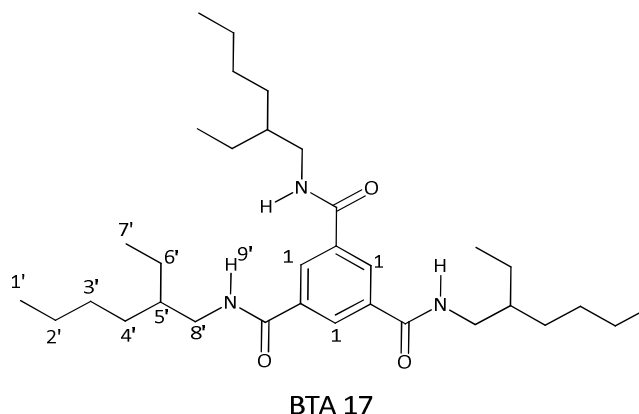


Table 6.17: Used components and key data for the synthesis of BTA 17.

		Sample weight (molar)
Core	Trimethyl-1,3,5-benzenetricarboxylate	15 g (59.5 mmol)
Amine	2-Ethylhexylamine	49 mL (297.5 mmol)
Recrystallization	Acetone	200 mL

Characterization:

¹H-NMR (300 MHz, DMSO, 25 °C):

δ (ppm) = 0.93 (m, 6 H, H_{1'}, H_{7'}); 1.31 (m, 8 H, H_{3'}, H_{4'}, H_{6'}); 1.42 (m, 1 H, H_{5'}); 3.48 (d, 2 H, J = 6.51, H_{8'}); 8.69 (s, 1 H, H₁)

FTIR-Spectroscopy (ATR):

3240 cm⁻¹; 3076 cm⁻¹; 2957 cm⁻¹; 2925 cm⁻¹; 2872 cm⁻¹; 2858 cm⁻¹; 1635 cm⁻¹; 1558 cm⁻¹; 1457 cm⁻¹; 1441 cm⁻¹

DSC-Measurement:

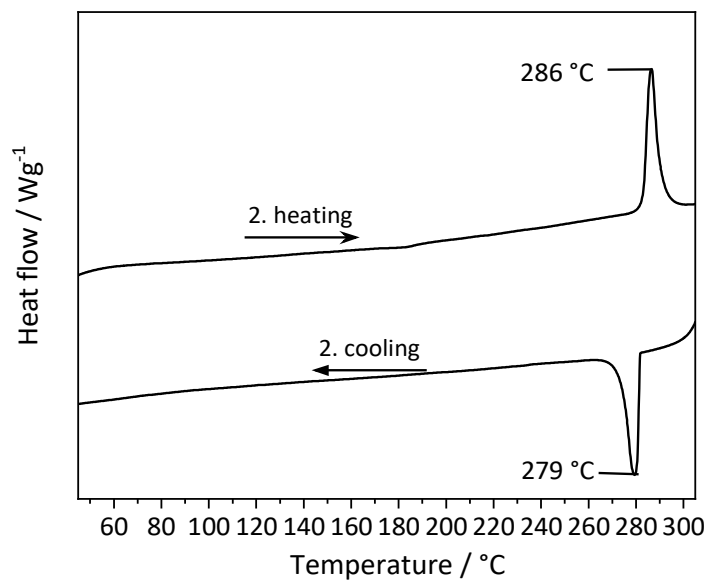


Figure 6.33: DSC heating and cooling scans of BTA 17. DSC data were recorded at a scanning rate of 10 K/min at temperatures ranging from 30 to 310 °C.

Thermogravimetric analysis:

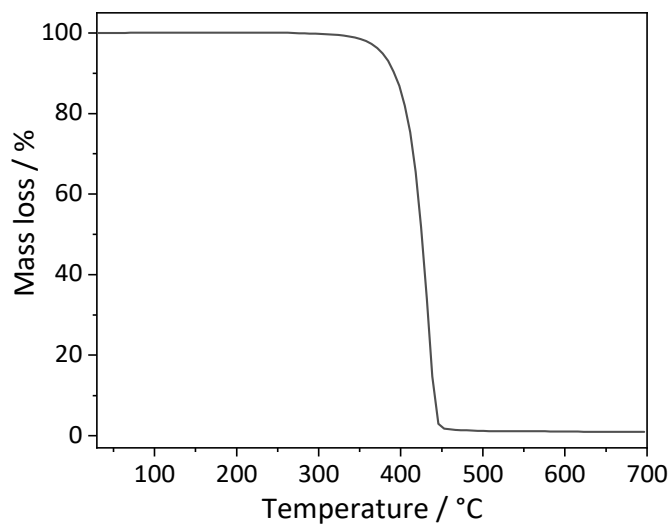


Figure 6.34: Thermogravimetric analysis curve of BTA 17. TGA data were recorded at a scanning rate of 10 K/min under a nitrogen atmosphere at temperatures ranging from 30 °C to 700 °C.

6.4 Silver nanoparticle synthesis

The silver nanoparticle suspensions were prepared according to the procedure of Li et al. and Rashid et al.^[203,204]

For the synthesis, 18 mg AgNO₃ were dissolved in 100 mL ultrapure water at room temperature. Then, the solution was heated up to the boiling temperature. Subsequently, 5 mL of a sodium citrate solution (1.0 wt. % sodium citrate in ultrapure water) were added to the solution while stirring very slowly. After 5 min, a slightly yellowish discoloration was visible and after 20 min the solution became dark yellow. The solution featured an absorption maximum of about 438 nm.

7 Literature

- [1] R. Connor, WWAP, *Water for a sustainable world*, UNESCO, Paris **2015**.
- [2] J. P. S. Cabral, *Water microbiology. Bacterial pathogens and water*, International journal of environmental research and public health **2010**, 7, 3657.
- [3] D. Werner, M. Valdivia-Garcia, P. Weir, M. Haffey, *Trihalomethanes formation in point of use surface water disinfection with chlorine or chlorine dioxide tablets*, Water and Environment Journal **2016**, 30, 271.
- [4] V. Verma, V. A. Arankalle, *Virological evaluation of domestic water purification devices commonly used in India emphasizes inadequate quality and need for virological standards*, Tropical medicine & international health TM & IH **2009**, 14, 885.
- [5] M. Thompson, *A critical review of water purification technology appropriate for developing countries: Northern Ghana as a case study*, Desalination and Water Treatment **2015**, 54, 3487.
- [6] S. Boisson, M. Kiyombo, L. Sthreshley, S. Tumba, J. Makambo, T. Clasen, *Field assessment of a novel household-based water filtration device: a randomised, placebo-controlled trial in the Democratic Republic of Congo*, PloS one **2010**, 5, e12613.
- [7] J. Beltrán-Heredia, J. Sánchez-Martín, *Municipal wastewater treatment by modified tannin flocculant agent*, Desalination **2009**, 249, 353.
- [8] P. B. Pavlinac, J. M. Naulikha, L. Chaba, N. Kimani, L. R. Sangaré, K. Yuhas, B. O. Singa, G. John-Stewart, J. L. Walson, *Water filter provision and home-based filter reinforcement reduce diarrhea in Kenyan HIV-infected adults and their household members*, The American journal of tropical medicine and hygiene **2014**, 91, 273.
- [9] P. Kalt, C. Birzer, H. Evans, A. Liew, M. Padovan, M. Watchman, *A Solar Disinfection Water Treatment System for Remote Communities*, Procedia Engineering **2014**, 78, 250.
- [10] R. Sharma, N. S. Singh, D. K. Singh, *Impact of heavy metal contamination and seasonal variations on enzyme's activity of Yamuna river soil in Delhi and NCR*, Appl Water Sci **2020**, 10, 794.
- [11] D. Paul, *Research on heavy metal pollution of river Ganga: A review*, Annals of Agrarian Science **2017**, 15, 278.
- [12] WWAP, *Wastewater: The untapped resource*, UNESCO, Paris **2017**.
- [13] WWAP, *The United Nations world water development report 2018: nature-based solutions for water; 2018*.
- [14] S. K. Sharma, R. Sanghi, *Wastewater Reuse and Management*, Springer Netherlands, Dordrecht **2013**.
- [15] B. Vriens, A. Voegelin, S. J. Hug, R. Kaegi, L. H. E. Winkel, A. M. Buser, M. Berg, *Quantification of Element Fluxes in Wastewaters: A Nationwide Survey in Switzerland*, Environmental science & technology **2017**, 51, 10943.

- [16] United Nations, *TRANSFORMING OUR WORLD: THE 2030 AGENDA FOR SUSTAINABLE DEVELOPMENT*, 2015.
- [17] K. Matthies, C. Schott, A. K. Anggraini, A. Silva, R. Diedel, H. Mühlebach, S. Fuchs, U. Obst, G. Brenner-Weiss, *Drinking water treatment for a rural karst region in Indonesia*, *Appl Water Sci* **2016**, *6*, 309.
- [18] T. Clasen, S. Nadakatti, S. Menon, *Microbiological performance of a water treatment unit designed for household use in developing countries*, *Tropical medicine & international health TM & IH* **2006**, *11*, 1399.
- [19] J. Hoslett, T. M. Massara, S. Malamis, D. Ahmad, I. van den Boogaert, E. Katsou, B. Ahmad, H. Ghazal, S. Simons, L. Wrobel, H. Jouhara, *Surface water filtration using granular media and membranes: A review*, *The Science of the total environment* **2018**, *639*, 1268.
- [20] G. Palmateer, D. Manz, A. Jurkovic, R. McInnis, S. Unger, K. K. Kwan, B. J. Dutka, *Toxicant and parasite challenge of Manz intermittent slow sand filter*, *Environmental toxicology* **1999**, *14*, 217.
- [21] M. A. Acheampong, R. J. Meulepas, P. N. Lens, *Removal of heavy metals and cyanide from gold mine wastewater*, *J. Chem. Technol. Biotechnol.* **2010**, *85*, 590.
- [22] G. Blanchard, M. Maunaye, G. Martin, *Removal of heavy metals from waters by means of natural zeolites*, *Water research* **1984**, *18*, 1501.
- [23] E. R. Christensen, J. T. Delwiche, *Removal of heavy metals from electroplating rinsewaters by precipitation, flocculation and ultrafiltration*, *Water research* **1982**, *16*, 729.
- [24] S. Herrmann, L. de Matteis, J. M. de La Fuente, S. G. Mitchell, C. Streb, *Removal of Multiple Contaminants from Water by Polyoxometalate Supported Ionic Liquid Phases (POM-SILPs)*, *Angewandte Chemie (International ed. in English)* **2017**, *56*, 1667.
- [25] P. D. Johnson, P. Girinathannair, K. N. Ohlinger, S. Ritchie, L. Teuber, J. Kirby, *Enhanced removal of heavy metals in primary treatment using coagulation and flocculation*, *Water environment research a research publication of the Water Environment Federation* **2008**, *80*, 472.
- [26] N. Mahfoudhi, S. Boufi, *Nanocellulose as a novel nanostructured adsorbent for environmental remediation: a review*, *Cellulose* **2017**, *24*, 1171.
- [27] N. Papaiconomou, G. Vite, N. Goujon, J.-M. Lévêque, I. Billard, *Efficient removal of gold complexes from water by precipitation or liquid–liquid extraction using ionic liquids*, *Green Chem.* **2012**, *14*, 2050.
- [28] H. A. Shaheen, H. M. Marwani, E. M. Soliman, *Selective adsorption of gold ions from complex system using oxidized multi-walled carbon nanotubes*, *Journal of Molecular Liquids* **2015**, *212*, 480.

- [29] Z. Yousefi and M.A. Zazouli, *Removal of Heavy Metals from Solid Wastes Leachates Coagulation-Flocculation Process*.
- [30] R. Vajtai, *Springer Handbook of Nanomaterials*, Springer Berlin Heidelberg, Berlin, Heidelberg **2013**.
- [31] T. Shimizu, *Self-Assembled Nanomaterials I*, Springer Berlin Heidelberg, Berlin, Heidelberg **2008**.
- [32] R. Nayak, R. Padhye, I. L. Kyratzis, Y. B. Truong, L. Arnold, *Recent advances in nanofibre fabrication techniques*, Textile Research Journal **2012**, 82, 129.
- [33] Z.-M. Huang, Y.-Z. Zhang, M. Kotaki, S. Ramakrishna, *A review on polymer nanofibers by electrospinning and their applications in nanocomposites*, Composites Science and Technology **2003**, 63, 2223.
- [34] P. K. Giri, D. K. Goswami, A. Perumal, *Advanced Nanomaterials and Nanotechnology*, Springer Berlin Heidelberg, Berlin, Heidelberg **2013**.
- [35] B. Bhushan, D. Luo, S. R. Schrickler, W. Sigmund, S. Zauscher, *Handbook of Nanomaterials Properties*, Springer Berlin Heidelberg, Berlin, Heidelberg **2014**.
- [36] A. Barhoum, M. Bechelany, A. S. H. Makhlof, *Handbook of Nanofibers*, Springer International Publishing, Cham **2019**.
- [37] D. Weiß, *Controlled Assembly of Supramolecular Nanofibers and their Applications: Dissertation*, Universität Bayreuth, Bayreuth **2016**.
- [38] S. Agarwal, A. Greiner, J. H. Wendorff, *Electrospinning of Manmade and Biopolymer Nanofibers-Progress in Techniques, Materials, and Applications*, Adv. Funct. Mater. **2009**, 19, 2863.
- [39] J. H. Wendorff, A. Greiner, S. Agarwal, *Electrospinning: Materials, processing, and applications*, Wiley-VCH, Weinheim **2012**.
- [40] I. M. Hutten, *Handbook of nonwoven filter media*, Elsevier/BH, Amsterdam **2007**.
- [41] S. Sinha-Ray, A. L. Yarin, B. Pourdeyhimi, *Meltblowing: I-basic physical mechanisms and threadline model*, Journal of Applied Physics **2010**, 108, 34912.
- [42] R. L. Shambaugh, *A macroscopic view of the melt-blowing process for producing microfibers*.
- [43] C. J. Ellison, A. Phatak, D. W. Giles, C. W. Macosko, F. S. Bates, *Melt blown nanofibers: Fiber diameter distributions and onset of fiber breakup*, Polymer **2007**, 48, 3306.
- [44] L. S. Pinchuk, V. A. Goldade, A. V. Makarevich, V. N. Kestelman, *Melt Blowing: Equipment, Technology, and Polymer Fibrous Materials*, Springer, Berlin, Heidelberg **2002**.
- [45] A. L. Yarin, S. Sinha-Ray, B. Pourdeyhimi, *Meltblowing: II-linear and nonlinear waves on viscoelastic polymer jets*, Journal of Applied Physics **2010**, 108, 34913.
- [46] R. Uppal, G. Bhat, C. Eash, K. Akato, *Meltblown nanofiber media for enhanced quality factor*, Fibers Polym **2013**, 14, 660.

- [47] C. J. Luo, S. D. Stoyanov, E. Stride, E. Pelan, M. Edirisinghe, *Electrospinning versus fibre production methods: from specifics to technological convergence*, *Chemical Society reviews* **2012**, *41*, 4708.
- [48] U. Boudriot, R. Dersch, A. Greiner, J. H. Wendorff, *Electrospinning approaches toward scaffold engineering--a brief overview*, *Artificial organs* **2006**, *30*, 785.
- [49] S. Agarwal, A. Greiner, J. H. Wendorff, *Polymere Nanofasern durch Elektrospinnen - Materialien für neue Anwendungen*, *Chemie Ingenieur Technik* **2008**, *80*, 1671.
- [50] W. Knoll, *Functional polymer films: 2 volume set*, Wiley, Chichester **2011**.
- [51] S. Kobayashi, K. Müllen, *Encyclopedia of Polymeric Nanomaterials*, Springer Berlin Heidelberg, Berlin, Heidelberg **2015**.
- [52] S. A. Theron, A. L. Yarin, E. Zussman, E. Kroll, *Multiple jets in electrospinning: experiment and modeling*, *Polymer* **2005**, *46*, 2889.
- [53] M. D. Calisir, A. Kilic, *A comparative study on SiO₂ nanofiber production via two novel non-electrospinning methods: Centrifugal spinning vs solution blowing*, *Materials Letters* **2020**, *258*, 126751.
- [54] T. Gries, D. Veit, B. Wulfhorst, *Textile Fertigungsverfahren: Eine Einführung*, Hanser, München **2019**.
- [55] S. Mahalingam, M. Edirisinghe, *Forming of polymer nanofibers by a pressurised gyration process*, *Macromolecular rapid communications* **2013**, *34*, 1134.
- [56] L. Ren, R. Ozisik, S. P. Kotha, P. T. Underhill, *Highly Efficient Fabrication of Polymer Nanofiber Assembly by Centrifugal Jet Spinning: Process and Characterization*, *Macromolecules* **2015**, *48*, 2593.
- [57] R. T. Weitz, L. Harnau, S. Rauschenbach, M. Burghard, K. Kern, *Polymer nanofibers via nozzle-free centrifugal spinning*, *Nano letters* **2008**, *8*, 1187.
- [58] X. Zhang, Y. Lu, *Centrifugal Spinning: An Alternative Approach to Fabricate Nanofibers at High Speed and Low Cost*, *Polymer Reviews* **2014**, *54*, 677.
- [59] W. Zou, R. Y. Chen, G. Z. Zhang, H. C. Zhang, J. P. Qu, *Recent Advances in Centrifugal Spinning Preparation of Nanofibers*, *AMR* **2014**, *1015*, 170.
- [60] J. J. Rogalski, L. Botto, C. W. M. Bastiaansen, T. Peijs, *A study of rheological limitations in rotary jet spinning of polymer nanofibers through modeling and experimentation*, *J Appl Polym Sci* **2020**, *3*, 48963.
- [61] M. Yanilmaz, A. M. Asiri, X. Zhang, *Centrifugally spun porous carbon microfibers as interlayer for Li-S batteries*, *J Mater Sci* **2020**, *55*, 3538.
- [62] S. Scheiner, *Noncovalent Forces*, Springer International Publishing, Cham **2015**.

- [63] M. Raynal, P. Ballester, A. Vidal-Ferran, van Leeuwen, Piet W N M, *Supramolecular catalysis. Part 1: non-covalent interactions as a tool for building and modifying homogeneous catalysts*, Chemical Society reviews **2014**, *43*, 1660.
- [64] H.-J. Schneider, R. M. Strongin, *Supramolecular interactions in chemomechanical polymers*, Accounts of chemical research **2009**, *42*, 1489.
- [65] J. W. Steed, J. L. Atwood, *Supramolecular chemistry*, Wiley, Chichester, UK **2009**.
- [66] M. Nič, J. Jirát, B. Košata, A. Jenkins, A. McNaught, *IUPAC Compendium of Chemical Terminology*, IUPAC, Research Triangle Park, NC **2009**.
- [67] P. A. Gale, J. W. Steed, *Supramolecular Chemistry*, John Wiley & Sons, Ltd, Chichester, UK **2012**.
- [68] A. Harada, *Supramolecular polymer chemistry*, Wiley-VCH, Weinheim Germany **2012**.
- [69] H. Dodziuk, *Introduction to Supramolecular Chemistry*, Kluwer Academic Publishers, Dordrecht **2002**.
- [70] J. D. Halley, D. A. Winkler, *Consistent concepts of self-organization and self-assembly*, Complexity **2008**, *14*, 10.
- [71] G. M. Whitesides, B. Grzybowski, *Self-assembly at all scales*, Science (New York, N.Y.) **2002**, *295*, 2418.
- [72] L. C. Palmer, S. I. Stupp, *Molecular self-assembly into one-dimensional nanostructures*, Accounts of chemical research **2008**, *41*, 1674.
- [73] X. Li, Y. Kuang, H.-C. Lin, Y. Gao, J. Shi, B. Xu, *Supramolecular nanofibers and hydrogels of nucleopeptides*, Angewandte Chemie (International ed. in English) **2011**, *50*, 9365.
- [74] T. Aida, E. W. Meijer, S. I. Stupp, *Functional supramolecular polymers*, Science (New York, N.Y.) **2012**, *335*, 813.
- [75] E. Mattia, S. Otto, *Supramolecular systems chemistry*, Nature nanotechnology **2015**, *10*, 111.
- [76] J. Meeuwissen, J. N. H. Reek, *Supramolecular catalysis beyond enzyme mimics*, Nature chemistry **2010**, *2*, 615.
- [77] Schenning, Albertus P H J, E. W. Meijer, *Supramolecular electronics; nanowires from self-assembled pi-conjugated systems*, Chemical communications (Cambridge, England) **2005**, 3245.
- [78] A. R. Hirst, B. Escuder, J. F. Miravet, D. K. Smith, *High-tech applications of self-assembling supramolecular nanostructured gel-phase materials: from regenerative medicine to electronic devices*, Angewandte Chemie (International ed. in English) **2008**, *47*, 8002.
- [79] K. K. Arora, V. R. Pedireddi, *A rational study of crystal engineering of supramolecular assemblies of 1,2,4,5-benzenetetracarboxylic acid*, The Journal of organic chemistry **2003**, *68*, 9177.
- [80] E. M. Pérez, N. Martín, *π - π interactions in carbon nanostructures*, Chemical Society reviews **2015**, *44*, 6425.

- [81] J. D. Badjić, A. Nelson, S. J. Cantrill, W. B. Turnbull, J. F. Stoddart, *Multivalency and cooperativity in supramolecular chemistry*, *Accounts of chemical research* **2005**, *38*, 723.
- [82] C. A. Hunter, J. K. M. Sanders, *The nature of .pi.-.pi. interactions*, *J. Am. Chem. Soc.* **1990**, *112*, 5525.
- [83] F. Wang, Y. A. Akimov, E. H. Khoo, C. He, *π - π interactions mediated self-assembly of gold nanoparticles into single crystalline superlattices in solution*, *RSC Adv.* **2015**, *5*, 90766.
- [84] C. G. Claessens, J. F. Stoddart, *π - π INTERACTIONS IN SELF-ASSEMBLY*, *J. Phys. Org. Chem.* **1997**, *10*, 254.
- [85] F. Würthner, Z. Chen, F. J. M. Hoeben, P. Osswald, C.-C. You, P. Jonkheijm, J. V. Herrikhuyzen, A. P. H. J. Schenning, P. P. A. M. van der Schoot, E. W. Meijer, E. H. A. Beckers, S. C. J. Meskers, R. A. J. Janssen, *Supramolecular p-n-heterojunctions by co-self-organization of oligo(p-phenylene vinylene) and perylene bisimide dyes*, *J. Am. Chem. Soc.* **2004**, *126*, 10611.
- [86] X. Yan, D. Xu, X. Chi, J. Chen, S. Dong, X. Ding, Y. Yu, F. Huang, *A multiresponsive, shape-persistent, and elastic supramolecular polymer network gel constructed by orthogonal self-assembly*, *Advanced materials (Deerfield Beach, Fla.)* **2012**, *24*, 362.
- [87] X. Yan, M. Zhou, J. Chen, X. Chi, S. Dong, M. Zhang, X. Ding, Y. Yu, S. Shao, F. Huang, *Supramolecular polymer nanofibers via electrospinning of a heteroditopic monomer*, *Chemical communications (Cambridge, England)* **2011**, *47*, 7086.
- [88] A. Bernet, R. Q. Albuquerque, M. Behr, S. T. Hoffmann, H.-W. Schmidt, *Formation of a supramolecular chromophore*, *Soft Matter* **2012**, *8*, 66.
- [89] R. C. T. Howe, A. P. Smalley, A. P. M. Guttenplan, M. W. R. Doggett, M. D. Eddleston, J. C. Tan, G. O. Lloyd, *A family of simple benzene 1,3,5-tricarboxamide (BTA) aromatic carboxylic acid hydrogels*, *Chemical communications* **2013**, *49*, 4268.
- [90] D. Kluge, J. C. Singer, B. R. Neugirg, J. W. Neubauer, H.-W. Schmidt, A. Fery, *Top-down meets bottom-up*, *Polymer* **2012**, *53*, 5754.
- [91] D. Kluge, J. C. Singer, J. W. Neubauer, F. Abraham, H.-W. Schmidt, A. Fery, *Influence of the molecular structure and morphology of self-assembled 1,3,5-benzenetrisamide nanofibers on their mechanical properties*, *Small (Weinheim an der Bergstrasse, Germany)* **2012**, *8*, 2563.
- [92] J. C. Singer, R. Giesa, H.-W. Schmidt, *Shaping self-assembling small molecules into fibres by melt electrospinning*, *Soft Matter* **2012**, *8*, 9972.
- [93] C. M. A. Leenders, T. Mes, M. B. Baker, M. M. E. Koenigs, P. Besenius, A. R. A. Palmans, E. W. Meijer, *From supramolecular polymers to hydrogel materials*, *Mater. Horiz.* **2014**, *1*, 116.
- [94] C. M. A. Leenders, L. Albertazzi, T. Mes, M. M. E. Koenigs, A. R. A. Palmans, E. W. Meijer, *Supramolecular polymerization in water harnessing both hydrophobic effects and hydrogen bond formation*, *Chemical communications* **2013**, *49*, 1963.

- [95] R. Q. Albuquerque, A. Timme, R. Kress, J. Senker, H.-W. Schmidt, *Theoretical investigation of macrodipoles in supramolecular columnar stackings*, Chemistry **2013**, *19*, 1647.
- [96] C. Zehe, M. Schmidt, R. Siegel, K. Kreger, V. Daebel, S. Ganzleben, H.-W. Schmidt, J. Senker, *Influence of fluorine side-group substitution on the crystal structure formation of benzene-1,3,5-trisamides*, CrystEngComm **2014**, *16*, 9273.
- [97] F. Abraham, S. Ganzleben, D. Hanft, P. Smith, H.-W. Schmidt, *Synthesis and Structure – Efficiency Relations of 1,3,5-Benzenetrisamides as Nucleating Agents and Clarifiers for Isotactic Poly(propylene)*, Macromol. Chem. Phys. **2010**, *211*, 171.
- [98] F. Abraham, R. Kress, P. Smith, H.-W. Schmidt, *A New Class of Ultra-Efficient Supramolecular Nucleating Agents for Isotactic Polypropylene*, Macromol. Chem. Phys. **2013**, *214*, 17.
- [99] M. Blomenhofer, S. Ganzleben, D. Hanft, H.-W. Schmidt, M. Kristiansen, P. Smith, K. Stoll, D. Mäder, K. Hoffmann, *“Designer” Nucleating Agents for Polypropylene*, Macromolecules **2005**, *38*, 3688.
- [100] D. Kluge, F. Abraham, S. Schmidt, H.-W. Schmidt, A. Fery, *Nanomechanical properties of supramolecular self-assembled whiskers determined by AFM force mapping*, Langmuir the ACS journal of surfaces and colloids **2010**, *26*, 3020.
- [101] M. Kristiansen, P. Smith, H. Chanzy, C. Baerlocher, V. Gramlich, L. McCusker, T. Weber, P. Pattison, M. Blomenhofer, H.-W. Schmidt, *Structural Aspects of 1,3,5-Benzenetrisamides – A New Family of Nucleating Agents*, Crystal Growth & Design **2009**, *9*, 2556.
- [102] H. Misslitz, K. Kreger, H.-W. Schmidt, *Supramolecular nanofiber webs in nonwoven scaffolds as potential filter media*, Small **2013**, *9*, 2053-8, 2025.
- [103] F. Richter, H.-W. Schmidt, *Supramolecular Nucleating Agents for Poly(butylene terephthalate) Based on 1,3,5-Benzenetrisamides*, Macromol. Mater. Eng. **2013**, *298*, 190.
- [104] M. Schmidt, J. J. Wittmann, R. Kress, D. Schneider, S. Steuernagel, H.-W. Schmidt, J. Senker, *Crystal Structure of a Highly Efficient Clarifying Agent for Isotactic Polypropylene*, Crystal Growth & Design **2012**, *12*, 2543.
- [105] A. Timme, R. Kress, R. Q. Albuquerque, H.-W. Schmidt, *Phase behavior and mesophase structures of 1,3,5-benzene- and 1,3,5-cyclohexanetricarboxamides: towards an understanding of the losing order at the transition into the isotropic phase*, Chemistry **2012**, *18*, 8329.
- [106] D. Weiss, D. Skrybeck, H. Misslitz, D. Nardini, A. Kern, K. Kreger, H.-W. Schmidt, *Tailoring Supramolecular Nanofibers for Air Filtration Applications*, ACS applied materials & interfaces **2016**, *8*, 14885.
- [107] S. Cantekin, de Greef, Tom F A, A. R. A. Palmans, *Benzene-1,3,5-tricarboxamide: a versatile ordering moiety for supramolecular chemistry*, Chemical Society reviews **2012**, *41*, 6125.

- [108] L. Brunsveld, A. Schenning, M. Broeren, H. M. Janssen, J. Vekemans, E. W. Meijer, *Chiral Amplification in Columns of Self-Assembled N,N',N''-Tris((S)-3,7-dimethyloctyl)benzene-1,3,5-tricarboxamide in Dilute Solution*, Chem. Lett. **2000**, 29, 292.
- [109] M. P. Lightfoot, F. S. Mair, R. G. Pritchard, J. E. Warren, *New supramolecular packing motifs: Π -stacked rods encased in triply-helical hydrogen bonded amide strands*, Chem. Commun. **1999**, 1945.
- [110] L. Rajput, V. V. Chernyshev, K. Biradha, *Assembling triple helical amide-to-amide hydrogen bonded columns of tris(4-halophenyl)benzene-1,3,5-tricarboxamides into porous materials via halogen...halogen interactions*, Chemical communications **2010**, 46, 6530.
- [111] S. Cantekin, T. F. A. de Greef, A. R. A. Palmans, *Benzene-1,3,5-tricarboxamide: a versatile ordering moiety for supramolecular chemistry*, Chemical Society reviews **2012**, 41, 6125.
- [112] Andreas T. Haedler, *Synthesis, Self-Assembly and Photophysical Properties of Multichromophoric Systems*: Dissertation, Universität Bayreuth **2014**.
- [113] M. Barboiu, J.-M. Lehn, *Dynamic chemical devices: modulation of contraction/extension molecular motion by coupled-ion binding/pH change-induced structural switching*, Proceedings of the National Academy of Sciences of the United States of America **2002**, 99, 5201.
- [114] K. K. Coti, M. E. Belowich, M. Liong, M. W. Ambrogio, Y. A. Lau, H. A. Khatib, J. I. Zink, N. M. Khashab, J. F. Stoddart, *Mechanised nanoparticles for drug delivery*, Nanoscale **2009**, 1, 16.
- [115] F. Ercole, T. P. Davis, R. A. Evans, *Photo-responsive systems and biomaterials*, Polym. Chem. **2010**, 1, 37.
- [116] H.-J. Kim, T. Kim, M. Lee, *Responsive nanostructures from aqueous assembly of rigid-flexible block molecules*, Accounts of chemical research **2011**, 44, 72.
- [117] C. Tsitsilianis, *Responsive reversible hydrogels from associative "smart" macromolecules*, Soft Matter **2010**, 6, 2372.
- [118] Y. Wang, H. Xu, X. Zhang, *Tuning the Amphiphilicity of Building Blocks*, Adv. Mater. **2009**, 21, 2849.
- [119] H. Zhang, M. Yu, A. Song, Y. Song, X. Xin, J. Shen, S. Yuan, *Modulating hierarchical self-assembly behavior of a peptide amphiphile/nonionic surfactant mixed system*, RSC Adv **2016**, 6, 9186.
- [120] B.-B. Wang, W.-S. Li, X.-R. Jia, M. Gao, Y. Ji, X. Zhang, Z.-C. Li, L. Jiang, Y. Wei, *Self-assembly and supramolecular transition of poly(amidoamine) dendrons focally modified with aromatic chromophores*, Journal of colloid and interface science **2007**, 314, 289.
- [121] M. A. J. Gillissen, M. M. E. Koenigs, J. J. H. Spiering, Vekemans, Jef A J M, A. R. A. Palmans, I. K. Voets, E. W. Meijer, *Triple helix formation in amphiphilic discotics: demystifying solvent effects in supramolecular self-assembly*, Journal of the American Chemical Society **2014**, 136, 336.

- [122] L. Rajput, G. Mukherjee, K. Biradha, *Influence of Solvents in Assembling Tris(4-halophenyl)benzene-1,3,5-tricarboxamides*, *Crystal Growth & Design* **2012**, *12*, 5773.
- [123] Frank Abraham, *Synthesis and structure-property relations of 1,3,5-benzenetrisamides as nucleating agents for isotactic polypropylene and poly(vinylidene fluoride)*: Dissertation Universität Bayreuth **2009**.
- [124] D. Weiss, K. Kreger, H.-W. Schmidt, *Self-Assembly of Alkoxy-Substituted 1,3,5-Benzenetrisamides Under Controlled Conditions*, *Macromol. Mater. Eng.* **2017**, *302*, 1600390.
- [125] N. E. Shi, H. Dong, G. Yin, Z. Xu, S. H. Li, *A Smart Supramolecular Hydrogel Exhibiting pH-Modulated Viscoelastic Properties*, *Adv. Funct. Mater.* **2007**, *17*, 1837.
- [126] A. Frank, A. Bernet, K. Kreger, H.-W. Schmidt, *Supramolecular microtubes based on 1,3,5-benzenetricarboxamides prepared by self-assembly upon heating*, *Soft Matter* **2020**, *16*, 4564.
- [127] X.-Z. Luo, X.-J. Jia, J.-H. Deng, J.-L. Zhong, H.-J. Liu, K.-J. Wang, D.-C. Zhong, *A microporous hydrogen-bonded organic framework: exceptional stability and highly selective adsorption of gas and liquid*, *Journal of the American Chemical Society* **2013**, *135*, 11684.
- [128] P. Jana, A. Paikar, S. Bera, S. K. Maity, D. Haldar, *Porous organic material from discotic tricarboxamide: side chain-core interactions*, *Organic letters* **2014**, *16*, 38.
- [129] Y. Ishioka, N. Minakuchi, M. Mizuhata, T. Maruyama, *Supramolecular gelators based on benzenetricarboxamides for ionic liquids*, *Soft Matter* **2014**, *10*, 965.
- [130] O. Kotova, R. Daly, C. M. G. dos Santos, M. Boese, P. E. Kruger, J. J. Boland, T. Gunnlaugsson, *Europium-directed self-assembly of a luminescent supramolecular gel from a tripodal terpyridine-based ligand*, *Angewandte Chemie (International ed. in English)* **2012**, *51*, 7208.
- [131] D. K. Kumar, D. A. Jose, P. Dastidar, A. Das, *Nonpolymeric Hydrogelators Derived from Trimesic Amides*, *Chem. Mater.* **2004**, *16*, 2332.
- [132] B.-C. Tzeng, B.-S. Chen, H.-T. Yeh, G.-H. Lee, S.-M. Peng, *Self-assembly of N,N',N''-tris(4-pyridyl)trimesic amide and N,N',N''-tris(3-pyridyl)trimesic amide with Ag I or Cd II ions*, *New J. Chem.* **2006**, *30*, 1087.
- [133] Anja R. A. Palmans, Jef A. J. M. Vekemans, Huub Kooijman, Anton L. Spek, E. W. Meijer, *Hydrogen-bonded porous solid derived from trimesic amide*, *Chem. Commun.*, *1997*, 2247.
- [134] S. Y. Ryu, S. Kim, J. Seo, Y.-W. Kim, O.-H. Kwon, D.-J. Jang, S. Y. Park, *Strong fluorescence emission induced by supramolecular assembly and gelation: luminescent organogel from nonemissive oxadiazole-based benzene-1,3,5-tricarboxamide gelator*, *Chemical communications (Cambridge, England)* **2004**, 70.
- [135] Y. Zhou, M. Xu, T. Yi, S. Xiao, Z. Zhou, F. Li, C. Huang, *Morphology-tunable and photoresponsive properties in a self-assembled two-component gel system*, *Langmuir the ACS journal of surfaces and colloids* **2007**, *23*, 202.

- [136] J. J. van Gorp, Vekemans, Jef A. J. M., E. W. Meijer, *C3 -Symmetrical Supramolecular Architectures*, J. Am. Chem. Soc. **2002**, *124*, 14759.
- [137] S. J. Lee, C. R. Park, J. Y. Chang, *Molecular aggregation of disklike benzenetricarboxamides containing diacetylenic groups in bulk and organic solvents*, Langmuir the ACS journal of surfaces and colloids **2004**, *20*, 9513.
- [138] A. Paikar, A. Pramanik, D. Haldar, *Influence of side-chain interactions on the self-assembly of discotic tricarboxyamides*, RSC Adv **2015**, *5*, 31845.
- [139] M. Aksit, B. Klose, C. Zhao, K. Kreger, H.-W. Schmidt, V. Altstädt, *Morphology control of extruded polystyrene foams with benzene-trisamide-based nucleating agents*, Journal of Cellular Plastics **2019**, *55*, 249.
- [140] M. Aksit, C. Zhao, B. Klose, K. Kreger, H.-W. Schmidt, V. Altstädt, *Extruded Polystyrene Foams with Enhanced Insulation and Mechanical Properties by a Benzene-Trisamide-Based Additive*, Polymers **2019**, *11*.
- [141] B. Lohrengel, *Einführung in die thermischen Trennverfahren: Trennung von Gas-, Dampf- und Flüssigkeitsgemischen*, Oldenbourg, München **2012**.
- [142] D. B. Purchas, K. Sutherland, *Handbook of filter media*, Elsevier Advanced Technology, Oxford **2002**.
- [143] N. P. Cheremisinoff, *Liquid filtration*, Butterworth-Heinemann, Boston **1998**.
- [144] T. C. Dickenson, *Filters and filtration handbook*, Elsevier Advanced Technology, Oxford **2000**.
- [145] H. Fuchs, J. Lünenschloss, W. Albrecht, W. Kittelmann (Eds.), *Nonwoven fabrics*, Wiley-VCH, Weinheim **2003**.
- [146] T. Sparks, G. Chase, *Filters and filtration handbook*, Butterworth-Heinemann, Oxford, UK **2016**.
- [147] R. J. Wakeman, E. S. Tarleton, *Filtration: Equipment selection modelling and process simulation*, Elsevier, Oxford **1999**.
- [148] M. Stieß, *Mechanische Verfahrenstechnik - Partikeltechnologie 1*, Springer Berlin Heidelberg, Berlin, Heidelberg **2009**.
- [149] I. M. Hutten, *Handbook of nonwoven filter media*, Elsevier/BH, Amsterdam **2007**.
- [150] K. W. Kolasinski, *Surface science: Foundations of catalysis and nanoscience*, Wiley, Chichester, West Sussex, United Kingdom **2012**.
- [151] K. S. W. Sing, *Reporting physisorption data for gas/solid systems with special reference to the determination of surface area and porosity (Recommendations 1984)*, Pure and Applied Chemistry **1985**, *57*.
- [152] K. Hauffe, S. R. Morrison, *Adsorption: Eine Einführung in die Probleme der Adsorption*, Walter De Gruyter, Berlin **1974**.

- [153] J. P. Muscat, D. M. Newns, *Chemisorption on metals*, Pergamon Press, Oxford, New York **1978**.
- [154] S. M. Russell, M. Shen, D.-J. Liu, P. A. Thiel, *Adsorption of sulfur on Ag(100)*, *Surface Science* **2011**, *605*, 520.
- [155] J. MCCARTY, *Thermodynamics of sulfur chemisorption on metals IV. Alumina-supported platinum*, *Journal of Catalysis* **1983**, *82*, 92.
- [156] J. G. McCarty, H. Wise, *Thermodynamics of sulfur chemisorption on metals. I. Alumina-supported nickel*, *The Journal of Chemical Physics* **1980**, *72*, 6332.
- [157] H. Sellers, A. Ulman, Y. Shnidman, J. E. Eilers, *Structure and binding of alkanethiolates on gold and silver surfaces: implications for self-assembled monolayers*, *J. Am. Chem. Soc.* **1993**, *115*, 9389.
- [158] N. Gonzalez-Lakunza, N. Lorente, A. Arnau, *Chemisorption of Sulfur and Sulfur-Based Simple Molecules on Au(111)*, *J. Phys. Chem. C* **2007**, *111*, 12383.
- [159] M. Waqif, A. M. Saad, M. Bensitel, J. Bachelier, O. Saur, J.-C. Lavalley, *Comparative study of SO₂ adsorption on metal oxides*, *Faraday Trans.* **1992**, *88*, 2931.
- [160] J. Bénard, *The Chemical Adsorption of Sulfur on Metals: Thermodynamics and Structure*, *Catalysis Reviews* **1970**, *3*, 93.
- [161] A. Ferral, P. Paredes-Olivera, V. A. Macagno, E. M. Patrino, *Chemisorption and physisorption of alkanethiols on Cu. A quantum mechanical investigation*, *Surface Science* **2003**, *525*, 85.
- [162] R. D. Köhn, L. Tomás Laudo, Z. Pan, F. Speiser, G. Kociok-Köhn, *Triangular tricopper(I) clusters supported by donor-substituted triazacyclohexanes*, *Dalton transactions (Cambridge, England 2003)* **2009**, 4556.
- [163] P. J. M. Stals, M. M. J. Smulders, R. Martin-Rapun, A. R. A. Palmans, E. W. Meijer, *Asymmetrically substituted benzene-1,3,5-tricarboxamides: self-assembly and odd-even effects in the solid state and in dilute solution*, *Chemistry* **2009**, *15*, 2071.
- [164] C. S. Zehe, J. A. Hill, N. P. Funnell, K. Kreger, K. P. van der Zwan, A. L. Goodwin, H.-W. Schmidt, J. Senker, *Mesoscale Polarization by Geometric Frustration in Columnar Supramolecular Crystals*, *Angewandte Chemie (International ed. in English)* **2017**, *56*, 4432.
- [165] J. Clayden, N. Greeves, S. G. Warren, P. Wothers, *Organic chemistry*, Oxford University Press, Oxford **2001**.
- [166] G. Cheng, C. Yin, H. Tu, S. Jiang, Q. Wang, X. Zhou, X. Xing, C. Xie, X. Shi, Y. Du, H. Deng, Z. Li, *Controlled Co-delivery of Growth Factors through Layer-by-Layer Assembly of Core-Shell Nanofibers for Improving Bone Regeneration*, *ACS nano* **2019**, *13*, 6372.
- [167] G. Duan, A. Greiner, *Air-Blowing-Assisted Coaxial Electrospinning toward High Productivity of Core/Sheath and Hollow Fibers*, *Macromol. Mater. Eng.* **2019**, *304*, 1800669.

- [168] M. F. Elahi, W. Lu, *Core-shell Fibers for Biomedical Applications-A Review*, J Bioeng Biomed Sci **2013**, *03*.
- [169] L. W. Honaker, S. Vats, M. Anyfantakis, J. P. F. Lagerwall, *Elastic sheath-liquid crystal core fibres achieved by microfluidic wet spinning*, J. Mater. Chem. C **2019**, *7*, 11588.
- [170] M. W. Lee, S. S. Yoon, A. L. Yarin, *Solution-Blown Core-Shell Self-Healing Nano- and Microfibers*, ACS applied materials & interfaces **2016**, *8*, 4955.
- [171] D. Liu, Q. Shi, S. Jin, Y. Shao, J. Huang, *Self-assembled core-shell structured organic nanofibers fabricated by single-nozzle electrospinning for highly sensitive ammonia sensors*, InfoMat **2019**, *1*, 525.
- [172] J. Meng, G. Wu, X. Wu, H. Cheng, Z. Xu, S. Chen, *Microfluidic-Architected Nanoarrays/Porous Core-Shell Fibers toward Robust Micro-Energy-Storage*, Advanced science (Weinheim, Baden-Wurttemberg, Germany) **2020**, *7*, 1901931.
- [173] A. L. Yarin, E. Zussman, J. H. Wendorff, A. Greiner, *Material encapsulation and transport in core-shell micro/nanofibers, polymer and carbon nanotubes and micro/nanochannels*, J. Mater. Chem. **2007**, *17*, 2585.
- [174] A. L. Yarin, *Coaxial electrospinning and emulsion electrospinning of core-shell fibers*, Polym. Adv. Technol. **2011**, *22*, 310.
- [175] E. Zussman, A. L. Yarin, A. V. Bazilevsky, R. Avrahami, M. Feldman, *Electrospun Polyaniline/Poly(methyl methacrylate)-Derived Turbostratic Carbon Micro-/Nanotubes*, Adv. Mater. **2006**, *18*, 348.
- [176] Y. M. Abul-Haija, S. Roy, P. W. J. M. Frederix, N. Javid, V. Jayawarna, R. V. Ulijn, *Biocatalytically triggered co-assembly of two-component core/shell nanofibers*, Small (Weinheim an der Bergstrasse, Germany) **2014**, *10*, 973.
- [177] R. G. Jones, C. K. Ober, P. Hodge, P. Kratochvíl, G. Moad, M. Vert, *Terminology for aggregation and self-assembly in polymer science (IUPAC Recommendations 2013)*, Pure and Applied Chemistry **2012**, *85*, 463.
- [178] Royal Society of Chemistry, *Co-assembly*, <https://www.rsc.org/publishing/journals/prospect/ontology.asp?id=CMO:0001990&MSID=c0cs00034e>.
- [179] L. Brunsveld, B. J. Folmer, E. W. Meijer, R. P. Sijbesma, *Supramolecular polymers*, Chemical reviews **2001**, *101*, 4071.
- [180] H. Thomas, X. Zhu, M. Möller, Kl. Kreger, D. Nardini, H.-W. Schmidt, *Supramolecular nanofiber composites for highly efficient and selective removal of gold(III) from aqueous media.*, Technische Textilien **2019**, 80 E.

- [181] J. M. Arnal Arnal, M. Sancho Fernández, G. Martín Verdú, J. Lora García, *Design of a membrane facility for water potabilization and its application to Third World countries*, *Desalination* **2001**, *137*, 63.
- [182] L. S. Abebe, Y.-H. Su, R. L. Guerrant, N. S. Swami, J. A. Smith, *Point-of-Use Removal of Cryptosporidium parvum from Water: Independent Effects of Disinfection by Silver Nanoparticles and Silver Ions and by Physical Filtration in Ceramic Porous Media*, *Environmental science & technology* **2015**, *49*, 12958.
- [183] S. Ede, L. Hafner, P. Dunlop, J. Byrne, G. Will, *Photocatalytic disinfection of bacterial pollutants using suspended and immobilized TiO₂ powders*, *Photochemistry and photobiology* **2012**, *88*, 728.
- [184] M. D. Sobsey, C. E. Stauber, L. M. Casanova, J. M. Brown, M. A. Elliott, *Point of use household drinking water filtration: A practical, effective solution for providing sustained access to safe drinking water in the developing world*, *Environmental science & technology* **2008**, *42*, 4261.
- [185] S.-L. Loo, A. G. Fane, W. B. Krantz, T.-T. Lim, *Emergency water supply: a review of potential technologies and selection criteria*, *Water research* **2012**, *46*, 3125.
- [186] D. Ren, L. M. Colosi, J. A. Smith, *Evaluating the sustainability of ceramic filters for point-of-use drinking water treatment*, *Environmental science & technology* **2013**, *47*, 11206.
- [187] C. K. Pooi, H. Y. Ng, *Review of low-cost point-of-use water treatment systems for developing communities*, *npj Clean Water* **2018**, *1*.
- [188] V. K. Gupta, I. Ali, T. A. Saleh, A. Nayak, S. Agarwal, *Chemical treatment technologies for waste-water recycling—an overview*, *RSC Adv.* **2012**, *2*, 6380.
- [189] A. S. Brady-Estévez, S. Kang, M. Elimelech, *A single-walled-carbon-nanotube filter for removal of viral and bacterial pathogens*, *Small (Weinheim an der Bergstrasse, Germany)* **2008**, *4*, 481.
- [190] A. Mollahosseini, A. Rahimpour, M. Jahamshahi, M. Peyravi, M. Khavarpour, *The effect of silver nanoparticle size on performance and antibacteriability of polysulfone ultrafiltration membrane*, *Desalination* **2012**, *306*, 41.
- [191] B. Pant, H. R. Pant, D. R. Pandeya, G. Panthi, K. T. Nam, S. T. Hong, C. S. Kim, H. Y. Kim, *Characterization and antibacterial properties of Ag NPs loaded nylon-6 nanocomposite prepared by one-step electrospinning process*, *Colloids and Surfaces A: Physicochemical and Engineering Aspects* **2012**, *395*, 94.
- [192] H. Zhang, *Application of Silver Nanoparticles in Drinking Water Purification*, Kingston Providence West Greenwich, Vereinigte Staaten **2013**.
- [193] X. Zan, M. Kozlov, T. J. McCarthy, Z. Su, *Covalently attached, silver-doped poly(vinyl alcohol) hydrogel films on poly(L-lactic acid)*, *Biomacromolecules* **2010**, *11*, 1082.

- [194] J. Thiel, L. Pakstis, S. Buzby, M. Raffi, C. Ni, D. J. Pochan, S. I. Shah, *Antibacterial properties of silver-doped titania*, *Small* **2007**, *3*, 799.
- [195] K. Shamel, M. B. Ahmad, S. D. Jazayeri, P. Shabanzadeh, P. Sangpour, H. Jahangirian, Y. Gharayebi, *Investigation of antibacterial properties silver nanoparticles prepared via green method*, *Chemistry Central journal* **2012**, *6*, 73.
- [196] K. Zodrow, L. Brunet, S. Mahendra, D. Li, A. Zhang, Q. Li, P. J. J. Alvarez, *Polysulfone ultrafiltration membranes impregnated with silver nanoparticles show improved biofouling resistance and virus removal*, *Water research* **2009**, *43*, 715.
- [197] F. Diagne, R. Malaisamy, V. Boddie, R. D. Holbrook, B. Eribo, K. L. Jones, *Polyelectrolyte and silver nanoparticle modification of microfiltration membranes to mitigate organic and bacterial fouling*, *Environmental science & technology* **2012**, *46*, 4025.
- [198] S. Lin, R. Huang, Y. Cheng, J. Liu, B. L. T. Lau, M. R. Wiesner, *Silver nanoparticle-alginate composite beads for point-of-use drinking water disinfection*, *Water research* **2013**, *47*, 3959.
- [199] M. Oves, M. Zain Khan, I. M.I. Ismail, *Modern Age Environmental Problems and their Remediation*, Springer International Publishing, Cham **2018**.
- [200] P. Jain, T. Pradeep, *Potential of silver nanoparticle-coated polyurethane foam as an antibacterial water filter*, *Biotechnology and bioengineering* **2005**, *90*, 59.
- [201] S. Kühn, S. Schneider, B. Meisterjahn, K. Schlich, K. Hund-Rinke, C. Schlechtriem, *Silver nanoparticles in sewage treatment plant effluents: chronic effects and accumulation of silver in the freshwater amphipod *Hyalella azteca**, *Environmental sciences Europe* **2018**, *30*, 7.
- [202] K. Schlich, T. Klawonn, K. Terytze, K. Hund-Rinke, *Hazard assessment of a silver nanoparticle in soil applied via sewage sludge*, *Environmental sciences Europe* **2013**, *25*.
- [203] H. Li, H. Xia, D. Wang, X. Tao, *Simple synthesis of monodisperse, quasi-spherical, citrate-stabilized silver nanocrystals in water*, *Langmuir the ACS journal of surfaces and colloids* **2013**, *29*, 5074.
- [204] M. U. Rashid, M. K. H. Bhuiyan, M. E. Quayum, *Synthesis of Silver Nano Particles (Ag-NPs) and their uses for Quantitative Analysis of Vitamin C Tablets*, *Dhaka Univ. J. Pharm. Sci* **2013**, *12*.

8 Acknowledgement

At first, I would like to thank my supervisor, Prof. Dr. Hans-Werner Schmidt, for giving me the opportunity to do this PhD thesis at the Chair of Macromolecular Chemistry I at the University of Bayreuth. I would especially like to thank him for the very interesting, exciting and application-oriented topic. I also thank him for the opportunity to work in a very well-equipped laboratory, as well as for the discussions, his advice his support.

I would like to thank the German Federation of Industrial Research Associations "Otto von Guericke" e.V. (AiF), which, within the framework of the program for the promotion of joint industrial research (IGF), has financially supported this work by the Federal Ministry for Economic Affairs and Energy on the basis of a resolution of the German Bundestag in the processing of the project "*IGF-Vorhaben-Nummer 19071 N: Funktionale Nanofaser-Komposite zur selektiven Schadstoffentfernung aus Stoffströmen*".

Prof. Dr. Martin Möller, Dr. Helga Thomas, Dr. Elisabeth Heine, Dr. Xiaomin Zhu, Olga Manova, Renate Jansen and Rita Gartzten at the Deutschen Wollforschungsinstitut (DWI) - Leibniz-Institut für Interaktive Materialien e.V. in Aachen. I would like to thank them for the very good cooperation and biological bacterial growth tests as part of this doctoral thesis. In particular, I would like to thank Helga Thomas for the many discussions and assistance throughout the PhD thesis and beyond.

Very special thanks also go to Dr. Klaus Kreger, who contributed to the success of this work through his constant support, many fruitful to discussions, and extensive expertise on this subject.

I would also like to thank the technical staff of the chair Macromolecular Chemistry I Jutta Failner and Sandra Ganzleben for synthesizing and providing the trisamides for this thesis. Special thanks also go to Alexander Kern through his support in case of problems with the filter test set up. A big thank you goes to Dr. Markus Winterer for the successful synthesis of BTA 10. I also thank him for his input during various project meetings.

Special thanks go to the staff of the Bavarian Polymer Institute (BPI). In particular, Dr. Beate Förster, Dr. Ulrich Mansfeld and Martina Heider for instruction and support in the area of scanning electron microscopy. Likewise, I thank Dr. Markus Drechsler for instruction on the transmission electron microscope. Big thanks to Dr. Holger Schmalz for the first important measurements of the co-assembled samples using Raman imaging, as well as the instruction and support on WITec 300 RA⁺. Without this instrument we would never have been able to discover the core-shell structures.

In addition, I would like to thank Petra Weiss and Christina Wunderlich for their support with many administrative problems. Likewise, my thanks go to Birgit Dollhopf and Ursula Peschek from Neue Materialien Bayreuth GmbH for their administrated support.

In addition, I would also like to thank the electronic and mechanical workshops of the University of Bayreuth for the production of various holders and equipment parts.

At this point I would like to thank my friends and former lab colleagues Dr. Daniel Buchholz and Dr. Daniel Kremer for many discussions and help even after they left the university.

Furthermore, I would like to thank the bachelor students Marcel Große, Paula Wolf, Agnes Specht, Youli Stephanoph and Joan Sander for their experimental support.

I would also like to thank all the other members of the Macromolecular Chemistry I group, especially Markus Drummer and Andreas Frank, for their constant willingness to discuss my work. A big thank you goes to my "tandem partner" Julia Wollmann, who motivated me to start writing this thesis early.

Likewise, I would like to thank all the friends who accompanied me during my studies.

A big thank you goes to my family, who always supported me throughout my studies and also during my doctoral thesis.

My greatest and all preceding thanks go to Lina Mayr, who, despite her own ongoing doctoral studies, always stood by my side and supported me as best as she could.

(Eidesstattliche) Versicherungen und Erklärungen

(§ 9 Satz 2 Nr. 3 PromO BayNAT)

Hiermit versichere ich eidesstattlich, dass ich die Arbeit selbstständig verfasst und keine anderen als die von mir angegebenen Quellen und Hilfsmittel benutzt habe (vgl. Art. 64 Abs. 1 Satz 6 BayHSchG).

(§ 9 Satz 2 Nr. 3 PromO BayNAT)

Hiermit erkläre ich, dass ich die Dissertation nicht bereits zur Erlangung eines akademischen Grades eingereicht habe und dass ich nicht bereits diese oder eine gleichartige Doktorprüfung endgültig nicht bestanden habe.

(§ 9 Satz 2 Nr. 4 PromO BayNAT)

Hiermit erkläre ich, dass ich Hilfe von gewerblichen Promotionsberatern bzw. -vermittlern oder ähnlichen Dienstleistern weder bisher in Anspruch genommen habe noch künftig in Anspruch nehmen werde.

(§ 9 Satz 2 Nr. 7 PromO BayNAT)

Hiermit erkläre ich mein Einverständnis, dass die elektronische Fassung meiner Dissertation unter Wahrung meiner Urheberrechte und des Datenschutzes einer gesonderten Überprüfung unterzogen werden kann.

(§ 9 Satz 2 Nr. 8 PromO BayNAT)

Hiermit erkläre ich mein Einverständnis, dass bei Verdacht wissenschaftlichen Fehlverhaltens Ermittlungen durch universitätsinterne Organe der wissenschaftlichen Selbstkontrolle stattfinden können.

.....

Bayreuth, Datum, David Nardini